Galaxy Clusters as Cosmological Probes: Mass Calibration, Matter Profiles, and Baryonic Feedback

Aditya Singh

München 2025

Galaxy Clusters as Cosmological Probes: Mass Calibration, Matter Profiles, and Baryonic Feedback

Aditya Singh

Dissertation
an der Fakultät für Physik
der Ludwig–Maximilians–Universität
München

vorgelegt von
Aditya Singh
aus Bhopal, India

München, den 12.08.2025

Erstgutachter: Prof. Dr. Joseph J. Mohr
Zweitgutachter: Prof. Dr. Simon D. M. White
Tag der mündlichen Prüfung: 26.09.2025

Contents

List of Figures

List of Tables

Zusammenfassung

Galaxienhaufen sind ein leistungsfähiges Mittel zur Erforschung der Astrophysik und Kosmologie und bieten Einblicke in die Strukturbildung, die Baryonphysik und das kosmologische Modell. Sie beherbergen riesige Reservoirs an heißem, ionisiertem Gas, das als Intracluster-Medium (ICM) bekannt ist. Das ICM emittiert Röntgenstrahlung und ist verantwortlich für den thermischen Sunyaev-Zel'dovich-Effekt (tSZE) auf den kosmischen Mikrowellenhintergrund (CMB), indem Photonen an den hochenergetischen Elektronen gestreut werden, was ein direktes Maß für den thermischen Druck eines Haufens darstellt. Gleichzeitig ist der schwache Gravitationslinseneffekt eine Schlüsseltechnik zur Untersuchung von Haufenmassen und Materieverteilungen. In dieser Arbeit werden Multi-Wellenlängen-Daten verwendet, darunter tSZE-Messungen des Southpole-Teleskops (SPT), Röntgenbeobachtungen von ROSAT und schwache Linsenscherungen vom Dark Energy Survey (DES), um eine Massenkalibrierung durchzuführen, Haufenprofile zu untersuchen und die Auswirkungen baryonischer Rückkopplungen auf das nichtlineare Materie-Leistungsspektrum zu bewerten.

Zunächst analysieren wir die von dem schwachen Linseneffekt abgeleiteten Materieprofile von 698 SPT Haufen anhand der DES-Messungen der schwachen Linsenscherung. Diese Profile weisen Selbstähnlichkeit auf, wenn sie um masse- und rotverschiebungsabhängige systematische Variationen skaliert werden, was eine neue Bayes'sche Methode zur Massenkalibrierung ermöglicht. Diese Kalibrierung stimmt mit den Ergebnissen unabhängiger Studien überein und bietet ein hohes Signal-Rausch-Verhältnis für die Form von Materieprofilen der Haufen, was sich auf die dunkle Materie und die baryonische Physik auswirkt.

Als Nächstes erweitern wir die Massenkalibrierung auf den MARD-Y3 Haufenkatalog von ROSAT aus, indem wir die SPT tSZE- und MARD-Y3 Röntgenkataloge kombinieren. Diese gemeinsame Kalibrierung verbessert die Unsicherheiten der beobachtbaren tSZE-Masse-Relation und bricht die Entartungen der reinen SPT-Analyse auf. Durch die Anwendung dieser Beschränkungen werden die Unsicherheiten der kosmologischen Parameter in der $\Omega_{\rm m} - \sigma_8$-Ebene um 40% verringert, was verbesserte Tests der sogenannten S_8-Spannung ermöglicht. Wir finden auch eine signifikante Abweichung von den ΛCDM-Vorhersagen in den Außenbezirken von Haufen, was auf Spannungen mit theoretischen Modellen hindeutet. Darüber hinaus stellen wir fest, dass sich optisch ausgewählte redMaPPer-Haufen mit geringerer Richness anders verhalten als ICM-ausgewählte Haufen, was darauf hindeutet, dass es in den optisch ausgewählten Haufen mit geringerer Richness eine erhebliche Kontamination geben könnte.

Schließlich untersuchen wir den Einfluss baryonischer Rückkopplung auf das nichtlineare Leistungsspektrum der Materie, die für korrekte kosmologische Aussagen über kosmische Scherung und Galaxienhaufen auf kleinen Skalen entscheidend ist. Zu diesem Zweck messen wir die beobachtbare $M_{\rm ICM}$-$M_{\rm 500c}$-Masse-Relation mit Hilfe von ICM-Messungen aus Röntgenbeobachtungen von Chandra und XMM-Newton, kombiniert mit DES-Massen, die durch den schwachen Linseneffekt für 122 SPT-ausgewählte Haufen bestimmt wurden. Durch den Vergleich der beobachteten $M_{\rm ICM}$-$M_{\rm 500c}$-Masse-Beziehung mit Ergebnissen aus hydrodynamischen Simulationen schließen wir auf die Unterdrückung des Materie-Leistungsspektrums aufgrund baryonischer Rückkopplungsmechanismen. Unsere Ergebnisse schließen extreme Rückkopplungsmodelle aus und deuten darauf hin, dass die baryonische Unterdrückung allein die S_8-Spannung zwischen den kosmischen Scherungsbeschränkungen bei niedriger Rotverschiebung ($z \lesssim 1$) und den Planck-CMB-Messungen nicht vollständig auflösen kann.

Diese Analysen liefern robuste Einschränkungen für die Beziehungen zwischen beobachtbarer Masse und Haufen, verbessern unser Verständnis von Haufenprofilen und tragen zur Modellierung von baryonischen Effekten in großskaligen Strukturmessungen bei, die für die Überprüfung des kosmologischen Modells und die Erforschung der dunklen Materie entscheidend sind.

Abstract

Galaxy clusters are powerful tools for studying astrophysics and cosmology, providing insights into structure formation, baryonic physics, and the cosmological model. They host vast reservoirs of hot, ionized gas known as the intracluster medium (ICM). This ICM emits copiously in X-rays and also imprints the thermal Sunyaev–Zel'dovich effect (tSZE) on the cosmic microwave background (CMB) as photons scatter off its high-energy electrons, providing a direct measure of the cluster thermal pressure. Meanwhile, weak gravitational lensing is a key technique for probing cluster masses and matter distributions. This thesis uses multi-wavelength data, including tSZE measurements from the South Pole Telescope (SPT), X-ray observations from ROSAT, and weak lensing shear from the Dark Energy Survey (DES), to perform mass calibration, study cluster profiles, and assess the impact of baryonic feedback on the non-linear matter power spectrum.

We first analyze weak lensing inferred matter profiles of 698 SPT-selected clusters using DES weak lensing shear measurements. When rescaled for mass- and redshift-dependent systematic variations, these profiles exhibit self-similarity, allowing for a new Bayesian method for mass calibration. This calibration is consistent with independent cluster lensing results and provides high signal-to-noise constraints on the shape of cluster matter profiles, with implications for dark matter and baryonic physics.

Next, we extend mass calibration to the MARD-Y3 cluster catalog from ROSAT by combining the SPT tSZE and MARD-Y3 X-ray samples. This joint calibration improves constraints on the tSZE observable-mass relation, breaking degeneracies in the SPT-only analysis. Applying these constraints tightens cosmological parameter constraints in the $\Omega_{\rm m} - \sigma_8$ plane by 40%, enabling improved tests of the so-called S_8 tension. We also find a significant deviation from ΛCDM predictions in the outskirts of clusters, suggesting tensions with theoretical models. Additionally, we find that lower-richness redMaPPer optically-selected clusters behave differently than ICM-selected clusters, providing clues suggesting there may be significant contamination in the low richness optically selected cluster sample.

Finally, we investigate the impact of baryonic feedback on the non-linear matter power spectrum, which is crucial for unbiased cosmological constraints from cosmic shear and galaxy clustering on small scales. To do so, we measure the $M_{\rm ICM}$-$M_{\rm 500c}$ observable-mass relation using ICM measurements from deep X-ray observations from Chandra and XMM-Newton, combined with DES weak lensing constrained masses for 122 SPT-selected clusters. By comparing the observed $M_{\rm ICM}$-$M_{\rm 500c}$ observable-mass relation with results from

hydrodynamical simulations, we infer the suppression of the matter power spectrum due to baryonic feedback mechanisms. Our results rule out extreme feedback models and suggest that baryonic suppression alone may not fully resolve the S_8 tension between cosmic shear constraints at low redshift ($z \lesssim 1$) and Planck CMB measurements.

These analyses provide robust constraints on cluster observable-mass relations, enhance our understanding of cluster profiles, and contribute to modeling baryonic effects in large-scale structure measurements, which are crucial for testing the cosmological model and probing dark matter.

Chapter 1

Introduction

Galaxy clusters constitute the most massive collapsed halos in the Universe. They contain hundreds of galaxies, vast amounts of hot intracluster gas, and significant dark matter components. A typical galaxy cluster has a total mass ranging from 10^{14} to 10^{15} solar masses ($M_{\odot}$)(Voit, 2005; Kravtsov & Borgani, 2012). Approximately 80–85% of this mass is dark matter, 10–15% is intracluster medium (ICM) gas, and the remaining 1–4% is in the form of galaxies (e.g., Andreon, 2010; Planelles et al., 2013b). The ICM is a hot, diffuse plasma with temperatures of 10^7 to 10^8 Kelvin, emitting X-rays detectable by space-based observatories (Voit, 2005). The ICM also imprints the thermal Sunyaev–Zel'dovich effect (tSZE) on the cosmic microwave background (CMB) as photons scatter off its high-energy electrons (Sunyaev & Zeldovich, 1972; Planck Collaboration et al., 2020). The galaxies within clusters are primarily elliptical and lenticular, with a lower fraction of spirals than field galaxies (Dressler, 1980).

Galaxy clusters are powerful tools for probing cosmology due to their abundance, distribution, and evolution over cosmic time (Allen et al., 2011; Kravtsov & Borgani, 2012). They provide constraints on cosmological parameters and insights into the underlying physics of the Universe (Allen et al., 2011; Vikhlinin et al., 2009), including the process driving the cosmic acceleration (Haiman et al., 2001). The number density of galaxy clusters as a function of mass and redshift, known as the cluster mass function, is sensitive to the matter density parameter ($\Omega_{\rm m}$) and the amplitude of matter fluctuations (σ_8). By comparing observed cluster abundances with theoretical predictions, we can constrain these parameters and test models of structure formation (Planck Collaboration et al., 2016; Bocquet et al., 2019; Bocquet et al., 2024b; Ghirardini et al., 2024).

Galaxy clusters also provide crucial insights into the feedback processes that regulate cosmic evolution (Fabian, 2012). The ICM, observed in X-rays, reveals how energy from active galactic nuclei (AGN) prevents excessive cooling and star formation (McNamara & Nulsen, 2007). AGN jets and outflows create shock waves and cavities in the ICM, redistributing energy and maintaining thermal balance (Forman et al., 2005; Fabian, 2012). Additionally, supernovae and galaxy interactions contribute to feedback by stirring turbulence and stripping gas from galaxies, influencing their evolution (Tonnesen & Bryan, 2008; Schaye et al., 2015). These processes shape the structure of galaxy clusters, control

star formation rates, and impact the growth of cosmic structures over time (Sijacki et al., 2007). Observations from X-ray, radio, and optical telescopes help us to understand how feedback mechanisms influence the Universe on large scales.

In this chapter, we will explore the formation of halos and the effects of feedback on these systems. This will lay the groundwork for the following chapters of the thesis, where we will study galaxy cluster profiles and constrain feedback using both observed and simulated galaxy clusters.

1.1 Formation of Galaxy Clusters

The Universe we observe today is a vast network of galaxies grouped into clusters, filaments, and voids. Understanding the formation of galaxy clusters requires a journey back to the beginning of the Cosmos, through the epochs of cosmic inflation, the emergence of primordial density fluctuations, the growth of dark matter halos, and the complex interplay of baryonic processes. This section aims to guide the reader through these stages, elucidating the key physical parameters and equations that underpin our current understanding of galaxy cluster formation.

1.1.1 The Early Universe and Cosmic Inflation

In the moments immediately following the Big Bang, the Universe underwent a dramatic and rapid phase of expansion known as cosmic inflation (Guth, 1981; Linde, 1982). This epoch, which lasted for only about 10^{-32} seconds, is thought to have expanded the Universe exponentially, increasing its size by many orders of magnitude. Inflation addresses several fundamental issues in cosmology, such as the horizon and flatness problems, by ensuring that regions currently separated by vast distances were once causally connected and that the Universe appears spatially flat on large scales.

1.1.1.1 Dynamics and Consequences of Inflation

Cosmic inflation is typically driven by a scalar field, often called the inflaton (denoted by ϕ), which has an associated potential energy $V(\phi)$. During inflation, the energy density of the inflaton field dominates the Universe, leading to an almost constant vacuum energy that fuels the exponential expansion. The dynamics of the inflaton field are described by the Klein-Gordon equation in an expanding background, and the *slow-roll* conditions are imposed to ensure that inflation lasts long. The two slow-roll parameters, ϵ and η, are defined as:

$$\epsilon = \frac{M_{\rm Pl}^2}{2}\left(\frac{V'(\phi)}{V(\phi)}\right)^2, \quad \eta = M_{\rm Pl}^2\frac{V''(\phi)}{V(\phi)}. \tag{1.1}$$

Here, $M_{\rm Pl}$ is the reduced Planck mass, and $V'(\phi)$ and $V"(\phi)$ are the first and second derivatives of the potential with respect to ϕ. For inflation to occur, these parameters must

satisfy $\epsilon \ll 1$ and $|\eta| \ll 1$ (Liddle & Lyth, 2000), ensuring that the inflaton rolls slowly down its potential and sustains the rapid expansion.

The inflationary model has several profound implications for the observable Universe:

- **Horizon Problem:** Before inflation, regions of the Universe that are now widely separated could not have been in causal contact. Inflation solves this by stretching a small, causally connected region to cosmic scales (Linde, 1982).
- **Flatness Problem:** The rapid expansion during inflation drives the spatial curvature of the Universe towards zero, explaining why the current Universe appears nearly flat on large scales (Planck Collaboration et al., 2020).
- **Monopole Problem:** Grand Unified Theories (GUTs) predict the production of heavy magnetic monopoles and other exotic relics in the early Universe. Inflation dilutes their density by expanding the Universe so rapidly that they become essentially undetectable (Guth, 1981).
- **Homogeneity and Isotropy:** The uniform expansion driven by inflation ensures the large-scale homogeneity and isotropy of the Universe, consistent with observations of the CMB (Planck Collaboration et al., 2020).

1.1.1.2 Quantum Fluctuations and Structure Formation

During inflation, quantum fluctuations in the inflaton field were stretched to macroscopic scales. These fluctuations are the seeds of all structure in the Universe and can be characterized by their statistical properties, typically described using the matter power spectrum $P(k)$ (Bardeen et al., 1986). The power spectrum quantifies the amplitude of these fluctuations as a function of the wavenumber k (the inverse of the spatial scale):

$$P(k) \propto k^n \, T^2(k). \tag{1.2}$$

Here:

- **k**: Spatial frequency; larger k corresponds to smaller scales.
- **n**: The *spectral index*; a scale-invariant (Harrison–Zel'dovich) spectrum has $n \approx 1$, indicating fluctuations of nearly equal amplitude across all scales.
- **T(k)**: The *transfer function*, which accounts for physical processes that modify the initial spectrum as the Universe evolves, such as the transition from radiation to matter domination.

These quantum fluctuations became imprinted in the CMB as tiny temperature anisotropies. They correspond to primordial density perturbations, which, under gravitational instability, grew into the galaxies, galaxy clusters, and cosmic web structures observed today. Inflation thus provides a natural mechanism for generating the initial conditions for structure formation, connecting early-universe physics with present-day cosmological observations.

1.1.2 Primordial Density Fluctuations and Linear Growth

Following cosmic inflation, the Universe contained small, nearly scale-invariant density fluctuations. These primordial perturbations are characterized by the density contrast

$$\delta(\mathbf{x}, t) = \frac{\rho(\mathbf{x}, t) - \bar{\rho}(t)}{\bar{\rho}(t)}, \tag{1.3}$$

where $\rho(\mathbf{x}, t)$ is the local matter density and $\bar{\rho}(t)$ is the cosmic mean matter density. This dimensionless quantity δ quantifies the relative deviation from the average density and serves as the starting point for understanding cosmic structure formation (Peebles, 1981).

The statistical distribution of these fluctuations is described by the matter power spectrum $P(k)$, which captures the variance of δ as a function of scale. It is defined via the two-point correlation function in Fourier space:

$$\langle \delta(\mathbf{k}) \delta^*(\mathbf{k}') \rangle = (2\pi)^3 \delta_D(\mathbf{k} - \mathbf{k}') P(k), \tag{1.4}$$

where $\delta(\mathbf{k})$ is the Fourier transform of $\delta(\mathbf{x}, t)$, and δ_D is the Dirac delta function. The functional form of $P(k)$ reflects the primordial spectrum and the physical processes that shape structure across cosmic time.

In the early Universe, when $|\delta| \ll 1$, the evolution of perturbations is well-described by linear theory. The time dependence of δ can be separated using a linear growth factor $D(t)$:

$$\delta(\mathbf{x}, t) = \delta(\mathbf{x}, t_i) \, \frac{D(t)}{D(t_i)}, \tag{1.5}$$

where t_i is a reference time and $D(t)$ encapsulates the effect of cosmic expansion on structure growth. The growth factor satisfies the differential equation

$$\ddot{D}(t) + 2H(t)\dot{D}(t) - 4\pi G \bar{\rho}(t) D(t) = 0, \tag{1.6}$$

where $H(t)$ is the Hubble parameter, G is the gravitational constant. This equation shows that both the expansion rate and the matter content govern the rate of structure formation. In a matter-dominated Universe, the solution reduces to $D(t) \propto a(t)$, where $a(t)$ is the scale factor (Liddle & Lyth, 2000; Dodelson, 2003).

Several physical parameters are central to this framework. The density contrast δ marks over- and under-densities, with $\delta > 0$ regions eventually collapsing under gravity. The power spectrum $P(k)$ sets the initial conditions for structure formation, and the growth factor $D(t)$ tracks their evolution through time. The Hubble parameter $H(t)$ acts as a friction term in the growth equation, while the mean matter density $\bar{\rho}(t)$ drives gravitational collapse.

Linear theory, though limited to early epochs when fluctuations are small, offers vital insight into the initial phases of structure formation. These small perturbations grow into non-linear structures—galaxies, groups, and clusters—through gravitational instability. The nearly scale-invariant nature of the primordial fluctuations, combined with their linear growth, provides the foundation for understanding the observed large-scale structure of the Universe (Peebles, 1981; Dodelson, 2003).

1.1.3 Dark Matter Halos and the Onset of Nonlinearity

As density perturbations grow, they eventually enter the non-linear regime where gravitational self-interaction dominates. This leads to the formation of bound structures—dark matter halos—which serve as the seeds for galaxies and clusters. The transition from linear to non-linear evolution marks a pivotal stage in cosmic structure formation.

A simplified model of this process is the spherical collapse scenario, in which a uniformly overdense sphere decouples from the Hubble expansion and collapses under its gravity. The collapse occurs when the linearly extrapolated density contrast exceeds a critical threshold:

$$\delta_c \approx 1.686, \tag{1.7}$$

valid in an Einstein-de Sitter Universe (Press & Schechter, 1974; Peebles, 1981). Regions where $\delta > \delta_c$ are thus expected to form collapsed objects.

The Press–Schechter formalism statistically connects the initial density field to the abundance of collapsed halos. It predicts the comoving number density of halos per unit mass via the mass function

$$\frac{dn}{dM} = \sqrt{\frac{2}{\pi}}\,\frac{\bar{\rho}}{M^2}\,\frac{\delta_c}{\sigma(M)}\left|\frac{d\ln\sigma}{d\ln M}\right|\exp\left(-\frac{\delta_c^2}{2\sigma^2(M)}\right), \tag{1.8}$$

where $\bar{\rho}$ is the mean matter density and $\sigma(M)$ is the root-mean-square amplitude of density fluctuations smoothed on a mass scale M. The exponential term captures the rarity of high-density peaks exceeding the collapse threshold.

While the spherical model is illustrative, it oversimplifies the true dynamics of structure formation. Real overdensities are triaxial and experience tidal interactions. Extensions like the Sheth–Tormen formalism (Sheth & Tormen, 1999) modify the collapse threshold to better match simulations, incorporating ellipsoidal collapse effects. These refinements lead to more accurate halo mass functions (Mo et al., 2010).

Non-linear gravitational collapse of these high-density regions results in virialized dark matter halos, which later accumulate baryonic matter. The evolution of these halos—including mergers and gas accretion—governs the formation of galaxies and clusters. A detailed review of halo statistics and their connection to large-scale structure is provided in (Cooray & Sheth, 2002).

In summary, Equations 1.7 and 1.8 link the linear regime of the early Universe to the non-linear structures observed today. The emergence and distribution of dark matter halos form the gravitational framework on which all visible cosmic structures are built.

1.1.4 Mergers, Accretion, and Shock Heating

As dark matter halos form and grow, galaxy clusters evolve through a series of dynamic processes. In addition to the initial collapse, clusters grow through mergers with other clusters and groups and through the continuous accretion of gas and dark matter from the surrounding cosmic web. These processes are accompanied by shock heating of the ICM, which plays a crucial role in setting the thermal properties of clusters.

1.1.4.1 Cluster Mergers

Galaxy clusters grow primarily via mergers, where two or more halos collide and coalesce. During a merger, the gravitational potential energy of the colliding clusters is converted into kinetic energy. This kinetic energy is then partially transformed into thermal energy through shock waves that propagate through the ICM. These shocks heat the gas to high temperatures, typically in the range of several 10^7 to 10^8 K, making the clusters luminous in X-ray wavelengths (Markevitch & Vikhlinin, 2007; Sarazin, 1986).

The merging process is complex and often involves multiple substructures, which can be observed as cold fronts, shock fronts, or other discontinuities in the X-ray surface brightness and temperature maps. Detailed studies of merging clusters, such as those by Ricker and Sarazin (Ricker & Sarazin, 2001), provide important constraints on the dynamical state and history of these systems.

1.1.4.2 Accretion and Shock Heating

In addition to discrete merger events, clusters grow continuously by accreting diffuse gas and dark matter from their surroundings. As gas falls into the deep potential well of a cluster, it is accelerated to high velocities. When this gas encounters the denser ICM, it undergoes a shock that converts its bulk kinetic energy into thermal energy. This process of shock heating is critical for maintaining the high temperatures observed in clusters.

A useful quantity in describing these shocks is the Mach number, $\mathcal{M}$, defined as

$$\mathcal{M} = \frac{v_{\text{shock}}}{c_s}, \tag{1.9}$$

where v_{shock} is the velocity of the shock and c_s is the sound speed in the pre-shock medium. For a strong shock in an ideal monatomic gas (with an adiabatic index $\gamma = 5/3$), the Rankine-Hugoniot jump conditions relate the pre-shock and post-shock temperatures. One commonly used relation for the temperature jump is

$$\frac{T_2}{T_1} = \frac{(5\mathcal{M}^2 - 1)(\mathcal{M}^2 + 3)}{16\mathcal{M}^2}, \tag{1.10}$$

where T_1 and T_2 are the temperatures of the gas before and after the shock, respectively. This equation illustrates how the strength of the shock (through $\mathcal{M}$) directly influences the degree of heating. For high Mach numbers ($\mathcal{M} \gg 1$), the temperature increase can be substantial.

1.1.4.3 Virial Temperature and Energy Considerations

Another useful way to think about the thermal state of the ICM is in terms of the virial theorem. As material collapses into a gravitational potential well, part of its potential energy is converted into kinetic and thermal energy. The virial temperature provides

an estimate of the equilibrium temperature a cluster would reach if its gas were fully thermalized:

$$T_{\rm vir} = \frac{GM\mu m_p}{2Rk_B}, \tag{1.11}$$

where G is the gravitational constant, M is the total mass of the cluster, R is the virial radius, μ is the mean molecular weight, m_p is the proton mass, and k_B is the Boltzmann constant.

This temperature sets a baseline for what we expect in a relaxed cluster, but in reality, ongoing mergers and accretion can boost the gas temperature above the simple virial estimate. Shocks from these processes inject additional heat and drive turbulence, both of which contribute to the overall energy budget of the ICM.

In short, mergers and accretion are not just mechanisms for mass growth—they are engines of thermal evolution. The high temperatures, complex structures, and extended X-ray emission we observe in clusters today are direct consequences of these violent processes. Equations 1.9, 1.10, and 1.11 together describe the physical framework that links the gravitational dynamics of structure formation with the thermal state of the cluster gas. For more on this topic, see Markevitch & Vikhlinin (2007); Sarazin (1986); Ricker & Sarazin (2001).

1.1.5 The Role of Feedback Processes

While gravity drives the large-scale formation of structures in the Universe, additional feedback mechanisms are crucial for regulating the thermodynamics of the ICM and for shaping galaxy evolution within clusters. Two primary sources of feedback—AGN and supernovae—inject energy into the ICM, helping to offset radiative cooling and suppress excessive star formation.

1.1.5.1 AGN Feedback

AGN feedback is widely regarded as the dominant mechanism for heating the ICM and preventing the overcooling of gas in massive halos. Supermassive black holes at the centers of galaxies accrete matter and release tremendous amounts of energy, often in the form of relativistic jets and wide-angle outflows. These interactions heat the surrounding gas, inflate buoyant cavities, and drive shocks that propagate through the ICM (McNamara & Nulsen, 2007; Fabian, 2012).

The energy released by AGN can be estimated in terms of the mass accreted onto the black hole:

$$E_{\rm AGN} = \epsilon\, M_{\rm acc}\, c^2, \tag{1.12}$$

where $M_{\rm acc}$ is the accreted mass, c is the speed of light, and ϵ is the radiative efficiency (typically $\sim$0.01–0.1). This feedback energy acts to suppress cooling flows and regulate the growth of massive galaxies at the centers of clusters.

1.1.5.2 Supernova Feedback and Other Processes

Although less energetic than AGN on a per-event basis, supernovae also contribute to cluster feedback, particularly in low-mass systems or at earlier cosmic times (Hopkins et al., 2006). The cumulative effect of many supernova explosions can inject significant energy into the ICM and enrich it with heavy elements. These explosions drive galactic-scale winds that expel gas and suppress further star formation.

The total mechanical energy released by supernovae is approximated by:

$$E_{\rm SN} = N_{\rm SN}\, E_0, \tag{1.13}$$

where $N_{\rm SN}$ is the number of supernovae and $E_0 \sim 10^{51}\,\mathrm{erg}$ is the typical energy released per event.

Additional processes—such as stellar winds and cosmic ray feedback—can contribute to the energy balance in clusters, but they generally play a secondary role compared to AGN and supernova feedback.

1.1.5.3 Impact on the Non-linear Power Spectrum

Feedback from AGN and supernovae plays a critical role not only in regulating galaxy formation but also in altering the matter distribution on cosmological scales. Energy injection from these processes redistributes baryons, especially in group- and cluster-scale halos, leading to a suppression of matter clustering on small and intermediate scales. This suppression modifies the non-linear matter power spectrum, an observable directly probed by weak lensing and galaxy clustering surveys. Neglecting baryonic effects in theoretical modeling can lead to significant biases in cosmological parameter inference, particularly for precision probes like cosmic shear, galaxy–galaxy lensing, and galaxy clustering (van Daalen et al., 2011a; Chisari et al., 2018).

Hydrodynamical simulations that incorporate realistic feedback physics—such as cosmo-OWLS, BAHAMAS, Horizon-AGN, and the recent large-volume FLAMINGO simulation—consistently find that baryonic feedback suppresses the total matter power spectrum by approximately 10–20% at scales of $k \sim 1\,h\,\mathrm{Mpc}^{-1}$, and up to 30% at $k \gtrsim 5\,h\,\mathrm{Mpc}^{-1}$ (van Daalen et al., 2011a; Chisari et al., 2018; Schaye et al., 2023). The amplitude and scale-dependence of this suppression are sensitive to the feedback model and evolve with redshift. Accurate modeling of this effect is essential for ongoing and future surveys like *Euclid*, Rubin LSST, and Roman, which aim to constrain cosmology at the percent level. Several approaches—such as halo model extensions (e.g., HMCode; Mead et al., 2021), baryonic correction models (Schneider & Teyssier, 2015; Schneider et al., 2025), or emulator-based frameworks (Salcido et al., 2023)—have been developed to incorporate these baryonic effects into cosmological analyses.

1.1.5.4 Balancing Cooling and Heating

The interplay between radiative cooling and feedback heating is key to understanding the observed state of the ICM. In the absence of feedback, hot cluster gas would cool and

collapse at unrealistically high rates, leading to star formation levels that are inconsistent with observations. Feedback counteracts this cooling and maintains a quasi-stable thermal balance.

This balance can be quantified by the cooling time:

$$t_{\rm cool} = \frac{3}{2}\frac{nk_BT}{n_e n_i \Lambda(T)}, \tag{1.14}$$

where n is the total particle number density, n_e and n_i are the electron and ion number densities, T is the temperature, and $\Lambda(T)$ is the temperature-dependent cooling function. If the energy injected by feedback mechanisms exceeds the rate of energy loss through radiation (roughly $E/t_{\rm cool}$), the gas remains hot and star formation is suppressed.

In summary, feedback processes—particularly AGN activity and supernova explosions—are essential for regulating the thermal and dynamical state of the ICM. AGN feedback plays the dominant role in high-mass systems, while supernovae are more influential in smaller halos or at early times. Both mechanisms affect not only galaxy evolution but also the matter distribution itself, as shown in simulations of the power spectrum. Maintaining a balance between heating and cooling is critical to understanding the long-term stability of galaxy clusters. For further discussion, see McNamara & Nulsen (2007); Fabian (2012); Hopkins et al. (2006).

1.1.6 Galaxy Clusters as Cosmological Probes

Galaxy clusters serve as powerful tracers of cosmic evolution. Their abundance, spatial distribution, and internal properties are highly sensitive to the underlying cosmological parameters and the growth of structure over time (Allen et al., 2011; Kravtsov & Borgani, 2012). In this section, we describe how clusters are detected, how their masses are inferred and calibrated, and how their abundance and baryonic content can be used to constrain cosmology.

1.1.6.1 X-ray, Sunyaev-Zel'dovich Effect, and Optical Observations

Clusters are first identified observationally through signatures that reflect the presence of hot gas and galaxy overdensities. In the X-ray band, the hot ICM emits bremsstrahlung radiation, which is detected by space-based telescopes. Early wide-field surveys conducted by ROSAT laid the groundwork for cluster cosmology by detecting thousands of clusters in its all-sky survey. More recently, eROSITA has extended this legacy with far greater sensitivity, enabling the detection of clusters out to higher redshifts and in larger numbers. Complementary high-resolution X-ray observatories like Chandra and *XMM-Newton* provide detailed measurements of gas temperature, density, and morphology.

The SZE—measured by instruments such as the South Pole Telescope (SPT) and the Atacama Cosmology Telescope (ACT)—detects spectral distortions in the cosmic microwave background caused by inverse Compton scattering off hot electrons in the ICM. A

key advantage of the SZE signature is that it remains nearly redshift-independent, making it particularly valuable for detecting distant clusters (Barbosa et al., 1996).

In the optical, surveys like the Sloan Digital Sky Survey (SDSS) and the Dark Energy Survey (DES) identify galaxy clusters through the spatial clustering of luminous red galaxies. The richness parameter, defined as the number of galaxies above a luminosity threshold within a specified radius, serves as a mass proxy (Rykoff et al., 2014).

Each detection method offers different strengths and systematics: X-ray observations trace the thermal structure of the ICM, SZE measurements provide a redshift-independent signal tied to the cluster's total thermal energy, and optical surveys capture the galaxy population. Combining multi-wavelength observations not only improves completeness and reduces selection biases but also enables robust cluster mass calibration, which is essential for precise cosmological constraints (Klein et al., 2023b; Bocquet et al., 2024b; Grandis et al., 2024b; Singh et al., 2025).

1.1.6.2 Observable–Mass Relations and Mass Calibration

Accurate mass calibration is a cornerstone of cosmological analyses based on galaxy cluster abundances. Since cluster mass is not a directly observable quantity, surveys rely on indirect observables—such as X-ray luminosity, tSZE signal, or optical richness—to infer cluster masses through empirical or theoretically motivated relations. These observable–mass relations introduce some of the largest systematic uncertainties in cluster-based cosmology, making their precise calibration a critical priority for current and future surveys (e.g. Pratt et al., 2019; Bocquet et al., 2024b; Ghirardini et al., 2024).

Several observable proxies have been widely adopted, each with distinct advantages and challenges:

- **X-ray Luminosity–Mass and Temperature–Mass Relations:**
  In X-ray surveys, the luminosity of the ICM, L_X, is a convenient and widely used mass proxy. However, it exhibits significant intrinsic scatter due to its sensitivity to the core properties of clusters, which are influenced by cooling, feedback, and dynamical activity (Mantz et al., 2016; Ghirardini et al., 2019). Conversely, the X-ray temperature, T_X, which scales approximately as

  $$T_X \propto M^{2/3},$$

  provides a more robust mass estimate with lower scatter, as it is less sensitive to core processes and better reflects the depth of the gravitational potential (Vikhlinin & et al., 2009; Bulbul et al., 2019).

- **Thermal Sunyaev–Zel'dovich Effect (tSZE)–Mass Relation:**
  The tSZE arises from inverse Compton scattering of cosmic microwave background photons by hot electrons in the ICM, leading to a spectral distortion that is independent of redshift. In SZE cluster surveys, the key observable is the detection

significance, ζ, which serves as a mass proxy. Under self-similar assumptions (Kaiser, 1986), ζ scales with mass and redshift approximately as

$$\zeta \propto M^{5/3} E(z)^{2/3},$$

where $E(z) = H(z)/H_0$ is the dimensionless Hubble parameter that describes the redshift evolution of the background cosmology. This relation exhibits relatively low intrinsic scatter compared to the X-ray luminosity–mass relation (de Haan et al., 2016; Bocquet et al., 2019, 2024b).

- **Optical Richness and Velocity Dispersion:**
  Optical cluster detection methods use galaxy counts (richness) or galaxy velocity dispersions as mass proxies. Richness, typically defined as the number of red-sequence galaxies within a given radius, shows a strong correlation with cluster mass but requires careful calibration to control for projection effects, and redshift-dependent systematics (Rykoff et al., 2014; Murata et al., 2018; Costanzi et al., 2019). Galaxy velocity dispersion also traces the gravitational potential but is more sensitive to dynamical state and line-of-sight interlopers, which can bias the inferred mass unless corrected (Sifón et al., 2013).

Each of these proxies plays a vital role in multi-wavelength cluster cosmology. Their combination, particularly when cross-calibrated across X-ray, SZE, and optical datasets, can reduce systematics and tighten constraints on cosmological parameters (Bocquet et al., 2024b; Ghirardini et al., 2024).

1.1.6.3 Gravitational Weak Lensing Mass Calibration

Gravitational weak lensing provides a direct and nearly assumption-free method for measuring the total mass of galaxy clusters. By statistically analyzing the coherent shape distortions (shear) induced in background galaxies by a foreground cluster's gravitational potential, weak lensing enables the reconstruction of the projected mass distribution without relying on assumptions about the dynamical or thermodynamic state of the cluster (Bartelmann & Schneider, 2001).

Because of its robustness and independence from baryonic physics, weak lensing is widely regarded as the gold standard for calibrating observable–mass scaling relations. It plays a crucial role in anchoring relations such as X-ray luminosity–mass, tSZE–mass, and optical richness–mass. Accurate weak-lensing mass estimates are therefore essential for reducing systematic uncertainties in cosmological analyses based on cluster abundances (Bocquet et al., 2024b; Ghirardini et al., 2024).

Forthcoming large-area surveys such as *Euclid* and the Vera C. Rubin Observatory's LSST will provide high-quality weak lensing measurements over thousands of square degrees, dramatically improving the statistical power and precision of lensing-based mass calibration (Vogt et al., 2024a).

1.1.6.4 Cluster Mass Function and Cosmological Parameters

Once cluster masses are accurately calibrated, the cluster mass function becomes a powerful tool for cosmological inference. It characterizes the number density of galaxy clusters as a function of mass and redshift, encapsulating how structure formation evolves across cosmic time. A simplified form is

$$N(M, z) \propto \left(\frac{M}{M_*}\right)^{-\alpha} \exp\left(-\frac{M}{M_*}\right), \tag{1.15}$$

where M_* denotes a characteristic mass scale that evolves with redshift, and α determines the slope at the low-mass end.

The cluster mass function is highly sensitive to fundamental cosmological parameters, particularly the present-day matter density Ω_m and the amplitude of matter fluctuations σ_8. Since cluster formation is governed by the growth of structure, deviations in the observed abundance of clusters from theoretical predictions can signal changes in the underlying cosmology.

By comparing the observed cluster mass function with theoretical predictions based on empirically calibrated halo mass functions from high-resolution N-body simulations, one can place constraints on both the expansion history of the Universe and the growth of cosmic structure (Tinker et al., 2008; Bocquet et al., 2016). When combined with other cosmological probes such as the CMB and baryon acoustic oscillations (BAO), cluster abundance measurements provide competitive and complementary constraints on fundamental cosmological parameters.

1.1.6.5 Baryon Fraction as a Cosmological Probe

The baryon fraction in galaxy clusters, defined as the ratio of baryonic mass (hot gas and stars) to the total cluster mass, provides a fundamental test of cosmological models. In the standard ΛCDM framework, the baryon fraction in massive clusters is expected to approach the cosmic mean baryon fraction, given by

$$f_b = \frac{\Omega_b}{\Omega_\mathrm{m}},$$

where Ω_b and Ω_m are the baryon and matter density parameters, respectively (Ettori et al., 2009).

X-ray and SZE studies reveal that most baryons reside in the hot ICM, with stars contributing only a small fraction (Gonzalez et al., 2013; Pratt et al., 2019). However, the measured baryon fraction is often lower than the expected cosmic mean. This discrepancy is attributed to feedback processes, such as AGN and supernova-driven outflows, that eject gas from the cluster potential (Planelles et al., 2013a).

If feedback processes are well understood, the baryon fraction can be used as a cosmological constraint, particularly for testing models of dark energy (Allen et al., 2008).

1.2 Gravitational Weak Lensing

Gravitational lensing, a phenomenon predicted by Einstein's General Theory of Relativity (Einstein, 1916), occurs when the path of light from a distant source is deflected by the gravitational field of an intervening mass (the lens). This deflection is a direct consequence of spacetime curvature induced by mass, and the effect can be categorized into strong and weak lensing regimes depending on the alignment and mass distribution of the lensing object.

In the weak lensing regime, the deflection angles are small, leading to subtle distortions in the shapes of background galaxies. Although individual distortions are too minute to notice, they can be statistically detected by analyzing the coherent alignment across large samples of galaxies.

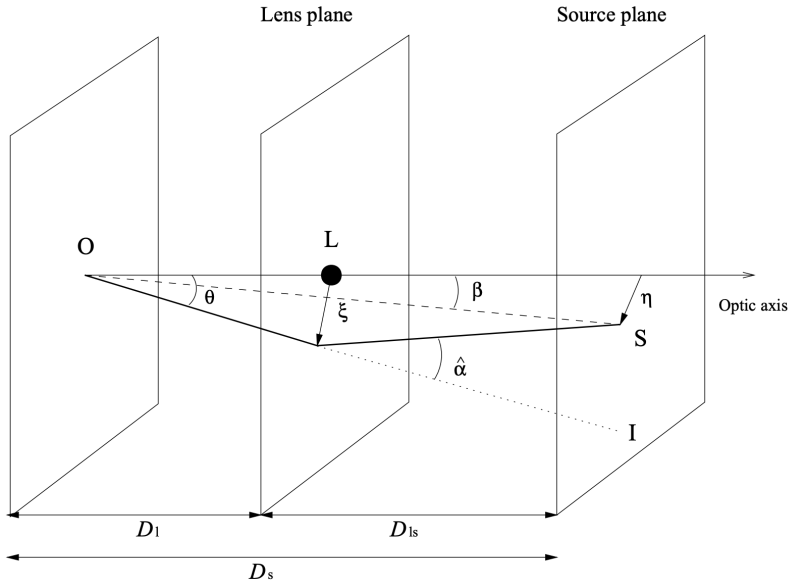

Figure 1.1: Schematic diagram of gravitational lensing. Light from a distant source (S) is deflected by the gravitational potential of an intervening lens (L) before reaching the observer (O). The deflection causes a shift in the observed position and a distortion in the image of the source. Adapted from Umetsu (2020).

The basic relation for the deflection angle $\hat{\alpha}$ of a light ray passing near a mass M is given by:

$$\hat{\alpha} = \frac{4GM}{c^2\xi}, \tag{1.16}$$

where G is the gravitational constant, c is the speed of light, and ξ is the impact parameter, defined as the perpendicular distance between the light ray and the lensing mass (see Fig. 1.1). Equation 1.16 illustrates that the deflection angle decreases with increasing ξ.

In a typical lensing configuration, the observer, the lens, and the source are approximately aligned along the line of sight. The positions in the source and image planes are

related by the lens equation:

$$\beta = \theta - \frac{D_{ls}}{D_s}\hat{\alpha}(\theta), \tag{1.17}$$

where:

- β is the true angular position of the source,
- θ is the observed angular position of the image,
- D_{ls} is the angular diameter distance between the lens and the source, and
- D_s is the angular diameter distance between the observer and the source.

In the weak lensing limit, where the deflection is small, we can linearize the mapping from the source to the image plane. This mapping is described by the Jacobian matrix $\mathbf{A}$:

$$\mathbf{A} = \frac{\partial \boldsymbol{\beta}}{\partial \boldsymbol{\theta}} = \begin{pmatrix} 1 - \kappa - \gamma_1 & -\gamma_2 \\ -\gamma_2 & 1 - \kappa + \gamma_1 \end{pmatrix}, \tag{1.18}$$

where:

- κ is the convergence, representing an isotropic magnification of the source image, and
- $\gamma = \gamma_1 + i\gamma_2$ is the shear, describing the anisotropic (elliptical) distortion.

The convergence κ is related to the projected surface mass density $\Sigma(\theta)$ of the lens by:

$$\kappa(\theta) = \frac{\Sigma(\theta)}{\Sigma_{\text{crit}}}, \tag{1.19}$$

with the critical surface mass density defined as:

$$\Sigma_{\text{crit}} = \frac{c^2}{4\pi G}\frac{D_s}{D_l D_{ls}}, \tag{1.20}$$

where D_l is the angular diameter distance to the lens.

The observable signature of weak lensing is the coherent distortion of background galaxy shapes. The observed ellipticity ϵ of a galaxy is related to its intrinsic (unlensed) ellipticity ϵ_s and the reduced shear g by:

$$\epsilon = \frac{\epsilon_s + g}{1 + g^* \epsilon_s}, \tag{1.21}$$

where $g = \gamma/(1-\kappa)$ and g^* is the complex conjugate of g. In the weak lensing regime (where $\kappa \ll 1$ and $|\gamma| \ll 1$, see (Bartelmann & Schneider, 2001)), this simplifies to:

$$\epsilon \approx \epsilon_s + g. \tag{1.22}$$

Since the intrinsic ellipticities ϵ_s are assumed to be randomly oriented, averaging the observed ellipticities over many galaxies yields an unbiased estimate of the shear:

$$\langle \epsilon \rangle \approx g. \tag{1.23}$$

1.2.1 Weak Lensing as a Probe of Cluster Mass

Over the past decade, significant progress has been made in measuring and interpreting weak lensing signals. Uniform and high-quality weak lensing surveys such as the Dark Energy Survey (DES), the Kilo-Degree Survey (KiDS), and the Subaru Hyper Suprime-Cam (HSC) have provided large datasets with well-controlled systematics (Mandelbaum, 2018; Aihara et al., 2018; Sevilla-Noarbe et al., 2021). The combination of this statistical power with advances in shape measurement techniques has enabled robust cluster mass calibration, paving the way for precision cosmology using clusters as mass tracers (Lesci et al., 2022; Bocquet et al., 2024b; Ghirardini et al., 2024).

One of the most impactful applications of these datasets has been the calibration of observable–mass relations. Weak lensing offers a direct probe of the total cluster mass, independent of the complex baryonic physics that affect X-ray or SZE measurements. This calibration is crucial for linking observable quantities—such as optical richness, X-ray count rate, or the tSZE signal—to the underlying halo mass distribution. Recent analyses have employed both individual cluster measurements and stacking techniques, which combine multiple clusters to enhance the signal-to-noise ratio (Simet et al., 2017; Medezinski et al., 2018; McClintock & et al., 2019; Murata et al., 2019; Bocquet et al., 2024b; Grandis et al., 2024b; Singh et al., 2025).

1.2.2 Weak Lensing Inferred Cluster Matter Profiles

Studies of cluster mass profiles are invaluable for understanding the interplay between baryonic matter and dark matter in galaxy clusters. Umetsu et al. (2014b) conducted a comprehensive analysis combining strong-lensing, weak-lensing shear, and magnification data for a sample of 20 galaxy clusters from the Cluster Lensing And Supernova survey with Hubble (CLASH) survey. Their joint analysis provided high-resolution mass density profiles (Fig. 1.2) revealing that the inclusion of both strong and weak lensing data is crucial for accurately constraining the inner and outer regions of clusters. This approach allowed for a more precise characterization of the mass distribution, leading to better constraints on the concentration parameters of the clusters. Similarly, Okabe et al. (2016) performed a detailed weak-lensing study of 30 X-ray luminous galaxy clusters using Subaru/Suprime-Cam imaging data. They detected weak-lensing signals with high statistical significance in each cluster, enabling the reconstruction of their mass distributions. Their findings highlighted the importance of large, uniform datasets in reducing statistical uncertainties. These studies underscore the critical role of weak-lensing analyses in probing the mass profiles of galaxy clusters, enhancing our understanding of the complex interactions between baryonic and dark matter components.

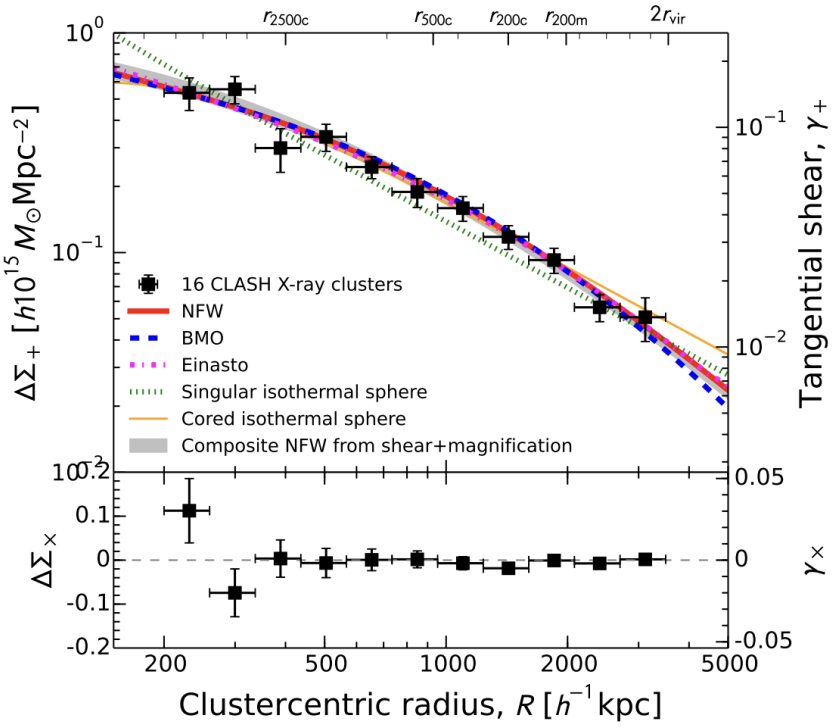

Figure 1.2: Average cluster matter profile (upper panel, black squares) obtained from stacking the X-ray-selected subsample of 16 clusters. The different lines show different models as labeled in the figure. The lower panel shows the 45°-rotated $\times$ component, which is consistent with a null signal, indicating the reliability of our distortion analysis. The figure is taken from Umetsu et al. (2014a).

1.2.3 Cosmic shear as a Probe of Cosmology

Cosmic shear, the weak lensing-induced distortion of galaxy shapes by the large-scale matter distribution, serves as a powerful probe of the Universe's structure and evolution. By statistically analyzing the shear field, one can extract valuable information about the underlying matter power spectrum and constrain key cosmological parameters, including the total matter density $\Omega_{\rm m}$ and the amplitude of structure formation σ_8 (Kilbinger, 2015; Mandelbaum, 2018; Amon et al., 2022a). However, the interpretation of cosmic shear measurements is complicated by uncertainties in the non-linear evolution of structure and, in particular, the influence of baryonic physics on small scales.

Baryonic feedback processes—including radiative cooling, star formation, supernova feedback, and AGN feedback—alter the matter distribution in ways that are not captured by dark matter-only simulations (van Daalen et al., 2011a; Chisari et al., 2018; Schneider & Teyssier, 2020). These processes can redistribute matter within halos, suppressing or enhancing power on different scales. AGN-driven winds, for example, can expel gas from halos, reducing the clustering of matter and leading to a suppression of the cosmic shear power spectrum at intermediate scales ($\ell \sim 1000$–5000). Conversely, radiative cooling and star formation increase the central concentration of halos, enhancing power on smaller scales (Semboloni et al., 2011; Mead et al., 2015).

The impact of baryonic feedback must be carefully accounted for in cosmic shear analyses to avoid biases in cosmological constraints. Various mitigation strategies have been developed to address this challenge. One common approach is to apply scale cuts, limiting the analysis to larger, quasi-linear scales where baryonic effects are less significant (MacCrann et al., 2016; Secco et al., 2022). Another strategy involves marginalizing over baryonic effects using flexible models calibrated against hydrodynamical simulations such as Illustris, EAGLE, and BAHAMAS (Eifler et al., 2015; Aricò et al., 2023a). Alternatively, combining weak lensing with complementary observables—such as kSZ measurements—offers a direct observational constraint on baryonic feedback (Bigwood et al., 2024).

The next generation of weak lensing surveys, including those from the Vera C. Rubin Observatory's Legacy Survey of Space and Time (LSST), the *Euclid* mission, and the Nancy Grace Roman Space Telescope, will provide cosmic shear measurements with unprecedented statistical precision (Euclid Collaboration et al., 2020; Ivezić et al., 2019). Given this increased sensitivity, correctly modeling baryonic feedback effects will be essential to extract unbiased cosmological constraints from these datasets. The calibration of the suppression of the non-linear matter power spectrum due to baryons in this thesis could pave the way for the analysis of future datasets.

1.3 Thesis Outline

In our introduction, we have covered the physics of galaxy cluster formation and evolution, as well as the role of baryonic feedback in shaping their properties and its impact on the non-linear matter power spectrum. We introduced weak lensing as a powerful tool for studying the total matter distribution of clusters, which enables accurate mass inference. Additionally, weak lensing can be used to constrain cosmological parameters through cosmic shear analysis. In this thesis, we use galaxy clusters in combination with weak lensing to calibrate cluster masses by integrating multi-wavelength observations, investigate their matter profiles, and calibrate the non-linear matter power spectrum of the Universe.

In Chapter 2, we study the weak lensing inferred matter profiles of 698 galaxy clusters selected from the South Pole Telescope (SPT) in the redshift range $0.25 < z < 0.94$, using weak lensing data from the Dark Energy Survey (DES). We demonstrate the average matter profiles when rescaled to account for mass-dependent size and redshift-dependent density, revealing a high degree of self-similarity. We develop a new Bayesian method for weak lensing mass calibration, using these rescaled profiles to simultaneously constrain richness-mass and tSZE-mass relations. We validate the method using mock datasets, and calibrate SPT×DES sample. The rescaled profiles also offer strong constraints on cluster matter shapes, consistent with hydrodynamical ΛCDM simulations.

In Chapter 3, we extend this analysis by including galaxy clusters detected in both the SPT and the ROSAT X-ray telescope (MARD-Y3 catalog) in the redshift range $0.05 < z < 0.95$. Using weak lensing data from DES, we perform a joint mass calibration of the MARD-Y3 and SPT samples, simultaneously constraining X-ray, tSZE, and optical observable-mass relations. This combined analysis leads to tighter constraints on the tSZE observable-mass relation and improves cosmological parameter constraints in the $\Omega_{\rm m} - \sigma_8$ plane. Additionally, we analyze rescaled cluster matter profiles and find a discrepancy in the outskirts compared to ΛCDM predictions. We further investigate cluster profiles in the DES Y3 redMaPPer catalog, finding that lower-richness clusters ($\lambda < 35$) exhibit distinct profile characteristics compared to SPT and MARD-Y3 clusters.

In Chapter 4, we focus on the impact of baryonic feedback on the non-linear matter power spectrum, which affects small-scale cosmic shear constraints. We use 122 SPT-selected galaxy clusters with intracluster medium (ICM) mass measurements from Chandra and XMM-Newton and newly calibrated weak lensing masses from DES to constrain the ICM mass–halo mass–redshift relation. Comparing our observational results with various hydrodynamical simulations that incorporate different feedback models, we extract the baryonic suppression of the matter power spectrum and determine its 68% credible interval. This analysis allows us to rule out extreme feedback scenarios and highlights the challenges of reconciling low-redshift cosmic shear results with Planck primary CMB constraints. Our findings demonstrate the value of galaxy clusters in constraining baryonic physics and improving the accuracy of cosmological constraints for future cosmic shear surveys such as Euclid and the Rubin Observatory.

Chapter 2

Galaxy cluster matter profiles: I. Self-similarity, mass calibration and observable-mass relation validation employing cluster mass posteriors

A. Singh, J. J. Mohr, C. T. Davies, S. Bocquet, S. Grandis, M. Klein, J. L. Marshall, M. Aguena, S. S. Allam, O. Alves, F. Andrade-Oliveira, D. Bacon, S. Bhargava, D. Brooks, A. Carnero Rosell, J. Carretero, M. Costanzi, L. N. da Costa, M. E. S. Pereir, S. Desai, H. T. Diehl, P. Doel, S. Everett , B. Flaugher , J. Frieman, J. García-Bellido, E. Gaztanaga, R. A. Gruendl, G. Gutierrez, D. L. Hollowood, K. Honscheid, D. J. James, K. Kuehn, M. Lima, J. Mena-Fernández, F. Menanteau, R. Miquel, J. Myles, A. Pieres, A. K. Romer, S. Samuroff, E. Sanchez, D. Sanchez Cid, I. Sevilla-Noarbe, M. Smith, E. Suchyta, M. E. C. Swanson, G. Tarle, C. To, D. L. Tucker, V. Vikram, N. Weaverdyck, P. Wiseman, *Published in Astronomy & Astrophysics*

We present a study of the weak lensing inferred matter profiles $\Delta\Sigma(R)$ of 698 South Pole Telescope (SPT) thermal Sunyaev-Zel'dovich effect (tSZE) selected and MCMF optically confirmed galaxy clusters in the redshift range $0.25 < z < 0.94$ that have associated weak gravitational lensing shear profiles from the Dark Energy Survey (DES). Rescaling these profiles to account for the mass dependent size and the redshift dependent density produces average rescaled matter profiles $\Delta\Sigma(R/R_{200c})/(\rho_{crit}R_{200c})$ with lower dispersion than the unscaled $\Delta\Sigma(R)$ versions, indicating a significant degree of self-similarity. Galaxy clusters from hydrodynamical simulations also exhibit matter profiles that suggest a high degree of self-similarity, with RMS variation among the average rescaled matter profiles with redshift and mass falling by a factor of $\approx$6 and $\approx$23, respectively, in comparison to the unscaled average matter profiles. We employ this regularity in a new Bayesian method for weak lensing mass calibration that employs the so-called cluster mass posterior $P(M_{200c}|\hat{\zeta}, \hat{\lambda}, z)$, which describes the individual cluster masses given their tSZE ($\hat{\zeta}$) and optical ($\hat{\lambda}$, z) observables. This method enables simultaneous constraints on richness λ-mass and tSZE detection significance ζ-mass relations using average, rescaled cluster matter profiles. We validate the method using realistic mock datasets and present observable-mass relation constraints for the SPT×DES sample, where we constrain the amplitude, mass trend, redshift trend, and intrinsic scatter. Our observable-mass relation results are in agreement with the mass calibration derived from the recent cosmological analysis of the SPT×DES data based on a cluster-by-cluster lensing calibration. Our new mass calibration technique offers higher efficiency when compared to the single cluster calibration technique. We present new validation tests of the observable-mass relation that indicate the underlying power-law form and scatter are adequate to describe the real cluster sample, but that suggest that a redshift variation in the intrinsic scatter of the λ-mass relation may offer a better description. In addition, the average rescaled matter profiles offer high signal-to-noise ratio (SNR) constraints on the shape of real cluster matter profiles, which are in good agreement with available hydrodynamical ΛCDM simulations. This high SNR profile contains information about baryon feedback, the collisional nature of dark matter, and potential deviations from general relativity.

2.1 Introduction

Galaxy clusters constitute the most massive collapsed halos in the Universe. Studying their abundance as a function of redshift and mass provides insights into structure formation history and therefore serves as a powerful tool for constraining cosmological models (e.g., White et al., 1993; Haiman et al., 2001; Vikhlinin et al., 2009a; Mantz et al., 2010; Planck Collaboration & et al., 2016; Chiu et al., 2023; Bocquet et al., 2024b). The ability to accurately measure cluster masses plays an important role in cluster cosmological studies, enabling constraints on the rate of cosmic structure growth, the dark energy equation of state, and other cosmological parameters such as the amplitude of matter fluctuations and

the matter density parameter. The development of robust weak lensing (WL) and CMB lensing informed mass calibration techniques (Becker & Kravtsov, 2011; von der Linden et al., 2014; Dietrich et al., 2019; Zubeldia & Challinor, 2019; Grandis et al., 2021; Bocquet et al., 2024a) and the availability of associated high quality weak lensing datasets from, e.g., Hyper Suprime-Cam Subaru Strategic Program (HSC-SSP), Dark Energy Survey (DES) and Kilo-Degree Survey (KiDS) has set the stage for progress in constraining the standard ΛCDM and wCDM parameters (Costanzi et al., 2019; Abbott et al., 2020; Costanzi et al., 2021; To et al., 2021; Chiu et al., 2023; Bocquet et al., 2024b; Ghirardini et al., 2024) as well as model extensions including modification of general relativity and interacting dark matter (e.g., Mantz et al., 2014; Cataneo et al., 2015; Vogt et al., 2024b; Mazoun et al., 2024).

These same WL datasets can be employed to study the matter distribution within galaxy clusters. A challenge is that in the existing WL datasets based on large photometric surveys, the matter profiles of individual clusters often have low signal-to-noise ratio (SNR). Combining WL matter profiles from multiple galaxy clusters provides a way to improve the SNR and also to reduce the intrinsic variations in the matter distribution from cluster to cluster that arise from their different formation histories. Previous works have employed WL measurements of multiple clusters to constrain cluster masses by combining tangential shear profiles or projected matter profiles of clusters (Oguri & Takada, 2011; Umetsu et al., 2016; McClintock et al., 2018; Bellagamba et al., 2019; Giocoli et al., 2021; Lesci et al., 2022). A challenge in this approach is that there are systematic variations in the projected matter profiles of galaxy clusters with cluster mass and redshift. An average WL matter profile therefore reflects the characteristics of the cluster sample, and it depends sensitively on the distribution of the sample in mass and redshift. This approach also requires careful modeling of the spatial distribution and masking of the WL source galaxies on a cluster by cluster basis to enable accurate modeling of the multi-cluster matter profile.

If the systematic variations of the matter profiles with mass and redshift can be accurately characterized, then they can also be scaled out, enabling average matter profiles of high SNR that are largely independent of the characteristics of the cluster sample from which they are constructed. In particular, if cluster matter profiles are approximately self-similar in nature– that is, they exhibit similar shapes that vary systematically with mass and redshift– then these systematic trends can be easily removed. In this limit, the need to accurately model the spatial distribution and masking of WL source galaxies is also no longer required.

Approximate self-similarity is a generic prediction of gravitational structure formation (Kaiser, 1986). In N-body simulations, cluster halos are well described by so-called Navarro, Frenk and White (NFW) models (Navarro et al., 1997a) that exhibit weak trends in concentration or shape with mass and redshift. In hydrodynamical simulations, self-similar behavior has been seen in cluster gas profiles (Lau et al., 2015) and pressure profiles (Nelson et al., 2014). Observationally, approximate self-similarity has been demonstrated in the intracluster medium (ICM) density, pressure profiles and temperature profiles (Vikhlinin et al., 2006; Arnaud et al., 2010; Baldi et al., 2012; McDonald et al., 2014a), whereas WL studies of cluster matter profiles have tended to focus on whether the NFW model is a

good description of the real matter profiles (e.g., Umetsu et al., 2014b; Niikura et al., 2015). In particular, Umetsu et al. (2014b) studied average matter profiles and found the NFW profile to be an excellent description of real clusters. In contrast, Niikura et al. (2015) analyzed scaled average matter profiles by rescaling with the scale radius of NFW profile and with the critical density of the Universe and found evidence of a single underlying or universal cluster matter profile.

In this analysis we use hydrodynamic structure formation simulations and direct WL observations of cluster samples to examine cluster matter profiles, revealing remarkable consistency and approximate self-similarity of simulated and real matter profiles. We then exploit this self-similarity to study high SNR cluster matter profiles and to employ them to perform a calibration of observable-mass relations. This mass calibration approach offers a computationally more efficient technique to analyze large cluster WL datasets compared to a cluster-by-cluster approach (Bocquet et al., 2019; Bocquet et al., 2024a), without loss of information.

The paper is organized as follows. We present the simulated and observed dataset in Section 2.2. The self-similarity of galaxy cluster matter profiles is explored in Section 2.3. The mass calibration method along with the likelihood calculation and the hydrodynamical model is discussed in Section 2.4. In Section 2.5 we validate the analysis method using mock data and present the results using the South Pole Telescope (SPT) clusters and DES-WL data. We conclude with a summary and outlook in Section 2.6. Throughout the paper we employ a flat ΛCDM cosmology with parameters $\Omega_{\rm m} = 0.3$, and $h = 0.7$. All uncertainties are quoted at the 68 percent credible interval, unless otherwise specified.

2.2 Data

In this section, we first describe the data used in our work: 1) the SPT cluster catalogs and 2) Dark Energy Survey (Year 3, hereafter Y3) weak-lensing and photometric redshift measurements. Then we summarize the simulation datasets from *Magneticum* and IllustrisTNG, which are used to explore the impact of baryons on cluster matter profiles.

2.2.1 SPT cluster catalogs

We use a combination of three thermal Sunyaev-Zel'dovich effect (tSZE) selected cluster catalogs that have been extracted from surveys carried out by the South Pole Telescope (Carlstrom et al., 2011) collaboration: SPT-SZ (Bleem et al., 2015; Klein et al., 2024), SPTpol ECS (Bleem et al., 2020) and SPTpol-500d (Bleem et al., 2024). The SPT-SZ survey covers 2,500 $\deg^2$, and the SPTpol ECS survey spans 2,770 $\deg^2$ in the southern sky, while the SPTpol-500d survey pushes to a greater depth within a 500 $\deg^2$ patch inside the SPT-SZ survey. Galaxy cluster candidates are selected from the mm-wave maps at 90 and 150 GHz using a matched filter technique (Melin et al., 2006), which employs galaxy cluster tSZE models with a range of angular scales (Vanderlinde et al., 2010). Only cluster candidates at redshifts $z > 0.25$ are considered, because clusters at lower redshifts are

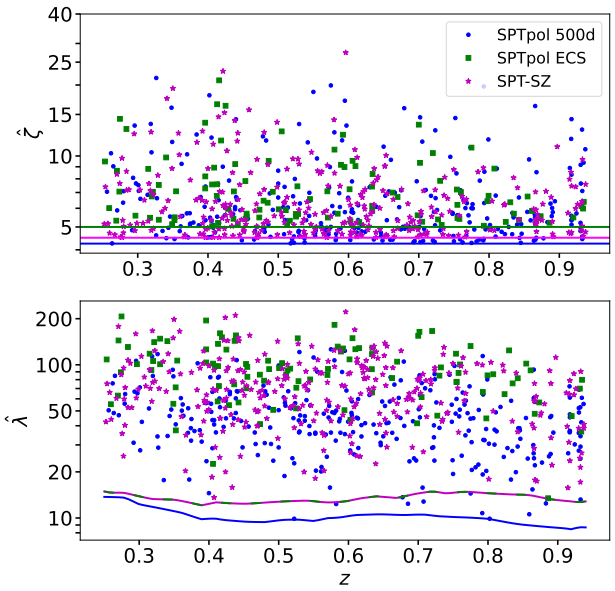

Figure 2.1: Distribution of observed tSZE detection significance $\hat{\zeta}$ and richness $\hat{\lambda}$ as a function of redshift for the 698 galaxy clusters in the SPT sample that overlap the DES region. The solid line in the top figure shows the detection threshold for the three survey regions. In the bottom figure, the colored lines correspond to the $\hat{\lambda}_{\rm min}(z)$ detection threshold for each survey.

larger in angular extent and therefore more strongly impacted by the matched filtering, which is designed to remove atmospheric noise as well as increased noise contributions from the primary CMB. At low redshift the angular scales filtered out overlap with the scales important for the galaxy cluster tSZE, strongly impacting the candidate detection significance and thereby complicating its use as a cluster halo mass proxy. Additionally, we only analyze clusters with a redshift $z < 0.95$ due to the depth and systematics of the DES WL sample described below.

These cluster candidates are then studied using the Multi-Component Matched Filter cluster confirmation tool (MCMF; Klein et al., 2018). This processing results in a cluster catalog that includes measurements of optical richnesses $\hat{\lambda}$, sky positions and redshifts. The measured optical richness allows for efficient removal of contaminants from the tSZE candidate list by evaluating the likelihood of each candidate being a random superposition of a physically unassociated optical system with a tSZE noise fluctuation (Klein et al., 2024). The exclusion threshold corresponds to an observed richness threshold that varies with redshift $\hat{\lambda}_{\rm min}(z)$ (Klein et al., 2019a) and has been determined by analyzing the richness distributions along random lines of sight within the survey. The final MCMF-confirmed cluster catalogs have a constant contamination fraction at all redshifts.

The selection threshold in the tSZE detection significance is $\hat{\zeta} > 4.25$ for SPTpol-500d, $\hat{\zeta} > 4.5$ for SPT-SZ and $\hat{\zeta} > 5$ for SPTpol ECS, while the MCMF selection threshold $\hat{\lambda}_{\rm min}(z)$ is adjusted to maintain a contamination fraction of $< 2\,\%$ in the final MCMF-

confirmed cluster lists from both surveys. Fig. 2.1 shows the distribution of observed richness and tSZE detection significance as a function of redshift for the MCMF confirmed SPT sample we study here.

2.2.2 DES Y3 lensing

The Dark Energy Survey is a photometric survey in five broadband filters ($grizY$) which covers an area of $\sim$5,000 deg^2 in the southern sky. The survey was conducted using the Dark Energy Camera (DECam; Flaugher et al., 2015) at the 4m Blanco telescope at the Cerro Tololo Inter-American Observatory (CTIO) in Chile. In this work, we use weak lensing data from the first three years of observations (DES Y3), which cover the entire 5,000 deg^2 survey footprint.

The DES Y3 shape catalog (Gatti & Sheldon et al. 2021) is constructed from the r, i, z-bands using the METACALIBRATION pipeline (Huff & Mandelbaum, 2017; Sheldon & Huff, 2017). Other DES Y3 works contain detailed information on the Point-Spread Function modeling (Jarvis et al., 2021), the photometric dataset (Sevilla-Noarbe et al., 2021), and image simulations (MacCrann et al., 2022). After all source selection cuts, the shear catalog consists of roughly 100 million galaxies over an area of 4,143 deg^2. The typical source density is 5 to 6 arcmin^{-2}, depending on the selection choices of a specific analysis.

Our work follows the selection of lensing source galaxies in four tomographic bins (Fig. 2.2 shows the three tomographic bins used in our analysis) as employed in the DES 3x2pt analysis (Abbott et al., 2022a). The selection is defined and calibrated in Myles et al. (2021) and Gatti et al. (2022), where source redshifts are estimated using Self-Organizing Maps Photo-z (SOMPZ). The final calibration accounts for the (potentially correlated) systematic uncertainties in source redshifts and shear measurements. For each tomographic source bin, the mean redshift distribution is provided, and the systematic uncertainties are captured using 1,000 realizations of the source redshift distribution. The amplitude of the source redshift distribution is scaled by a factor $1+m$ to account for the multiplicative shear bias m. In addition to the tomographic bins and SOMPZ, we use Directional Neighbourhood Fitting (DNF; De Vicente et al., 2016) galaxy photo-z estimates when determining the expected fraction of the lensing source galaxy population in each tomographic bin that is contributed by member galaxies from a particular cluster of interest– the so-called cluster member contamination.

2.2.3 Hydrodynamical simulations

In this work, we use the *Magneticum* Pathfinder suite of cosmological hydrodynamical simulations (Hirschmann et al., 2014; Teklu et al., 2015; Beck et al., 2016; Bocquet et al., 2016; Dolag et al., 2017). We use Box1, which has a box size of $896\,h^{-1}$ Mpc on a side with 2×1526^3 particles and the particle mass $1.3 \times 10^{10}\,h^{-1} M_\odot$ for dark matter particles, and $2.6 \times 10^9\,h^{-1} M_\odot$ for gas particles. The simulation is run with cosmological parameters ($\Omega_m = 0.272$, $\Omega_b = 0.0457$, $H_0 = 70.4$, $n_s = 0.963$, $\sigma_8 = 0.809$), which correspond to the

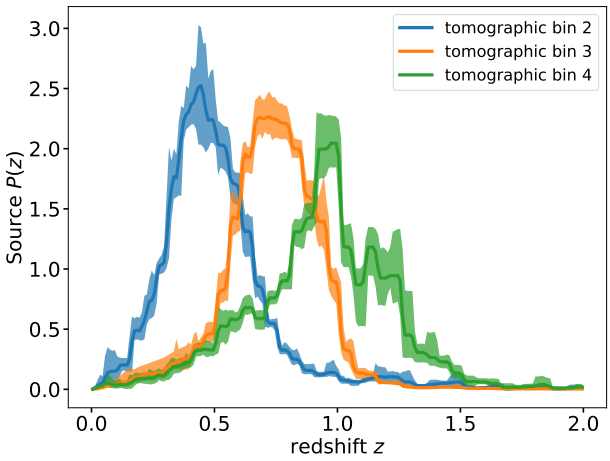

Figure 2.2: The DES Y3 lensing source redshift distribution for tomographic bins 2 through 4 that are used in this analysis. The solid line represents the mean and the shaded region depicts the 2σ uncertainties on the redshift distributions.

WMAP7 constraints for a spatially flat ΛCDM model (Komatsu et al., 2011). From this simulation, we use snapshots at five redshifts $z_{\rm snap} = 0.01, 0.25, 0.47, 0.78, 0.96$.

In addition, we also use the data from IllustrisTNG300-1 (Pillepich et al., 2018; Marinacci et al., 2018; Springel et al., 2018; Nelson et al., 2018; Naiman et al., 2018; Nelson et al., 2019). These include 2×2500^3 resolution elements for a box size of $205\,h^{-1}\,$Mpc on a side. The cosmology corresponds to the Planck2015 constraints for a spatially flat ΛCDM cosmology (Planck Collaboration & et al., 2016): $\Omega_m = 0.3089$, $\Omega_b = 0.0486$, $\sigma_8 = 0.8159$, $n_s = 0.9667$, and $h = 0.6774$. We use snapshots correponding to redshift $z_{\rm snap} \in \{0.01, 0.24, 0.42, 0.64, 0.95\}$. From these simulation snapshots, we then extract halos with $M_{\rm 200c} > 3 \times 10^{13}\,h^{-1}\,{\rm M}_\odot$. Shear maps are generated following Grandis et al. (2021) in a cylinder with a projection depth of 20 $h^{-1}\,$Mpc.

2.3 Self-similarity in cluster matter profiles

Gravitational lensing is the phenomenon through which photon geodesics are perturbed by gravitational potentials. For a distant galaxy, this causes a distortion in the observed image relative to its true shape (Schneider, 2006). In this work, we are interested in WL, where distortions in source galaxy images induced by intervening matter along the line of sight are small. In this regime, the WL signal must be extracted through statistical correlations of source galaxies. The observable of interest in this context is the reduced shear, which is defined as

$$g = \frac{\gamma}{1-\kappa}, \tag{2.1}$$

where γ is the weak lensing shear and κ is the weak lensing convergence (for detailed discussion see Schneider, 2006). The ensemble averaged source ellipticity, e, and the shear

response, R_γ, are related to the reduced shear as

$$\langle g \rangle = \langle R_\gamma \rangle^{-1} \langle e \rangle. \tag{2.2}$$

R_γ is the average response of the measured ellipticity to a shear. Due to instrumental and atmospheric effects and noise this shear response typically is less than 1. The tangential reduced shear profile induced by an object with a projected mass distribution $\Sigma(R)$ is related to the critical surface mass density $\Sigma_{\rm crit}$ by

$$\Delta\Sigma(R) = \Sigma_{\rm crit}\, \gamma_{\rm t}(R) = \langle \Sigma(< R) \rangle - \Sigma(R), \tag{2.3}$$

where $\Sigma_{\rm crit}$ depends on the geometry of the source-lens system and is defined as

$$\Sigma_{\rm crit}(\mathrm{z_s}, \mathrm{z_l}) = \frac{c^2}{4\pi G} \frac{D_{\rm s}}{D_{\rm l} D_{\rm ls}}, \tag{2.4}$$

where $z_{\rm s}$ and $z_{\rm l}$ are the source and lens redshifts, respectively, and $D_{\rm s}, D_{\rm l}, D_{\rm ls}$ are the angular diameter distances to the source, lens, and between the source-lens pair. When $z_{\rm s} \leq z_{\rm l}$, $\Sigma_{\rm crit}^{-1}$ is defined to be zero.

Analogous to Eq. 2.3, we introduce an observed quantity

$$\Delta\Sigma_{\rm reduced}(R) = \Sigma_{\rm crit}\, g_{\rm t}(R) \tag{2.5}$$

In this paper, we use the excess surface mass density as defined in the above equation but refer to it as $\Delta\Sigma(R)$. Note that, although $\Sigma(R)$ is the more fundamental quantity, we use $\Delta\Sigma(R)$ (calculated using eq. 2.5) in our work because it can be directly measured through weak lensing. For convenience we refer to $\Delta\Sigma(R)$ simply as the cluster matter profile.

For a given source redshift distribution $P(\mathrm{z_s})$, we can compute the average lensing efficiency for a given lens as

$$\Sigma_{\rm crit}^{-1}(\mathrm{z_l}) = \int \mathrm{d z_s} P(\mathrm{z_s}) \Sigma_{\rm crit}^{-1}(\mathrm{z_s}, \mathrm{z_l}). \tag{2.6}$$

From Eq. 2.3 we can see that the differential surface mass density at a given projected radius R can be expressed as the difference between the mean enclosed surface mass density and the surface mass density Σ at that projected radius, which is expressed as follows

$$\Sigma(R) = \int_{-\infty}^{\infty} \mathrm{d}\chi \rho\left(\sqrt{R^2 + \chi^2}\right), \tag{2.7}$$

$$\langle \Sigma(< R) \rangle = \frac{2}{R^2} \int_0^R \mathrm{d}R' R' \Sigma(R'). \tag{2.8}$$

Where $\rho(r)$ is the density distribution of the halo and χ is the comoving distance along the line of sight. For the shear signal induced by a halo of mass M, the average excess three-dimensional matter density is given by

$$\rho(r) = \rho_{\rm m} \xi_{\rm hm}(r|M), \tag{2.9}$$

where $\rho_{\rm m} = \Omega_{\rm m,0}\rho_{\rm crit,0}(1+z)^3$ is the mean matter density of the universe and $\xi_{\rm hm}(r|M)$ is the halo-matter correlation function at the halo redshift. At small radius $\xi_{\rm hm}(r|M)$ is dominated by the cluster density profile and this regions is called the "1-halo" region; at larger radius, most of the contribution comes from correlated structures around the halo and it therefore referred to as the "2-halo" region. In this work, we examine both regions but focus on the 1-halo region for the cluster mass calibration.

There is a strong theoretical expectation that, barring the impact of baryonic effects, the 1-halo region of a halo should be described by the NFW model Navarro et al. (1996, 1997a). In this model, the cluster matter profile within the radius $r_{\rm 200c}$, which encloses a region with a mean density that is 200 times the critical density $\rho_{\rm crit}$ is well described as

$$\rho(r) = \delta_{\rm s}\rho_{\rm crit}\left[\frac{r}{cr_{\rm 200c}}\left(1+\left(\frac{r}{cr_{\rm 200c}}\right)^2\right)\right]^{-1}, \tag{2.10}$$

where $\delta_{\rm s}$ is a characteristic overdensity depending on c, which is the halo concentration parameter. Such a halo characterized by $r_{\rm 200c}$ has a mass which can be expressed as

$$M_{\rm 200c} = 200\rho_{\rm crit}(z)\frac{4\pi}{3}r^3_{\rm 200c}. \tag{2.11}$$

This underlying density profile implies a particular projected $\Delta\Sigma$ matter profile (Bartelmann, 1996), whose amplitude scales with the extent of the cluster along the line of sight (i.e., $r_{\rm 200c}$) and depends on the critical density, which varies with redshift as $\rho_{\rm crit} = 3H^2(z)/8\pi G$, where $H(z)$ is the Hubble parameter at redshift z and G is the Gravitational constant. For the projected profiles discussed below, we rename $r_{\rm 200c}$ to be $R_{\rm 200c}$, corresponding to the projected distance equal to the 3d radius that encloses the mass $M_{\rm 200c}$.

Within simulations the halo shapes vary from cluster to cluster due to formation history differences, and systematic trends in concentration with mass and redshift have been identified (Bhattacharya et al., 2013; Covone et al., 2014). But in the limit that the systematic variation in c with mass and redshift is small, the average projected matter profiles would have the same shape in the space of $R/R_{\rm 200c}$. The amplitudes of these projected matter profiles would scale as $R_{\rm 200c}\rho_{\rm crit}$. This suggests a rescaled projected matter profile $\widetilde{\Delta\Sigma}$ that would allow easy exploration of departures from self-similarity

$$\widetilde{\Delta\Sigma}\left(\frac{R}{R_{\rm 200c}}, z\right) = \frac{\Delta\Sigma\left(\frac{R}{R_{\rm 200c}}, z\right)}{R_{\rm 200c}\rho_{\rm crit}(z)}. \tag{2.12}$$

We note here that for any given R_Δ, where Δ represents the overdensity with respect to the critical or mean background densities, one can create a rescaled profile $\widetilde{\Delta\Sigma}$. If one chooses mean background density $\langle\rho(z)\rangle$, i.e. a scale radius of $R_{\rm 200m}$ rather than $R_{\rm 200c}$, the rescaling in amplitude would have to be adjusted to follow the correct redshift evolution of the mean background density $\langle\rho(z)\rangle = \Omega_{\rm m}\rho_{\rm crit}(z=0)\,(1+z)^3$.

Finally, because observationally determined cluster centers are not perfect tracers of the true halo center, one must consider also the impact that this mis-centering will have on the observed matter profile. When considering a mis-centering radius $R_{\rm mis}$ the azimuthal average of the surface mass density can be expressed as

$$\Sigma(R, R_{\rm mis}) = \frac{1}{2\pi}\int_0^{2\pi} {\rm d}\theta\, \Sigma\left(\sqrt{R^2 + R_{\rm mis}^2 - 2RR_{\rm mis}{\rm cos}\theta}\right). \tag{2.13}$$

Generally speaking, the mis-centering effects when using optical centers (MCMF adopts the brightest cluster galaxy (BCG) position or the center of mass of the red galaxy distribution if the BCG is significantly offset from that; Klein et al., 2024) or X-ray or even tSZE centers, the impact of mis-centering has only a minor impact outside the inner core region of the cluster. We return to this issue in Section 2.4.4.1.

2.3.1 Average matter profiles: Hydrodynamical simulations

To enable our study of the average cluster matter profiles, we extract cluster $\Delta\Sigma$ profiles following the method described in Grandis et al. (2021) for each redshift for both the IllustrisTNG and *Magneticum* simulations. In total, we extract 903, 852, 780, 684, and 528 cluster matter profiles at redshifts of 0.01, 0.25, 0.47, 0.78, and 0.96 respectively. In the absence of measurement uncertainties, we construct average $\Delta\Sigma$ profiles for further study using

$$\Delta\Sigma(R_j) = \frac{1}{N}\sum_i \Delta\Sigma_i(R_j), \tag{2.14}$$

where the sum is over the N clusters i in the sample and R_j is the radial binning adopted for the cluster matter profiles.

2.3.1.1 $\Delta\Sigma(R)$ dependence on mass and redshift

To start, we compute the average matter profiles within each of the five redshifts. We compare the average matter profiles $\Delta\Sigma(R)$ at different redshifts using the *Magneticum* sample in the left panel of Fig. 2.3. To ensure we are seeing only trends with redshift, we average a narrow range of cluster mass ($14.65 < \log(M/M_\odot) < 14.85$) for all of the redshifts. The average cluster matter profiles show a significant dependence on redshift.

In the right panel of Fig. 2.3 we plot average matter profiles $\Delta\Sigma(R)$ at three redshifts of 0.25, 0.47, and 0.78. Each redshift bin is divided into three mass bins ($14.30 < \log(M/M_\odot) < 14.45$, $14.45 < \log(M/M_\odot) < 14.65$ and $14.65 < \log(M/M_\odot) < 14.85$). Profiles show a significant dependence on halo mass for all three redshifts. Higher mass clusters have higher amplitude $\Delta\Sigma(R)$ when compared to the low mass clusters for a given redshift, due chiefly to the increased extent of the cluster along the line of sight. Fig. 2.3 makes clear that averaging cluster matter profiles in this way will therefore lead to results that are sensitive to the distribution of the cluster sample in redshift and mass (as well as the spatial distribution and masking of the source galaxies), which complicates the interpretation and characterization of such a mean matter profiles.

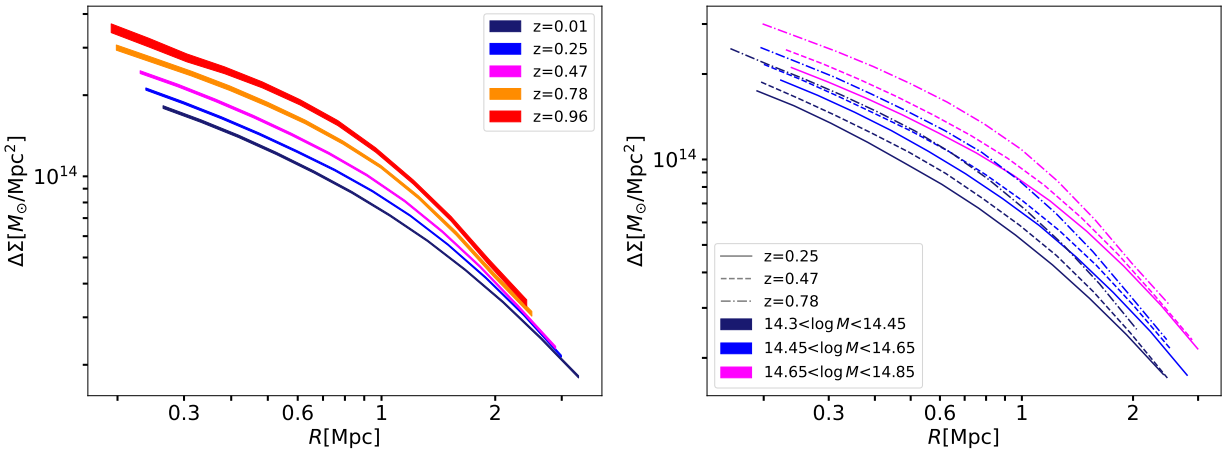

Figure 2.3: Average cluster matter profiles $\Delta\Sigma(R)$ in the *Magneticum* simulation at five redshifts (color-coded on left) for the same halo-mass bin ($14.65 < \log(M_{200c}/M_\odot) < 14.85$) and for three mass and redshift bins (color and line-type coded on right). The dependence of the matter profiles on cluster mass and redshift is clearly visible. The thickness of the lines represents the 68% credible region in the average matter profiles.

2.3.1.2 Evidence for self-similarity in mass and redshift

Motivated by the results from the previous section and the behavior of NFW profiles derived from N-body simulations, we now use the same simulated clusters to explore a rescaled matter profile $\widetilde{\Delta\Sigma}(R/R_{200c})$ (see Eq. 2.12) that would be the same for all samples of clusters if the population were truly self-similar.

To determine the average $\widetilde{\Delta\Sigma}$ profiles we combine the individual cluster matter profiles $\widetilde{\Delta\Sigma}_i$ as

$$\widetilde{\Delta\Sigma}\left(\frac{R}{R_{200c}}\right)_j = \frac{1}{N}\sum_i \widetilde{\Delta\Sigma}_i\left(\frac{R}{R_{200c}}\right)_j , \tag{2.15}$$

where the summation i is over the N clusters in the sample, and j denotes the radial bin in units of R/R_{200c}.

In the left panel of Fig. 2.4 we show average rescaled cluster matter profiles $\widetilde{\Delta\Sigma}\,(R/R_{200c})$ at five redshifts: 0.01, 0.25, 0.47, 0.78 and 0.96. We average all the clusters for a given redshift and then analyze the redshift trend. The profiles show very small variations and little change in amplitude with redshift as seen in the bottom left panel. This is in contrast to the behavior observed in Fig. 2.3 where we show $\Delta\Sigma(R)$. The average matter profiles line up for all redshifts from $R/R_{200c} \approx 0.6$ to $R/R_{200c} \approx 1$ with some small, remaining redshift trend at low and high R/R_{200c}.

Similarly, in the right panel of Fig. 2.4 we combine all the redshift samples and divide them into three mass bins ($14.30 < \log(M/M_\odot) < 14.45$, $14.45 < \log(M/M_\odot) < 14.65$ and $14.65 < \log(M/M_\odot) < 14.85$) to study the mass trends in average $\widetilde{\Delta\Sigma}\,(R/R_{200c})$. The profiles show remarkably small variation. This is an indication that even when hydrodynamical effects are included, simulated galaxy clusters over this range of mass and redshift

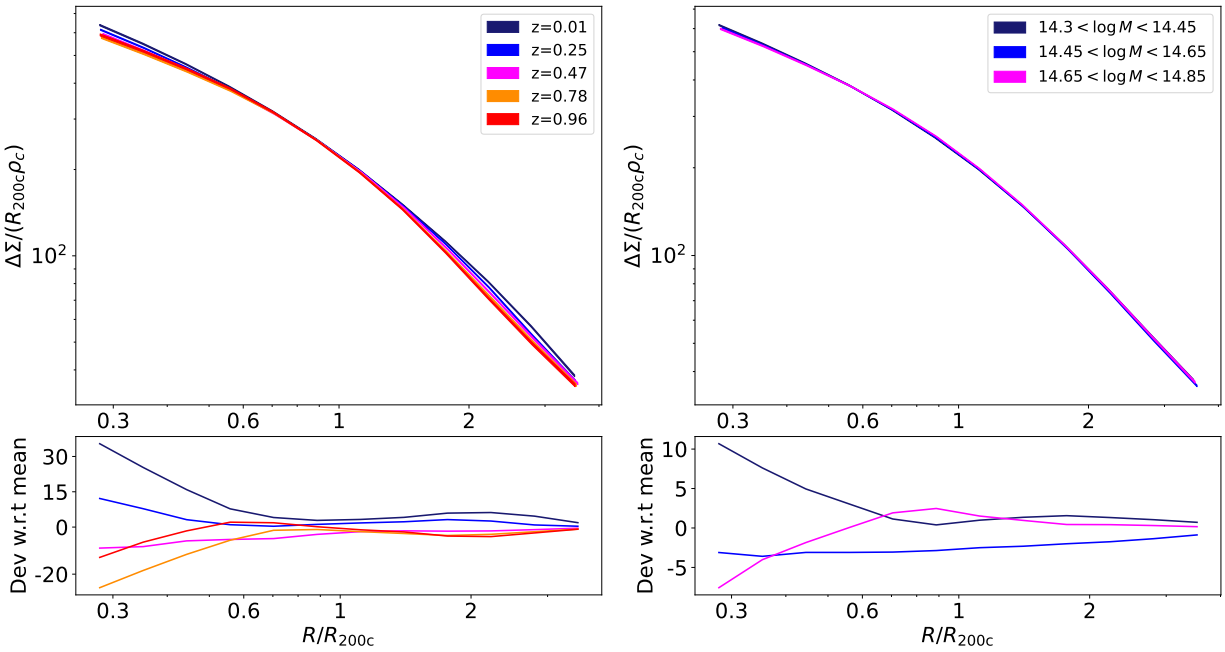

Figure 2.4: Average cluster matter profiles in the *Magneticum* simulation rescaled as in Eq. (2.12) to $\widetilde{\Delta\Sigma}(R/R_{200c})$. In the left plot, we average all the clusters ($14.3 < \log(M_{200c}/M_\odot) < 15$) for a given redshift and analyze the redshift trend. In the right plot, we average clusters over all redshift ranges ($0.01 \leq z \leq 0.96$) within a mass bin and analyze the mass trends. In both panels, the bottom plot shows the deviation of average profiles with respect to the mean of all the profiles. The rescaling dramatically reduces systematic trends in mass and redshift, highlighting the degree of self-similarity in the matter profiles even when baryonic components are included. The thickness of the lines in the upper panels represents the 68% credible region in the average matter profiles.

have matter profiles that exhibit strikingly similar shape. As discussed in Section 2.3, the lack of variation in shape is an indication of the self-similarity of cluster matter profiles along dimensions of mass and redshift.

2.3.1.3 Variations in average matter profiles

In this section, we aim to quantify the degree of variation we see in cluster matter profiles. For this, we calculate the fractional scatter in the average matter profiles as a function of redshift and mass. We also compare this to the fractional scatter values obtained when averaging profiles in physical space. The fractional scatter is given by $\sigma_{\Delta\Sigma}/ < \Delta\Sigma >$, where $\sigma_{\Delta\Sigma}$ is the standard deviation of the sample and $< \Delta\Sigma >$ is the mean of the sample.

We use the *Magneticum* simulation, which has a larger volume and therefore contains many more halos in comparison to IllustrisTNG. This allows us to measure a higher SNR through averaging profiles, which in turn enables us to better quantify the intrinsic scatter in the average matter profiles. We ignore the uncertainty on the average matter profiles

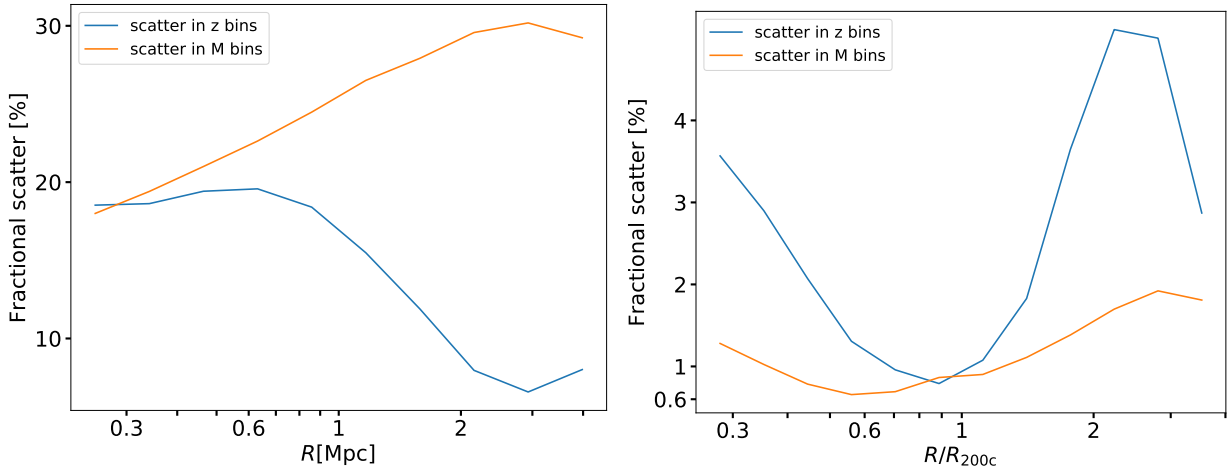

Figure 2.5: The fractional variation in the average matter profiles versus radius is shown for $\Delta\Sigma(R)$ on the left and for average rescaled matter profiles $\widetilde{\Delta\Sigma}(R/R_{200c})$ on the right. We track the scatter due to redshift variations in blue and mass variations in orange. The average rescaled matter profiles exhibit a factor ≈ 6 and ≈ 23 less variation on average with redshift and mass, respectively, within the 1-halo region.

when calculating the fractional scatter with redshift and mass, because the uncertainty is much smaller than the scatter.

Starting with the $\Delta\Sigma(R)$ profiles, we first divide each redshift bin into four mass bins. We calculate the fractional scatter as a function of redshift in a given mass bin and then report the average value of fractional scatter as a function of redshift of four mass bins as a function of radius in the left panel (blue curve) of Fig. 2.5. The scatter ranges from $\approx 7\%$ to $\approx 19\%$ with an average of $\approx 17\%$. Similarly, when analyzing the fractional scatter as a function of mass, we compute the scatter at each redshift bin and report the mean value for five redshift bins. The orange curve in the left panel of Fig. 2.5 shows the mean scatter values as a function of radius R with an average of $\approx 26\%$.

Moving to the average rescaled matter profiles $\widetilde{\Delta\Sigma}\,(R/R_{200c})$, we average all of the clusters for a given redshift and then report the fractional scatter among the five redshift bins. The blue curve in the right panel of Fig. 2.5 shows the fractional scatter as a function of redshift. The value varies from $\approx 0.8\%$ to $\approx 5\%$ with an average value of $\approx 2.6\%$ and the minimum value is achieved around $\approx 0.9R/R_{200c}$. The scatter in $\widetilde{\Delta\Sigma}\,(R/R_{200c})$ is reduced by a factor of 6 in comparison to the scatter obtained in $\Delta\Sigma(R)$. Similarly, when analyzing the fractional scatter as a function of mass, we divide each redshift into four mass bins and stack all of the clusters with different redshifts in a given mass bin. The orange curve in Fig. 2.5 shows the trend of the fractional scatter as a function of mass with scaled radius with an average value of $\approx 1.1\%$, which is 23 times smaller relative to the scatter with mass in $\Delta\Sigma(R)$.

2.3.2 Average matter profiles: Observations

In this section, we examine the matter profiles of the 698 SPT tSZE-selected clusters using the WL data from DES in physical and rescaled space. Given the cosmological parameters $\vec{p}$ (Table 2.1), the average $\Delta\Sigma$ estimator for the cluster ensemble in a radial bin R_j is a triple sum over clusters k, lensing source galaxy tomographic bins b and individual lensing source galaxies i as

$$\Delta\Sigma(R_j|\vec{p}) = \frac{\sum_{k,b,i} \frac{\Sigma_{\mathrm{crit},k,b} w_{k,b} \mathcal{W}^{\mathrm{s}}_{k,b,i} e_{\mathrm{t},k,b,i}}{(1-f_{\mathrm{cl},k,b})}}{\sum_{k,b,i} w_{k,b} \mathcal{W}^{\mathrm{s}}_{k,b,i} (R_{\gamma_{\mathrm{t},i}} + R_{\mathrm{sel}})}. \tag{2.16}$$

Here $\mathcal{W}^{\mathrm{s}}_i$ are the scaled source weights, and $w_{k,b}$ are the tomographic bin weights

$$\begin{aligned} \mathcal{W}^{\mathrm{s}}_{k,b,i} = &\quad w^{\mathrm{s}}_i \left(\frac{1-f_{\mathrm{cl},k,b}}{\Sigma_{\mathrm{crit},k,b}}\right)^2 \\ w_{k,b} = &\quad \Sigma^{-1}_{\mathrm{crit},k,b}, \end{aligned} \tag{2.17}$$

where the w^{s}_i represent individual source weights (defined as the inverse variance in the measured ellipticity). Following Bocquet et al. (2024a), we employ only tomographic bins 2 to 4 in this analysis. Additionally, we note that we only use the tomographic bins for which the median source redshift is larger than the cluster redshift. $\Sigma_{\mathrm{crit},k,b}$ is the critical surface density, which depends on cluster redshift and source galaxy redshift distribution, calculated as in Eq. 2.6. The ellipticity of a source galaxy i from a tomographic bin b and lying in the background of a cluster k is $e_{\mathrm{t},k,b,i}$, and $R_{\gamma_{\mathrm{t},i}}$ is the shear response for galaxy i, which is needed to scale the ellipticity to the reduced shear. Additionally, the selection response R_{sel} accounts for the fact that lensing sources are selected based on their (intrinsically) sheared observations. We use $R_{\mathrm{sel}} = -0.0026$ for optical centers as measured previously for this sample (Bocquet et al., 2024a). We also scale the ellipticity with a factor of $1/(1-f_{\mathrm{cl},k,b})$ to correct the profiles for the cluster member contamination, which is measured separately for each tomographic bin (see discussion in Section 2.4.4).

The corresponding uncertainty in $\Delta\Sigma$ for a radial bin R_j in the average cluster matter profile is calculated as

$$\sigma^2_{\Delta\Sigma}(R_j|\vec{p}) = \frac{\sum_{k,b,i} \left(\frac{\Sigma_{\mathrm{crit},k,b} w_{k,b} \mathcal{W}^{\mathrm{s}}_{k,b,i} \sigma_{\mathrm{eff},b}}{(1-f_{\mathrm{cl},k,b})}\right)^2}{(\sum_{k,b,i} w_{k,b} \mathcal{W}^{\mathrm{s}}_{k,b,i})^2}. \tag{2.18}$$

Here $\sigma^2_{\mathrm{eff},b}$ is the effective shape variance for sources in a given tomographic bin, and all other elements are as described in Eq. 2.16.

Similarly, after accounting for the rescaling described in Eq. 2.12 and given the cosmological parameters $\vec{p}$ and the cluster mass $M_{200\mathrm{c}}$ or equivalently the cluster radius $R_{200\mathrm{c}}$, the inverse variance weighted average $\widetilde{\Delta\Sigma}$ estimator in a radial bin $(R/R_{200\mathrm{c}})_j$ is given by

$$\widetilde{\Delta\Sigma}\left(\frac{R}{R_{200\mathrm{c}}}\middle| \vec{M_{200\mathrm{c}}}, \vec{p}\right)_j = \frac{\sum_{k,b,i} \frac{\Sigma_{\mathrm{crit},k,b} w_{k,b} \widetilde{\mathcal{W}}^{\mathrm{s}}_{k,b,i} e_{\mathrm{t},k,b,i}}{\rho_{\mathrm{crit}_k} R_{200\mathrm{c}_k} (1-f_{\mathrm{cl},k,b})}}{\sum_{k,b,i} w_{k,b} \widetilde{\mathcal{W}}^{\mathrm{s}}_{k,b,i} (R_{\gamma_{\mathrm{t},i}} + R_{\mathrm{sel}})}, \tag{2.19}$$

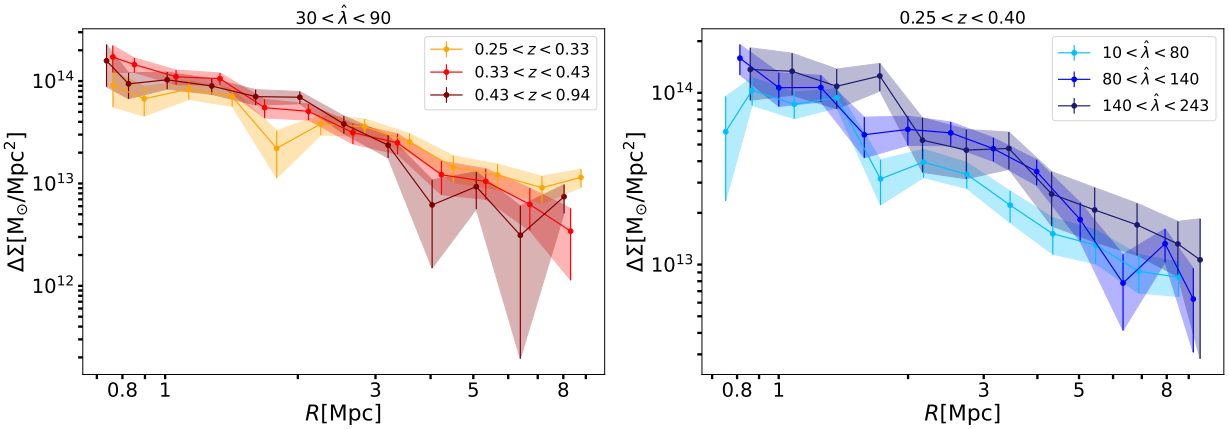

Figure 2.6: SPT tSZE-selected cluster average matter profiles $\Delta\Sigma(R)$ for three redshift bins in a given richness bin, and in the right panel we show average matter profiles $\Delta\Sigma(R)$ for different richness bins in a given redshift bin. The color bands encode the 68% credible region for each profile. The profiles show variation with redshift and richness that is consistent with that shown in Fig. 2.3 for the simulated clusters in redshift and mass.

where $\widetilde{\mathcal{W}}^{\rm s}_{k,b,i}$ is the re-scaled source weight corresponding to $\widetilde{\Delta\Sigma}$, which is defined as

$$\widetilde{\mathcal{W}}^{\rm s}_{k,b,i} = w^{\rm s}_i \left(\frac{\rho_{{\rm crit}_k} R_{200{\rm c}_k} (1 - f_{{\rm cl},k,b})}{\Sigma_{{\rm crit},k,b}} \right)^2 , \tag{2.20}$$

and the corresponding uncertainty is given by

$$\sigma^2_{\widetilde{\Delta\Sigma}} \left(\frac{R}{R_{200{\rm c}}} \middle| \vec{M_{200{\rm c}}}, \vec{p} \right)_j = \frac{\sum_{k,b,i} \left(\frac{\Sigma_{{\rm crit},k,b} w_{k,b} \widetilde{\mathcal{W}}^{\rm s}_{k,b,i} \sigma_{{\rm eff}_b}}{\rho_{{\rm crit},k} R_{200{\rm c}_k} (1 - f_{{\rm cl},k,b})} \right)^2}{(\sum_{k,b,i} w_{k,b} \widetilde{\mathcal{W}}^{\rm s}_{k,b,i})^2} . \tag{2.21}$$

The mean estimated scaled radius of a given radial bin j is calculated from the equation

$$\left(\frac{R}{R_{200{\rm c}}} \middle| \vec{M_{200{\rm c}}}, \vec{p} \right)_j = \frac{\sum_{k,b,i} w_{k,b} \widetilde{\mathcal{W}}^{\rm s}_{k,b,i} R_{k,b,i} / R_{200{\rm c}_k}}{\sum_{k,b,i} w_{k,b} \widetilde{\mathcal{W}}^{\rm s}_{k,b,i}} , \tag{2.22}$$

where $R_{k,b,i}$ is the projected separation of ellpiticity i in tomographic bin b from the center of cluster k. A similar expression for the mean radius R_j within a bin pertains, but without the $1/R_{200{\rm c}}$ scaling.

In the left panel of Fig. 2.6 we show the average cluster matter profile $\Delta\Sigma(R)$, in three redshift bins (for a richness bin, $30 < \hat{\lambda} < 90$ containing 426 clusters), and in the right panel, we show the average cluster matter profiles in three richness bins (for a redshift bin, $0.25 < z < 0.40$ containing 123 clusters). While the measurement uncertainties are significant in this sample (color bands represent 68% credible regions), it is still possible to discern variations among the presented average matter profiles.

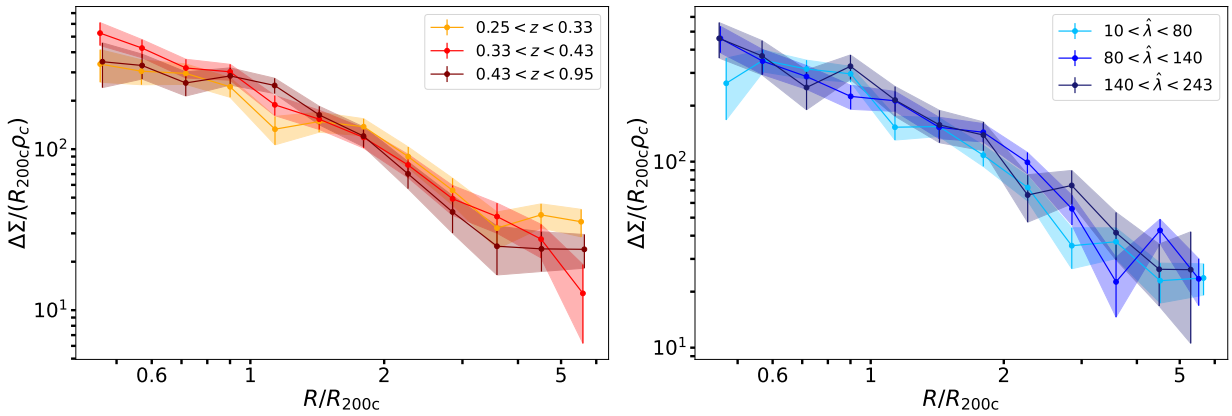

Figure 2.7: Average rescaled SPT cluster matter profiles $\widetilde{\Delta\Sigma}\,(R/R_{200c})$ constructed using the mass calibration posteriors from Bocquet et al. (2024b). In the left panel, we show $\widetilde{\Delta\Sigma}\,(R/R_{200c})$ profiles for three redshift bins, and in the right panel we show $\widetilde{\Delta\Sigma}\,(R/R_{200c})$ profiles for different richness bins. The average rescaled matter profiles show regularity similar to that seen in Fig. 2.4 for the cluster simulations.

To study the average $\widetilde{\Delta\Sigma}\,(R/R_{200c})$ profiles, we need a robust value of R_{200c} for each cluster, which then implies we need good mass constraints for each system (Eq. 2.11). For this purpose, we adopt the observable-mass relation (ζ-mass and λ-mass– see discussion in Section 2.4.1) posteriors from Bocquet et al. (2024b), where the mass calibration constraints were obtained using the same DES WL data as part of the cosmological cluster abundance analysis of the sample (Bocquet et al., 2024a). We use the full sample while analyzing clusters in redshift or richness bins. The average rescaled cluster matter profiles exhibit less evidence for variation than the $\Delta\Sigma(R)$ profiles in Fig. 2.7. In other words, the tSZE selected clusters show indications of self-similarity with redshift and richness similar to those presented above for the clusters from hydrodynamical simulations with redshift and mass.

This simplicity in the average rescaled matter profiles $\widetilde{\Delta\Sigma}\,(R/R_{200c})$ of the simulated and observed galaxy cluster population offers some advantages. It allows us to combine large ensembles of clusters with a wide halo mass and redshift range, creating higher SNR cluster matter profiles, which can be used to test different models of structure formation. Moreover, the modeling of average cluster matter profiles $\widetilde{\Delta\Sigma}\,(R/R_{200c})$ for observed cluster samples becomes more straightforward, because the final average profile is insensitive to the redshift and mass distribution of the cluster sample (and to the spatial distribution and masking of the source galaxies). We employ this simplicity in matter profiles in Section 2.4, where we present a new method of galaxy cluster mass calibration that exploits the approximate self-similarity of galaxy clusters.

2.4 Mass calibration method

Measurements of the weak lensing signal induced by foreground galaxy clusters can be used to robustly estimate the cluster mass. However, because the SNR of the WL signal is low for individual clusters, it is practical to perform mass calibration using the lensing signal averaged over many clusters (e.g. Umetsu et al., 2014b, 2016; Okabe et al., 2010, 2013). Because the average rescaled matter profiles $\widetilde{\Delta\Sigma}\left(R/R_{200c}\right)$ are particularly simple to model, they offer the possibility to improve upon previous average matter profile based weak lensing mass calibration methods.

The method presented below involves 1) building an ensemble of average rescaled matter profiles– one for each bin in cluster observable, 2) extracting a likelihood of these matter profiles given a model profile and then 3) iterating with a Markov Chain Monte Carlo method to characterize the posteriors of the model parameters thatdescribe the galaxy cluster observable-mass relations discussed in Section 2.4.1. The mean posteriors describe the parameters for which the observed and model average matter profiles are consistent over the full range of cluster observables. The average matter profile model is discussed in Section 2.4.2, and the mass calibration likelihood is presented in Section 2.4.3. A discussion of the systematic effects and their correction then appears in Section 2.4.4.

2.4.1 Observable-mass relations

In our analysis, each confirmed cluster has four associated observable quantities. These include the tSZE detection significance $\hat{\zeta}$, the MCMF obtained richness $\hat{\lambda}$ and redshift z and the weak lensing mass $M_{\rm WL}$ that is derived using the WL shear and photometric redshift measurements of the background, lensed source galaxies. The WL masses are measured using average matter profiles $\widetilde{\Delta\Sigma}\left(R/R_{200c}\right)$, and these masses are used to constrain the so-called cluster observable–mass relations (e.g. Mohr & Evrard, 1997; Mohr et al., 1999; Finoguenov et al., 2001; Chiu et al., 2016b, 2018; Bulbul et al., 2019) that describe the redshift dependent statistical binding between the observables (i.e., detection significance, richness and weak lensing mass) and the underlying halo mass, which for this analysis we take to be M_{200c}.

2.4.1.1 tSZE detection significance $\hat{\zeta}$

As described in an early SPT analysis (Vanderlinde et al., 2010), the tSZE detection significance or signal-to-noise ratio $\hat{\zeta}$ is related to the unbiased significance ζ as

$$P(\hat{\zeta}|\zeta) = \mathcal{N}\left(\sqrt{\zeta^2+3}, 1\right), \tag{2.23}$$

where $\mathcal{N}$ denotes a Gaussian distribution. This relationship accounts for the maximization bias in $\hat{\zeta}$ caused during the cluster matched filter candidate selection (Melin et al., 2006), which has three free parameters (cluster sky location and cluster model filter scale). The

normal distribution models the impact of the unit noise in the appropriately rescaled mm-wave maps. The mean unbiased detection significance is modeled as a power-law relation in mass and redshift

$$\langle \ln \zeta | M_{200c}, z \rangle = \ln \zeta_0 + \zeta_M \ln \left(\frac{M_{200c}}{M_{piv}} \right) + \zeta_z \ln \left(\frac{E(z)}{E(z_{piv})} \right), \tag{2.24}$$

where $\ln \zeta_0$ is the normalization, ζ_M is the mass trend, ζ_z is the redshift trend, $E(z)$ is the dimensionless Hubble parameter, $M_{piv} = 3 \times 10^{14} h^{-1} M_\odot$ is the pivot mass and $z_{piv} = 0.6$ is the pivot redshift, which are chosen to reflect the median mass and redshift of our confirmed cluster sample. To account for the variable depth of the SPT survey fields, we rescale the amplitude ζ_0 on a field-by-field basis

$$\zeta_{0,i} = \gamma_i \zeta_0, \tag{2.25}$$

where γ_i is obtained from simulated maps (Bleem et al., 2015; Bleem et al., 2020, 2024). This approach allows us to combine the full SPT cluster sample when empirically modeling the ζ-mass relation. We model the intrinsic scatter in ζ at fixed mass and redshift as log-normal $\sigma_{\ln \zeta}$. This single scatter parameter has been shown to be sufficient to model the SPT tSZE-selected cluster sample ζ-mass relation (Bocquet et al., 2019; Bocquet et al., 2024b). We return to this question with new validation tools in Section 2.5.2.1.

2.4.1.2 Cluster richness $\hat{\lambda}$

The observed cluster richness $\hat{\lambda}$ is related to the intrinsic richness λ as

$$P(\hat{\lambda} | \lambda) = \mathcal{N} \left(\lambda, \sqrt{\lambda} \right), \tag{2.26}$$

which models the Poisson sampling noise in the limit of a normal distribution where the dispersion is $\sigma = \sqrt{\lambda}$. The mean intrinsic richness is modeled as a power law in mass and redshift

$$\langle \ln \lambda | M_{200c}, z \rangle = \ln \lambda_0 + \lambda_M \ln \left(\frac{M_{200c}}{M_{piv}} \right) + \lambda_z \ln \left(\frac{1+z}{1+z_{piv}} \right), \tag{2.27}$$

where λ_0 is the normalization, λ_M is the mass trend, λ_z is the redshift trend and, as above, $M_{piv} = 3 \times 10^{14} h^{-1} M_\odot$ and $z_{piv} = 0.6$. The intrinsic scatter of the intrinsic richness λ at fixed mass and redshift is modeled as a log-normal distribution with the parameter $\sigma_{\ln \lambda}$. This scatter is the same for all redshifts and masses, which has been shown to be adequate for modeling the λ-mass relation of the SPT selected cluster sample (Bocquet et al., 2024b). We return to this question also with new validation tools in Section 2.5.2.1.

2.4.1.3 Weak lensing mass M_{WL}

In addition to the ζ-mass and λ-mass relations, we also include a mapping between the so-called weak lensing mass M_{WL}, which is the mass one would infer by fitting a model

profile to an individual cluster matter profile, and the halo mass M_{200c}. This follows the approach adopted in previous work (Becker & Kravtsov, 2011; Dietrich et al., 2019; Grandis et al., 2021; Bocquet et al., 2024a) and is a mechanism for incorporating corrections for systematic biases that may arise from the interpretation of the average matter profiles and for marginalising over the remaining systematic uncertainties in those bias corrections. For example, the uncertainties associated with hydrodynamical simulations and the subgrid physics they incorporate can be modeled with this $M_{\rm WL}$-mass relation, incorporating an effective systematic floor in the accuracy of the final, calibrated masses. We characterize this relation as

$$\begin{aligned}\left\langle \ln\left(\frac{M_{\rm WL}}{M_{\rm piv}}\right)\right\rangle =& \ln M_{\rm WL_0} + M_{\rm WL_M}\ln\left(\frac{M_{\rm 200c}}{M_{\rm piv}}\right) \\ &+ M_{\rm WL_z}\ln\left(\frac{1+z}{1+z_{\rm piv}}\right),\end{aligned} \tag{2.28}$$

where $\ln M_{\rm WL_0}$ is the logarithmic bias at $M_{\rm 200c} = M_{\rm piv}$ and $M_{\rm WL_M}$ and $M_{\rm WL_z}$ are the mass and redshift trends, respectively, of this bias. For symmetry with the other observable-mass relations, we explicitly include the redshift trend parametrization, whereas in previous analyses (see Bocquet et al., 2024a) the relation has been defined at specific redshifts where the required simulation outputs are available.

The weak lensing mass $M_{\rm WL}$ estimated from individual clusters exhibits a mass dependent log-normal scatter $\sigma_{\ln \rm WL}$ about the mean relation, which we model as

$$\begin{aligned}\ln \sigma^2_{\ln \rm WL} =& \ln \sigma^2_{\ln \rm WL_0} + \sigma^2_{\ln \rm WL_M}\ln\left(\frac{M_{\rm 200c}}{M_{\rm piv}}\right) \\ &+ \sigma^2_{\ln \rm WL_z}\ln\left(\frac{1+z}{1+z_{\rm piv}}\right),\end{aligned} \tag{2.29}$$

where $\ln \sigma^2_{\ln \rm WL_0}$ is the logarithm of the variance of $M_{\rm WL}$ around $M_{\rm 200c}$ at $M_{\rm piv}$ and $z_{\rm piv}$ and $\sigma^2_{\ln \rm WL_M}$ and $\sigma^2_{\ln \rm WL_z}$ are the mass and redshift trends, respectively, of this variance. For an average rescaled matter profile that is produced using N clusters, the effective scatter of the extracted $M_{\rm WL}$ about the true mass would scale down as $1/\sqrt{N}$, reducing the stochasticity associated with the estimate of the underlying halo mass and reducing the importance of possible correlations between the scatter in $M_{\rm WL}$ and other observables.

The parameter posteriors on these relations are extracted through a $M_{\rm WL}$ calibration exercise carried out on hydrodynamical simulations of clusters output over a range of redshifts (Grandis et al., 2021). This calibration exercise employs a model profile or set of model profiles as discussed in the next section and characterizes the biases and scatter associated with that model. In addition, systematic uncertainties on photometric redshifts, the multiplicative shear bias, the cluster member contamination model and the cluster mis-centering model are also incorporated into the posteriors on these parameters, making it straightforward to marginalize over all critical systematic uncertainties in the mass calibration analysis. We return to this in Section 2.4.4.

2.4.2 Average rescaled matter profile model $\widetilde{\Delta\Sigma}_{\rm mod}$

We use the IllustrisTNG and the *Magneticum* simulations at five redshifts between 0 to 1 (as described in the Section 2.2.3) to create an average weak lensing model for use in mass calibration. Because there is little variation in the average rescaled matter profiles $\widetilde{\Delta\Sigma}\,(R/R_{\rm 200c})$ with mass and redshift, we could adopt a single average matter profile at all redshifts and masses for the model used in mass calibration. We could then correct for the small biases introduced by this assumption of perfect self-similarity using the $M_{\rm WL}$-mass relations (Eq. 2.28 and 2.29). However, an examination of the average matter profiles presented in Fig. 2.4 provides clear evidence for small departures from self-similarity with redshift, while showing no convincing evidence of departures from self-similarity in mass. Therefore, we adopt a model $\widetilde{\Delta\Sigma}\,(R/R_{\rm 200c})$ profile that varies with redshift, while assuming perfect self-similarity in mass. This approach sets the mean logarithmic bias $\ln M_{\rm WL_0}$ in the $M_{\rm WL}$-mass relation to zero over all masses and redshifts.

To construct an average weak lensing model that represents the typical behavior across both sets of simulations, we select the same number of simulated clusters from both the *Magneticum* and IllustrisTNG simulations. Since the subgrid physics differ between the two, the average matter profiles may differ. Given that IllustrisTNG has fewer halos, we randomly choose an equal number of halos from *Magneticum*. Specifically, we select 301, 284, 260, 228, and 176 halos corresponding to the redshifts 0.01, 0.25, 0.47, 0.78, and 0.96, respectively.

For each halo, we extract 3 mis-centered cluster matter profiles (using the method described in Grandis et al. (2021)) and average all of the clusters at a given redshift from both simulations. We follow the mis-centering distribution model as described in the Section 2.4.4.1. Because mis-centering depends on the richness of the cluster, we assign each halo a richness value using the richness-mass relation (Eq. 2.27) using the parameters obtained in a previous cluster cosmology analysis (Chiu et al., 2023). These individual $\Delta\Sigma(R)$ profiles are then rescaled into $\widetilde{\Delta\Sigma}\,(R/R_{\rm 200c})$ profiles and averaged following Eq. 2.15.

Given that the two sets of simulations do not have outputs at exactly the same redshifts, e.g., 0.42 vs. 0.47 and 0.64 vs. 0.78, we quantify the differences in the average $\widetilde{\Delta\Sigma}\,(R/R_{\rm 200c})$ profiles at these redshifts, verifying that this induces a negligible uncertainty. This is achieved by interpolating the profiles from both simulations as a function of redshift separately and comparing for each simulation the differences in the profiles at both the redshifts, and finding them to be very small (percentage error of ≈ 0.4 %, see Fig. A.1). We therefore adopt the mean value of the redshift (in case the redshifts are different) while combining the profiles from both simulations. The combined profiles are then interpolated as a function of redshift to capture the slight differences we see with redshift in the average $\widetilde{\Delta\Sigma}\,(R/R_{\rm 200c})$ profiles.

Once an average rescaled matter profile model has been chosen, it is used to characterize the bias and scatter in the $M_{\rm WL}$ estimates with respect to the true underlying halo masses, determining posteriors of the parameters in Eqs. 2.28 and 2.29. As part of this calibration process, uncertainties on the other crucial systematics (uncorrelated large-scale structure covariance, cluster mis-centering, cluster member contamination of the source

galaxy sample, and hydrodynamical uncertainties on the model) are also included. Note that our model uses Eq. 2.3 to calculate $\Delta\Sigma$, while we use Eq. 2.5 to calculate the observed profiles. This introduces a 1% bias in our modeling; however, given that our analysis is dominated by statistical uncertainties, this has no significant impact on our conclusions.

2.4.3 Mass calibration likelihood

In this section, we present the mass calibration likelihood that we employ with the average rescaled matter profile $\widetilde{\Delta\Sigma}\,(R/R_{200c})$. The lowest level observational constraint from weak gravitational lensing is a tangential reduced shear profile (Eq. 2.1) constructed for each of a series of tomographic bins within which the shear galaxy sample is organized. A complication with using the tangential shear profiles (see, e.g., Bocquet et al., 2024a), is that the profiles from the different bins have amplitudes that depend on $\Sigma_{\rm crit}$, which in turn depends on the redshift distributions of the background galaxies (Eq. 2.4). The matter profile $\Delta\Sigma(R)$ (Eq. 2.3) is simpler in that the profiles for each tomographic bin are all estimators of the same underlying projected matter density of the cluster (see, e.g., McClintock et al., 2018). The observable we adopt here $\widetilde{\Delta\Sigma}\,(R/R_{200c})$ (Eq. 2.12) offers additional simplicity, because this profile is approximately the same for all clusters, independent of their mass and redshift. However, the matter profile $\Delta\Sigma(R)$ and rescaled matter profile $\widetilde{\Delta\Sigma}\,(R/R_{200c})$ are no longer pure observables. They both have dependences on cosmological parameters that impact the distance-redshift relation, and the rescaled matter profile also has dependences on the masses and redshifts of the constituent clusters. This dependence has to be considered within the likelihood, as outlined in the next subsection.

2.4.3.1 Likelihood of the rescaled matter profile

The lensing likelihood for an average rescaled matter profile is given by a product of the independent Gaussian probabilities of obtaining the observed matter profile given the model within each radial bin. Because the rescaled matter profile $\widetilde{\Delta\Sigma}\,(R/R_{200c})$ depends on cosmological parameters and the masses and radii of the constituent clusters, the likelihood has to be altered to account for these dependencies. The likelihood transformation for a data vector t_θ which is some function of a data vector y (independent of model parameters) and model parameters θ is given by (Severini, 2004)

$$P(t_\theta|\theta)d\theta \longrightarrow P(t_\theta|\theta)\left|\frac{\partial t_\theta}{\partial \mu}\right|\mathrm{d}\mu. \tag{2.30}$$

Here μ denotes a function of data y that has the same dimension as t_θ and is independent of the model parameters θ. In the case where μ cannot be expressed with the same dimension as t_θ, the likelihood transformation is then given by

$$P(t_\theta|\theta)d\theta \longrightarrow P(t_\theta|\theta)\left|\frac{\partial t_\theta}{\partial \mu}\left(\frac{\partial t_\theta}{\partial \mu}\right)^{\mathrm{T}}\right|^{1/2}\mathrm{d}\mu. \tag{2.31}$$

Using Eq. 2.31 we can write the transformed Gaussian likelihood (lensing likelihood) for a rescaled matter profile $\widetilde{\Delta\Sigma}\left(\vec{M_{200c}}, \vec{p}\right)$ (given by Eq. 2.19) with j radial bins as

$$P(\widetilde{\Delta\Sigma}\left(\vec{M_{200c}}, \vec{z}, \vec{p}\right)|\widetilde{\Delta\Sigma}_{\rm mod}, \vec{z}) = \prod_j P_{{\rm G},j} \left| \frac{\partial\widetilde{\Delta\Sigma}_j}{\partial\vec{e}_{t,j}} \left(\frac{\partial\widetilde{\Delta\Sigma}_j}{\partial\vec{e}_{t,j}}\right)^{\rm T}\right|^{1/2}, \tag{2.32}$$

where $\widetilde{\Delta\Sigma}_{\rm mod}$ is the model profile and the second factor in the above equation is the transformation calculation for all the radial bins, $\vec{e}_{t,j} = [e_t^1, e_t^2, e_t^3 ... e_t^n]$ is the vector containing the n source ellipticities in a given radial bin j and $P_{{\rm G},j}$ is the Gaussian likelihood for that bin

$$P_{{\rm G},j} = \left(\sqrt{2\pi}\sigma_{\widetilde{\Delta\Sigma},j}\right)^{-1} \exp\left[-\frac{1}{2}\left(\frac{\widetilde{\Delta\Sigma}_j - \widetilde{\Delta\Sigma}_{\rm mod,j}}{\sigma_{\widetilde{\Delta\Sigma},j}}\right)^2\right], \tag{2.33}$$

where $\sigma_{\widetilde{\Delta\Sigma},j}$ is the rescaled shape noise as described in Eq. 2.21. The likelihood transformation is a 1-dimensional partial derivative matrix with length n and is given by

$$\frac{\partial\widetilde{\Delta\Sigma}_j}{\partial\vec{e}_{t,j}} = \left[\frac{\partial\widetilde{\Delta\Sigma}_j}{\partial e_{t,j}^1}, \frac{\partial\widetilde{\Delta\Sigma}_j}{\partial e_{t,j}^2}, ..., \frac{\partial\widetilde{\Delta\Sigma}_j}{\partial e_{t,j}^n}\right]. \tag{2.34}$$

The transformation factor can then be expressed as

$$\begin{aligned}\left|\frac{\partial\widetilde{\Delta\Sigma}_j}{\partial\vec{e}_{t,j}}\left(\frac{\partial\widetilde{\Delta\Sigma}_j}{\partial\vec{e}_{t,j}}\right)^T\right|^{1/2} = & \left(\left(\frac{\partial\widetilde{\Delta\Sigma}_j}{\partial e_{t,j}^1}\right)^2 + \left(\frac{\partial\widetilde{\Delta\Sigma}_j}{\partial e_{t,j}^2}\right)^2 + ... \right. \\ & \left. + \left(\frac{\partial\widetilde{\Delta\Sigma}_j}{\partial e_{t,j}^n}\right)^2\right)^{1/2},\end{aligned} \tag{2.35}$$

where we just compute the derivative of Eq. 2.19 with respect to the measured ellipticities.

2.4.3.2 Likelihood of single cluster rescaled matter profile

The intrinsic scatter in the observable mass relations, the measurement noise on the observables, and the posteriors of the observable-mass relation parameters and the cosmological parameters all contribute to create the posterior mass distribution $P(M|\hat{\zeta}, \hat{\lambda}, z, \vec{p})$ for a given cluster. Even in the limit of perfect knowledge of the observable-mass relation and cosmological parameters, this posterior distribution has some characteristic width determined by the mass trends in each observable together with the sources of scatter mentioned above. Moreover, even in the case of a perfect match between the observed and model rescaled matter profiles, the resulting weak lensing mass estimate is a biased and scattered estimator of the true halo mass M_{200c} as described by the $M_{\rm WL}$-halo mass relations (Eq. 2.28 and 2.29).

The cluster mass uncertainty represented by this mass posterior and any biases and scatter in the weak lensing mass estimate have to be accounted for. Therefore, the single cluster

lensing likelihood for cluster k with the weak lensing mass posterior $P_k(M_{\rm WL}|\hat{\zeta},\hat{\lambda},z,\vec{p})$ and rescaled matter profile $\widetilde{\Delta\Sigma}_k$ is written as

$$P(\widetilde{\Delta\Sigma}_k|\widetilde{\Delta\Sigma}_{\rm mod},z)=\int {\rm d}M_{\rm WL}P_k(M_{\rm WL}|\hat{\zeta},\hat{\lambda},z,\vec{p})P(\widetilde{\Delta\Sigma}_k(M_{\rm WL})|\widetilde{\Delta\Sigma}_{\rm mod},z), \tag{2.36}$$

where we are explicit with subscript k to emphasize that this expression represents a weighted likelihood for a single cluster. We note that the $M_{\rm WL}$ dependence of $\widetilde{\Delta\Sigma}_k$ is due to the cluster radius (Eq. 2.12), which is mass dependent as in Eq. 2.11.

We calculate the mass posterior using three observables $\hat{\zeta}$, $\hat{\lambda}$ and z (we neglect the cluster photometric redshift uncertainty because it is too small relative to other sources of scatter to be important). According to Bayes' theorem, the expression for the mass posterior of a cluster that accounts for intrinsic and measurement scatter in the observables is

$$P(M_{\rm WL}|\hat{\zeta},\hat{\lambda},z,\vec{p})=\frac{\iiint {\rm d}M{\rm d}\lambda{\rm d}\zeta P(\hat{\lambda}|\lambda)P(\hat{\zeta}|\zeta)P(\zeta,\lambda,M_{\rm WL}|M,z,\vec{p})P(M|z,\vec{p})}{P(\hat{\lambda},\hat{\zeta}|z,\vec{p})}, \tag{2.37}$$

where the measurement noise is represented by $P(\hat{\lambda}|\lambda)$ and $P(\hat{\zeta}|\zeta)$, the intrinsic scatter and any bias in the observable about mass by $P(\zeta,\lambda,M_{\rm WL}|M,z,\vec{p})$, $P(M|z,\vec{p})$ is the halo mass function factor which allows us to account for Eddington bias due to the selection, and $P(\hat{\lambda},\hat{\zeta}|z,\vec{p})$ is just the numerator integrated over $M_{\rm WL}$.

In the context of multiple observables, the single cluster mass calibration likelihood $\mathcal{L}_{\rm single}$ can be written (assuming $\widetilde{\Delta\Sigma}$ is uncorrelated with other observables) as a product of the single cluster lensing likelihood and the likelihood of the observables

$$\mathcal{L}_{\rm single}=P(\widetilde{\Delta\Sigma}_k|\widetilde{\Delta\Sigma}_{\rm mod},z)P(\hat{\lambda}|\hat{\zeta},z,p), \tag{2.38}$$

where the second component is the likelihood of the observed richness $\hat{\lambda}$ given the observed tSZE detection significance $\hat{\zeta}$ and redshift z. It can be calculated using Bayes' theorem accounting for intrinsic scatter in the observables

$$P(\hat{\lambda}|\hat{\zeta},z,\vec{p})=\frac{\iiint {\rm d}M{\rm d}\lambda{\rm d}\zeta P(\hat{\lambda}|\lambda)P(\hat{\zeta}|\zeta)P(\zeta,\lambda|M,z,\vec{p})P(M|z,\vec{p})}{P(\hat{\zeta}|z,\vec{p})}, \tag{2.39}$$

where $P(\hat{\zeta}|z,\vec{p})$ is just the normalization that comes from integrating the numerator over all $\hat{\lambda}$, including importantly the $\hat{\lambda}_{\rm min}(z)$ selection threshold, which is crucial for accounting for Malmquist bias. Additionally, in this study, we assume that there is no correlated scatter between ζ and λ, so $P(\zeta,\lambda|M,z,\vec{p})$ can be further simplified as $P(\zeta|M,z,\vec{p})P(\lambda|M,z,\vec{p})$.

2.4.3.3 Likelihood of multi-cluster average rescaled matter profile

For a given $\hat{\zeta}-\hat{\lambda}-z$ bin containing n clusters, the rescaled matter profile $\widetilde{\Delta\Sigma}$ is notionally calculated as in Eq. 2.19. However, as discussed above for the single cluster rescaled matter

profile, the mass posteriors of the clusters must be included. Rather than extracting an average likelihood by marginalizing over the weak lensing mass posterior $P(M_{\rm WL}|\hat{\zeta},\hat{\lambda},z,\vec{p})$ as in the single cluster case (Eq. 2.36), in the multi-cluster case we adopt a Monte Carlo integration approach that allows us to efficiently marginalize over the mass posteriors of all n clusters simultaneously. In effect, we rebuild the average matter profile $\widetilde{\Delta\Sigma}$ for the cluster ensemble many times and use those profiles to extract likelihoods and then estimate the average likelihood of the rescaled matter profile.

Following the likelihood for a single cluster matter profile in Eq. 2.38, we write the weak lensing mass calibration likelihood for an ensemble of n clusters with associated observables $\hat{\lambda}_i$, $\hat{\zeta}_i$ and z_i as

$$\mathcal{L}_{\rm bin} = \langle P\left(\widetilde{\Delta\Sigma}(\vec{\hat{\zeta}},\vec{\hat{\lambda}},\vec{z},\vec{p})|\widetilde{\Delta\Sigma}_{\rm mod},\vec{z}\right)\rangle \prod_{i=1}^{n} P(\hat{\lambda}_i|\hat{\zeta}_i,z_i,\vec{p}), \tag{2.40}$$

where $\langle P\left(\widetilde{\Delta\Sigma}(\vec{\hat{\zeta}},\vec{\hat{\lambda}},\vec{z},\vec{p})|\widetilde{\Delta\Sigma}_{\rm mod},\vec{z}\right)\rangle$ is the average lensing likelihood of the average rescaled matter profile built from the ensemble. The observable vectors $\vec{\hat{\zeta}}$, $\vec{\hat{\lambda}}$, and $\vec{z}$ each contain the measurements for the n clusters in the ensemble. For an n cluster ensemble, it takes the form

$$\begin{aligned}\langle P\left(\widetilde{\Delta\Sigma}\left(\vec{\hat{\zeta}},\vec{\hat{\lambda}},\vec{z},\vec{p}\right)|\widetilde{\Delta\Sigma}_{\rm mod},\vec{z}\right)\rangle = \\ \int\cdots\int {\rm d}M_{\rm WL_1}...{\rm d}M_{\rm WL_n} P(M_{\rm WL_1}|\hat{\zeta}_1,\hat{\lambda}_1,z_1,\vec{p})\times ... \\ P(M_{\rm WL_n}|\hat{\zeta}_n,\hat{\lambda}_n,z_n,\vec{p}) \\ P\left(\widetilde{\Delta\Sigma}(M_{\rm WL_1},...,M_{\rm WL_n},\vec{p})|\widetilde{\Delta\Sigma}_{\rm mod},\vec{z}\right),\end{aligned} \tag{2.41}$$

where we note that the $M_{\rm WL}$ is needed to build the rescaled matter profile (using Eq. 2.19 with $M_{\rm WL}$ instead of $M_{\rm 200c}$) and is calculated from observables ($\hat{\lambda}$, $\hat{\zeta}$ and z) and the $M_{\rm WL}$-mass relation using Eq. 2.28.

The final likelihood for m $\hat{\zeta}-\hat{\lambda}-z$ bins can be written as the product of the likelihood of individual bins

$$\mathcal{L} = \prod_{\rm bin=1}^{m} \mathcal{L}_{\rm bin}. \tag{2.42}$$

2.4.4 Modeling and correcting for systematic effects

2.4.4.1 Cluster mis-centering distribution

For each of the clusters in our sample, we have two measurements of the cluster center. The first is the tSZE center as measured by the SPT and the second is the optical center extracted using the MCMF algorithm. MCMF adopts the BCG as the center if it is within 250 kpc of the cluster position determined by SPT; otherwise, the position of the peak of

the galaxy density map is used. We only make use of MCMF centers for our analysis. As the observationally determined center is not a perfect tracer of the true halo center, the effect of this mis-centering must be taken into account when modeling the cluster matter profile. We adopt the mis-centering model and the parameters from the recent work by Bocquet et al. (2024a). The mis-centering distribution for the tSZE and optical centers is modeled using the double Rayleigh distribution.

$$\begin{aligned} P_{\rm offset}(r) &= \rho {\rm Rayl}(r, \sigma_0) + (1-\rho){\rm Rayl}(r, \sigma_1), \\ \sigma_i &= \sigma_{i,0} \left(\frac{\lambda}{60}\right)^{1/3} \text{ for } i \in \{0, 1\}. \end{aligned} \tag{2.43}$$

The double Rayleigh distribution is a good description of the mis-centering of the optical center with respect to the true halo center. The constraints on the mis-centering parameters $(\rho, \sigma_0, \sigma_1)$ are obtained by simultaneously fitting for SPT and optical centers. A large fraction of clusters ($\rho \approx 0.89$) are well centered, and the two scatter parameters are $\sigma_0 \approx 0.007\ h^{-1}$Mpc and $\sigma_1 \approx 0.18\ h^{-1}$Mpc (for additional details, see Bocquet et al., 2024a).

Crucial for our mass calibration analysis is to include the effects of uncertainties on the mis-centering distribution. We do this as part of the $M_{\rm WL}$-mass relation calibration. However, given the radial range we adopt for mass calibration ($R > 500\ h^{-1}$ kpc), the miscentering itself and the uncertainties on the mis-centering have little impact on our results.

2.4.4.2 Cluster member contamination

Cluster galaxies are generally included in the WL source galaxy sample in the case where the cluster redshift lies within the source galaxy redshift distribution associated with a tomographic bin (see Fig 2.2). These cluster galaxies are not sheared by their host cluster halo, and therefore, their inclusion biases the lensing signal low. To correct for this shear bias, we follow the methodology described in Paulus (2021), developed for the DES Y1 WL dataset, and in Bocquet et al. (2024a), where the method was extended for application to the DES Y3 WL tomographic bin based dataset. The method follows notionally the work by Varga et al. (2019) but more explicitly accounts for varying cluster redshift $z_{\rm cl}$. Here we extend this method again by modeling the contamination within each tomographic bin separately.

In our analysis, the fractional contamination by cluster members $f_{{\rm cl},b}$ in tomographic source bin b is extracted by modeling the probability density function of galaxies in redshift along the line of sight toward the cluster as the weighted sum of the cluster member distribution $P_{{\rm cl},b}(z)$ and the average source galaxy field distribution in tomographic bin b as

$$P_b(z) = f_{{\rm cl},b} P_{{\rm cl},b}(z) + (1 - f_{{\rm cl},b}) P_{{\rm field},b}(z), \tag{2.44}$$

where $P_{{\rm field},b}(z)$ corresponds to the field component, which has been divided into three tomographic bins $b \in 2, 3, 4$. For this analysis, the individual source galaxy DNZ photo-z's (De Vicente et al., 2016) are employed.

To determine both the cluster and field components as described, the source galaxies from the DES Y3 shear catalog associated with each cluster are divided into nine logarithmically spaced bins in projected radius, ranging from $0.7h^{-1}\,\mathrm{Mpc}$ to $10h^{-1}\,\mathrm{Mpc}$ from each cluster center. Because the projected cluster galaxy population falls off rapidly with radial distance from the cluster, the outermost two bins are dominated by the field source distribution. As previously reported in Paulus (2021), the depth inhomogeneities and masking variations in the DES WL source galaxy catalog lead to a field component surface density associated with each tomographic bin being relatively homogeneous on the scale of a cluster but varying significantly over the survey. Thus, we use a local measure of the field surface density around each cluster when modeling the contamination.

The redshift distribution of the cluster component $P_{\mathrm{cl},b}(z)$ is modeled as a Gaussian distribution in the space of $z - z_{\mathrm{cl}}$ with a redshift dependent characteristic width of $\sigma_{\mathrm{z},b}(z)$ and redshift offset parameter $z_{\mathrm{off,b}}(z)$ as

$$P_{\mathrm{cl},b}(z) = \frac{1}{\sqrt{2\pi}\sigma_{\mathrm{z},b}(z)} e^{-\frac{(z-z_{\mathrm{cl}}-z_{\mathrm{off},b}(z))^2}{2\sigma^2_{\mathrm{z},b}(z)}}. \tag{2.45}$$

The characteristic width of the cluster members in redshift reflects the typical photo-z uncertainties, and the offset in redshift away from the cluster redshift can result from, e.g., the selection applied in dividing source galaxies into tomographic bins.

The spatial distribution of the cluster component is modeled as a projected NFW profile $f_{\mathrm{NFW}}(R, c_\lambda)$ whose amplitude varies with observed cluster richness as $\hat{\lambda}^{\mathrm{B}_\lambda}$ and whose redshift variation is extracted directly through measurements within independent redshift bins (Paulus, 2021). For convenience, this projected NFW spatial model is normalized to a value of 1.0 at a projected radius of $1\,h^{-1}\,\mathrm{Mpc}$, and the NFW concentration 10^{c_λ} is modeled as a function of richness as

$$r_s = \frac{(\hat{\lambda}/60)^{1/3}}{10^{c_\lambda}} h^{-1}\mathrm{Mpc}. \tag{2.46}$$

This approach allows adequate freedom to describe the galaxy populations around tSZE selected clusters over our redshift range of interest (Hennig et al., 2017). Note that we measure the contamination around the same cluster centers used for the matter profile analysis, and so mis-centering effects are automatically included. In our analysis, we exclude the core region of the cluster where blending is more common. Moreover, we apply no correction for weak lensing magnification bias (e.g., Chiu et al., 2016a), which is strongest in the excluded cluster core region.

The fractional cluster member contamination extracted is used to apply a radially dependent correction $1/(1-f_{\mathrm{cl},b}(R))$ to the amplitude of each cluster matter profile $\Delta\Sigma(R)$ derived from each tomographic bin b before these matter profiles are averaged. It can be expressed as

$$\frac{1}{1-f_{\mathrm{cl},b}(R)} = 1 + e^{A_{\mathrm{eff},b}(z_{\mathrm{cl}})} \left(\frac{\hat{\lambda}}{60}\right)^{B_{\lambda,b}} f_{\mathrm{NFW}}(R, c_{\lambda,b}), \tag{2.47}$$

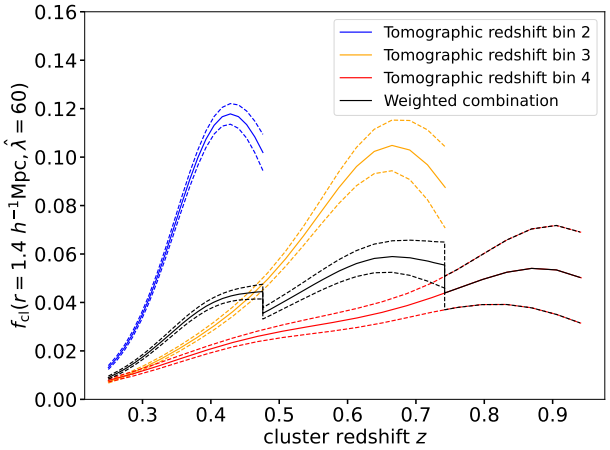

Figure 2.8: Fractional cluster member contamination for a cluster with $\hat{\lambda}$=60 as a function of redshift for the three source galaxy tomographic bins (see Fig. 2.2) and their weighted combination. The solid (dashed) lines show the mean (68% credible interval) of the contamination. The colored lines extend over the redshift ranges for which each tomographic bin is employed in constructing the cluster matter profiles. The $1.4h^{-1}$ Mpc radius is chosen because that is a characteristic radius from which the WL constraints are coming, given the adopted radial fitting range and the increasing number of source galaxies with radius.

where

$$A_{{\rm eff},b}(z_{\rm cl}) = A_\infty + \sum_i A_i e^{-\frac{1}{2}\frac{(z_{\rm cl}-z_i)^2}{\rho^2_{\rm corr}}}, \tag{2.48}$$

is a normalization factor that is dependent on the cluster redshift and the extracted amplitudes A_i that are extracted within redshift bins z_i, where the redshift centers of the bins are $z_i \in \{0.2, 0.28, 0.36, 0.44, 0.52, 0.6, 0.68, 0.76, 0.84, 0.92, 1.0\}$. In this expression we have integrated over the cluster member redshift distribution. For each tomographic bin b, the parameters A_∞, A_i, $\rho_{\rm corr}$, $B_{\lambda,b}$, $c_{\lambda,b}$, $z_{{\rm off},b}(z)$ and $\sigma_{{\rm z},b}(z)$ are obtained by fitting to the entire cluster population. The redshift dependence of the redshift width and offset in Eq. 2.45 are assumed to be simple linear functions in redshift around a pivot redshift $z = 0.5$ as $\sigma_{\rm z}(z) = \sigma_{{\rm z}_0} + \sigma_{{\rm z}_{\rm z}}(z - 0.5)$ and $z_{\rm off}(z) = z_{{\rm off}_0} + z_{{\rm off}_{\rm z}}(z - 0.5)$, respectively (again, within each tomographic bin b).

To solve for the parameters of the cluster member contamination model, we iterate over all clusters in the sample comparing our model (Eq. 2.44) to the observed surface density of source galaxies as a function of redshift and projected separation from the cluster. Following Paulus (2021), we apply a regularization term to the likelihood with a correlation length in redshift $\rho_{{\rm corr}-{\rm z}}$ to the pairs of neighboring amplitudes $e^{A_{i,b}}$, which then prefers a solution with smooth variation in redshift (as noted explicitly in Eqns. 24 through 27 in Bocquet et al., 2024a). With larger cluster samples, these regularization terms would no longer be important. The parameter constraints for each tomographic bin are given in Table A.1. Because the method applied here is similar to that in Bocquet et al. (2024a), we direct the reader to Figure 9 in Bocquet et al. (2024a) for validation tests of

the model.

Fig. 2.8 shows the fractional cluster member contamination at a projected radius of $1.4h^{-1}$ Mpc as a function of cluster redshift for the three source galaxy tomographic bins. The mean model is shown in color-coded solid lines corresponding to the model parameters as listed in Table A.1 over the redshift range for which each tomographic bin is used. The dashed lines show the 68% credible intervals. For a cluster at a given redshift, the total fractional contamination would be a weighted sum of the fractional contamination within each tomographic bin, where we apply the weight $\Sigma_{\rm crit}^{-1}$ appropriate for each bin. This weighted contamination is shown as the black black line with associated dashed lines corresponding to the 68% credible interval. The radius $1.4h^{-1}$ Mpc is the characteristic radius for the cluster fitting when considering our radial fitting range and the increase of the number of source galaxies with radius. Thus, the typical contamination for a $\hat{\lambda}$=60 cluster varies from ∼1% at the lowest cluster redshifts to ∼6% at the highest, and the contamination varies as $\hat{\lambda}^{B_\lambda}$ where B_λ=0.78, 0.60 and 0.53 for tomographic bins 2, 3 and 4, respectively.

2.5 Results and discussion

In this section, we first present validation tests of our new calibration method applied to mock data in Section 2.5.1. In Section 2.5.2 we show the resulting constraints from the real data, discuss the choices made in this analysis, such as which systematics are included, and present a validation of our adopted form for the observable-mass relations using the real data. We then present the average cluster matter profile out to larger radii (including the 2-halo dominated region) and compare it with the simulation in Section 2.5.3. Section 2.5.4 contains a comparison of our results with those reported in the recent literature.

2.5.1 Validation of method using mock dataset

We validate our analysis method using a realistic SPT+MCMF mock catalog with DES-like mock weak lensing data. For this purpose, we create mock clusters and lensing data following the approach taken in the recent SPT×DES analysis (Bocquet et al., 2024a).

The first step in creating a mock SPT+MCMF cluster catalog within a fiducial cosmological model is to calculate the expected number of halos as a function of redshift and mass; for this we adopt the Tinker et al. (2008) halo mass function scaled by the surveyed volume as a function of redshift, imposing a mass range $10^{13}M_\odot < M_{200c} < 10^{16}M_\odot$ and a redshift range 0.25 ¡ z ¡ 0.94. We draw a Poisson realization of this sample, and then for each halo we assign cluster observables using the observable-mass relations presented in Section 2.4.1. We then apply survey selection cuts in tSZE detection significance $\hat{\zeta}$ and optical richness $\hat{\lambda}$ consistent with those used to produce the real sample. These realistic mocks follow the SPT and MCMF related survey depth geometry and produce a mock sample similar to the real dataset (see Fig. 2.1) that is fully consistent with the form of the observable-mass relations that we will use to analyze the real dataset.

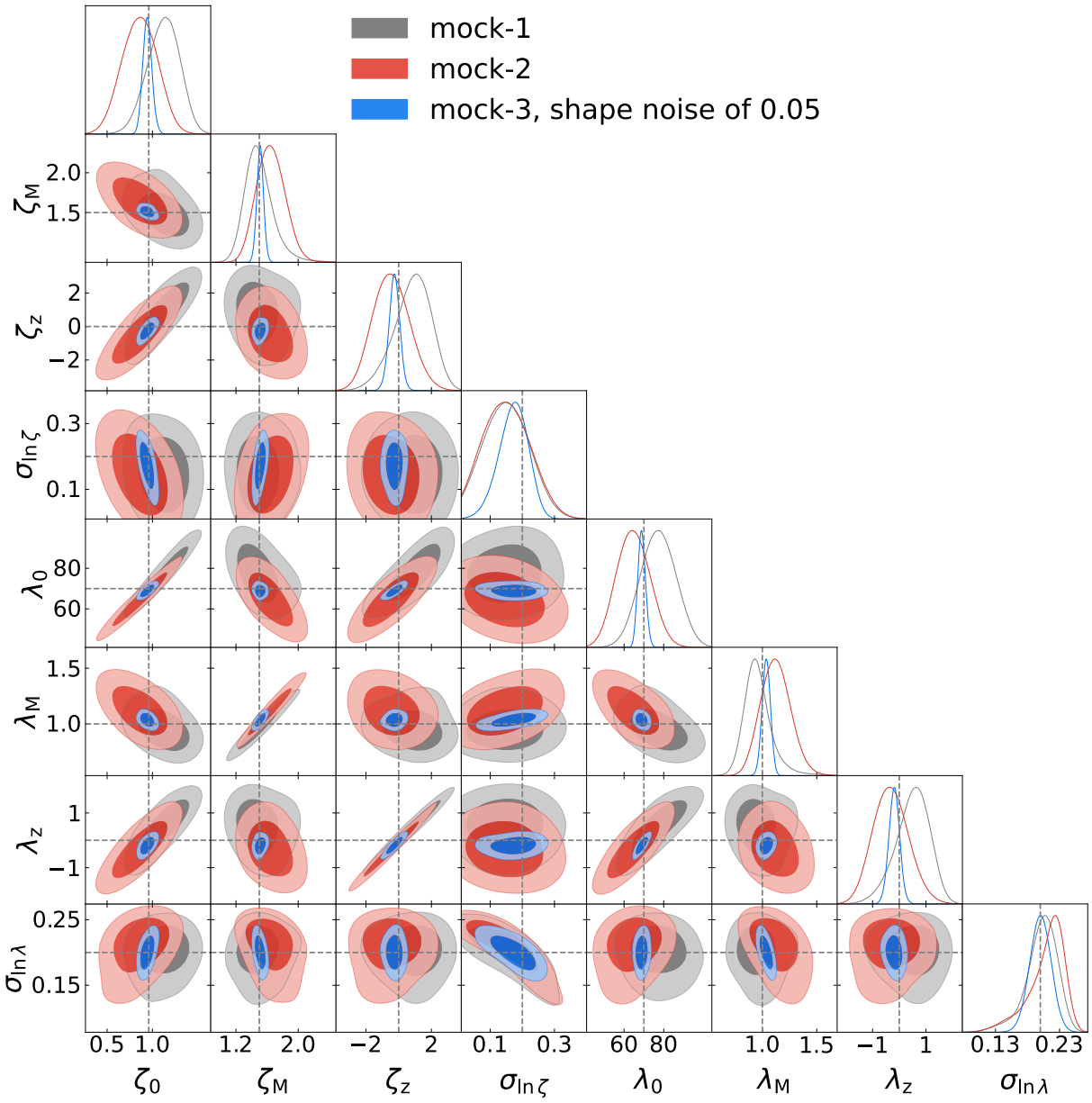

Figure 2.9: Posterior constraints for average cluster mass calibration of three different mock SPT samples in a fiducial flat ΛCDM cosmology. The grey dashed line shows the input parameters used to generate the mock samples, which are recovered within the uncertainties.

To generate mock weak lensing data for each selected cluster in our mock catalog, we first estimate the total source galaxies associated with the cluster by calculating its area on the sky (corresponding to the radial distance to cluster center $R = 10h^{-1}\mathrm{Mpc}$) and assuming a source galaxy density of $6\,\mathrm{arcmin}^{-2}$. We assume the same source redshift distribution as the DES Y3 data for each tomographic bin for the mock source galaxies. For each source, we assign a weight by randomly drawing source weights from real DES data. We divide the total source galaxies equally among the three tomographic bins. We then assign a radial distance to each source galaxy by randomly drawing distance $\propto R$. We then sample the amplitude of the rescaled matter profile $\widetilde{\Delta\Sigma}$ at the distance R_i/R_{200c} for each galaxy i, given the cluster radius R_{200c} and using our rescaled matter profile model (see Section 2.4.2). We add tomographic bin-dependent cluster member contamination, consistent with our measurement using the DES data (see Section 2.4.4.2) and then convert the $\widetilde{\Delta\Sigma}$ amplitude for each galaxy to g_t using $\langle\Sigma_{\mathrm{crit},b}\rangle$ for the appropriate tomographic bin b. We apply scatter to each g_t measurement by drawing g_t from a normal distribution with $\sigma_{\mathrm{eff}} = 0.3$ (effective shape noise for DES data). This process produces realistically noisy and biased tangential shear data for each cluster. Specifically, these shear data include all the known systematic and stochastic effects needed to model cluster shear profiles in DES data.

We create several statistically independent mock catalogs to assess the performance of our likelihood model and the software. For the analysis, we divide our data into $3 \times 3 \times 3$ $\hat{\zeta}-\hat{\lambda}-z$ observable bins, and the likelihood calculation is performed following the formalism outlined in Section 2.4.3. Fig. 2.9 shows the posteriors for three mock catalogs with the same set of input observable-mass relation and cosmological parameters but with different uniform random deviate seeds. As expected, all the mock catalogs contain a number of clusters that is similar to the real SPT sample. The corresponding sets of lensing data are also generated with different random number seeds. Mock-1 and mock-2 are generated with a shape noise ($\sigma_{\mathrm{eff}} = 0.3$), similar to DES Y3, while mock-3 is created with a shape noise value of 0.05, which is equivalent to scaling up the lensing source galaxy density by a factor of 36, therefore providing a more stringent test of the software.

To effectively and efficiently sample the high dimensional parameter space, we use the Markov Chain Monte Carlo algorithm MultiNest (Feroz et al., 2009, 2019) for our likelihood analysis. As is clear in Fig. 2.9, the posteriors are in good agreement with the input parameters (plotted as dashed lines). These validation tests show no signs of biases.

Our $\widetilde{\Delta\Sigma}$ profile analyses of both mock and real datasets typically converge in a factor of 5 less time on similar computing resources than in the case of the cluster-by-cluster analysis. Interestingly, the time required for a single iteration of the $\widetilde{\Delta\Sigma}$ likelihood is similar to that for the cluster-by-cluster analysis, but the number of iterations required for convergence is typically five times less. This faster convergence seems to be due to the difference in SNR of the average profiles as compared to the individual cluster matter profiles, which influences the stability of the likelihood far away from the best fit parameter values. In future analyses using the average profile method, we plan to present further efficiency improvements. Ongoing testing indicates that these approximate methods reduce the time

Table 2.1: Observable-mass relation and cosmology parameter priors.

Parameter	Description	Prior
tSZE detection significance ζ-mass relation		
$\ln \zeta_0$	amplitude	$\mathcal{U}(0.01, 1.5)$
ζ_M	mass trend	$\mathcal{U}(0.5, 3)$
ζ_z	redshift trend	$\mathcal{U}(-5, 5)$
$\sigma_{\ln \zeta}$	intrinsic scatter	$\mathcal{U}(0.01, 0.5)$
Optical richness λ-mass relation		
λ_0	amplitude	$\mathcal{U}(10, 70)$
λ_M	mass trend	$\mathcal{U}(0.2, 2)$
λ_z	redshift trend	$\mathcal{U}(-5, 5)$
$\sigma_{\ln \lambda}$	intrinsic scatter	$\mathcal{U}(0.01, 0.5)$
$M_\mathrm{WL} - M_\mathrm{200c}$ relation		
$\ln M_{\mathrm{WL}_0}$	amplitude of bias	0
$\sigma_{\ln M_{\mathrm{WL}_{0,1}}}$	error on amplitude	$\mathcal{N}(0, 1)$
$\sigma_{\ln M_{\mathrm{WL}_{0,2}}}$	error on amplitude	$\mathcal{N}(0, 1)$
$M_{\mathrm{WL}_\mathrm{M}}$	mass trend of bias	$\mathcal{N}(1.000, 0.006^2)$
$\ln \sigma^2_{\ln \mathrm{WL}_0}(z_0)$	amplitude of scatter	$\mathcal{N}(-3.11, 0.04)$
$\ln \sigma^2_{\ln \mathrm{WL}_0}(z_1)$	amplitude of scatter	$\mathcal{N}(-3.07, 0.05)$
$\ln \sigma^2_{\ln \mathrm{WL}_0}(z_2)$	amplitude of scatter	$\mathcal{N}(-2.84, 0.06)$
$\ln \sigma^2_{\ln \mathrm{WL}_0}(z_3)$	amplitude of scatter	$\mathcal{N}(-1.94, 0.10)$
$\sigma^2_{\ln \mathrm{WL}_\mathrm{M}}$	mass trend of scatter	$\mathcal{N}(-0.23, 0.04^2)$
Cosmology		
Ω_m	matter density	$\mathcal{N}(0.315, 0.007)$
$\log_{10} A_s$	amplitude of $P(k)$	Fixed to -8.696
H_0	Hubble parameter	Fixed to 70
$\Omega_{\mathrm{b},0}$	baryon density	Fixed to 0.0493
n_s	scalar spectral index	Fixed to 0.96
w_0, w_a	EoS parameters	Fixed to -1, 0
$\sum m_\nu$	sum of neutrino masses	Fixed to 0.06
$\Omega_{\mathrm{k},0}$	curvature density	Fixed to 0

required for a single likelihood evaluation by more than an order of magnitude.

2.5.2 SPT×DES analysis

With the validation of the code, we move on to apply the analysis method outlined above to the SPT×DES sample. Following Grandis et al. (2021), we restrict our analysis to the radial range $0.5 < R/(h^{-1}\mathrm{Mpc}) < 3.2/(1+z_{\mathrm{cl}})$. This radial cut allows us to restrict the analysis to the 1-halo region while simultaneously avoiding the central region of the cluster, which is most affected by cluster member contamination, mis-centering, and baryonic processes. Throughout the analysis, we use DNF redshifts (De Vicente et al., 2016), which are used to calibrate cluster member contamination. The shape noise per tomographic bin for the DES Y3 data is taken from Amon et al. (2022a), which is in good agreement with our bootstrap error estimates

$$\sigma_{\mathrm{eff},b} = \begin{cases} 0.262 & b = 2 \\ 0.259 & b = 3 \\ 0.301 & b = 4. \end{cases}$$

We analyze the SPT clusters in the redshift range $0.25 \leq z < 0.94$, which contains 698 clusters with DES weak lensing data. As with the mock validation, we divide the data into $3 \times 3 \times 3$ $\hat{\zeta} - \hat{\lambda} - z$ bins, leading to 27 independent average rescaled matter profiles $\widetilde{\Delta\Sigma}$. Because the weak lensing signal in our sample has a higher SNR for lower redshift clusters, the highest redshift bin is chosen to be wider so that it has a sufficient SNR to approximately equal the SNR in the two lower redshift bins. Each redshift bin is further divided into 9 bins ($3{\times}3$ $\hat{\zeta} - \hat{\lambda}$). Here, also, we choose bin boundary values such that each bin has a similar SNR. The observable bins for each redshift range are as follows

$$\begin{aligned}
&0.25 \leq z < 0.33 \\
&\qquad 0 \leq \hat{\lambda} < 60, \quad 60 \leq \hat{\lambda} < 120, \quad 120 \leq \hat{\lambda} < 250 \\
&\qquad 4.25 \leq \hat{\zeta} < 5, \quad 5 \leq \hat{\zeta} < 7, \quad 7 \leq \hat{\zeta} < 50 \\
&0.33 \leq z < 0.43 \\
&\qquad 0 \leq \hat{\lambda} < 75, \quad 75 \leq \hat{\lambda} < 120, 120 \leq \hat{\lambda} < 250 \\
&\qquad 4.25 \leq \hat{\zeta} < 6.5, \quad 6.5 \leq \hat{\zeta} < 8.5, \quad 8.5 \leq \hat{\zeta} < 50 \\
&0.43 \leq z < 0.94 \\
&\qquad 0 \leq \hat{\lambda} < 65, \quad 65 \leq \hat{\lambda} < 110, \quad 110 \leq \hat{\lambda} < 250 \\
&\qquad 4.25 \leq \hat{\zeta} < 5, \quad 5 \leq \hat{\zeta} < 7, \quad 7 \leq \hat{\zeta} < 50.
\end{aligned}$$

Parameter priors for our run are listed in Table 2.1. In summary, we fix the sum of neutrino masses to the minimum allowed value of 0.06 eV. All other cosmological parameters are fixed to their mean Planck values (Planck Collaboration et al., 2020), except for Ω_{m}, which has a Gaussian prior (our results are unaffected when using a wide flat prior on

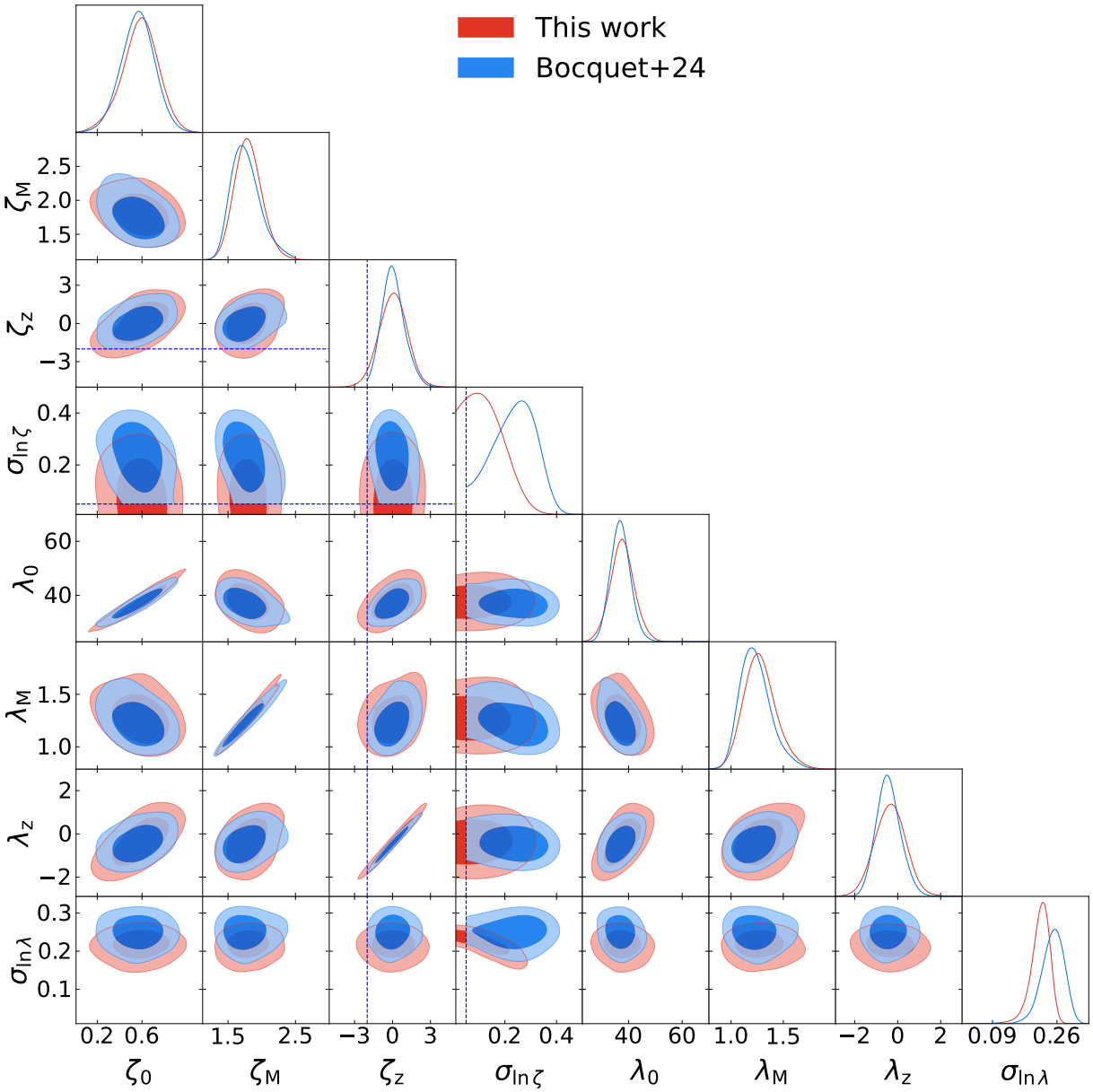

Figure 2.10: Contour plot showing the posterior constraints for cluster mass calibration using average matter profiles (in red) of the SPT cluster sample in a ΛCDM model. The blue contour shows cluster-by-cluster WL-only mass calibration results from Bocquet et al. (2024b) for the same SPT sample. The dashed blue line shows the prior boundary used in Bocquet et al. (2024b) for two parameters which is smaller than ours.

Table 2.2: Mean parameter posteriors and 1-σ uncertainties from our mass calibration analysis.

Parameter	Posterior
tSZE detection significance ζ-mass relation	
$\ln \zeta_0$	0.586 ± 0.158
$\zeta_{\rm M}$	1.797 ± 0.195
$\zeta_{\rm z}$	0.045 ± 1.054
$\sigma_{\ln \zeta}$	0.127 ± 0.068
Optical richness λ-mass relation	
λ_0	37.69 ± 4.37
$\lambda_{\rm M}$	1.275 ± 0.150
$\lambda_{\rm z}$	-0.349 ± 0.690
$\sigma_{\ln \lambda}$	0.216 ± 0.025
$M_{\rm WL} - M_{\rm 200c}$ relation	
$\sigma_{\ln M_{\rm WL_{0,1}}}$	-0.35 ± 0.80
$\sigma_{\ln M_{\rm WL_{0,2}}}$	0.20 ± 1.00
$M_{\rm WL_M}$	1.000 ± 0.004
$\ln \sigma^2_{\ln {\rm WL_0}}(z_0)$	-3.08 ± 0.02
$\ln \sigma^2_{\ln {\rm WL_0}}(z_1)$	-3.04 ± 0.03
$\ln \sigma^2_{\ln {\rm WL_0}}(z_2)$	-2.80 ± 0.03
$\ln \sigma^2_{\ln {\rm WL_0}}(z_3)$	-1.88 ± 0.05
$\sigma^2_{\ln {\rm WL_M}}$	-0.22 ± 0.04
Cosmology	
$\Omega_{\rm m}$	0.315 ± 0.006

$\Omega_{\rm m}$). The observable-mass relation parameters are assigned a wide flat prior. Moreover, we assume no correlated scatter between ζ and λ.

Rather than precisely following the form of the $M_{\rm WL} - M_{\rm 200c}$ relation presented in Eqns 2.28 and 2.29, our analysis follows the approach adopted in Bocquet et al. (2024a) where they analyze the same SPT×DES sample. We follow the redshift variation by interpolating between the relations determined through mock observations of specific simulation outputs at redshifts $z \in \{0.252, 0.470, 0.783, 0.963\}$. We set the amplitude and mass trend of the bias to 0 and 1, respectively, because we have adopted the simulation matter profiles as our model. We adopt the scatter parameter priors from the mock analysis of the simulations at four different redshifts, and we interpolate linearly to obtain the expectation at a given redshift. Additionally, we include the redshift dependent uncertainty on the amplitude of the bias with Gaussian random deviates whose values are scaled using the parameters $\sigma_{\ln M_{\rm WL_{0,1}}}$ and $\sigma_{\ln M_{\rm WL_{0,2}}}$.

The resulting posteriors inferred from applying the new mass calibration software to the SPT×DES data are shown in Fig. 2.10. The mean posterior, along with the corresponding 68% credible intervals, are listed in Table 2.2. We find that the mass trend $\zeta_{\rm M}$ of the ζ-mass

relation has a value of 1.797±0.195, which is close to the 5/3 scaling one would expect for the tSZE measured within the cluster virial region (e.g., $r < r_{200c}$). However, given that the angular filtering in the tSZE cluster detection removes more flux from larger, more massive clusters, this measured mass trend is likely evidence for a steeper than self-similar relation. The redshift trend ζ_z is consistent with 0. We find that the redshift trend λ_z of the λ-mass relation and the mass trend λ_M, are statistically consistent with 0 and 1, respectively.

We note that we marginalize over all the crucial systematic errors in our analysis by adopting the $M_{WL} - M_{200c}$ relation. We have repeated the analysis without marginalizing over the systematics, and we do not notice any significant difference. This is expected, because our analysis is shape-noise dominated. Bocquet et al. (2024b) find the same as shown in their Fig. 3.

The blue contours in Fig. 2.10 show the constraints from Bocquet et al. (2024b) weak lensing analysis of the same SPT×DES sample with MCMF center and DNF redshifts. They perform the analysis on a cluster-by-cluster basis compared to our average profile approach and they use the same radial fitting range as ours. Our analysis is done with a prior on Ω_m unlike in Bocquet et al. (2024b), where they use a flat prior. We use a wider prior on $\sigma_{\ln\zeta}$ and ζ_z compared to their work as can be seen in Fig. 2.10. The slight differences in intrinsic scatter posteriors can be attributed to the different modeling of the observational Poisson noise on the richness in this and the Bocquet et al. (2024b) analyses. In general, the results from our analysis show very good agreement with their single cluster analysis method and every parameter agrees on average at the $\approx 0.4\sigma$ level.

2.5.2.1 Goodness of fit

To assess the goodness of fit of the data to our model, we compare the average matter profile model to the average cluster matter profile in $3 \times 2 \times 2$ $\hat{\zeta} - \hat{\lambda} - z$ bins and perform a χ^2 fit to all bins. Fig. 2.11 shows 12 average matter profiles (observations represented with black data points), each for a given $\hat{\zeta} - \hat{\lambda} - z$ bin along with the model and its corresponding 2σ region (shown in shaded blue region). The profiles are extracted corresponding to the mean parameter obtained from our posterior. We obtain a chi-squared value of $\chi^2 = 97.83$ from 84 data points, effectively constraining 8 parameters. This corresponds to a reduced chi-squared value of $\chi^2_{red} = 1.27$ and a probability of exceeding the observed χ^2 of p=0.047.

2.5.2.2 Observable-mass relation validation

To further validate our mass calibration results, we perform a series of tests on the richness and tSZE observable-mass relations. In these tests we are determining whether the data are consistent with our model description of the observable-mass relations. In Fig. 2.12 we show the $\hat{\lambda}$-mass (top) and $\hat{\lambda}$-redshift (bottom) relations. To analyze the $\hat{\lambda}$-mass relation, we calculate the richnesses at the pivot redshift by simply dividing $\hat{\lambda}$ by $((1+z)/(1+z_{piv}))^{\lambda_z}$. This factor removes the measured redshift trend and allows us to study only the mass trend. On the x-axis, we show mean mass posteriors obtained using dual-observables, given by

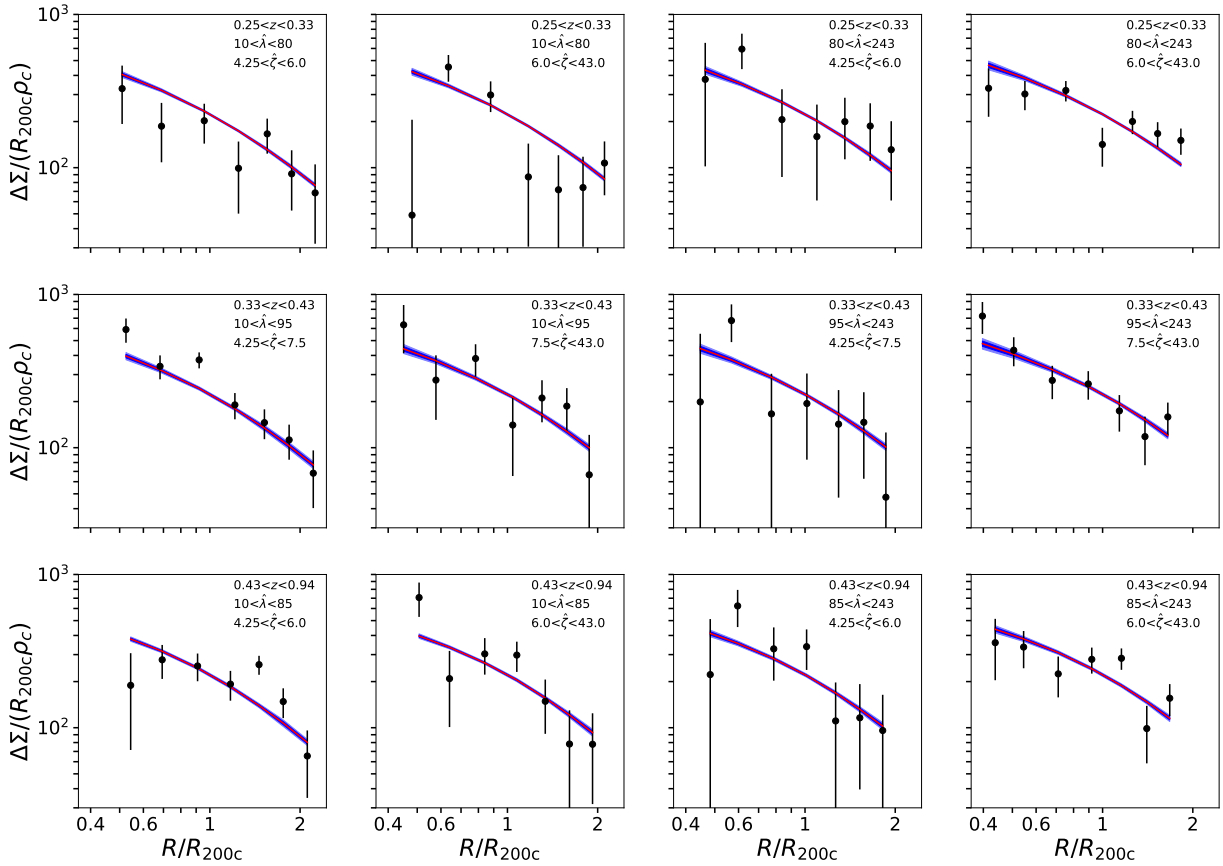

Figure 2.11: Average SPT cluster matter profiles corresponding to the mean recovered parameters in twelve $\hat{\zeta} - \hat{\lambda} - z$ bins are shown with black data points with 1σ error bars. The weak lensing model is shown in the red line and the shaded blue region represents 2σ error region on the model.

the following equation

$$P(M_{200c}|\hat{\zeta}, \hat{\lambda}, z, \vec{p}) = \frac{\int\int \mathrm{d}\lambda \mathrm{d}\zeta P(\hat{\lambda}|\lambda) P(\hat{\zeta}|\zeta) P(\zeta, \lambda|M_{200c}, z, \vec{p}) P(M_{200c}|z, \vec{p})}{\int\int\int \mathrm{d}M \mathrm{d}\lambda \mathrm{d}\zeta P(\hat{\lambda}|\lambda) P(\hat{\zeta}|\zeta) P(\zeta, \lambda|M_{200c}, z, \vec{p}) P(M_{200c}|z, \vec{p})}. \quad (2.49)$$

where of course the parameters of the observable-mass relations have been constrained using the weak lensing mass calibration described above.

Similarly, we study the richness-redshift relation by normalizing the richnesses with $(\mathrm{M_{200c}}/\mathrm{M_{piv}})^{\lambda_\mathrm{M}}$. In both panels, the solid black line shows the intrinsic observable-mass relation (Eq. 2.27) corresponding to the mean posterior values. The dark and light-shaded blue bands represent 68% and 95% credible intervals on the intrinsic observable-mass relation model. The grey error bar on the data points represents the statistical errors and uncertainties in the observable-mass relations and the estimated cluster halo masses.

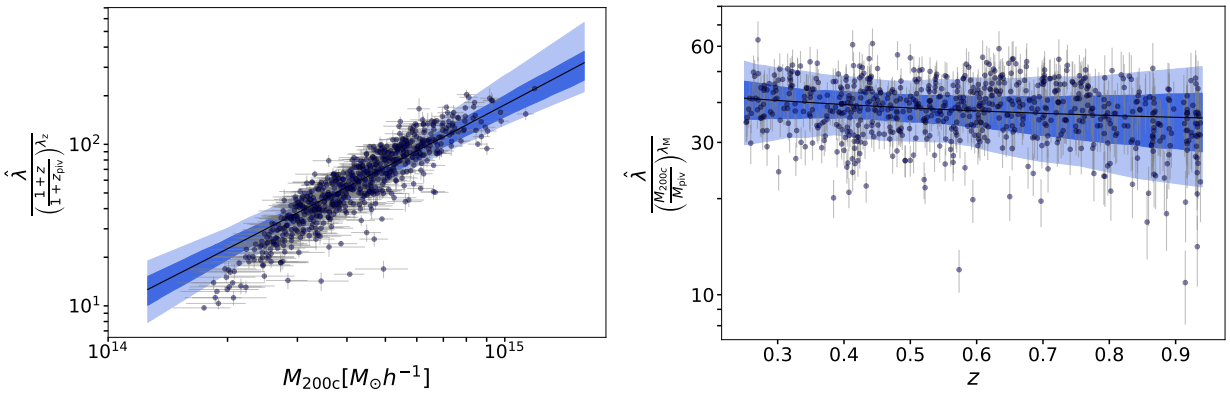

Figure 2.12: The observed optical richness $\hat{\lambda}$ of SPT clusters as a function of the cluster halo mass (top) and redshift (bottom). The clusters are shown with filled circles, where the error bars also capture the error in the observable-mass relations and the estimated cluster halo mass. The top and bottom plots shows the richness $\hat{\lambda}$ normalized at the pivot redshift $z_{\rm piv} = 0.6$ and the pivot mass $M_{\rm piv} = 3 \times 10^{14} h^{-1}$Mpc, respectively. The intrinsic model (Eq. 2.27) is shown in blue. The light and dark-shaded regions in both panels represent 68% and 95% credible intervals of the mean model, respectively.

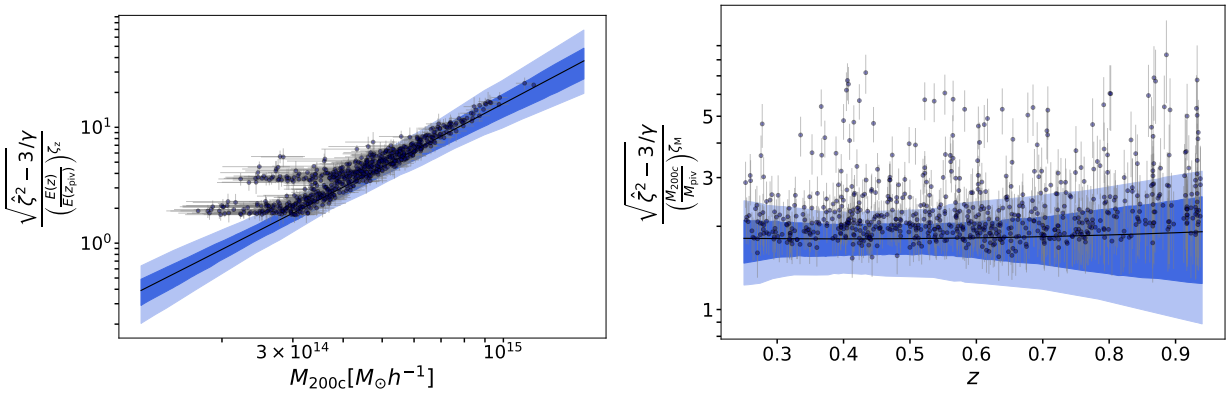

Figure 2.13: The observed debiased detection significance $\hat{\zeta}$ of SPT clusters as a function of the cluster halo mass (top) and redshift (bottom). The intrinsic model (Eq. 2.24) is shown in blue. The plotting scheme is the same as Fig. 2.12. The effects of Eddington bias and selection on $\hat{\zeta}$ can be seen in the above plots.

In Fig. 2.13 we show $\hat{\zeta}$-mass and $\hat{\zeta}$-redshift relation. On the y-axis, we plot $(\sqrt{\hat{\zeta}^2 - 3})/\gamma$, where γ is a scale factor that is used to correct for the different depths of fields in the SPT survey. Again, we normalize the y-axis with a factor of $(E(z)/E(z_{\rm piv}))^{\zeta_z}$ while analyzing the relation with mass and with a factor of $(\mathrm{M_{200c}}/\mathrm{M_{piv}})^{\zeta_M}$ while analyzing its relation with redshift. The intrinsic observable-mass relation model (Eq. 2.24) with mean posterior parameters is shown with a black line and the error region is shown in blue bands as in the previous figure.

Compared to the intrinsic observable-mass relations (defined by blue bands) the observ-

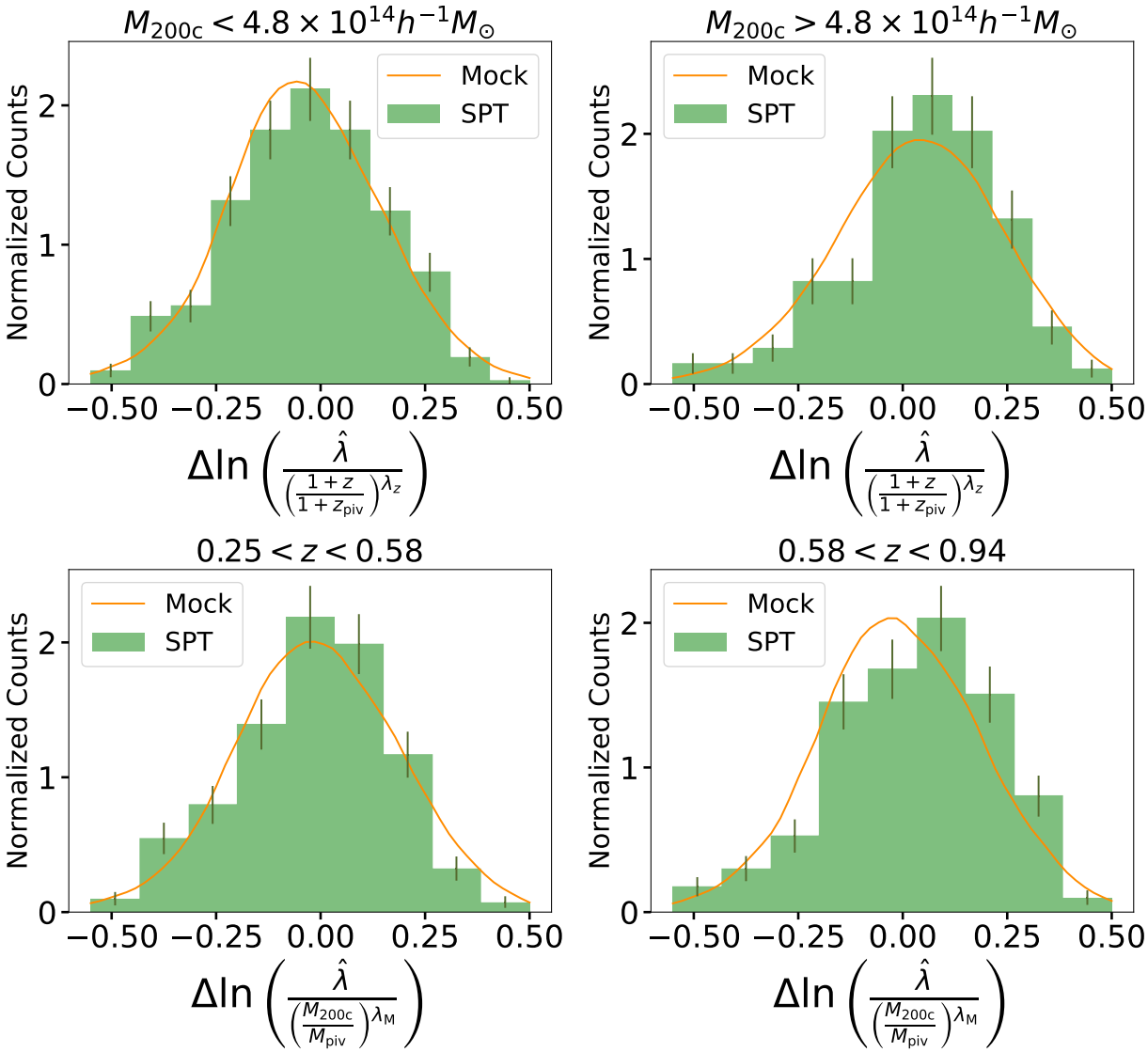

Figure 2.14: The distributions of deviations in $\hat{\lambda}$ about the intrinsic observable-mass relation are shown for the SPT sample (green histogram) and a mock dataset (100 times larger) drawn from that same intrinsic relation (orange line). The top (bottom) panels show the deviations in low and high mass (redshift) with the measured redshift (mass) trend removed as in Fig. 2.12.

ables in our analysis suffer from selection effects, which can be seen in Fig. 2.12 & 2.13 (we further dicuss this in Appendix A.2). The Eddington bias is clearly visible in the left side (low mass portion) of the top panels in Figs. 2.12 and 2.13 from the points lying above the best-fitting line in $\hat{\zeta}$-mass and below the relation in $\hat{\lambda}$-mass. These points are preferentially scattered away from the mean expected observables $\hat{\zeta}$ and $\hat{\lambda}$. A particularly strong feature is the two extensions of the observable $\hat{\zeta}$ to lower mass away from the mean relation. These

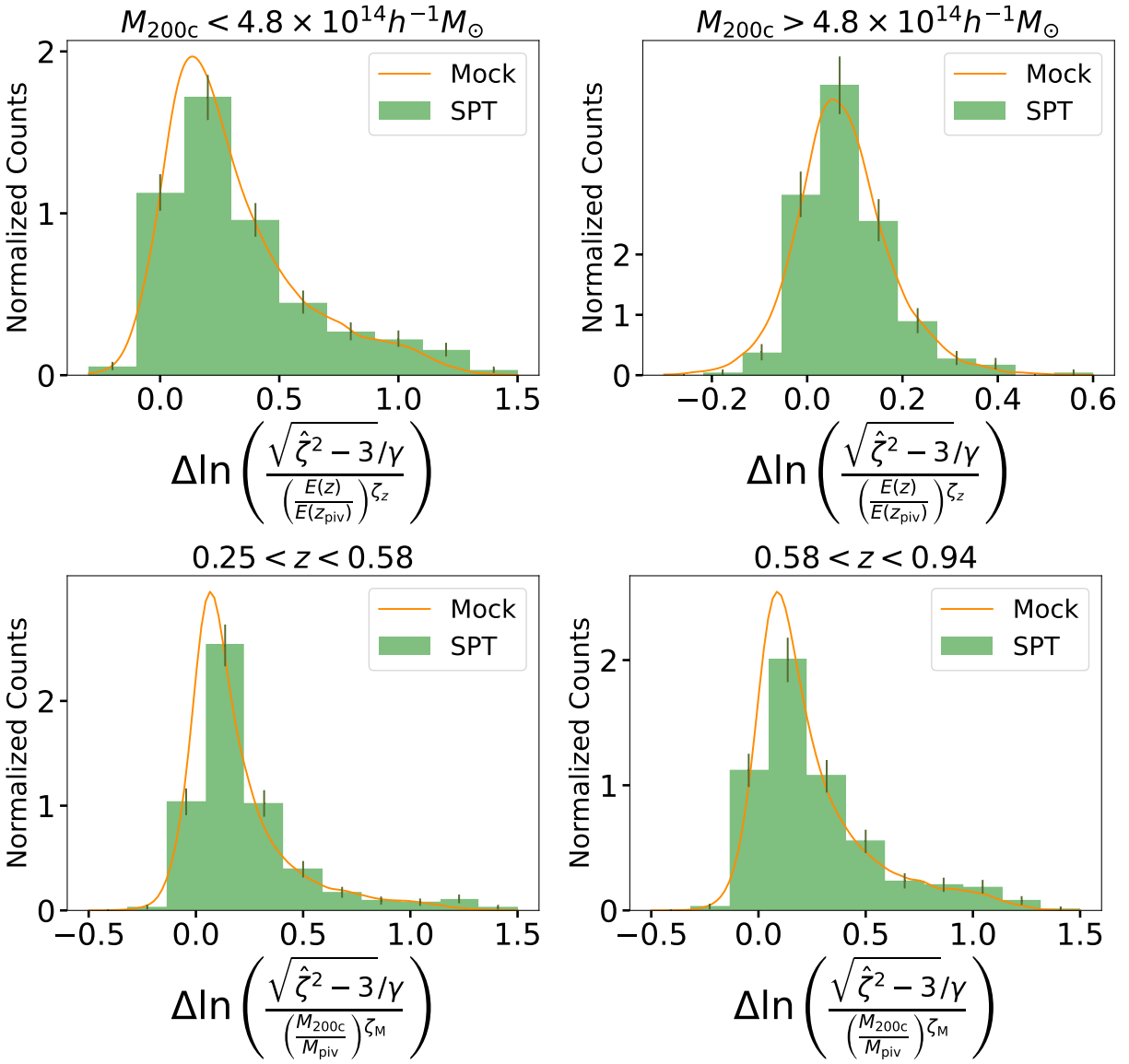

Figure 2.15: Same as Fig. 2.14 but for normalized $\hat{\zeta}$. The top (bottom) panels show the deviations in low and high mass (redshift) with the measured redshift (mass) trend removed as in Fig. 2.13.

two features are created by the $\hat{\zeta}$ selection thresholds in the two SPT survey fields, and these are often referred to as Malmquist bias.

To understand whether the data points are behaving consistently with expectation, we create a mock sample 100 times larger than SPT sample using the mean parameter values from the measured posteriors and apply the same selection in $\hat{\zeta}$ and $\hat{\lambda}$ that was applied in creating the real cluster sample. The comparison of the mock and the real data then allows for robust validation.

In Fig. 2.14 we plot the difference between the observed $\hat{\lambda}$ and the mean intrinsic

observable-mass relation model in log space, within two different mass bins (top panels) and two different redshift bins (bottom panels). The orange line represents the 100 times larger mock sample and the green histogram is the real SPT sample. Poisson uncertainties are shown as error bars for each real data bin. We see good agreement between the mocks and the real sample in bins of high ($\chi^2 = 20.68$, p=0.04) and low mass ($\chi^2 = 15.15$, p=0.17) and high ($\chi^2 = 26.92$, p=0.002) and low redshift ($\chi^2 = 16.86$, p=0.05), indicating that our observable-mass relation model (including intrinsic and observed scatter components) provides a reasonably good description of the real dataset. The p value in the high redshift deviation plot indicates a $\sim 3\sigma$ tension, which is notable. This tension could likely be reduced by introducing a redshift dependent intrinsic scatter component in the λ-mass relation, but we leave that for a future discussion. Note that the deviations in the top panels have the redshift trend scaled out, and the deviations in the bottom panels have the mass trend scaled out, similar to what we show in Fig. 2.12.

Similarly, in Fig. 2.15 we show the distribution of deviations in observed debiased $\hat{\zeta}$ around the mean intrinsic observable-mass relation for the SPT sample (green histogram) and the 100 times larger mock sample (orange line). The top panels present data within two mass ranges, and the bottom panels show two redshift ranges. We obtain quite reasonable χ^2 in all four cases, with p values of 0.21 and 0.35 for the high- and low-mass bins, respectively, while the p values corresponding to the high- and low-redshift bins are 0.48 and 0.11, respectively. Overall, the scatter of the real and mock clusters around the intrinsic observable-mass relation is similar, indicating that the ζ-mass relation we adopt (together with its intrinsic scatter and measurement noise) provides a good description of the real dataset. The shift in the histogram peak away from zero is reflective of the Eddington bias introduced by the $\hat{\zeta}$ selection, which is more pronounced when compared to richness. As with the previous plot, the deviations in the top panels have the redshift trend scaled out, and the deviations in the bottom panels have the mass trend scaled out, similar to what we show in Fig. 2.13.

In the appendix, we present in Fig. A.2 a version of the $\hat{\zeta}$-mass figure shown for real data in Fig. 2.13 that is created by down-sampling the 100 times larger mock sample to a similar number of clusters as for the real data. The mock and real data behave similarly, showing the same selection related scatter of the data around the best fits intrinsic relation.

2.5.3 Matter profile extending to cluster outskirts

In our mass calibration analysis, we restricted our radial range to $R < 3.2/(1+z)h^{-1}$Mpc to avoid the impact of the 2-halo regime. Using our mass calibration results (Table 2.2), we combine the whole SPT sample with redshift, $0.25 < z < 0.94$ and all masses to create an average rescaled matter profile $\widetilde{\Delta\Sigma}$ that includes regions beyond the 1-halo region. We create 200 realizations of the average matter profile using the parameter posteriors to marginalize over the observable-mass relation parameter uncertainty in the profile. The SNR of the full average matter profile is $\sim$36 out to 6 R/R_{200c}. Fig. 2.16 shows the full profile compared to the mean model calculated at the mean redshift of the sample. The light and dark-shaded red bands represent the 68% and 95% credible intervals,respectively. We

obtain $\chi^2 = 15.51$ for 12 degrees of freedom, which corresponds to a probability to exceed observed χ^2 of p=0.21. This suggests that the model and data are in good agreement, even in the cluster outskirts.

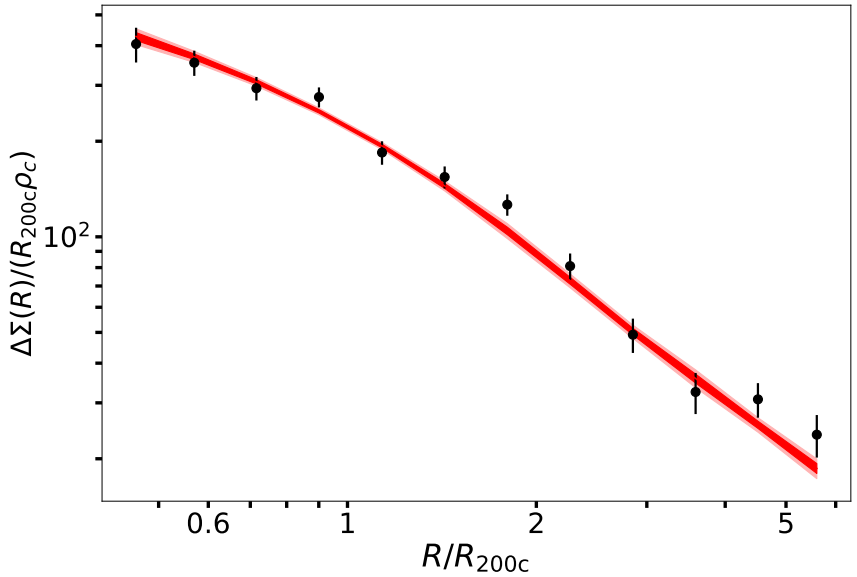

Figure 2.16: Average rescaled matter profile $\widetilde{\Delta\Sigma}(R/R_{200c})$ of the full sample of 698 clusters over the full mass and redshift ranges estimated using the mean mass posterior $P(M_{200c}|\hat{\zeta}, \hat{\lambda}, z, \vec{p})$ for each cluster (see Eq. 2.49). The black points represent the measured mean profile, and the error bars include not only shape noise but also marginalization over the cluster mass uncertainties. The dark and light-shaded red bands show 68% and 95% credible intervals, respectively, on the model profile extracted from hydrodynamical simulations.

The agreement between simulations (red) and observations (points) in this high SNR measured profile over this radial range is quite interesting. It suggests that structure formation modeled using CDM and baryonic physics within a ΛCDM context provides quite a good description of not only cluster halo profiles but also cluster infall regions. Extending the profile inward to smaller radii should enable interesting tests of baryonic feedback and the CDM scenario in the limit that cluster mis-centering and cluster member contamination can be sufficiently controlled. This topic lies beyond the scope of the current analysis.

2.5.4 Comparison to previous work

In this section, we compare our tSZE and richness observable-mass relation results to those from previous studies. Chiu et al. (2023) analyzed the eROSITA Final Equatorial Depth Survey (eFEDS) cluster sample with Hyper Suprime-Cam (HSC) weak lensing data along with MCMF richness and calibrated the richness-mass-redshift relation. Their results are shown in shaded blue color in Fig. 2.17 plotted at our pivot redshift of 0.6 and pivot mass

of $M_{200c} = 3 \times 10^{14} h^{-1}$Mpc. Because their analysis is performed with M_{500c}, we use the conversion relation provided in Ragagnin et al. (2020) to convert M_{500c} to M_{200c}. Our work (in pink) results in tighter constraints than those presented in Chiu et al. (2023). Our mass trend is slightly steeper and redshift trend is slightly weaker than those from Chiu et al. (2023), but given the uncertainties there is no tension between the two analyses.

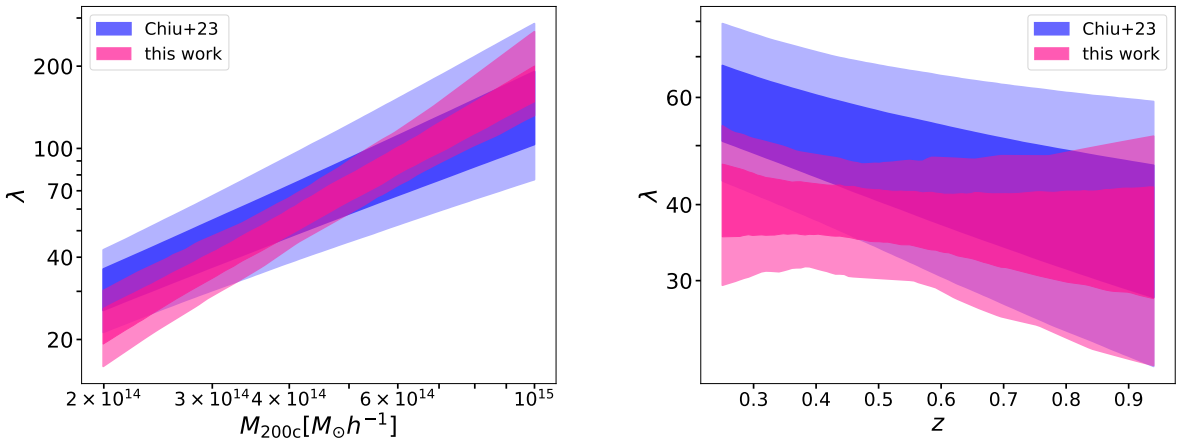

Figure 2.17: Best fit λ-mass (top) and λ-redshift (bottom) relations evaluated at our pivot mass and redshift, compared to Chiu et al. (2023) work (in blue). Dark and light-shaded regions represent 68% and 95% credible intervals, respectively. Our analysis of the tSZE selected and MCMF confirmed sample (in pink) shows good agreement with the analysis of an X-ray extent-selected sample (blue).

2.6 Conclusions

In this work, we study galaxy cluster matter profiles in both observations and simulations, developing a new mass calibration technique that employs average matter profiles and employing it on the SPT+MCMF tSZE selected and optically confirmed cluster sample with associated DES weak gravitational lensing measurements.

Our analysis begins with a comparison of the scaling properties or so-called self-similarity of the simulated and observed matter profiles $\Delta\Sigma(R)$ of the cluster samples. An examination of *Magneticum* and IllustrisTNG simulations indicates remarkable self-similarity among galaxy clusters with varying redshift and masses. In particular, we analyze the rescaled matter profiles $\widetilde{\Delta\Sigma}(R/R_{200c})$, which is $\Delta\Sigma(R/R_{200c})/(R_{200c}\rho_{crit})$. Rescaling individual profiles by their corresponding R_{200c} and associated critical density $\rho_{crit}(z)$ significantly reduces the mass and redshift dependences, respectively. We quantify the observed self-similarity by computing fractional variation with redshift and mass in the rescaled space and comparing it with the fractional variation obtained with the original matter profiles $\Delta\Sigma(R)$. The fractional variation with redshift is roughly 6 times lower in the

rescaled matter profile. We see a remarkably low fractional variation with mass of $\approx 1\%$, which is ≈ 23 times lower than the fractional variation obtained in $\Delta\Sigma(R)$. This self-similar behavior is ideal for analyzing the average cluster matter profiles, because it minimizes the cluster-to-cluster variation among the profiles and allows one to combine clusters with a wide range of redshift and mass, enabling studies of cluster matter profiles in a high SNR regime.

We exploit the self-similarity of the average matter profiles in the rescaled space to develop a new mass calibration method that relies on average rescaled matter profiles, and we employ that method to calibrate the masses of SPT tSZE-selected and MCMF optically confirmed clusters. For this method, we use hydrodynamical simulations to construct a model average rescaled matter profile $\widetilde{\Delta\Sigma}(R/R_{200c})$, while accounting for small residual redshift trends and assuming perfect self-similarity with mass. We create average SPT $\times$ DES-WL cluster matter profiles with their appropriate weights and account for all crucial systematic errors through the $M_{\rm WL} - M_{200c}$ relation. Our likelihood constrains the $\lambda - M - z$ and $\zeta - M - z$ relation parameters and takes into account the observational and intrinsic scatter on the observables. Additionally, we account for the Eddington and Malmquist biases that arise from the selection applied to the observables in defining the cluster sample.

We calibrate the $\lambda - M - z$ and $\zeta - M - z$ observable-mass relations using the average rescaled matter profile calibration method described in Section 2.4, which simultaneously constrains the amplitude, the mass trend, the redshift trend, and the intrinsic scatter for both observable-mass relations. Our constraints on the observable-mass relation parameters show mass trends that are steeper than but statistically consistent with the self-similar expectations for both the richness and tSZE observable-mass relations. Moreover, we find no statistically significant evidence for a redshift trend in richness, $\lambda_z = -0.349 \pm 0.690$, or tSZE ζ, $\zeta_z = 0.045 \pm 1.054$. Our constraints on $\lambda - M - z$ parameters are in good agreement with Chiu et al. (2023), who has analyzed the eFEDS X-ray extent-selected cluster sample with HSC weak lensing.

In addition, Bocquet et al. (2024b) have previously analyzed the SPT selected and MCMF confirmed cluster sample with DES WL using a cluster-by-cluster weak lensing calibration method together with a simultaneous fit to the tSZE halo observable function; our results from the average rescaled matter profile analysis for both the observable-mass relations are in good agreement with their work. Because our analysis uses no information from the underlying halo mass function (HMF), which is strongly cosmologically dependent, the agreement between the two methods is an interesting indication that with the DES WL dataset, the direct mass constraints from weak lensing are not significantly biased by the inclusion of the cluster abundance information.

We present a new validation of the observable-mass relations that examines the scatter of the cluster sample observables around the mean intrinsic relations. Using a large sample of mock clusters drawn from the best-fit relation, we find no significant differences between the real and mock samples for the ζ-mass relation. This indicates that the power-law form of the observable-mass relations, including our modeling of intrinsic scatter and measurement noise, provides a good description of the data. For the λ-mass relation, however, we

find that the high-redshift bin indicates a $\sim 3\sigma$ tension, which could suggest a potential redshift dependence of the intrinsic scatter in the λ-mass relation.

Both the 1) validation of the form of the observable-mass relations together with 2) the evidence that the mass calibration reported using the Bocquet et al. (2024a) method appears to be unaffected by potential biases coming from the use of the underlying HMF, lend further weight to the recent standard cosmological, interacting dark matter, modified gravity and combined probe results reported using variations of that method to analyze the SPTxDES dataset (Bocquet et al., 2024b; Mazoun et al., 2024; Vogt et al., 2024b; Bocquet et al., 2024c).

Employing the rescaled matter profile method, we produce a high SNR average rescaled matter profile from the entire SPT and MCMF selected sample of 698 clusters that extends to $6R/R_{200c}$ (see Fig. 2.16). This profile deviates from a null profile with a SNR$\sim$36, providing the most precise measurement of the average ICM selected cluster matter profile to date. A comparison of this profile to hydrodynamical simulations carried out within the ΛCDM paradigm over the same radial range shows good agreement within the current uncertainties.

The upcoming stage IV weak-lensing surveys will offer us a vast amount of much higher quality lensing data. The average rescaled matter profile mass calibration method, which we have successfully demonstrated here, provides a promising new tool for analyzing these future datasets. Moreover, this new method will enable efficient analyses of much larger cluster samples for cosmology and structure formation constraints. Analyzing average cluster matter profiles in rescaled space will further help us create high SNR profiles by combining cluster measurements over wide redshift and mass ranges. The shape of the average cluster matter profile can then be used to study baryonic feedback, different modified gravity models, and the collisional nature of dark matter.

Chapter 3

Galaxy cluster matter profiles: II. Multi-observable calibration, redMaPPer sample validation and the average matter profile of a 2000 cluster sample

A. Singh, J. J. Mohr, C. T. Davies, S. Bocquet, D. H. Lang, M. Klein, S. M. L. Vogt, *Soon to be submitted to Astronomy & Astrophysics*

We present a study of the weak lensing profiles of galaxy clusters detected by the South Pole Telescope (SPT) and the ROSAT X-ray telescope (using the MARD-Y3 catalog) in the redshift range $0.05 < z < 0.95$, leveraging weak gravitational lensing data from the Dark Energy Survey (DES). We first perform a mass calibration of the MARD-Y3 clusters, constraining the optical and X-ray observable-mass relations. We then conduct a joint mass calibration of the MARD-Y3 and SPT samples, simultaneously constraining the X-ray, thermal Sunyaev-Zel'dovich Effect (tSZE), and optical observable-mass relations. This combined calibration helps break degeneracies between the optical and tSZE observable-mass parameters, resulting in significantly tighter constraints on the tSZE observable-mass relation compared to an SPT-only analysis. We demonstrate that a cosmology analysis of the SPT-like sample, using these tighter constraints on the tSZE and richness observable-mass relations, leads to $\sim 40\%$ tighter cosmological parameter constraints in the $\Omega_{\rm m} - \sigma_8$ plane. Using our mass posteriors, we analyze rescaled cluster matter profiles extending to the cluster outskirts and find a 4.14σ discrepancy with the ΛCDM model in the outskirts. Additionally, we examine the redMaPPer cluster profiles in the DES Y3 data using the richness observable-mass constraints from our combined analysis. We find that redMaPPer cluster profiles with $\lambda < 35$ behave differently than SPT or MARD-Y3 cluster profiles, suggesting high contamination in optically selected clusters.

3.1 Introduction

Over the past decade, galaxy clusters have been extensively used to constrain cosmological models of the universe, leveraging data from cutting-edge telescopes such as the South Pole Telescope (SPT; Carlstrom et al., 2011), the Atacama Cosmology Telescope (ACT; Fowler et al., 2007), the eROSITA (Predehl et al., 2021; Sunyaev, R. et al., 2021), and the Roentgen Satellite (ROSAT; Truemper, 1982). When combined with weak gravitational lensing (WL) surveys like the Dark Energy Survey (DES; Collaboration, 2005), the Kilo-Degree Survey (KiDS; de Jong et al., 2012), and the Hyper Suprime-Cam (HSC-SSP; Miyazaki et al., 2012; Aihara et al., 2018), galaxy clusters have proven to be a powerful tool for advancing our understanding of the universe (e.g., Vikhlinin et al., 2009b; Bocquet et al., 2015, 2019; Lesci, G. F. et al., 2022; Chiu et al., 2023b; Grandis et al., 2024b; Bocquet et al., 2024b; Ghirardini et al., 2024).

Clusters detected through the thermal Sunyaev-Zel'dovich Effect (tSZE; Sunyaev & Zeldovich, 1972) form a nearly mass-limited sample, largely independent of their redshifts. This characteristic allows for the creation of cluster samples that extend to very high redshifts (Hilton et al., 2021; Bleem et al., 2024; Klein, M. et al., 2024), making tSZE-selected clusters particularly valuable for probing the early universe and studying the evolution of large-scale structure over cosmic time. However, tSZE selection tends to undersample low-redshift clusters because the SZ signal from clusters becomes harder to distinguish from the cosmic microwave background (CMB) anisotropies in this regime. On the other hand, X-ray-selected cluster samples, such as those created using X-ray observations from surveys like eROSITA, are highly efficient at identifying clusters at low redshifts (Bulbul et al., 2024). X-ray emission, driven by thermal bremsstrahlung and line emission processes in the intracluster medium, is more concentrated toward cluster centers and less affected by contamination from background signals. However, X-ray selection suffers from significant surface brightness dimming with increasing redshift, making detecting clusters at high redshifts challenging. This disadvantage and potential biases related to cluster dynamical state (e.g., preferentially detecting cool-core systems) underscore the complementarity between tSZE and X-ray selection methods. By combining tSZE and X-ray-selected cluster samples, one can capitalize on the strengths of each method while mitigating their individual limitations, resulting in more complete and less biased cluster catalogs across a wide redshift range. Abundance analysis of such comprehensive datasets enhances the statistical power and accuracy of cosmological analyses, as they provide a more representative sampling of the cluster population, thereby improving constraints on cosmological parameters.

Optically selected galaxy clusters are identified by detecting concentrations of galaxies in optical surveys, utilizing algorithms that recognize spatial overdensities and characteristic color patterns indicative of cluster membership. A widely used method for optical cluster selection is the redMaPPer (Red-sequence Matched-filter Probabilistic Percolation) algorithm (Rykoff et al., 2014), which identifies clusters by searching for a tight red sequence of passive galaxies and assigning probabilistic membership weights to potential

cluster members. It iteratively refines cluster centers, estimates richnesses ($\hat{\lambda}$) as a robust mass proxy, and mitigates contamination effects, making it a powerful tool for cluster cosmology. Clusters detected through optical telescopes produce a much larger sample than ICM-selected clusters identified via X-ray or tSZE observations and have been used to constrain cosmology (Abbott et al., 2020). However, optical selection is susceptible to projection effects, where line-of-sight superpositions of galaxies can lead to false cluster identifications or inaccurate richness estimates, potentially biasing mass determinations and cosmological inferences (Zhou et al., 2023). Additionally, the reliance on galaxy light can introduce biases against detecting high-redshift clusters or those with low optical luminosity. To mitigate these challenges, combining optical data with other wavelengths, such as X-ray or Sunyaev-Zel'dovich Effect observations, has proven effective, enhancing the reliability and completeness of cluster identification (Willis et al., 2021).

Galaxy cluster matter profiles describe the distribution of both dark and baryonic matter within galaxy clusters. Studying them offers critical insights into the distribution and evolution of matter in clusters (Voit, 2005; Kravtsov & Borgani, 2012). Additionally, the infall region of the galaxy cluster is sensitive to cosmological parameters such as $\Omega_{\rm m}$ and σ_8 (Diemer & Kravtsov, 2014; Adhikari et al., 2014; More et al., 2015). Models such as the Navarro-Frenk-White (NFW) profile (Navarro et al., 1997b) and the Einasto profile (Einasto, 1965; Navarro et al., 2004) are commonly used to characterize these observed cluster matter profiles. Analyzing these matter profiles enables tests of cosmological models and theories of structure formation. For instance, deviations from the expected NFW profile can indicate the influence of non-standard physics or the need to modify our understanding of dark matter properties (Voit, 2005; Newman et al., 2013). Comparing observed cluster matter profiles with predictions from simulations allows us to test the validity of the ΛCDM model and alternative theories. For example, the self-similarity observed in galaxy cluster matter profiles at redshifts > 0.25 supports the predictions of the ΛCDM model (Singh et al., 2025). Studies have also employed weak lensing measurements to assess cluster masses and constrain cosmological parameters, such as the total matter density parameter, $\Omega_{\rm m}$ (Lesci, G. F. et al., 2022). Furthermore, accurate inference of cluster mass profiles through techniques like weak gravitational lensing facilitates the calibration of observable-mass relations, which are essential for using clusters as cosmological probes (Bocquet et al., 2019; Bocquet et al., 2024b; Ghirardini et al., 2024).

In this work, we perform a mass calibration of an X-ray selected cluster catalog using DES Y3 WL data. We employ the state-of-the-art analysis method proposed in an earlier work (Singh et al., 2025), which properly accounts for both systematic and statistical uncertainties. After calibrating the X-ray cluster masses, we perform a combined mass calibration of tSZE and X-ray clusters, constraining the tSZE-mass, X-ray count rate-mass, and optical richness-mass observable-mass relations. We use the constraints from the combined mass calibration analysis to test the ΛCDM model further and test the galaxy cluster matter profiles of redMaPPer clusters identified in the DES Y3 data.

This paper is organized as follows. In Section 3.2, we present the simulated and observed datasets. Section 3.3 provides an overview of the mass calibration method, including the likelihood calculation and the hydrodynamical model. In Section 3.4, we validate our

methodology using mock data, present mass calibration results based on real data, and examine the average cluster matter profile using all clusters. The implications of our mass calibration for cosmological constraints and redMaPPer clusters are discussed in Section 3.5. Finally, we conclude with a summary and outlook in Section 3.6. Throughout the paper we employ a flat ΛCDM cosmology with parameters $\Omega_{\rm m} = 0.315$, and $h = 0.7$. Unless otherwise specified, all uncertainties are quoted at the 68 percent credible interval.

3.2 Data

In this section, we first describe the data used in our work, including the MARD-Y3 and SPT cluster catalogs and the Dark Energy Survey (Y3) weak-lensing and photometric redshift measurements. We then summarize the simulation datasets from *Magneticum* and Illustris-TNG, which are employed to study the impact of baryons on cluster matter profiles.

3.2.1 MARD-Y3 Cluster Catalog

The second ROSAT All-Sky Survey source catalog, 2RXS (Boller et al., 2016), was used to produce the X-ray-selected MARD-Y3 cluster catalog over the full 5000 $\deg^2$ footprint of DES (Klein et al., 2019). The 2RXS is based on the RASS-3 processed photon event files and incorporates an improved methodology compared to the 1RXS catalogs (Voges et al., 1999, 2000). The complete 2RXS catalog contains approximately 135,000 sources, of which around 30% are attributed to spurious detections (Boller et al., 2016). Within the DES footprint, around 20,000 2RXS sources are present, with only 1,000–2,000 expected to be clusters (Henry et al., 2006; Ebeling et al., 2013; Klein et al., 2018). Due to this low fraction, optical confirmation is required to identify a 2RXS source as a cluster. Furthermore, due to the clustering of a large number of optical systems, as well as the high density of 2RXS sources, the likelihood of chance superposition is significant. Hence, the probability that a 2RXS source with an optical counterpart is actually a cluster needs to be characterized. To address this, the Multi-Component Matched Filter Cluster Confirmation tool (MCMF) (Klein et al., 2018) was developed. MCMF automates cluster confirmation and redshift estimation using data from large-scale imaging surveys like DES. Specifically, the internally available DES Y3A2 GOLD catalog—a value-added version of the previously published DES DR1 dataset (Abbott et al., 2018)—was utilized for this purpose.

In our analysis, we use the optical centers of the optical counterparts instead of the X-ray centers of the 2RXS sources, due to the low resolution of 2RXS in survey mode, especially compared to modern telescopes such as XMM, Chandra, or eROSITA. To maintain a constant sample purity with redshift, we allow $\lambda_{\rm min}$ to evolve with redshift and count rate (Fig. 3.1). We utilize two samples based on contamination fraction thresholds, $f_{\rm cont} < 0.1$ and $f_{\rm cont} < 0.05$, corresponding to sample purities of approximately 95% and 97.5%, respectively. The final cluster sample used in our analysis includes 1433 clusters with $f_{\rm cont} < 0.1$ and 1,067 clusters with $f_{\rm cont} < 0.05$, spanning a redshift range of

$0.05 < z < 0.95$.

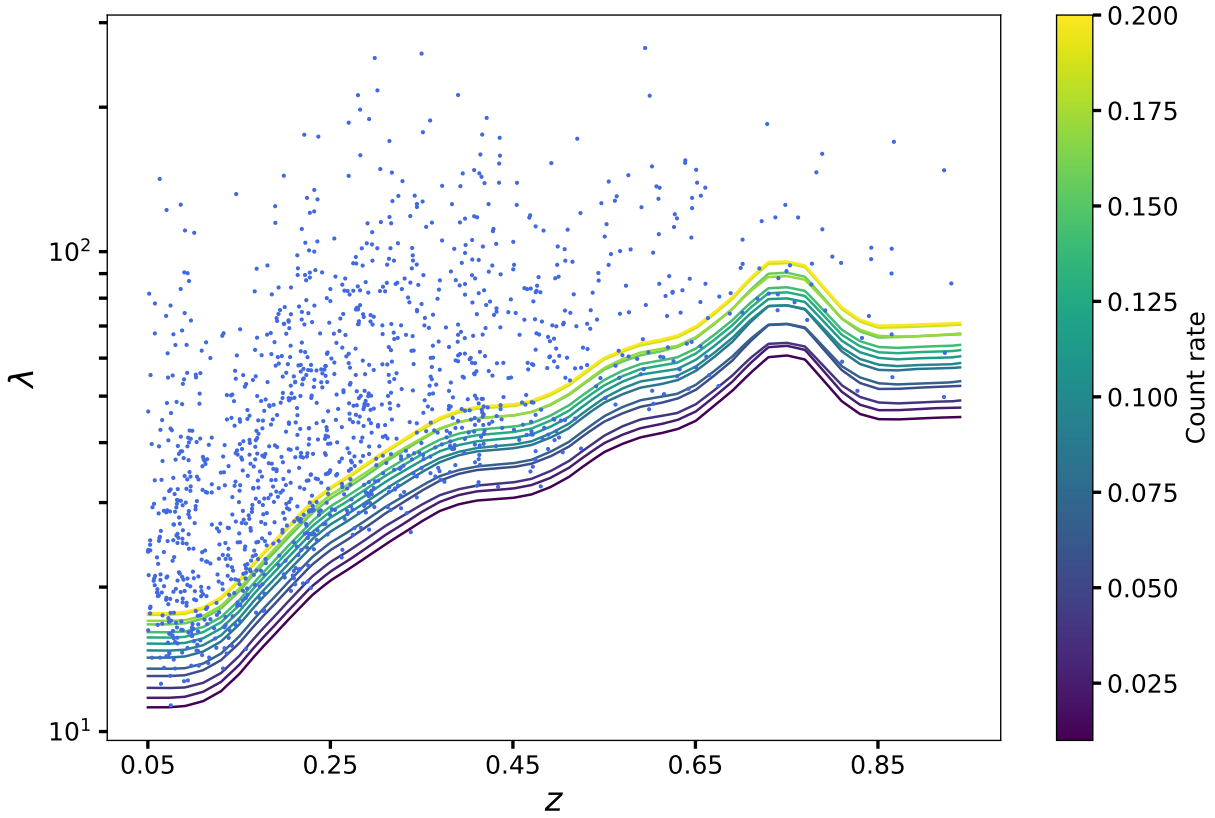

Figure 3.1: Richness plotted against redshift for the MARD-Y3 sample ($f_{\rm cont} < 0.1$). The solid lines correspond to $\lambda_{\rm min}$ evolution with redshift and count rate, coded with different color lines as seen in the color-map.

3.2.2 SPT Cluster Catalogs

We use two thermal Sunyaev-Zel'dovich effect (tSZE)-selected galaxy cluster catalogs derived from surveys conducted by the South Pole Telescope collaboration: the SPT-SZ survey (Bleem et al., 2015; Klein et al., 2024) and the SPTpol-500d survey (Bleem et al., 2024). The SPT-SZ survey covers 2,500 deg^2 of the southern sky, while the SPTpol-500d survey extends to greater depth within a 500 deg^2 region that lies inside the SPT-SZ footprint. Cluster candidates are identified in mm-wave maps at 90 and 150 GHz using a matched filter technique (Melin et al., 2006), which applies cluster tSZE models across a range of angular scales (Vanderlinde et al., 2010).

Due to the matched filtering process removing angular scales that are critical for the tSZE signal—particularly at low redshifts where it is needed to filter out atmospheric noise and primary CMB contributions—only cluster candidates at redshifts $z > 0.25$ are considered to ensure robust detections. At lower redshifts, the overlap between the scales

removed by the filter and those carrying the galaxy cluster tSZE signal significantly reduces the detection significance, making the tSZE signal a less reliable proxy for cluster halo mass. We further restrict the analysis to clusters with redshifts $z < 0.95$ due to the depth and systematics of the DES WL sample described below.

These cluster candidates are subsequently analyzed using the MCMF, which provides measurements of optical richness ($\hat{\lambda}$), sky positions, and redshifts. The optical richness measurements enable efficient removal of contaminants from the tSZE candidate list by assessing the likelihood of a candidate being a random superposition of unassociated optical systems with tSZE noise fluctuations (Klein et al., 2024; Bleem et al., 2024).

The exclusion threshold for contaminants is defined by a redshift-dependent observed richness limit, $\hat{\lambda}_{\rm min}(z)$ (Klein et al., 2019a), which is determined by analyzing richness distributions along random lines of sight within the survey. This ensures a constant contamination fraction across all redshifts in the final cluster catalogs.

The tSZE detection significance thresholds are $\hat{\zeta} > 4.25$ for SPTpol-500d and $\hat{\zeta} > 4.5$ for SPT-SZ. The MCMF richness selection threshold, $\hat{\lambda}_{\rm min}(z)$, is calibrated to maintain a contamination fraction below 2% in the final confirmed cluster lists from both surveys.

3.2.3 DES Y3 lensing

The Dark Energy Survey is a wide-field photometric survey conducted in five broadband filters ($grizY$), covering an area of approximately 5,000,deg^2 in the southern sky. Observations were carried out using the Dark Energy Camera (DECam; Flaugher et al., 2015), installed on the 4m Blanco Telescope at the Cerro Tololo Inter-American Observatory (CTIO) in Chile. This study incorporates weak lensing data from the first three years of DES observations (DES Y3), spanning the entire 5,000,deg^2 survey footprint.

The DES Y3 shape catalog (Gatti & Sheldon et al. 2021) was produced using the r, i, z-band data, processed with the METACALIBRATION pipeline (Huff & Mandelbaum, 2017; Sheldon & Huff, 2017). Additional details on Point-Spread Function (PSF) modeling, photometric data, and image simulations are provided in Jarvis et al. (2021), Sevilla-Noarbe et al. (2021), and MacCrann et al. (2022), respectively. After applying source selection cuts, the shear catalog contains around 100 million galaxies over an area of 4143 deg^2, with a source density ranging from 5 to 6 galaxies per arcmin^2, depending on specific analysis criteria.

This analysis uses the selection of lensing source galaxies in four tomographic bins as employed in the DES 3x2pt analysis (Abbott et al., 2022a). The selection and calibration of these galaxies are detailed in (Myles et al., 2021; Gatti et al., 2022), with source redshifts estimated using Self-Organizing Maps Photo-z (SOMPZ). Systematic uncertainties in source redshifts and shear measurements are incorporated into the final calibration. The mean redshift distribution for each tomographic source bin is provided, with systematic uncertainties captured through 1,000 realizations of the source redshift distribution. To correct for multiplicative shear bias m, the source redshift distribution is scaled by a factor $1 + m$. Additionally, Directional Neighbourhood Fitting (DNF; (De Vicente et al., 2016)) is used to estimate galaxy photometric redshifts, which is used in determining the

expected fraction of the lensing source galaxy population in each tomographic bin that is contributed by member galaxies from a particular cluster of interest– the so-called cluster member contamination.

3.2.4 Hydrodynamical Simulations

In this study, we use the *Magneticum* Pathfinder suite of cosmological hydrodynamical simulations (Hirschmann et al., 2014; Teklu et al., 2015; Beck et al., 2016; Bocquet et al., 2016; Dolag et al., 2017). Specifically, we use Box1, which has a side length of 896 h^{-1} Mpc and contains 2×1526^3 particles, with a particle mass of $1.3 \times 10^{10} h^{-1} M_\odot$ for dark matter and $2.6 \times 10^9 h^{-1} M_\odot$ for gas. The simulation adopts cosmological parameters based on WMAP7 constraints for a flat ΛCDM model (Komatsu et al., 2011): $\Omega_m = 0.272$, $\Omega_b = 0.0457$, $H_0 = 70.4$, $n_s = 0.963$, and $\sigma_8 = 0.809$. From this simulation, we use snapshots at five redshifts $z_{\rm snap} = 0.01, 0.25, 0.47, 0.78, 0.96$.

Additionally, we use data from the IllustrisTNG300-1 simulation (Pillepich et al., 2018; Marinacci et al., 2018; Springel et al., 2018; Nelson et al., 2018; Naiman et al., 2018; Nelson et al., 2019), which includes 2×2500^3 resolution elements within a box size of 205 h^{-1} Mpc per side. The simulation assumes cosmological parameters from Planck2015 for a flat ΛCDM model (Planck Collaboration & et al., 2016): $\Omega_m = 0.3089$, $\Omega_b = 0.0486$, $\sigma_8 = 0.8159$, $n_s = 0.9667$, and $h = 0.6774$. Snapshots are analyzed at redshifts $z_{\rm snap} = 0.01, 0.24, 0.42, 0.64, 0.95$.

For both simulation datasets, halos with $M_{\rm 200c} > 3 \times 10^{13} h^{-1}$ $\rm M_\odot$ are extracted from all snapshots. Shear maps are then generated following the methodology of Grandis et al. (2021), using a cylindrical projection depth of 20 h^{-1} Mpc.

3.3 Mass Calibration Analysis Method

The methodology employed in this work is introduced and described in detail in Singh et al. (2025). We briefly review the details here.

3.3.1 Summary of Analysis Strategy

We use the Bayesian method outlined in Singh et al. (2025) to simultaneously constrain multiple observable-mass relations through an average (binned) analysis of galaxy cluster matter profiles. Given a catalog of galaxy clusters with an associated set of observables (redshift, tSZE detection significance, count rate, and weak lensing measurements), we constrain masses by calibrating observable-mass relations.

3.3.1.1 Observable-mass relations

Following recent studies (Grandis et al., 2019; Chiu et al., 2023b), we employ a count rate observable–mass relation, $\eta - M_{500} - z$, of the form

$$\begin{aligned}\left\langle \ln\left(\frac{\eta}{\text{counts/sec}}\middle| M, z\right)\right\rangle = \eta_0 - 2\ln\left(\frac{D_{\rm L}(z)}{D_{\rm L}(z_{\rm piv})}\right) \\ + \left[\eta_{\rm M} + \eta_{\rm M,z}\ln\left(\frac{1+z}{1+z_{\rm piv}}\right)\right]\ln\left(\frac{M}{M_{\rm piv}}\right) \\ + \eta_z \ln\left(\frac{1+z}{1+z_{\rm piv}}\right) + 2\ln\left(\frac{E(z)}{E(z_{\rm piv})}\right).\end{aligned} \tag{3.1}$$

Here, $z_{\rm piv}$ and $M_{\rm piv}$ are the pivot redshift and mass, respectively. $D_{\rm L}$ denotes the luminosity distance, and $E(z) = H(z)/H_0$ characterizes the expansion history of the Universe. This relation allows for the evolution of the mass trend with redshift. It differs from the formulation in Chiu et al. (2023b) by excluding the eROSITA-based bias factor, b.

We assume a log-normal intrinsic scatter, $\sigma_{\ln\eta}$, which is constant across all redshifts and masses, defined as

$$\sigma_{\ln\eta} = (\text{Var}[\ln\eta|M, z])^{\frac{1}{2}}. \tag{3.2}$$

Additionally, the measurement uncertainty in $\hat{\eta}$ is modeled using a Poisson distribution with a mean equal to the expected number of photons, $n_\gamma = \eta\ t_{\rm exp}$, where $t_{\rm exp}$ is the exposure time. Explicitly, this is expressed as

$$P(\hat{\eta}|\eta, t_{\rm exp}) = \frac{1}{t_{\rm exp}}\frac{n_\gamma^{\hat{n}_\gamma} e^{-n_\gamma}}{\hat{n}_\gamma!}. \tag{3.3}$$

Following an early SPT analysis (Vanderlinde et al., 2010), the tSZE detection significance or signal-to-noise ratio, $\hat{\zeta}$, relates to the unbiased detection signifacance, ζ, via

$$P(\hat{\zeta}|\zeta) = \mathcal{N}\left(\sqrt{\zeta^2 + 3}, 1\right), \tag{3.4}$$

where $\mathcal{N}$ represents a Gaussian distribution. This model accounts for the maximization bias in $\hat{\zeta}$, arising from matched filter cluster candidate selection (Melin et al., 2006), and incorporates three free parameters (sky location and filter scale). The mean unbiased detection significance, ζ, is modeled as a power-law function of mass and redshift

$$\langle\ln\zeta|M_{\rm 200c}, z\rangle = \ln\zeta_0 + \zeta_{\rm M}\ln\left(\frac{M_{\rm 200c}}{M_{\rm piv}}\right) + \zeta_{\rm z}\ln\left(\frac{E(z)}{E(z_{\rm piv})}\right), \tag{3.5}$$

where $E(z)$ is the dimensionless Hubble parameter. Amplitude ζ_0 is field-dependent:

$$\zeta_{0,i} = \gamma_i\zeta_0, \tag{3.6}$$

with γ_i determined from simulated maps (Bleem et al., 2015; Bleem et al., 2020, 2024). Intrinsic scatter in ζ is log-normal, parameterized by $\sigma_{\ln\zeta}$. A single scatter parameter

suffices for the SPT tSZE-selected sample, as shown in recent analyses (Bocquet et al., 2019; Bocquet et al., 2024b; Singh et al., 2025).

Observed cluster richness ($\hat{\lambda}$) relates to intrinsic richness (λ) as

$$P(\hat{\lambda}|\lambda) = \mathcal{N}\left(\lambda, \sqrt{\lambda}\right), \tag{3.7}$$

where this model approximates the Poisson sampling noise in the limit of a normal distribution, with the dispersion given by $\sigma = \sqrt{\lambda}$. The mean intrinsic richness is modeled as a power law

$$\langle \ln \lambda | M_{200c}, z \rangle = \ln \lambda_0 + \lambda_M \ln\left(\frac{M_{200c}}{M_{piv}}\right) + \lambda_z \ln\left(\frac{1+z}{1+z_{piv}}\right), \tag{3.8}$$

scatter in λ, $\sigma_{\ln\lambda}$, is modeled as log-normal and assumed to be constant across all masses and redshifts. This assumption is supported by recent studies (Bocquet et al., 2024b; Singh et al., 2025).

Using the relations defined in Eqs. 3.1−3.8, along with weak-lensing data of the sample clusters, we empirically calibrate the observable-mass relation parameters while accounting for measurement and systematic uncertainties, resulting in a robust analysis.

3.3.1.2 Weak Lensing Observable and Mass Profile Model

The weak lensing observable used in our work is rescaled $\Delta\Sigma$, given by

$$\widetilde{\Delta\Sigma}\left(\frac{R}{R_{200c}}, z\right) = \frac{\Delta\Sigma\left(\frac{R}{R_{200c}}, z\right)}{R_{200c}\rho_{crit}(z)}, \tag{3.9}$$

where ρ_{crit} is the critical density of the universe and R_{200c} is the halo radius that encloses the mass M_{200c}. This choice of weak lensing observable simplifies the modeling of cluster profiles, as the average galaxy cluster profile shows remarkable self-similarity in the $\widetilde{\Delta\Sigma}$ vs R/R_{200c} space (Singh et al., 2025).

The cluster mass profile model is constructed using an equal number of halos from the Magneticum and IllustrisTNG simulations. We create cluster mass profiles at five snapshots, spanning redshifts from 0 to 1, in the $\widetilde{\Delta\Sigma}(R/R_{200c})$ space. These profiles are then interpolated as a function of redshift. Given the strong self-similarity of these profiles with mass, we assume the profiles to be constant across mass.

We use the $M_{WL} - M_{200c}$ relation as calibrated and described in Bocquet et al. (2023), and employed in Singh et al. (2025), to marginalize over crucial systematics (photo-z uncertainties, uncorrelated large-scale structure covariance, cluster mis-centering, cluster member contamination of the source galaxy sample, and hydrodynamical uncertainties on the model). Details about the mis-centering model (we use MCMF centers throughout this paper) and the cluster member contamination model, along with their constraints, are provided in Singh et al. (2025).

3.3.2 Likelihood

Given a cluster sample with observables z, $M_{\rm WL}$, $\hat{\lambda}$, $\hat{X} = \hat{\zeta}$ or $\hat{\eta}$ (corresponding to SPT or MARD Y3 cluster catalog, respectively), we bin clusters in observable bins $\hat{X} - \hat{\lambda} - z$. We write the weak lensing mass calibration likelihood for an ensemble of n clusters with associated observables, $M_{{\rm WL},i}$ $\hat{\lambda}_i$, $\hat{X}_i$ and z_i as

$$\mathcal{L}_{\rm bin} = \langle P\left(\widetilde{\Delta\Sigma}(\vec{M_{\rm WL}}, \vec{p})|\widetilde{\Delta\Sigma}_{\rm mod}, \vec{z}\right)\rangle \prod_{i=1}^{n} P(\hat{\lambda}_i|\hat{X}_i, z_i, \vec{p}), \tag{3.10}$$

where $\langle P\left(\widetilde{\Delta\Sigma}(\vec{M_{\rm WL}}, \vec{p})|\widetilde{\Delta\Sigma}_{\rm mod}, \vec{z}\right)\rangle$ is the average lensing likelihood of the average rescaled matter profile built from the ensemble. The observable vectors $\vec{M_{\rm WL}}$, $\vec{\hat{\lambda}}$, $\vec{\hat{X}}$, and $\vec{z}$ each contain the n measurements for the clusters in the ensemble. For an n cluster ensemble, it takes the form

$$\begin{aligned}
&\langle P\left(\widetilde{\Delta\Sigma}\left(\vec{M_{\rm WL}}, \vec{p}\right)|\widetilde{\Delta\Sigma}_{\rm mod}, \vec{z}\right)\rangle = \\
&\int\cdots\int {\rm d}M_{{\rm WL}_1}...{\rm d}M_{{\rm WL}_n} P(M_{{\rm WL}_1}|\hat{X}_1, \hat{\lambda}_1, z_1, \vec{p}) \times ... \\
&\qquad P(M_{{\rm WL}_n}|\hat{X}_n, \hat{\lambda}_n, z_n, \vec{p}) \\
&\qquad P\left(\widetilde{\Delta\Sigma}(M_{{\rm WL}_1}, ..., M_{{\rm WL}_n}, \vec{p})|\widetilde{\Delta\Sigma}_{\rm mod}, \vec{z}\right),
\end{aligned} \tag{3.11}$$

where, we note that $\vec{M_{\rm WL}}$ is required to construct the rescaled matter profile. It is calculated via

$$\begin{aligned}
&P(M_{\rm WL}|\hat{X}, \hat{\lambda}, z, \vec{p}) = \\
&\frac{\iiint {\rm d}M{\rm d}\lambda{\rm d}X P(\hat{\lambda}|\lambda)P(\hat{X}|X)P(X, \lambda, M_{\rm WL}|M, z, \vec{p})P(M|z, \vec{p})}{P(\hat{X}, \hat{\lambda}|z, \vec{p})},
\end{aligned} \tag{3.12}$$

where the measurement noise is represented by $P(\hat{\lambda}|\lambda)$ and $P(\hat{X}|X)$, the intrinsic scatter and any bias in the observable about mass by $P(X, \lambda, M_{\rm WL}|M, z, \vec{p})$, $P(M|z, \vec{p})$ is the halo mass function which accounts for Eddington bias, and $P(\hat{\lambda}, \hat{X}|z, \vec{p})$ is the numerator integrated over $M_{\rm WL}$. The last term in the Eq. 3.11 is calculated via

$$P(\widetilde{\Delta\Sigma}\left(\vec{M_{\rm 200c}}, \vec{p}\right)|\widetilde{\Delta\Sigma}_{\rm mod}, \vec{z}) = P_{\rm G}\prod_j \left(\left|\frac{\partial\widetilde{\Delta\Sigma}_j}{\partial\vec{e}_{t,j}}\left(\frac{\partial\widetilde{\Delta\Sigma}_j}{\partial\vec{e}_{t,j}}\right)^{\rm T}\right|^{1/2}\right), \tag{3.13}$$

where, $\widetilde{\Delta\Sigma}\left(\vec{M_{\rm 200c}}, \vec{p}\right)$ represents the rescaled matter profile with j radial bins, while $\widetilde{\Delta\Sigma}_{\rm mod}$ denotes the model matter profile. The second factor in the equation is a transformation term necessary because our weak-lensing observable depends on halo masses (refer to Singh et al. (2025) for a detailed derivation). Finally, $P_{\rm G}$ is the Gaussian likelihood, defined as

$$P_{\rm G} = \prod_j \left(\sqrt{2\pi}\sigma_{\widetilde{\Delta\Sigma},j}\right)^{-1} \exp\left[-\frac{1}{2}\left(\frac{\widetilde{\Delta\Sigma}_j - \widetilde{\Delta\Sigma}_{\rm mod,j}}{\sigma_{\widetilde{\Delta\Sigma},j}}\right)^2\right], \tag{3.14}$$

where $\sigma_{\widetilde{\Delta\Sigma},j}$ is the rescaled shape noise correspoding to $\widetilde{\Delta\Sigma}$.

For each cluster, the second term in Eq. 3.10 is computed using Bayes' theorem, incorporating the intrinsic scatter in the observables, and is expressed as

$$P(\hat{\lambda}|\hat{X},z,\vec{p}) = \frac{\iiint \mathrm{d}\lambda \mathrm{d}M \mathrm{d}X P(\hat{\lambda}|\lambda)P(\hat{X}|X)P(X,\lambda|M,z,\vec{p})P(M|z,\vec{p})}{\int_{\lambda_{\min}(\hat{X})}^{\infty} \mathrm{d}\lambda \iint \mathrm{d}M \mathrm{d}X P(\hat{\lambda}|\lambda)P(\hat{X}|X)P(X,\lambda|M,z,\vec{p})P(M|z,\vec{p})}, \tag{3.15}$$

where, $\lambda_{\min}(\hat{X})$ represents the minimum richness calibrated by MCMF, which differs for the SPT and MARD Y3 samples, and is given by

$$\lambda_{\min}(\hat{X}) = \begin{cases} \lambda_{\min}(z), & \hat{X} = \hat{\zeta}, \\ \lambda_{\min}(z,\hat{\eta}), & \hat{X} = \hat{\eta}. \end{cases} \tag{3.16}$$

The inclusion of the halo mass function and $\lambda_{\min}(\hat{X})$ in our likelihood is crucial to properly account for both the Eddington and Malmquist biases.

The final likelihood for m $\hat{\zeta} - \hat{\lambda} - z$ bins can be written as the product of the likelihood of individual bins

$$\mathcal{L} = \prod_{\mathrm{bin}=1}^{m} \mathcal{L}_{\mathrm{bin}}. \tag{3.17}$$

3.3.3 X-ray completeness function

To properly account for selection effects in our mass calibration likelihood, we adopt a completeness model based on the existence likelihood (EXI_ML), which is also used for X-ray selection in the 2RXS catalog. The existence likelihood measures the detection significance of a cluster and depends primarily on its X-ray flux (or count rate, $\hat{\eta}$), while also being sensitive to the intracluster medium (ICM) distribution (e.g., angular size and morphology) and survey parameters such as the background and exposure time. Following the approach of Klein et al. (2023a), we model the logarithm of the measured count rate as a function of these quantities

$$\begin{aligned} \langle \ln(\hat{\eta} \mid \mathrm{EXI\_ML}, t_{\mathrm{exp}}, \mathrm{Bkg}) \rangle = \ln A_{\mathrm{C}} + B_{\mathrm{C}} \ln \mathrm{EXI\_ML} \\ + C_{\mathrm{C}} \ln t_{\mathrm{exp}} + D_{\mathrm{C}} \ln \mathrm{Bkg}, \end{aligned} \tag{3.18}$$

where t_{exp} is the exposure time and $\mathrm{Bkg} = \mathrm{Background}/t_{\mathrm{exp}}$ is the background count rate. This relation includes an intrinsic log-normal scatter given by

$$s_{\ln\hat{\eta}} = \sqrt{\mathrm{Var}[\ln\hat{\eta} \mid \mathrm{EXI\_ML}, t_{\mathrm{exp}}, \mathrm{Bkg}]}. \tag{3.19}$$

Table 3.1: Observable-mass relation and cosmology parameter priors in our modeling.

Parameter	Description	Prior
Count rate η-mass relation		
η_0	amplitude	$\mathcal{U}(-4.5, -3.0)$
η_M	mass trend	$\mathcal{U}(0.5, 3)$
$\eta_\mathrm{M,z}$	z evolution of mass trend	$\mathcal{U}(-4, 4)$
η_z	redshift trend	$\mathcal{U}(-4, 4)$
$\sigma_{\ln\eta}$	intrinsic scatter	$\mathcal{U}(0.01, 1.2)$
tSZE detection significance ζ-mass relation		
ζ_0	amplitude	$\mathcal{U}(0.01, 1.5)$
ζ_M	mass trend	$\mathcal{U}(0.5, 3)$
ζ_z	redshift trend	$\mathcal{U}(-5, 5)$
$\sigma_{\ln\zeta}$	intrinsic scatter	$\mathcal{U}(0.01, 0.5)$
Optical richness λ-mass relation		
λ_0	amplitude	$\mathcal{U}(10, 70)$
λ_M	mass trend	$\mathcal{U}(0.2, 2)$
λ_z	redshift trend	$\mathcal{U}(-5, 5)$
$\sigma_{\ln\lambda}$	intrinsic scatter	$\mathcal{U}(0.01, 0.5)$
$M_\mathrm{WL} - M_\mathrm{200c}$ relation		
$\ln M_{\mathrm{WL}_0}$	amplitude of bias	0
$\sigma_{\ln M_{\mathrm{WL}_{0,1}}}$	error on amplitude	$\mathcal{N}(0, 1)$
$\sigma_{\ln M_{\mathrm{WL}_{0,2}}}$	error on amplitude	$\mathcal{N}(0, 1)$
$M_{\mathrm{WL}_\mathrm{M}}$	mass trend of bias	$\mathcal{N}(1.0, 0.006^2)$
$\ln\sigma^2_{\ln\mathrm{WL}_0}(z_0)$	amplitude of scatter	$\mathcal{N}(-3.11, 0.043)$
$\ln\sigma^2_{\ln\mathrm{WL}_0}(z_1)$	amplitude of scatter	$\mathcal{N}(-3.07, 0.048)$
$\ln\sigma^2_{\ln\mathrm{WL}_0}(z_2)$	amplitude of scatter	$\mathcal{N}(-2.84, 0.059)$
$\ln\sigma^2_{\ln\mathrm{WL}_0}(z_3)$	amplitude of scatter	$\mathcal{N}(-1.94, 0.10)$
$\sigma^2_{\ln\mathrm{WL}_\mathrm{M}}$	mass trend of scatter	$\mathcal{N}(-0.226, 0.04^2)$
Cosmology		
Ω_m	matter density	$\mathcal{N}(0.315, 0.007)$
$\log_{10} A_s$	amplitude of $P(k)$	Fixed to -8.696
H_0	Hubble parameter	Fixed to 70
$\Omega_{\mathrm{b},0}$	baryon density	Fixed to 0.0493
n_s	scalar spectral index	Fixed to 0.96
w_0	EoS parameter	Fixed to -1
w_a	EoS parameter	Fixed to 0
$\sum m_\nu$	sum of neutrino masses	Fixed to 0.06
$\Omega_{\mathrm{k},0}$	curvature density	Fixed to 0

With this scaling relation, a selection threshold in the observed existence likelihood ln EXI_ML translates into a selection in $\ln \hat{\eta}$ that follows an error function. Consequently, the completeness function is modeled as

$$C(\hat{\eta}, z) = \frac{1}{2}\left[1 + \mathrm{erf}\left(\frac{\ln \hat{\eta} - (\ln \hat{\eta}_{50} + \delta \ln \hat{\eta}_{50})}{\sqrt{2}\, s_{\ln \hat{\eta}}}\right)\right], \tag{3.20}$$

where $\hat{\eta}_{50}$ is the count rate corresponding to 50% completeness (EXI_ML = 6.5) and $\delta \ln \hat{\eta}_{50}$ is a parameter that allows for deviations from the expected threshold. We adopt the same model and best-fit parameter values as derived from the RASS-MCMF clusters in Klein et al. (2023a), ensuring that our analysis properly accounts for the selection effects inherent in the X-ray catalog.

3.4 Results

The analysis in this work closely follows our recent study (Singh et al., 2025), where we performed mass calibration of the SPT sample using average rescaled matter profiles, $\widetilde{\Delta\Sigma}$. In this work, we apply the same framework to analyze the MARD-Y3 × DES Y3 sample. Since the SPT and MARD-Y3 catalogs cover different redshift ranges, and because MCMF-derived richnesses are available for both catalogs, we also perform a combined analysis of the SPT + MARD-Y3 × DES Y3 sample. We first start by analyzing and validating the X-ray pipeline using mocks.

3.4.1 Mock Validation of X-ray analysis

We validate our methodology using a realistic MARD-Y3 mock catalog with DES-like weak lensing data. For this purpose, we create mock clusters and lensing data following the approach taken in the recent SPT×DES analysis (Singh et al., 2025; Bocquet et al., 2023).

We create mock MARD-Y3 cluster catalogs within a fiducial cosmological model using the Tinker et al. (2008) halo mass function scaled by the surveyed volume as a function of redshift to calculate the expected number of halos as a function of redshift and mass. We impose a mass range $10^{13} M_\odot < M_{200c} < 10^{16} M_\odot$ and a redshift range $0.05 < z < 0.94$. We draw a Poisson realization of this sample. For each halo, we assign cluster observables using the observable-mass relations presented in Section 3.3. We then apply survey selection cuts based on EXI_ML > 6.5 and richness $\hat{\lambda}$. These cuts are applied as a function of redshift z and observed count rate $\hat{\eta}$, following Fig. 3.1. The selection criteria are consistent with those used to produce the real sample.

We generate mock DES Y3-like weak lensing data following our recent analysis (Singh et al., 2025). In summary, our mock WL data mimics DES Y3 data, which has an effective shape noise of 0.3 and a source galaxy density of 6 galaxies per arcmin^2. Our data is distributed in four DES Y3 tomographic bins, and we apply cluster member contamination

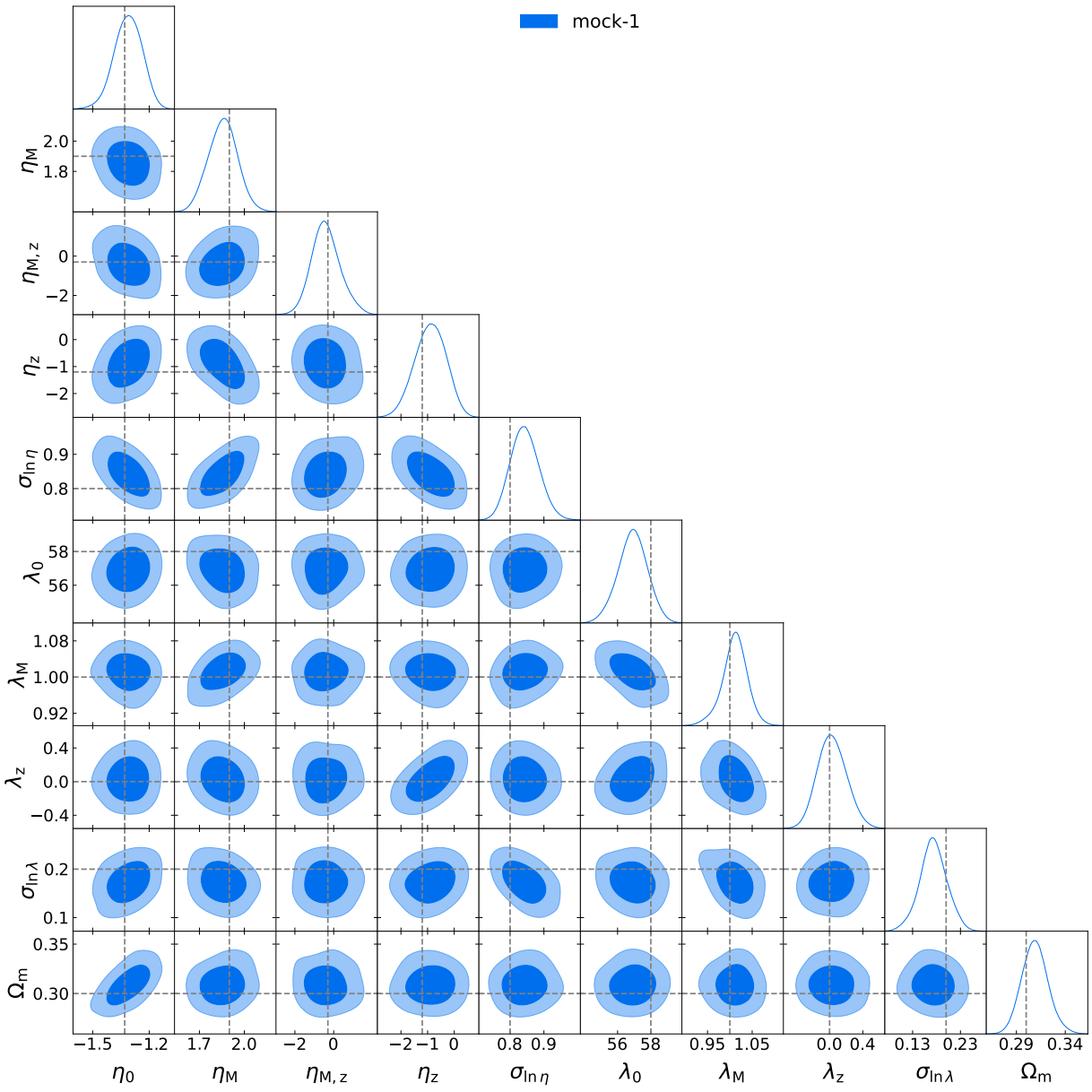

Figure 3.2: Posterior of the observable-mass relation parameters for a MARD-Y3 like mock sample with DES Y3 like WL.

to our mock WL data using the cluster member contamination model as in our previous work (Singh et al., 2025). The final WL mocks include all known systematics and stochastic effects needed to model cluster shear profiles in DES data.

We create several independent mock catalogs to assess the performance of our pipeline. For the analysis, we divide our data into $3 \times 3 \times 4$ $\hat{\eta} - \hat{\lambda} - z$ observable bins, and the likelihood calculation is performed following the formalism outlined in Section 3.3.2. To sample the high-dimensional parameter space, we use the Markov Chain Monte Carlo

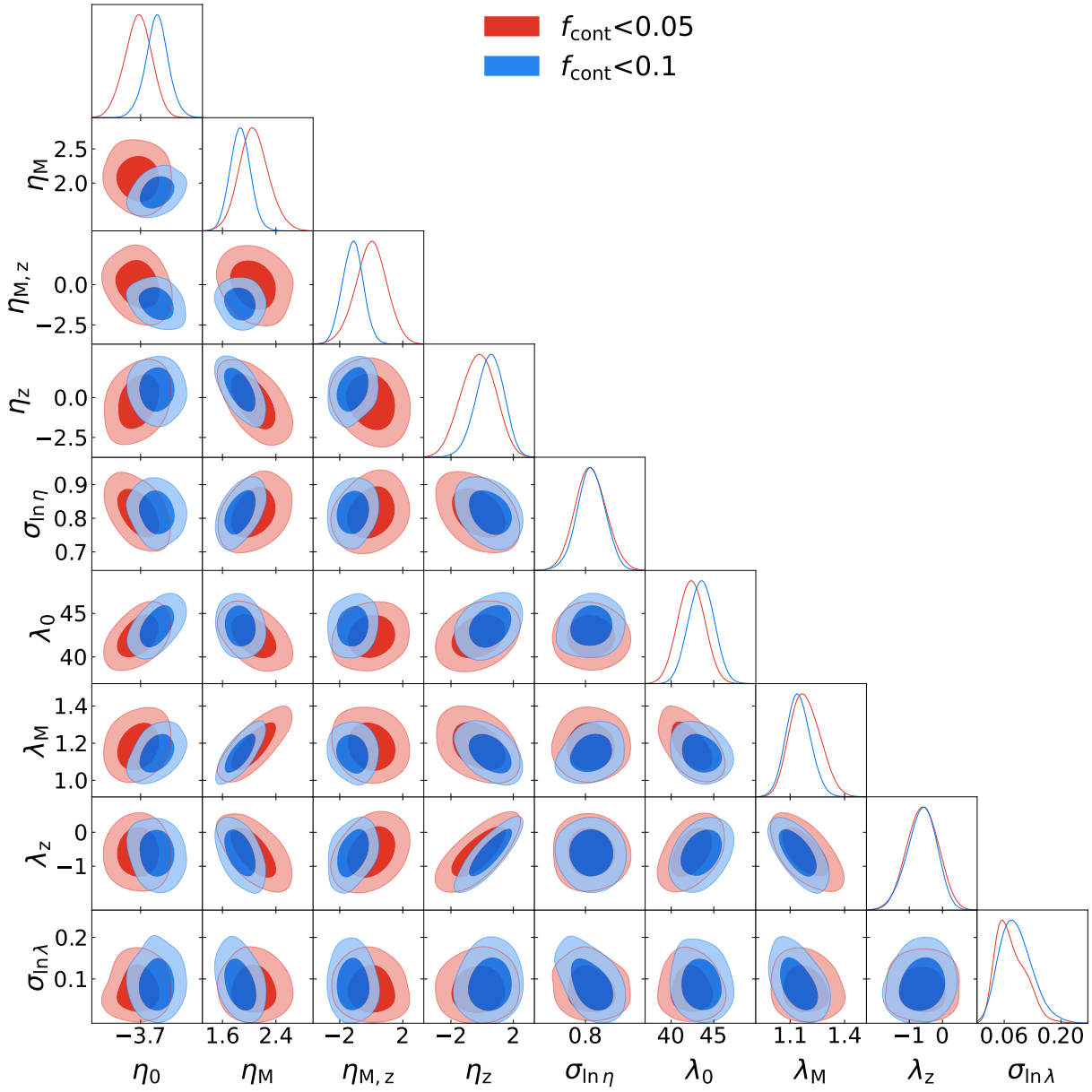

Figure 3.3: Posterior of the observable-mass relation parameters for the MARD-Y3 sample, corresponding to two different $f_{\rm cont}$ selections. The two samples show very good agreement with each other.

algorithm MultiNest (Feroz et al., 2009, 2019) for our likelihood analysis. Fig. 3.2 shows the posteriors for one such mock catalog. The mock catalog contains a similar number of clusters to the real MARD-Y3 sample. We recover all parameters within 1σ of the input values, and these validation tests show no signs of bias.

3.4.2 MARD-Y3 cluster analysis

After validating the pipeline, we perform the mass calibration analysis of MARD-Y3 clusters using DES Y3 weak lensing data. Specifically, we analyze two cluster samples with purities of 95% and 97.5%, corresponding to $f_{\rm cont} < 0.1$ (1433 clusters) and $f_{\rm cont} < 0.05$ (1067 clusters), respectively. Following our previous analysis of SPT clusters (Singh et al., 2025), we restrict the radial range of the analysis to $0.5 < R/(h^{-1}\mathrm{Mpc}) < 3.2/(1+z_{\rm cl})$ and use DNF redshifts (De Vicente et al., 2016). The shape noise per tomographic bin for the DES Y3 data is taken from Amon et al. (2022a) and is in good agreement with our bootstrap error estimates,

$$\sigma_{\mathrm{eff},b} = \begin{cases} 0.243 & b = 1 \\ 0.262 & b = 2 \\ 0.259 & b = 3 \\ 0.301 & b = 4. \end{cases}$$

We bin the clusters into $3\times3\times4$ observable bins $(\hat{\eta}-\hat{\lambda}-z)$, ensuring each bin has a similar signal-to-noise ratio. Parameter priors for the analysis are listed in Table 3.1. To break the degeneracy in our $\eta - M - z$ scaling relation, which relies on distance measurements, we adopt a Gaussian prior on $\Omega_{\rm m}$ (Planck Collaboration & et al., 2016). Other cosmological parameters are fixed: the sum of neutrino masses is set to the minimum allowed value of 0.06 eV, the Hubble parameter to 70, and the remaining parameters to their mean Planck values. In our analysis, we marginalize over key systematics using the $M_{\rm WL} - M_{\rm 200c}$ relation. The calibration of this relation is based on the model and parameters outlined in (Bocquet et al., 2023), which we adopt for our analysis. We incorporate these into our analysis, accounting for the fact that our weak lensing mass model is derived from hydrodynamical simulations. Therefore, we set the amplitude of bias, $\ln M_{\rm WL_0}$, to zero and adopt a Gaussian prior on $M_{\rm WL_M}$ around one, consistent with the strong self-similar behavior observed in average matter profiles (Singh et al., 2025).

Figure 3.3 illustrates the constraints on the η and λ scaling relation parameters. The red contours correspond to $f_{\rm cont} < 0.05$. The derived $\eta_{\rm M}$ is 2.07 ± 0.22, slightly larger than the recent eRASS1 constraints (Grandis et al., 2024b), but consistent with their results. The redshift evolution of the mass trend, $\eta_{\rm M,z}$, is consistent with zero, while the redshift trend parameter, $\eta_{\rm z}$, is slightly negative but also consistent with zero. The resulting intrinsic scatter, $\sigma_{\ln\eta}$, is 0.81 ± 0.05, which is significantly larger than the intrinsic scatter in the tSZE or richness-mass relations (Bocquet et al., 2024b; Chiu et al., 2023b; Singh et al., 2025). The eRASS1 analysis also reports a high intrinsic scatter value of 0.61 ± 0.19, consistent with our findings. Constraints on the richness-mass relation align with our recent analysis (Singh et al., 2025), with the mass trend slightly greater than one and the redshift trend slightly less than zero. The constraints for $f_{\rm cont} < 0.1$ are shown in blue contours. These constraints are marginally tighter than the red contours, as the sample includes slightly more galaxy clusters. Overall, there is good agreement between the blue and red contours, although the blue contours indicate a slightly smaller mass trend and a

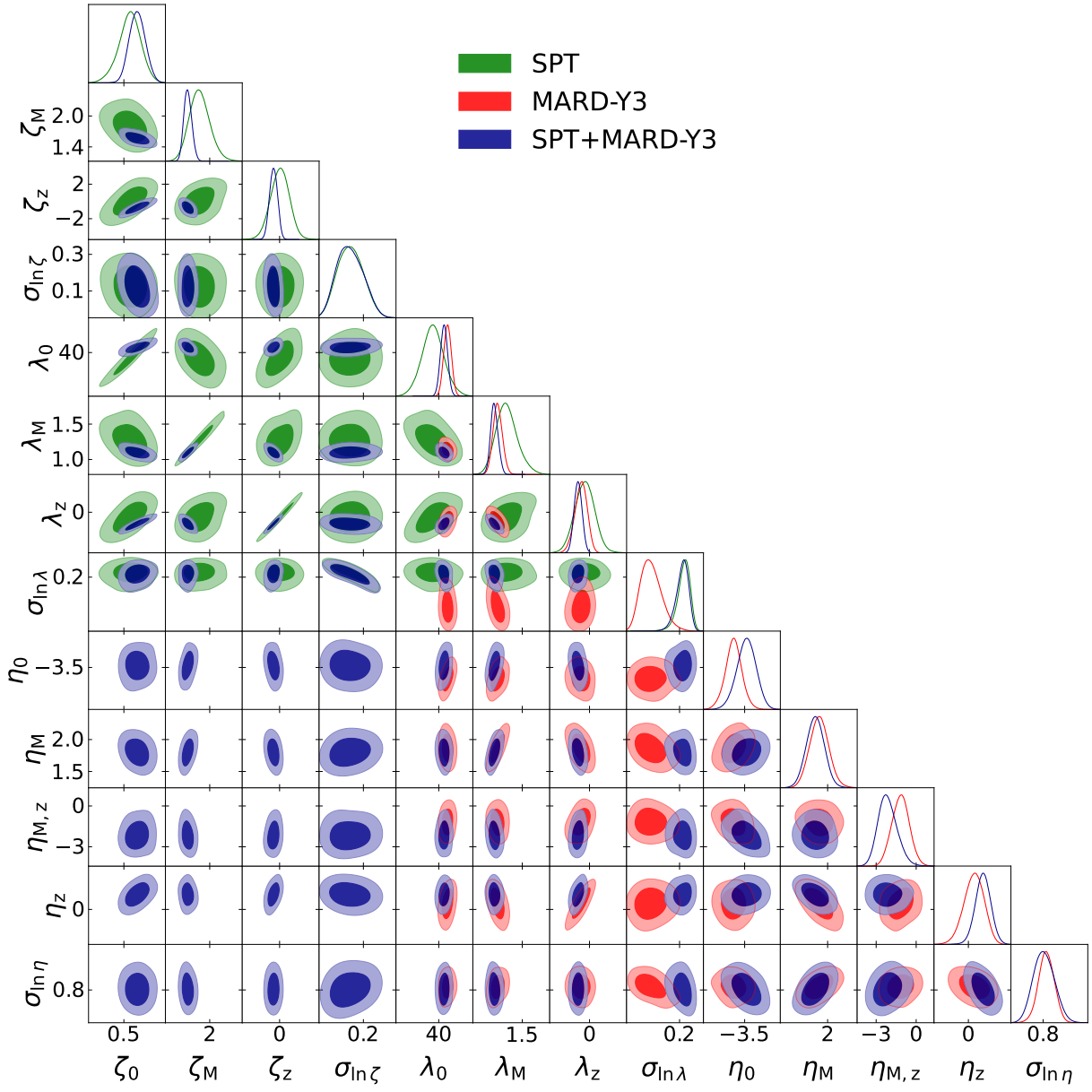

Figure 3.4: Posterior distributions of the observable-mass relation parameters, comparing results from SPT-only, MARD-Y3-only, and the combined SPT and MARD-Y3 analysis. For the combined analysis, if the cluster is present in both the catalogs, we select its SPT counterpart. The combined analysis yields significantly tighter constraints on the tSZE parameters, as the degeneracy between the λ and tSZE parameters is reduced due to the improved constraints on the λ observable-mass parameters.

more pronounced redshift evolution of the mass trend.

Table 3.2: Mean parameter posteriors and 1σ uncertainties from our mass calibration analyses. We only show well-constrained parameters.

Parameter	MARD-Y3 ($f_{\rm cont} < 0.05$)	MARD-Y3 ($f_{\rm cont} < 0.1$)	MARD-Y3 + SPT
count rate η-mass relation			
η_0	-3.715 ± 0.082	-3.596 ± 0.071	-3.484 ± 0.081
$\eta_{\rm M}$	2.07 ± 0.21	1.86 ± 0.14	1.80 ± 0.14
$\eta_{\rm M,z}$	-0.04 ± 0.96	-1.17 ± 0.64	-2.14 ± 0.69
$\eta_{\rm z}$	-0.24 ± 1.05	0.50 ± 0.85	1.29 ± 0.66
$\sigma_{\ln \eta}$	0.815 ± 0.045	0.817 ± 0.040	0.804 ± 0.054
Optical richness λ-mass relation			
λ_0	42.35 ± 1.51	43.53 ± 1.44	42.11 ± 1.38
$\lambda_{\rm M}$	1.186 ± 0.079	1.145 ± 0.065	1.098 ± 0.052
$\lambda_{\rm z}$	-0.59 ± 0.45	-0.61 ± 0.43	-0.83 ± 0.27
$\sigma_{\ln \lambda}$	0.075 ± 0.036	0.088 ± 0.039	0.211 ± 0.024
tSZE detection significance ζ-mass relation			
$\ln \zeta_0$	-	-	0.696 ± 0.112
$\zeta_{\rm M}$	-	-	1.566 ± 0.074
$\zeta_{\rm z}$	-	-	-0.72 ± 0.45
$\sigma_{\ln \zeta}$	-	-	0.125 ± 0.070

3.4.3 MARD-Y3 + SPT-cl analysis

The MARD-Y3 and SPT cluster samples span different ranges of mass and redshift while sharing a common MCMF-derived observable richness, $\hat{\lambda}$. The MARD-Y3 catalog primarily consists of low-mass, low-redshift clusters, whereas the SPT sample includes high-mass, high-redshift clusters. We perform a combined mass calibration analysis to achieve tighter scaling relation constraints. The MARD-Y3 clusters are divided into $\hat{\eta} - \hat{\lambda} - z$ $(3 \times 3 \times 4)$ bins, while the SPT clusters are divided into $\hat{\zeta} - \hat{\lambda} - z$ $(3 \times 3 \times 3)$ bins. If a cluster belongs to both samples, we use its SPT counterpart. The combined likelihood is computed as the product of the SPT and MARD-Y3 likelihoods. For this analysis, we adopt the priors listed in Table 3.1 and use the MARD-Y3 catalog with $f_{\rm cont} < 0.1$.

Figure 3.4 presents the constraints on the η-mass, λ-mass, and ζ-mass scaling relation parameters for the SPT-only analysis (green, Singh et al., 2025), MARD-Y3-only analysis (red), and the combined analysis (blue). The combined analysis improves constraints on the λ-mass scaling relation parameters, with the most significant improvement observed in $\lambda_{\rm z}$, along with more minor improvements in λ_0, $\lambda_{\rm M}$, and $\sigma_{\ln \lambda}$. There is no change in the η-mass scaling parameter constraints except for $\eta_{\rm z}$, due to the degeneracy between $\eta_{\rm z}$ and $\lambda_{\rm z}$. The most notable changes are observed in the ζ-mass scaling relation parameters. The tight degeneracy between ζ and λ parameters is alleviated by the improved constraints on the λ-mass parameters, resulting in significantly more precise constraints on the ζ-mass parameters. This combined analysis provides the most stringent constraints on the ζ-mass

scaling relation parameters to date, derived solely from weak lensing data. These results are comparable to the recent SPT cosmology analysis (Bocquet et al., 2024b) and are in good agreement with their findings. Table 3.2 lists posteriors from combined and individual analyses.

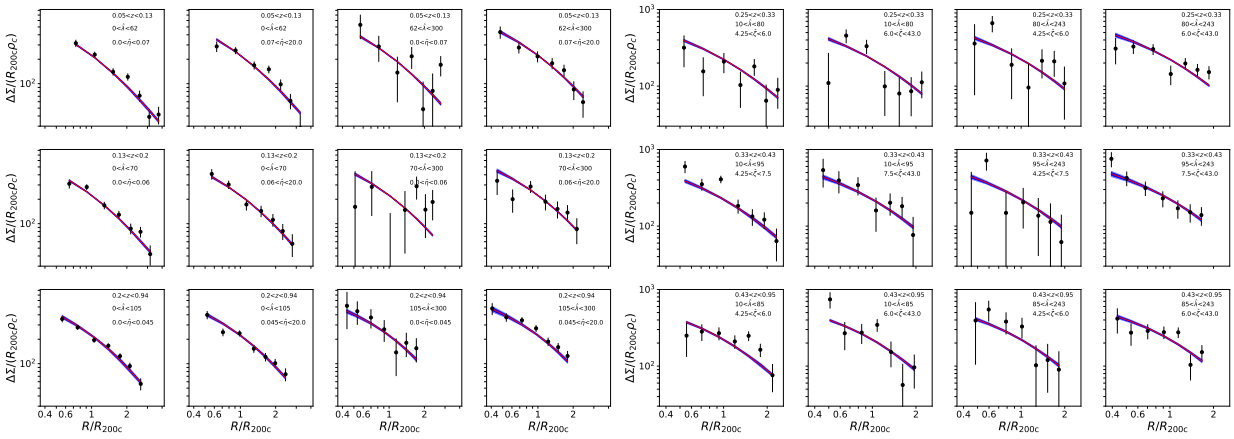

Figure 3.5: Average MARD-Y3 cluster matter profiles (left) and average SPT cluster matter profiles (right) corresponding to the mean recovered parameters from the combined analysis in twelve $\hat{\eta} - \hat{\lambda} - z$ and $\hat{\zeta} - \hat{\lambda} - z$ bins, respectively. Data points are shown in black with 1σ error bars. The WL model is represented by the red line, and the shaded blue region denotes the 2σ error region of the model.

3.4.4 Goodness of fit

To assess the goodness of fit of the data to our model in the combined analysis, we compare the average matter profile model to the average cluster matter profiles in 12 $\hat{\eta} - \hat{\lambda} - z$ and 12 $\hat{\zeta} - \hat{\lambda} - z$ bins and perform a χ^2 fit across all bins. Figure 3.5 displays the 12 MARD-Y3 average matter profiles (left panel) and the 12 SPT cluster matter profiles (right panel). The data points are shown in black, along with the model (red line) and its corresponding 2σ region (shaded blue region). The profiles are extracted based on the mean parameter values obtained from the posterior of the combined analysis. We get a chi-squared value of $\chi^2 = 184.68$ from 168 data points, effectively constraining 13 parameters. This corresponds to a reduced chi-squared value of $\chi^2_{\rm red} = 1.19$ and a probability of exceeding the observed χ^2 of $p = 0.052$.

3.4.5 Average cluster matter profile extending to cluster outskirts

Taking advantage of the self-similar behavior of the rescaled $\widetilde{\Delta\Sigma}$ space, we combine the matter profiles of MARD-Y3 and SPT clusters across all redshift and mass ranges to create a high-SNR profile. The black points in Fig.3.6 show the average cluster profiles

measured up to $\approx 6\ R/R_{200c}$. The ΛCDM model derived from hydrodynamical simulations is shown by the red line, with the red shaded region representing the 2σ error region of the model. The data points in the outer region consistently lie more than 1σ above the model prediction from approximately $2-6\ R/R_{200c}$, as seen in the residual plot at the bottom of Fig.3.6. Note that we only use the lensing data from the 1-halo region when performing the mass calibration.

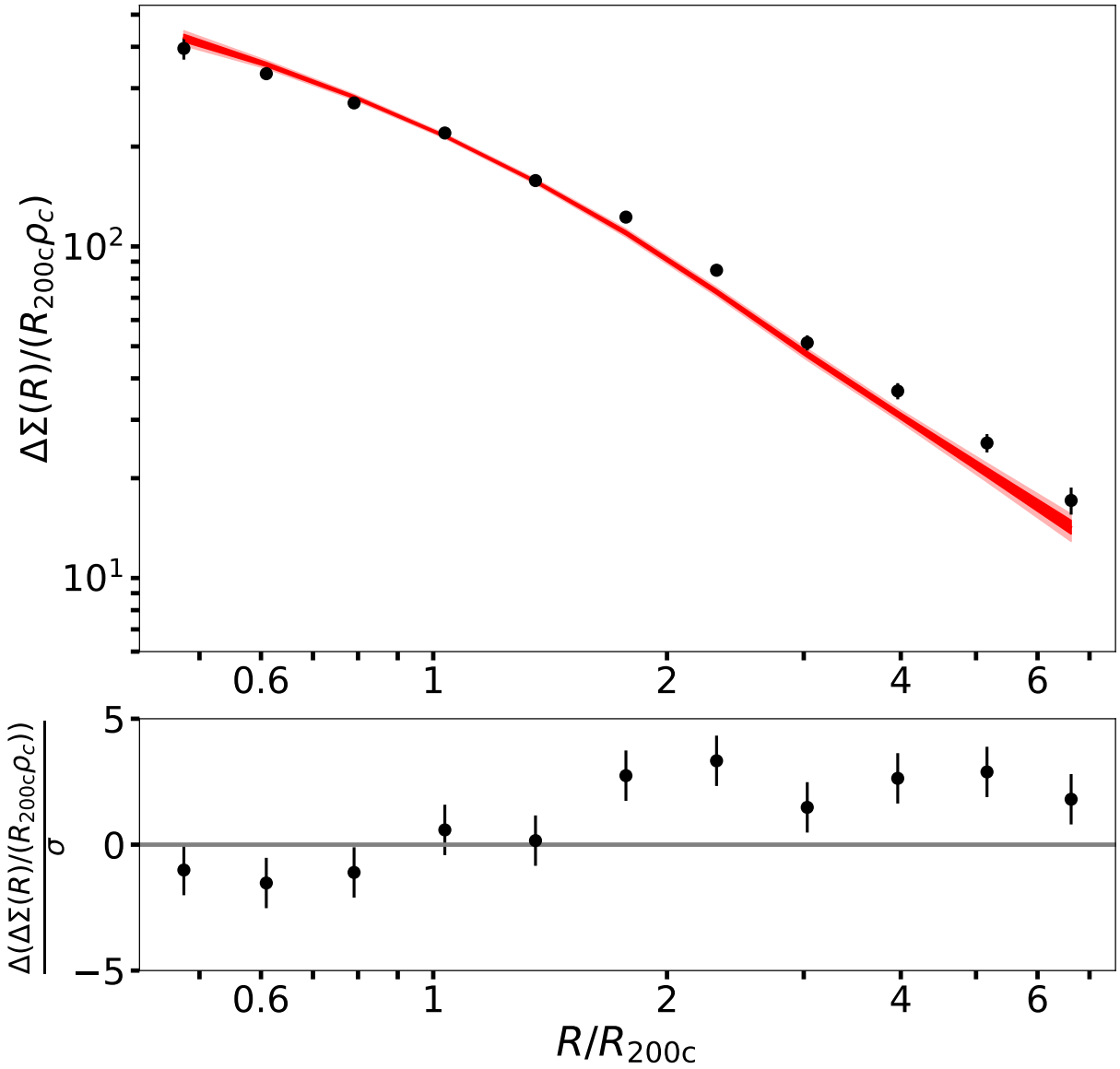

Figure 3.6: Average matter profile of the combined SPT and MARD-Y3 cluster sample using DES Y3 WL data shown in black data points. The red line shows the ΛCDM model derived from hydrodynamical simulations. The red shaded regions show the 2σ error region. The bottom panel shows the difference between the data and the model, normalized with error on data points.

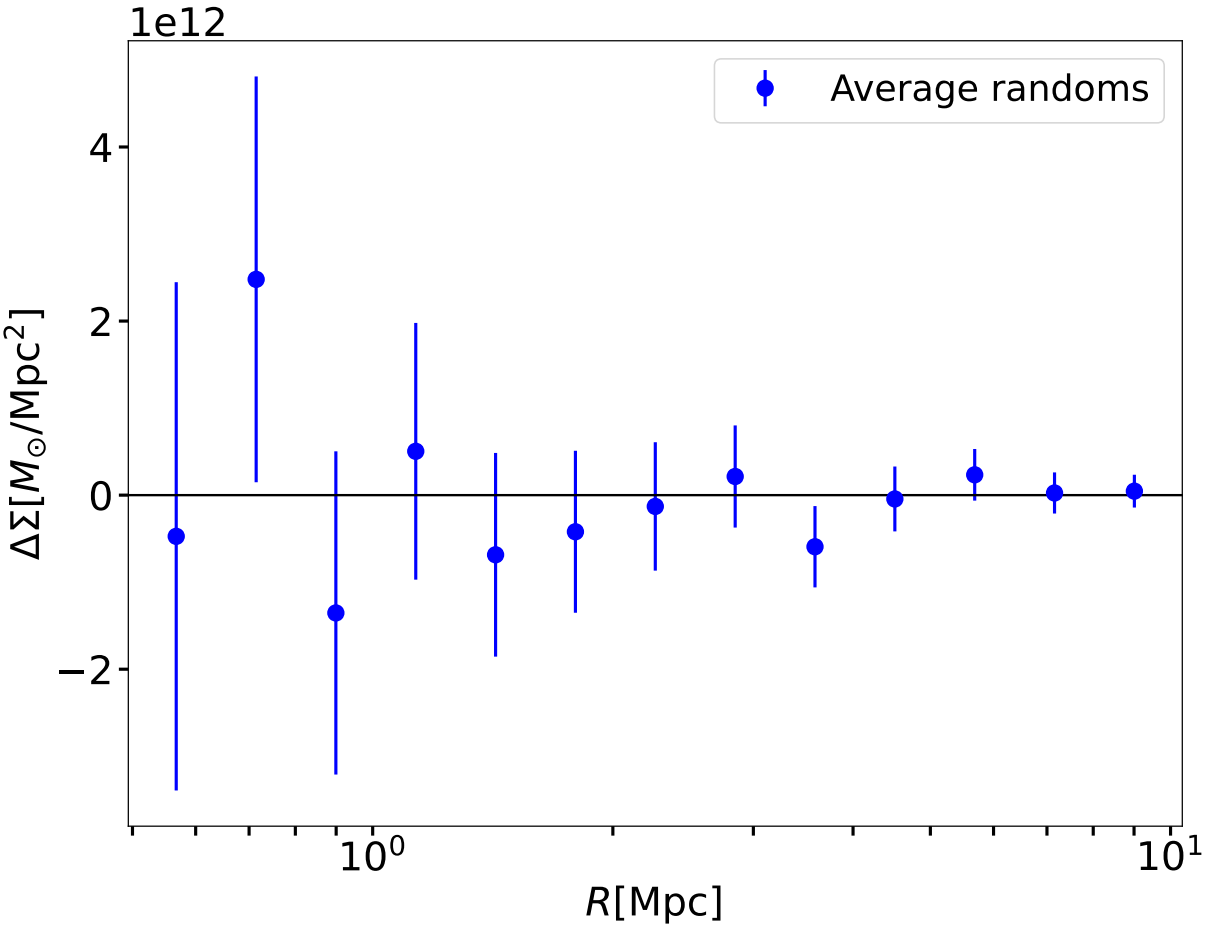

Figure 3.7: Average $\Delta\Sigma$ signal around 2325 random positions in the DES Y3 footprint out to radius of 10 Mpc. The redshift distribution of the random position is the same as of the SPT + MARD-Y3 catalog. The random positions are chosen such that there are no clusters within a radius of 30 Mpc.

To test the effects of large-scale correlations in the DES Y3 lensing signal, we perform a test using random positions within the DES Y3 footprint. We select positions in the sky at random while ensuring that each position lies at least 30 Mpc away from any cluster. We also ensure that the redshift distribution of the randoms is similar to the SPT and MARD-Y3 samples. We then extract the lensing signal around these 2325 random positions (a similar number to the combined SPT and MARD-Y3 sample) and measure the average lensing signal. Fig. 3.7 shows the average signal of all the randoms out to a radius of approximately 10 Mpc. We do not observe any excess signal, and our data points are consistent with the expectation of zero.

Our analysis of high-SNR cluster matter profiles reveals an excess signal in the cluster outskirts, deviating from the ΛCDM expectation by approximately 4.14σ in the cluster outskirts ($R/R_{200c} > 2$). Modified gravity (MG) theories—such as $f(R)$ gravity—offer a possible explanation, as they alter the structure formation of the universe. In these

models, the unscreened fifth force modifies galaxy cluster mass profiles in low-density environments, while high-density regions (e.g., the Solar System) remain unaffected due to efficient screening. In $f(R)$ gravity, for instance, chameleon screening suppresses the fifth force in dense regions, so that the gravitational force in the inner parts of clusters is similar to that in ΛCDM. However, in the outer, low-density regions, the unscreened fifth force enhances gravitational attraction, leading to a steeper fall-off or higher density relative to the ΛCDM expectation. Similarly, the normal-branch Dvali-Gabadadze-Porrati (nDGP) model (Dvali et al., 2000), which originates from braneworld theories where gravity propagates in higher dimensions, induces a fifth force that is efficiently suppressed by Vainshtein screening (Vainshtein, 1972) in high-density regions but becomes significant in the outskirts. As a result, the density profiles in these modified gravity models can differ from those in a ΛCDM universe, often exhibiting an enhancement in the outer regions or a change in the overall shape of the profile. Both $f(R)$ and nDGP gravity thus offer compelling alternatives to explore in light of the observed deviations in the MARD-Y3+SPT cluster mass profiles, as shown in Fig. 3.6. We leave a more detailed analysis of these effects for future work.

Alternatively, this discrepancy can also be explained by stronger baryonic feedback models. Our work adopts the Magneticum and IllustrisTNG simulations to model cluster profiles. However, recent studies have highlighted the need for even stronger baryonic feedback than what is implemented in both IllustrisTNG and Magneticum simulations (Aricò et al., 2023b; Bigwood et al., 2024; Grandis et al., 2024a; Singh et al., 2025a). Stronger feedback alters the profile shape by reducing the amplitude at small radii while slightly increasing it at $R/R_{200c} > 1$. This occurs because baryonic feedback expels gas from the cluster center, redistributing it beyond the virial radius. These changes in the profile shape can lead to a better fit by requiring slightly higher M_{200c} values.

3.5 Discussion

Our state-of-the-art multi-wavelength mass calibration analysis places strong constraints on the λ-mass, ζ-mass, and η-mass scaling relations, derived purely from the analysis of weak lensing data. The inclusion of all systematics, along with statistical and selection effects, ensures a robust calibration. In this section, we discuss the implications of tighter constraints on the λ-mass and ζ-mass relations for cosmological constraints. Additionally, we analyze the impact of the optical λ-mass relation constraints by examining the galaxy cluster mass profiles of redMaPPer clusters identified in the DES Y3 data.

3.5.1 Implications for cosmological constraints

Given that our constraints on the ζ and λ observable-mass relations from the SPT+MARD-Y3 × DES Y3 WL analysis alone are comparable to those derived from the SPT cluster abundance + SPT × DES Y3 WL analysis (Bocquet et al., 2024b), we analyze a mock SPT cluster abundance using priors on the ζ and λ observable-mass relations from our combined

analysis. We then compare the results to those presented in Bocquet et al. (2024b) to assess the impact of these improved constraints on cosmological parameter estimation.

To carry out this analysis, we first generate a mock SPT-like catalog following the procedure described in our previous work (Singh et al., 2025). The mock catalog is constructed to have a similar number of clusters as the real SPT catalog used for cosmological studies in Bocquet et al. (2024b). Additionally, the catalog is designed to match the selection criteria and the mass and redshift distributions of the real SPT cluster sample. This ensures that our mock analysis closely mimics the conditions of the actual SPT cluster abundance study.

Once the mock catalog is generated, we analyze it using the same cosmological inference pipeline employed in the SPT cosmology analysis, as described in (Bocquet et al., 2024b). We adopt the same priors on the cosmological parameters to maintain consistency with the original study. However, for the observable-mass relation parameters, we use the posterior distributions obtained from our combined SPT+MARD-Y3 $\times$ DES Y3 WL analysis (as listed in Table 3.2) as priors. Importantly, we ensure that the cosmology analysis properly accounts for the correlation between the ζ and λ observable-mass relation parameters. This allows us to accurately incorporate the additional constraints from our combined analysis and evaluate their impact on the cosmological constraints derived from SPT cluster abundances.

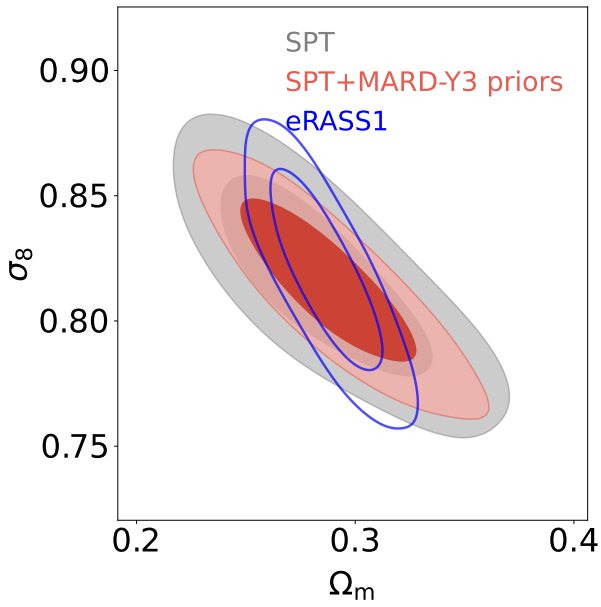

Figure 3.8: Constrains on $\Omega_m - \sigma_8$ (68% and 95% credible regions) in a ΛCDM universe for a mock SPT clusters with observable-mass relation priors based on our combined SPT+MARD-Y3 $\times$ DES Y3 WL analysis (red contour). For comparison, we show the latest constraints from SPT (grey; Bocquet et al., 2024b) and eROSITA (blue; Ghirardini et al., 2024) shifted to the input cosmology of the mock run.

Figure 3.8 presents the $\Omega_m - \sigma_8$ constraints derived from our mock SPT clusters analy-

sis, which incorporates priors on the ζ and λ observable-mass relations from the combined SPT+MARD-Y3 $\times$ DES Y3 WL analysis. We compare these results to the constraints obtained in the original SPT cluster analysis (Bocquet et al., 2024b) and the eRASS1 cluster analysis (Ghirardini et al., 2024). Our analysis demonstrates that incorporating the tighter observable-mass relation priors leads to a significantly improved constraint on cosmological parameters. Specifically, the uncertainty in the $\Omega_{\rm m} - \sigma_8$ plane is reduced by approximately 40% compared to the original SPT cluster abundance analysis, which relied solely on SPT$\times$DES WL data to constrain the observable-mass relations. This improvement is equivalent to effectively doubling the sample size of clusters used in the analysis, highlighting the substantial impact of the additional constraints from our combined study.

3.5.2 Implications for redMaPPer clusters

Recently, Abbott et al. (2020) studied redMaPPer galaxy clusters from the DES Y1 survey. Their analysis initially led to a very low $\Omega_{\rm m}$ value, which was partially mitigated by removing low-richness clusters from the sample. Subsequent studies have suggested that projection effects can lead to false detections of clusters in optical samples, potentially biasing analyses (Zhou et al., 2023). In this section, we analyze the redMaPPer (DES Y3) cluster matter profiles to determine whether they exhibit similar behavior to ICM-selected clusters to test for spurious redmapper clusters.

First, we verify that the redMaPPer richnesses and the MCMF richnesses are in agreement. We cross-match the redMaPPer sample with $\hat{\lambda} > 20$ (applied to select clusters) against the MARD-Y3 and SPT cluster samples. We then compare the richness values (redMaPPer and MCMF) for the overlapping clusters and find them consistent, with no evidence for systematic offsets.

We apply the λ observable-mass relation constraints from Section 3.4.3 to the redMaPPer cluster sample to compute M_{200c} values for each cluster, accounting for the redMaPPer richness selection function, $\hat{\lambda}_{\rm min} > 20$. The derived masses are then used to compute matter profiles of the redMaPPer sample in the rescaled $\widetilde{\Delta\Sigma}$ versus R/R_{200c} space.

Figure 3.9 shows the redMaPPer sample divided into 16 redshift-richness bins, where the profiles are plotted out to $5R/R_{200c}$. The columns correspond to increasing redshift bins from top to bottom, while the rows correspond to increasing richness bins from left to right. The solid red line represents the model to which our richness-mass scaling is calibrated, and the shaded blue region indicates the 2σ range of the model. The redMaPPer cluster profiles consistently fall below the model for clusters with $20 < \hat{\lambda} < 35$ across the redshift range. The significance levels corresponding to the deviation in this richness bin at increasing redshifts are: $> 10\sigma$, 8.0σ, 7.2σ, and 7.8σ. For clusters with $35 < \hat{\lambda} < 75$ in the low-redshift bin ($0.05 < z < 0.25$), the profiles also tend to lie below the model at $R/R_{200c} < 2$ at a significance level of 6.2σ. Conversely, redMaPPer profiles for clusters with $z > 0.25$ and $\lambda > 35$ generally agree well with the model and closely align with the MARD-Y3 and SPT cluster profiles. This analysis suggests high contamination in the redMaPPer sample at low richness and redshifts, potentially due to projection effects.

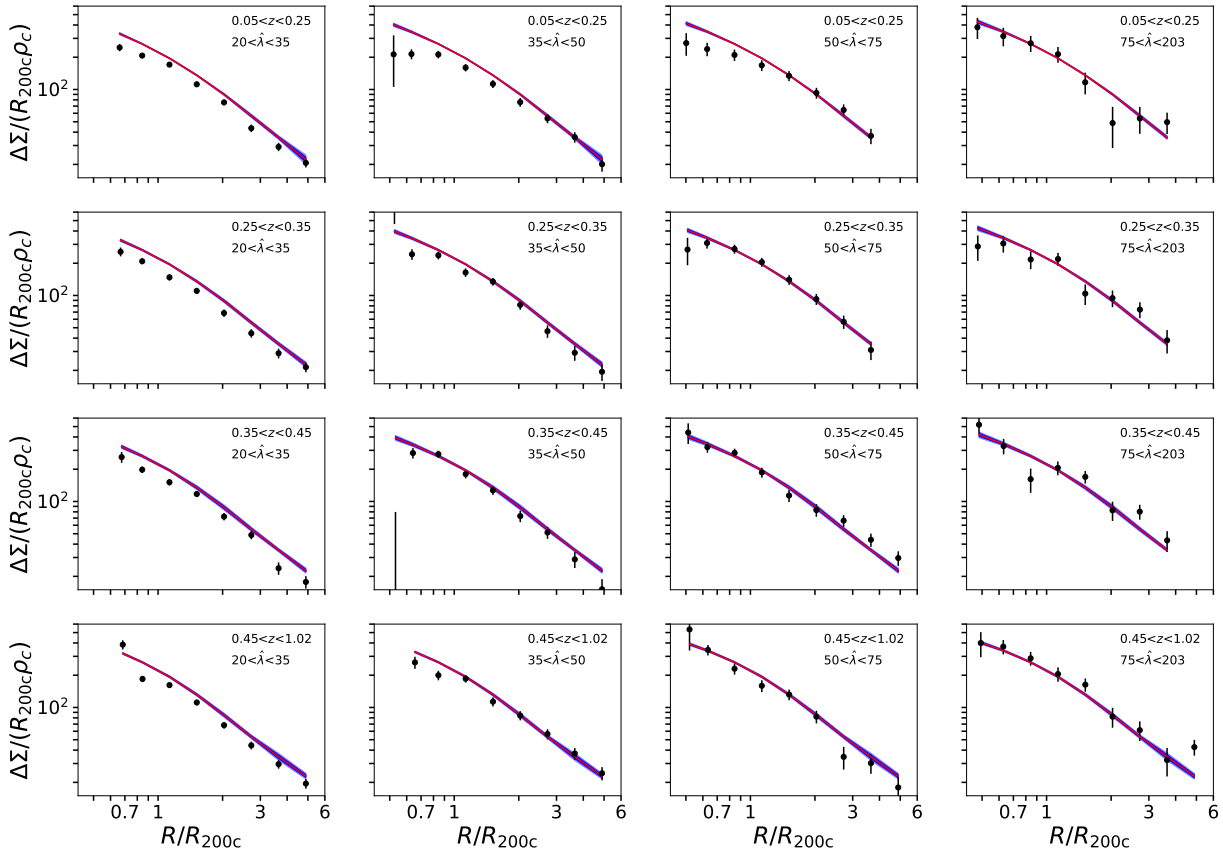

Figure 3.9: Average redMaPPer clusters in 16 $\hat{\lambda} - z$ bins in the rescaled space. The data points are shown in black, while the model is represented by a red line, with the shaded blue regions indicating the 2σ uncertainty region. We use the combined analysis's λ observable-mass relation to calculate R_{200c}. The redMaPPer clusters in the lowest richness bin ($\lambda < 35$) show deviations from the model, suggesting that low-richness redMaPPer clusters behave differently compared to SPT or MARD-Y3 (ICM-selected) clusters.

3.6 Conclusions

In this paper, we calibrate the η-mass and λ-mass observable-mass relations for two MARD-Y3 cluster samples ($\times$ DES Y3 lensing data) corresponding to $f_{\rm cont}$ cuts of 0.05 (97.5% purity) and 0.1 (95% purity). We account for key systematics by marginalizing over the $M_{\rm WL} - M_{200c}$ relation. Additionally, we incorporate statistical errors and selection effects, which are crucial for correcting Eddington and Malmquist biases. We find slightly tighter constraints from the $f_{\rm cont} < 0.1$ sample (due to the increased number of clusters) compared to the $f_{\rm cont} < 0.05$ sample, with the results in good agreement between the two.

To complement the MARD-Y3 cluster sample, which primarily spans low-redshift and low-mass regimes, we incorporate the SPT cluster sample, which occupies the high-redshift and high-mass regions. Both samples share a common observable, MCMF richness. We

perform a combined mass calibration of the two samples using DES Y3 lensing data, simultaneously constraining the ζ-mass, λ-mass, and η-mass observable-mass relations. The shared observable, $\hat{\lambda}$, combined with the wide redshift and mass coverage, enables tight constraints on the λ-mass relation. These tighter constraints on the λ-mass relation help break the degeneracy between ζ and λ, resulting in significantly improved constraints on the ζ-mass relation (compared to the SPT-only analysis). Our constraints on the ζ-mass relation, derived from this multi-wavelength analysis, are the most stringent to date. These results are comparable to, and in good agreement with, the recent cosmological analysis of the SPT cluster sample by Bocquet et al. (2024b).

We study the galaxy cluster matter profiles in the cluster outskirts using the robust mass calibration results derived from this multi-wavelength analysis. To achieve this, we combine all cluster profiles into the self-similar space ($\widetilde{\Delta\Sigma}$ vs. R/R_{200c}) and construct an average matter profile extending out to $\approx 6R/R_{200c}$. We compare this average matter profile to the ΛCDM model predictions constructed using hydrodynamical simulations, *Magneticum* and IllustrisTNG. Our results indicate that the model consistently underpredicts the observed signal in the cluster outskirts at the 4.14σ level.

We use the constraints on the λ-mass relation to discuss its implications for redMaPPer clusters identified in the DES Y3 survey. Given the agreement between the MCMF and redMaPPer richnesses, we apply the MCMF richness-mass relation constraints to the redMaPPer cluster sample to estimate masses. After cross-matching the redMaPPer clusters with the MARD-Y3 and SPT samples and removing overlapping clusters, we analyze the remaining redMaPPer sample. Using DES Y3 lensing data, we create an average matter profile in self-similar space. Our findings reveal that redMaPPer clusters with $20 < \hat{\lambda} < 35$ across $0.05 < z < 1.02$ exhibit behavior distinct from that of MARD-Y3 or SPT clusters with similar richnesses, and they tend to have a lower signal than predicted by our model, suggesting a significant contamination at low richness in the redMaPPer cluster sample.

Our work demonstrates that multi-wavelength mass calibration analyses can place tight constraints on observable-mass relations by leveraging shared observables and breaking degeneracies. Although galaxy cluster abundance analyses have long served as a cornerstone of cosmological constraints, our approach leverages detailed observable-mass information to further enhance the constraining power without requiring larger cluster samples, as demonstrated in Fig. 3.8. This framework is ideally suited for future datasets–such as clusters detected by eROSITA and SPT-3G, coupled with WL data from Euclid and Rubin.

Finally, stronger baryonic feedback and modified gravity provide viable explanations for the enhanced signal observed in cluster outskirts. Stronger feedback, particularly from AGN, can redistribute gas beyond the virial radius, increasing the signal at large radii while suppressing it in the inner regions. At the same time, modified gravity models, such as $f(R)$ gravity and the nDGP model, predict enhanced clustering in the outskirts, deviating from General Relativity. These effects are inherently degenerate, as both can alter the matter distribution. Future high-resolution hydrodynamical simulations with improved feedback prescriptions, combined with precise weak lensing, will be crucial for disentangling these scenarios and determining whether baryonic physics alone can explain the observed deviations or if new physics beyond ΛCDM is required.

Chapter 4

Constraining the baryonic suppression of P(k) using the galaxy cluster ICM mass to halo mass relation

A. Singh, J. J. Mohr, C. T. Davies, S. Bocquet, J. Schaye, V. Springel, I. G. McCarthy, K. Dolag, S. M. L. Vogt, *Soon to be submitted to Astronomy & Astrophysics*

Extracting precise cosmological constraints from cosmic shear observations requires accurate modeling of the non-linear matter power spectrum, which is suppressed at small scales ($k \sim$1 to $10\,h$ Mpc^{-1}) due to baryonic feedback. Various hydrodynamical simulations predict different levels of matter power spectrum suppression based on the type and strength of the feedback mechanisms employed. The intracluster medium (ICM) mass in galaxy clusters is strongly correlated with the cluster halo mass, and this relation— especially the mass dependence of the relation– is sensitive to baryonic feedback processes. While measuring ICM masses $M_{\rm ICM}$ within a specified radius has long been routine using X-ray observations, extracting robust cluster halo masses and their uncertainties using survey weak lensing datasets is relatively new. We constrain the $M_{\rm ICM}$-$M_{\rm 500c}$-z relation using 122 South Pole Telescope (SPT) thermal Sunyaev-Zel'dovich effect (tSZE) selected galaxy clusters with $M_{\rm ICM}$ measurements based on deep observations with the Chandra X-ray Observatory and *XMM-Newton*, along with newly calibrated halo masses $M_{\rm 500c}$ derived using gravitational weak lensing data from the Dark Energy Survey (DES). By comparing the observed cluster relation with the relation extracted from a variety of hydrodynamical simulations that incorporate a range of feedback models, we extract a marginal likelihood for each simulation. We use these marginal likelihoods and the matter power spectrum from each simulation to infer the baryon-suppressed matter power spectrum and its 68% credible interval. This methodology allows us to rule out extreme feedback scenarios with too much or too little feedback. These findings suggest that baryonic suppression alone may not be sufficient to reconcile the differences between cosmological parameters from $z \lesssim 1$ cosmic shear and Planck primary CMB analyses. This approach underscores the usefulness of well-defined galaxy cluster samples with associated deep X-ray observations and survey weak lensing data for constraining baryonic feedback, thereby limiting power spectrum suppression. These results and future analyses with larger samples and improved weak lensing datasets will be essential for obtaining unbiased cosmological constraints and improving our understanding of dark matter with future cosmic shear experiments like those planned with the Euclid mission and the Rubin Observatory.

4.1 Introduction

The standard ΛCDM model has proven effective in describing the Universe across a wide range of redshifts, supported by experiments such as cosmic microwave background data at high redshift (Planck Collaboration et al., 2020) and baryon acoustic oscillation observations at low redshift (Eisenstein et al., 2005). Weak gravitational lensing (WL), the distortions in observed galaxy shapes induced by intervening matter, is sensitive to small scales at low redshift and provides stringent tests of ΛCDM (Li et al., 2023; Abbott et al., 2022b; Dalal et al., 2023). Accurate power spectrum modeling at scales $k \gtrsim 0.1\,h\,{\rm Mpc}^{-1}$ requires understanding the effects of baryons and the non-linear evolution of dark matter due to gravity. Suppression of the matter power spectrum at these scales is tightly corre-

lated with the baryonic fraction, as demonstrated by van Daalen et al. (2020). Physical processes such as Active Galactic Nuclei (AGN), stellar winds, supernova feedback, and gas cooling (van Daalen et al., 2011b) redistribute gas to the outskirts of halos, affecting the non-linear matter power spectrum (Chisari et al., 2019). Our understanding of baryonic feedback physics limits the current precision of cosmic shear analysis (Amon et al., 2022b; Abbott et al., 2023). Cosmic shear surveys tightly constrain the parameter combination $S_8 = \sigma_8(\Omega_\mathrm{m}/0.3)^{0.5}$ but consistently find these values to be lower than those from the primary Planck CMB analysis. This discrepancy has become known as the S_8 tension. A better understanding of baryonic effects and their impact on the matter power spectrum suppression could inform the S_8 tension and indicate the potential need for non-standard dark matter particles (Amon & Efstathiou, 2022; Preston et al., 2023).

Several studies of hydrodynamical simulations have shown that powerful AGN feedback alters the total matter distribution by ejecting baryons beyond the virial region, redistributing gas to the outer regions of halos (McCarthy et al., 2011; Springel et al., 2017). When baryons are ejected from the center of haloes, the gravitational potential at the center decreases, causing dark matter to move into orbits with larger radii. When the baryons cool and re-enter the halo center, the dark matter does not return to its original orbits, even if the potential returns to its prior level, as work has been done by the baryons. This physical process results in the suppression of the matter power spectrum at scales of $0.1 \lesssim k[h\ \mathrm{Mpc}^{-1}] \lesssim 10$, relative to gravity-only simulations. While these simulations successfully reproduce many observed properties of galaxies and galaxy clusters, there remains significant uncertainty regarding the exact scales and amplitudes of suppression in the power spectrum, which vary between simulations due to differences in the modelling of baryons.

Small-scale processes (e.g., AGN feedback) significantly impact galaxy formation, the distribution of baryons, and the suppression of the matter power spectrum. In hydrodynamical simulations, these processes are incorporated through sub-grid physics. To benchmark the simulations and ensure that the sub-grid models are correctly calibrated, X-ray measurements of the hot gas fractions in groups and clusters within the virial radius are widely used (McCarthy et al., 2016; Schaye et al., 2023; Pakmor et al., 2023). The large number of parameters in sub-grid physics, modeling choices, and the choice of box size and resolution lead to significant variation in the suppression of the matter power spectrum (van Daalen et al., 2011b; Schaye et al., 2023; Salcido et al., 2023).

An alternative to running hydrodynamical simulations is the baryon correction model (BCM; Schneider & Teyssier, 2015), which modifies the output of gravity-only simulations in a semi-analytic way to mimic the effects of baryonic feedback. Recent studies have used this method (Schneider et al., 2022; Chen et al., 2023; Aricò et al., 2023a; Grandis et al., 2024b) to constrain BCM model parameters.

The relationships between galaxy cluster observables and their connection to cluster halo masses have been thoroughly investigated using X-ray data over many years. (Mohr & Evrard, 1997; Mohr et al., 1999; Arnaud & Evrard, 1999; Arnaud et al., 2007; Pratt et al., 2009; Mantz et al., 2016; Chiu et al., 2018; Bulbul et al., 2019; Bahar, Y. Emre et al., 2022; Chiu, I-Non et al., 2022). Observations have shown that galaxy clusters display strong

correlations among various X-ray observables. One such relation, which is of particular interest, the relation between the X-ray isophotal size or intracluster medium (ICM) mass and cluster halo mass proxies such as the emission-weighted mean ICM temperature, is sensitive to baryonic feedback. The redistribution of gas due to the enhanced entropy from the feedback reduces the ICM mass in the central area, with a more significant effect in low-mass clusters, thereby increasing the mass dependence of the ICM mass to halo mass relation (Mohr & Evrard, 1997; Mohr et al., 1999). Moreover, the radiative cooling timescales of the ICM across the cluster's virial region are long compared to the cluster's age. Therefore, the ICM mass to halo mass relation offers a rather direct method for constraining the integrated baryonic feedback throughout cosmic time.

Accurate calibration of cluster masses is crucial for precisely determining the relation between the ICM and halo masses. Advances in this field have been significantly supported by high-quality WL datasets from surveys such as the Hyper Suprime-Cam Subaru Strategic Program (HSC-SSP; Miyazaki et al., 2012; Aihara et al., 2018), the Dark Energy Survey (DES; Collaboration, 2005), and the Kilo-Degree Survey (KiDS; de Jong et al., 2012). The availability of large cluster samples extending to high redshifts, facilitated by thermal Sunyaev-Zel'dovich Effect (tSZE; Sunyaev & Zeldovich, 1972) selection using mm-wave surveys like those from the South Pole Telescope (Carlstrom et al., 2011) and the Atacama Cosmology Telescope (Fowler et al., 2007). Additionally, X-ray selection using survey data from missions such as ROSAT (Truemper, 1982) and eROSITA (Predehl et al., 2021; Sunyaev, R. et al., 2021), have underscored the need for more robust and reliable cluster masses. These survey lensing datasets, along with large cluster samples and their associated WL analyses, have been instrumental in refining the calibration of galaxy cluster masses, as highlighted by recent studies (Chiu et al., 2023a; Bocquet et al., 2024b; Grandis et al., 2024b; Ghirardini et al., 2024; Singh et al., 2025).

In this study, we use the galaxy cluster ICM mass and halo mass relation to constrain baryonic feedback. We employ the clusters selected using their tSZE signatures from the SPT survey data. This relation is accurately calibrated through ICM measurements from the Chandra X-ray Observatory and *XMM-Newton*, coupled with precise and accurate weak lensing-calibrated cluster halo masses. We compare this relation with several hydrodynamical simulations that feature varying sub-grid physics, box sizes, and resolutions —FLAMINGO (Schaye et al., 2023), *Magneticum* (Hirschmann et al., 2014; Ragagnin et al., 2017), MillenniumTNG (Pakmor et al., 2023), BAHAMAS (Mantz et al., 2016), and cosmo-OWLS (Le Brun et al., 2014). For each simulation, we calculate the marginal likelihood of the observational data given the simulation. Using these marginal likelihoods as weights, we calculate a weighted average of the total matter power spectrum suppression of the Universe that incorporates all of the available simulations.

The paper is organized as follows: We present the datasets used, including simulated and observed data, in Section 4.2. The ICM to halo mass relation is calibrated in Section 4.3.1. We compare the above-calibrated relation to multiple state-of-the-art simulations in Section 4.3.2. In Section 4.4, we constrain the total matter power spectrum suppression at small scales using the calibrated ICM to halo mass relation and simulations. We compare our results to previous studies in Section 4.5 and provide constraints

on different emulators in Section 4.6. Finally, we discuss implications for dark matter in Section 4.7, and conclude our work in Section 4.8.

Throughout the paper we employ a flat ΛCDM cosmology with the following parameters $\Omega_{\rm m} = 0.315$ (Planck Collaboration et al., 2020), and $h = 0.7$. Unless otherwise specified, all uncertainties are quoted at the 68 percent credible interval. The cluster halo mass M_{500c} is estimated at the overdensity of 500 times the critical density $\rho_{\rm crit}$ at the cluster redshift $z_{\rm cl}$. The cluster radius R_{500c} is calculated using M_{500c}.

4.2 Data

In this section, we describe the cluster sample used in our work and the ICM and cluster mass measurements used to constrain the ICM to halo mass relation. In the last subsection, we summarize all the hydrodynamical simulations used to constrain the suppression of the matter power spectrum.

4.2.1 Cluster ICM mass sample

We use galaxy clusters selected from the SPT-SZ (Bleem et al., 2015; Klein et al., 2023b), SPTpol ECS (Bleem et al., 2020), and SPTpol 500d (Bleem et al., 2024) catalogs, derived from surveys conducted by the SPT collaboration. A subset of 122 clusters from this survey has been observed with the Chandra X-ray Observatory and *XMM-Newton*. This subset, previously analyzed by the SPT collaboration (McDonald et al., 2013, 2014b; Chiu et al., 2018; Bulbul et al., 2019), covers a redshift range from 0.2 to 1.5 and a M_{500c} range from $2.5{\times}10^{14} M_\odot$ to $1.5{\times}10^{15} M_\odot$. These previous analyses extracted an ICM density profile and associated ICM mass, $M_{\rm ICM}(R_{500c})$, from the X-ray observations. The halo radii R_{500c} used for these measurements were derived from a previous mass calibration analysis. That analysis relied on indirect mass estimates from the cluster halo mass function, constrained using a sample of 377 clusters and a weak-lensing-based prior on the observable–mass relations (de Haan et al., 2016). For our analysis, we adopt updated redshift measurements for these clusters as presented in Klein et al. (2023b).

4.2.2 Cluster mass measurement

As noted above, previous studies of the $M_{\rm ICM}$-M_{500c}-z relation with subsets of this sample (Chiu et al., 2016c; Chiu et al., 2018; Bulbul et al., 2019) employed halo masses from the mass calibration analysis by de Haan et al. (2016). This analysis included a sample of 377 SPT-SZ clusters, incorporating X-ray data for 82 clusters and a weak-lensing-based prior for the observable-mass relation. Cluster halo mass posteriors $p(M_{500c}|\hat{\zeta}, z)$ and associated halo radii R_{500c} were derived for each cluster using the resulting constraints on the ζ-M_{500c}-z relation together with the individual measurements of the tSZE signature $\hat{\zeta}$ and redshift z (note that in that paper the tSZE observable is referred to as ξ rather than $\hat{\zeta}$).

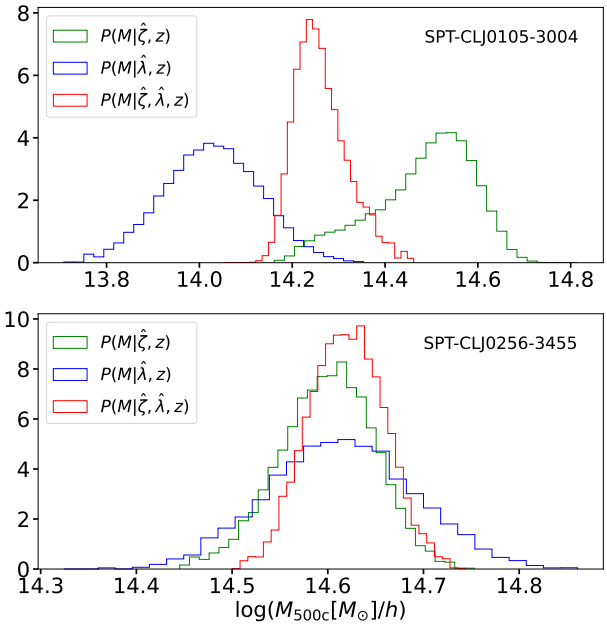

Figure 4.1: Cluster halo mass posteriors for two galaxy clusters (top and bottom), each showing the mass posterior derived from tSZE $\hat{\zeta}$ and redshift (green), optical richness $\hat{\lambda}$ and redshift (blue), and all three observables (red). The posteriors reflect marginalization over the relevant observable-mass relation parameter posterior distributions in all cases.

In this work, we use cluster masses derived purely from WL measurements. Building on the work of Singh et al. (2025), a state-of-the-art WL analysis of DES Y3 data, where we perform a mass calibration of 698 SPT clusters using DES Y3 WL data. The analysis accounts for all significant systematics, resulting in a robust mass calibration. For this study, we perform a mass calibration of a combined sample of 698 clusters identified in SPT-SZ, SPTpol ECS, and SPTpol 500d surveys together with 1433 RASS clusters (Klein et al., 2019b). The merged sample contains ≈2000 galaxy clusters, with redshifts ranging from 0.05 to 0.94. The whole sample overlaps with the DES Y3 survey area, and we have DES-Y3 WL data available for each cluster. Additionally, as all these clusters have been followed up with MCMF (Klein et al., 2018), we have optical richness measurements for all clusters. To summarize, we have access to four observables for each cluster: tSZE/X-ray count rate, optical richness, DES-Y3 WL, and redshift. We use the SPT counterparts for the clusters present in both the SPT and RASS samples. Using multiple observables for mass calibration enhances the accuracy of halo mass estimates and reduces the statistical uncertainty of individual mass estimation. Fig. 4.1 illustrates the mass posterior for two different SPT clusters, showing that using only optical richness or only tSZE yields broader mass constraints (blue and green histograms, respectively), whereas incorporating both observables results in a more precise and tighter mass constraint (red histogram).

The mass calibration constraints from the combined SPT and RASS data, achieved through this multi-observable analysis, offer much tighter constraints on the tSZE observable-

mass relation compared to analysis using only SPT data (see Singh et al., 2025). This improvement is due to better constraints on the shared optical richness, which reduces the degeneracy between optical and tSZE parameters. Our constraints on the tSZE observable-mass relation from the combined analysis (Singh et al., 2025b, in prep.) are the tightest to date and comparable to the most recent cosmological analysis of the same SPT sample that integrates cluster abundance and WL data (Bocquet et al., 2024b).

4.2.3 ICM mass measurement

The ICM mass $M_{\rm ICM}$ of each cluster is estimated by fitting the X-ray surface brightness profile. The detailed procedure for the fitting can be found in Bulbul et al. (2012) and McDonald et al. (2013). In summary, the surface brightness profile is extracted in the energy range of 0.7-2.0 keV out to $1.5R_{\rm 500c}$. The profiles are then further corrected for the spatial variation of the ICM properties as well as the telescope's effective area. Then, the modified β-model (Vikhlinin et al., 2006) is projected along the line of sight to fit the observed surface brightness profile. $M_{\rm ICM}$ is then obtained by integrating the best-fit modified β-model to the radius of $R_{\rm 500c}$.

In this study, we use the $M_{\rm ICM}$ values and their associated measurement uncertainties as listed in Table 2 and Table 3 of Chiu et al. (2018) and Bulbul et al. (2019), respectively. Given that the β value for galaxy clusters is approximately 0.66, indicating $M_{\rm ICM} \propto R_{\rm 500c}$, we update our $M_{\rm ICM}$ values based on our new WL calibrated $R_{\rm 500c}$ values (Singh et al., 2025; Singh et al., 2025b). We note that later in Section 4.3.1 we update $M_{\rm ICM}$ on the fly while marginalizing over the halo mass uncertainties.

4.2.4 Hydrodynamical simulations

In this work, we use $M_{\rm ICM}$ and $M_{\rm 500c}$ measurements along with power spectrum suppression data from various hydrodynamical simulations. These include the *Magneticum* simulation Box2, with a volume of $(352\ {\rm Mpc}/h)^3$ (Hirschmann et al., 2014; Ragagnin et al., 2017), which uses 2×1528^3 dark matter and gas particles with a gas-particle mass of $1.4\times10^8 M_\odot$. The FLAMINGO simulation, with a volume of $(1\ {\rm Gpc})^3$, which employs a gas-particle mass of $10^9 M_\odot$ (Schaye et al., 2023). The BAHAMAS simulation box, with a volume of $(400\ {\rm Mpc}/h)^3$ and $\Theta_{\rm AGN} = 7.6,\ 8.0$, contains 1024^3 dark matter and baryonic particles (McCarthy et al., 2016). The cosmo-OWLS with a $(400\ {\rm Mpc}/h)^3$ box size, containing 2×1024^3 dark matter and baryonic particles with a baryonic particle mass of $6.3\times10^9 M_\odot$ (Le Brun et al., 2014). The MillenniumTNG simulation, with a volume of $(740\ {\rm Mpc})^3$, which has a gas mass resolution of $3.1\times10^7 M_\odot$ (Pakmor et al., 2023). These simulations vary in box size, resolution, strength of baryonic feedback, feedback implementations, and hydrodynamical schemes. The suppression of the total matter power spectrum is sensitive to all of these aspects. Therefore, to ensure the robustness of our analysis, we include a diverse set of simulations that capture these variations.

4.3 $M_{\rm ICM}$-$M_{\rm 500c}$-z relation of the real data, simulations, and their comparison

4.3.1 Updated ICM mass to halo mass relation

We analyze the sample of 122 galaxy clusters to constrain the galaxy cluster $M_{\rm ICM}$-$M_{\rm 500c}$-z relation. We assume that the mean ICM mass $\langle M_{\rm ICM}\rangle$ follows a power law relation with $M_{\rm 500c}$ and $1+z$, and that the intrinsic scatter about this mean relation is log-normal. The relation is then given by

$$\langle M_{\rm ICM}\rangle = {\rm ICM_0}\left(\frac{M_{\rm 500c}}{M_{\rm piv}}\right)^{\rm ICM_M}\left(\frac{1+z}{1+z_{\rm piv}}\right)^{\rm ICM_z}, \tag{4.1}$$

where the parameters $\rm ICM_0$, $\rm ICM_M$, and $\rm ICM_z$ are the normalization, mass trend, and redshift trend, respectively. The pivot mass $M_{\rm piv}$ and redshift $z_{\rm piv}$ are chosen to reflect the median mass and median redshift of our sample, respectively. For this sample $M_{\rm piv} = 6\times10^{14}{\rm M}_\odot$ and $z_{\rm piv} = 0.6$. The intrinsic log-normal scatter in this relation is denoted by $\sigma_{\ln\rm ICM}$.

Since the uncertainty in halo masses is approximately log-normal, the likelihood $P(M_{\rm ICM}|M_{\rm 500c}, z, \vec{p})$ of observing a particular ICM mass $M_{\rm ICM}$ for a cluster with a certain halo mass $M_{\rm 500c}$ and redshift z, given the parameters of the observable-mass relation $\vec{p}$, is described by a log-normal distribution

$$P(M_{\rm ICM}|M_{\rm 500c}, z, \vec{p}) = \frac{1}{\sigma_{\rm tot}\sqrt{2\pi}}\exp\left(-\frac{(\ln M_{\rm ICM} - \ln\langle M_{\rm ICM}\rangle)^2}{2\sigma^2_{\rm tot}}\right), \tag{4.2}$$

where the mean ICM mass $\langle M_{\rm ICM}\rangle$ is calculated using the observable-mass relation (Eq. 4.1) and $\sigma_{\rm tot}$ is the total log-normal scatter, which is given by

$$\sigma^2_{\rm tot} = \sigma^2_{\ln\rm ICM} + \sigma^2_{\ln M_{\rm ICM}} + {\rm ICM^2_M}\sigma^2_{\ln M_{\rm 500c}}, \tag{4.3}$$

where $\sigma_{\ln\rm ICM}$ is the intrinsic scatter about the mean relation, and $\sigma_{\ln M_{\rm ICM}}$ and $\sigma_{\ln M_{\rm 500c}}$ are the measurement uncertainties (stochastic component only) on the ICM and halo masses, respectively. In the last term, the mass trend parameter $\rm ICM_M$ transforms the halo mass uncertainty into an effective ICM mass uncertainty.

In our analysis, we also account for systematic uncertainties in cluster halo masses due to uncertainties in the parameters of the observable-mass relations. We sample 450 sets of parameters from the posterior chains of the observable-mass relations obtained from our mass calibration analysis (Singh et al., 2025b). For each set of observable-mass parameters $\vec{p}_m$, we compute the mass posterior $P(M_{\rm 500c}|\hat{\zeta}, \hat{\lambda}, z, \vec{p}_m)$ for each cluster and adjust our ICM mass measurements $M_{\rm ICM}$ accordingly (see Section 4.2.3). Thereafter, we refit the $M_{\rm ICM}$-$M_{\rm 500c}$-z relation, creating a posterior distribution of relations that reflect

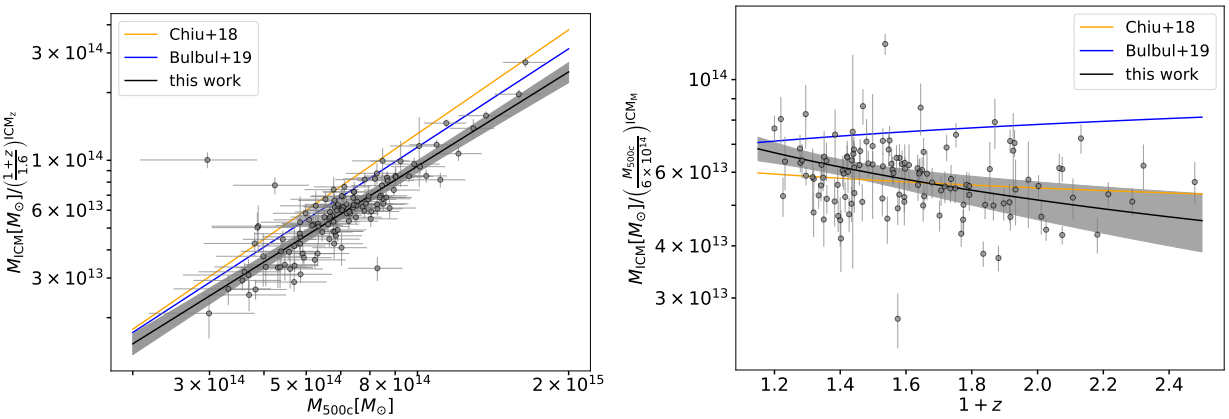

Figure 4.2: Cluster ICM masses as a function of halo masses $M_{\rm 500c}$ and redshift. The y-axis is rescaled so we see only the mass trend (left) and the redshift trend (right). The grey data points represent the tSZE-selected clusters, with error bars indicating measurement errors in ICM and halo mass. The black line is the mean fit to the data, and the grey band represents the 68% credible interval. We compare our results to two previous SPT analyses: Chiu et al. (2018) (orange) and Bulbul et al. (2019) (blue), which use the same X-ray data but halo masses derived from cluster abundance analysis.

the uncertainties in the halo masses arising from the uncertainties in the observable-mass relation parameters.

The $M_{\rm 500c}$ posteriors are derived from the cluster observables as follows (for more detail see Singh et al., 2025)

$$P(M_{\rm 500c}|\hat{\zeta},\hat{\lambda},z,\vec{p}_m) = \frac{\iint {\rm d}\lambda{\rm d}\zeta P(\hat{\lambda}|\lambda)P(\hat{\zeta}|\zeta)P(\zeta,\lambda|M_{\rm 500c},z,\vec{p}_m)P(M_{\rm 500c}|z,\vec{p}_m)}{\iiint {\rm d}M{\rm d}\lambda{\rm d}\zeta P(\hat{\lambda}|\lambda)P(\hat{\zeta}|\zeta)P(\zeta,\lambda|M_{\rm 500c},z,\vec{p}_m)P(M_{\rm 500c}|z,\vec{p}_m)}, \tag{4.4}$$

where quantities with hats are observed, quantities without hats are intrinsic, and $\vec{p}_m$ are the parameters of the observable-mass relations. The last factor in the numerator and denominator is the halo mass function, which is cosmology-dependent. Importantly, our framework, described by Eq. 4.4, accounts for both Malmquist and Eddington biases.

We repeat our likelihood analysis (Eq. 4.2) 450 times, corresponding to 450 sets of observable-mass relation parameters. The final parameter values and errors of the $M_{\rm ICM}$-$M_{\rm 500c}$-z relation are calculated using posterior distributions from all 450 iterations. Table 4.1 shows the mean and 68% credible interval of the $M_{\rm ICM}$-$M_{\rm 500c}$-z mass relation parameters.

Fig. 4.2 shows the relationship between the observed ICM mass and halo mass (left panel) and the ICM mass and redshift (right panel). The data points are shown as grey dots, with error bars indicating the measurement uncertainties. The black line represents the mean fit to the data points, while the grey shaded region denotes the 68% credible interval. We compare our fit to the relations from previous works: Chiu et al. (2018)

Table 4.1: Mean parameter posteriors and 68% credible intervals for the ICM to halo mass relation

Parameter	Description	Posterior
ICM_0	normalization	$5.77\times10^{13} \pm 3.25\times10^{12}$
ICM_M	mass trend	1.208 ± 0.075
ICM_z	redshift trend	-0.514 ± 0.258
$\sigma_{\ln \mathrm{ICM}}$	intrinsic scatter	0.055 ± 0.036

(orange line) and Bulbul et al. (2019) (blue line), both of which analyzed a subset of this sample. Our mass trend yields a less steep value than both studies but remains consistent with their results, and it is approximately 3σ away from the self-similar expectation of 1. Similarly, the redshift trend is slightly shallower than previous studies but remains consistent with zero. We emphasize that there is an overall shift in the amplitude of the relation compared to earlier works. This shift arises because our new halo mass constraints are, on average, ≈18% larger than the previous mass constraints from de Haan et al. (2016), which relied primarily on cluster abundance to calibrate masses. In contrast, our mass constraints are purely based on WL.

4.3.2 Comparing the ICM mass to halo mass relation with simulations

As described in Section 4.2.4, we compare our measured relation with several state-of-the-art simulations. Since each simulation is based on different cosmological parameters and our mass calibration was performed assuming the Planck Collaboration et al. (2020) cosmology, we must account for these differences, as ICM mass measurements depend on the baryonic fraction of the Universe. The ICM mass in simulations scales with $f_b^{0.7}$ (Singh et al., 2020), where $f_b = \frac{\Omega_\mathrm{b}}{\Omega_\mathrm{m}}$. Therefore, for any simulation with a baryonic fraction $f_{b,\mathrm{SIM}}$, the ICM mass at Planck cosmology is computed as

$$M_{\mathrm{ICM,Planck}} = M_{\mathrm{ICM,SIM}} \left(\frac{f_{b,\mathrm{Planck}}}{f_{b,\mathrm{SIM}}} \right)^{0.7} . \tag{4.5}$$

We note that a fixed cosmology is assumed while constraining the matter power spectrum of the Universe. This assumption is expected to have a negligible impact on the analysis, given the small uncertainties in the Planck measurements of Ω_m and Ω_b. Fig. 4.3 compares the observed mass trend of M_ICM-M_500c-z relation to several simulations. The observed data points are shown in grey, and the black line represents the mean fit to the data. MTNG ($z = 0.5$), BAHAMAS ($\Theta_\mathrm{AGN} = 8.0$, $z = 0$), C-OWLS ($\Theta_\mathrm{AGN} = 8.7$, $z = 0$), FLAMINGO (strongest, $z = 0.6$), and Magneticum ($z = 0.56$) are shown in blue, orange, green, red, and purple, respectively. ICM mass measurements in each of the simulations are adjusted to Planck cosmology.

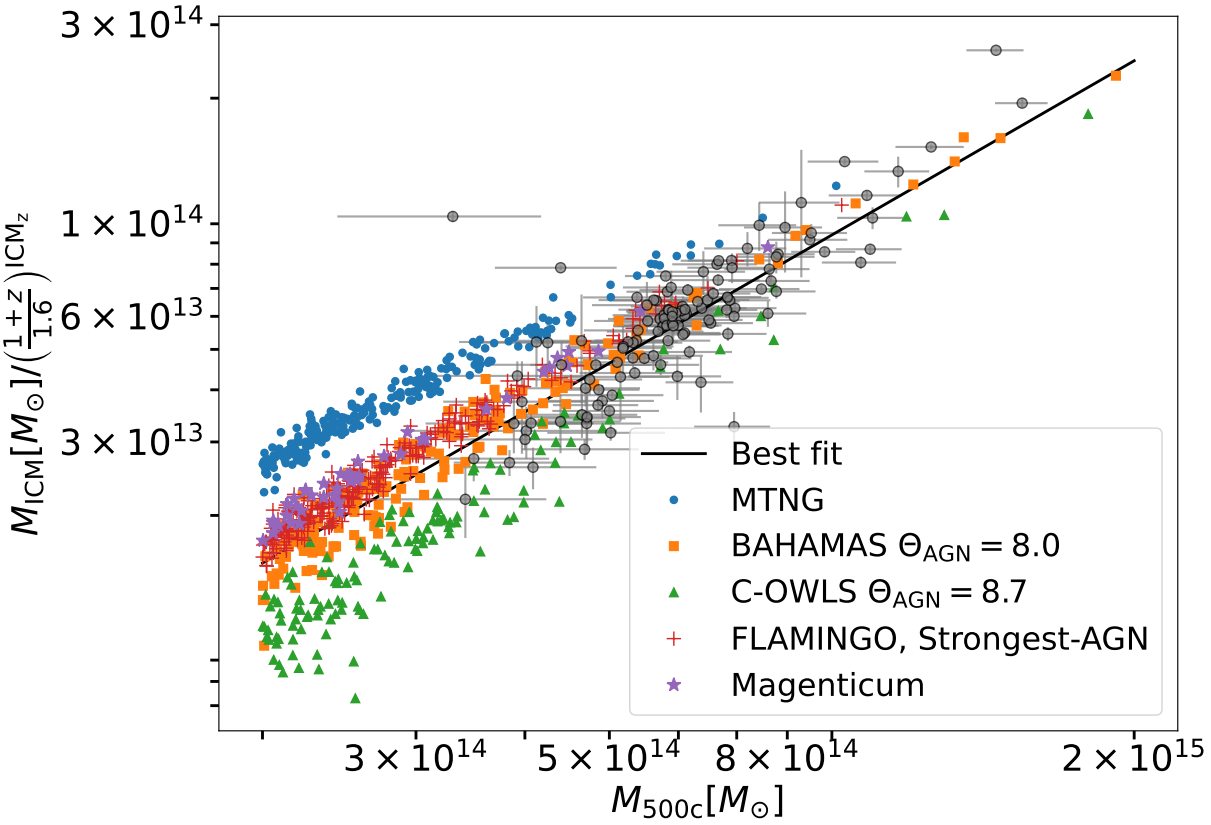

Figure 4.3: Comparison of the observed ICM to halo mass relation (grey data points) to a subset of the simulations. The mean fit for the SPT sample is shown as the black line. The ICM masses in the simulations are adjusted (using Eq. 4.5) to the Planck cosmology. MTNG ($z = 0.5$), BAHAMAS ($\Theta_{\rm AGN} = 8.0$, $z = 0$), C-OWLS ($\Theta_{\rm AGN} = 8.7$, $z = 0$), FLAMINGO (strongest, $z = 0.6$), and Magneticum ($z = 0.56$) are shown in blue, orange, green, red, and purple, respectively.

To quantitatively compare our relation with simulations, we fit a power-law relation with scatter to each simulation. For this, we use Eq. 4.1 and Eq. 4.2 and set $\sigma^2_{\rm tot} = \sigma^2_{\ln {\rm ICM}}$, as the measurement uncertainty is zero in simulations. We use multiple snapshots within the redshift range of 0 to 1.25 and select clusters with masses greater than $M_{\rm 500c} > 2 \times 10^{14} M_\odot$ to match the redshift and mass range of the SPT sample. Table 4.2 summarizes the fitting results for each simulation.

Table 4.2: Mean parameter posteriors and 68% credible intervals for the ICM to halo mass relations derived from simulations. The ICM_z parameter is set to zero for C-OWLS and BAHAMAS since only redshift-zero data is available for these simulations.

Simulation	$\mathrm{ICM}_0(10^{13}M_\odot)$	ICM_M	ICM_z	$\sigma_{\ln \mathrm{ICM}}$
MilleniumTNG	8.27 ± 0.04	1.03 ±0.06	-0.0487 ± 0.0164	0.0536 ± 0.0014
Magneticum	6.70 ± 0.10	1.16 ± 0.01	0.259 ± 0.040	0.0628 ± 0.0037
C-OWLS AGN	5.99 ± 0.06	1.06 ± 0.01	0.0	0.072 ± 0.004
C-OWLS ($\Theta_{\mathrm{AGN}} = 8.5$)	6.10 ± 0.10	1.27 ± 0.02	0.0	0.010 ± 0.006
C-OWLS ($\Theta_{\mathrm{AGN}} = 8.7$)	4.49 ± 0.14	1.36 ± 0.04	0.0	0.157 ± 0.010
BAHAMAS AGN	6.90 ± 0.07	1.15 ± 0.01	0.0	0.082 ± 0.004
BAHAMAS ($\Theta_{\mathrm{AGN}} = 7.6$)	7.13 ± 0.07	1.10 ± 0.01	0.0	0.077 ± 0.003
BAHAMAS ($\Theta_{\mathrm{AGN}} = 8.0$)	6.19 ± 0.09	1.27 ± 0.02	0.0	0.115 ± 0.006
FLAMINGO (weak)	7.34 ± 0.01	1.079 ± 0.002	0.0315 ± 0.0037	0.0450 ± 0.0005
FLAMINGO (fiducial)	7.343 ± 0.001	1.107 ± 0.002	0.0650 ± 0.0044	0.0515 ± 0.0006
FLAMINGO (strong)	7.24 ± 0.02	1.144 ± 0.002	0.103 ± 0.050	0.0603 ± 0.0006
FLAMINGO (stronger)	7.09 ± 0.02	1.185 ± 0.003	0.134 ± 0.006	0.0691 ± 0.0008
FLAMINGO (strongest)	6.77 ± 0.03	1.264 ± 0.004	0.195 ± 0.008	0.0858 ± 0.0010
FLAMINGO (strong supernova)	7.48 ± 0.01	1.116 ± 0.002	0.0623 ± 0.0044	0.0521 ± 0.0006
FLAMINGO (stronger AGN strong supernova)	7.20 ± 0.02	1.185 ± 0.003	0.104 ± 0.059	0.0661 ± 0.0007
FLAMINGO (strong jets)	6.94 ± 0.03	1.186 ± 0.004	0.121 ± 0.007	0.0869 ± 0.0010

Next, we calculate the likelihood of the data given the simulation. The likelihood $P(\vec{D}|\mathcal{M}_{\rm SIM}, \vec{p}_{\rm SIM}, \vec{p}_m)$ is assumed to be a log-normal distribution and takes a form similar to Eq. 4.2, which is given by

$$\begin{aligned} &P(\vec{D}|\mathcal{M}_{\rm SIM}, \vec{p}_{\rm SIM}, \vec{p}_m) = \\ &\frac{1}{\sigma_{\rm tot}\sqrt{2\pi}} \exp\left(-\frac{(\ln M_{\rm ICM} - \ln M_{\rm ICM,SIM})^2}{2\sigma^2_{\rm tot}}\right), \\ &\sigma^2_{\rm tot} = \sigma^2_{\ln {\rm ICM,SIM}} + \sigma^2_{\ln M_{\rm ICM}} + {\rm ICM}^2_{\rm M,SIM}\sigma^2_{\ln M_{\rm 500c}}. \end{aligned} \tag{4.6}$$

Here $\vec{p}_{\rm SIM}$ represents the power-law relation parameters for a given simulation (Table 4.2), and the $M_{\rm ICM,SIM}$ is calculated using Eq. 4.1 with $\vec{p}_{\rm SIM}$. $\vec{p}_m$ are the parameters of the observable-mass relations, as defined earlier in Eq. 4.4. Similar to the analysis of the SPT sample, we account for both statistical and systematic uncertainties in halo masses and marginalize over them using the procedure detailed in Section 4.3.1. Additionally, we account for the small uncertainties in the ICM to halo mass relation within the simulations by applying Gaussian priors to the parameters, as provided in Table 4.2. The resulting marginalized likelihood is given by

$$\begin{aligned} \mathcal{L}_{\rm marg} = \iint P(\vec{D}|\mathcal{M}_{\rm SIM}, &\vec{p}_{\rm SIM}, \vec{p}_m) P(\vec{p}_{\rm SIM}) \\ &P(\vec{p}_m) d\vec{p}_{\rm SIM} d\vec{p}_m \end{aligned} \tag{4.7}$$

We also compute the marginal likelihood associated with the mean fit and normalize all marginal likelihoods $\mathcal{L}_{\rm marg}$ using it. The resulting normalized marginal log-likelihoods ($\ln\mathcal{L}_{\rm marg-norm}$) for each simulation are presented in Table 4.3. The $\ln\mathcal{L}_{\rm marg-norm}$ value for MTNG is significantly smaller than zero, indicating that the observational data disfavour it. Similarly, the weak and fiducial feedback scenarios in the FLAMINGO simulations are also disfavored. Instead, our observations show a preference for higher feedback scenarios, such as FLAMINGO-strongest, FLAMINGO-strong-jets, BAHAMAS ($\Theta_{\rm AGN} = 8.0$), and C-OWLS AGN.

4.4 Constraints on power spectrum suppression at small scales

The magnitude and type of baryonic feedback influence the suppression of the matter power spectrum at small scales. This feedback also redistributes gas from the center to the outskirts of galaxy clusters. It has a stronger impact on low-mass clusters than high-mass clusters, thereby affecting the slope ${\rm ICM_M}$ of the $M_{\rm ICM}$-$M_{\rm 500c}$-z relation. Since feedback modifies the $M_{\rm ICM}$-$M_{\rm 500c}$-z relation, we can use constraints on this relation to estimate the extent and amplitude of the power spectrum suppression. We test this using the available simulations. First, we measure the amount of suppression in the matter

Table 4.3: Normalized marginal log-likelihood of the SPT sample given the simulations

Simulation	$\ln\mathcal{L}_{\rm marg-norm}$
MilleniumTNG	-46.38
Magneticum	-3.84
C-OWLS AGN	-1.73
C-OWLS ($\Theta_{\rm AGN} = 8.5$)	-1.78
C-OWLS ($\Theta_{\rm AGN} = 8.7$)	-31.95
BAHAMAS AGN	-4.65
BAHAMAS ($\Theta_{\rm AGN} = 7.6$)	-9.76
BAHAMAS ($\Theta_{\rm AGN} = 8.0$)	-2.63
FLAMINGO (weak)	-14.81
FLAMINGO (fiducial)	-14.17
FLAMINGO (strong)	-12.31
FLAMINGO (stronger)	-7.44
FLAMINGO (strongest)	-4.68
FLAMINGO (strong supernova)	-16.10
FLAMINGO (stronger AGN strong supernova)	-9.99
FLAMINGO (strong jets published)	-5.08

power spectrum ($P_{\rm hydro}/P_{\rm gravity-only}$) for each simulation at a particular k value. We then plot the suppression from all simulations at a given k against the $\rm ICM_M$ (as calculated in Section 4.3.2) of each simulation. Fig. 4.4 shows the suppression of the matter power spectrum at $k = 2h$ Mpc^{-1} as a function of the mass trend of the $M_{\rm ICM}$-$M_{\rm 500c}$-z relation ($\rm ICM_M$) for 14 different simulation feedback scenarios (Fig. B.2 shows the same relation at 9 different k values). Generally, there is a correlation between suppression and mass trend, with stronger feedback resulting in greater suppression.

The amount of suppression also correlates with $\rm ICM_0$ and $\sigma_{\ln \rm ICM}$, though this correlation is weaker than with $\rm ICM_M$. Since feedback influences the mass trend and we can effectively constrain this slope ($\rm ICM_M$) through observations, we marginalize over the allowed range of mass trends while calculating the suppression caused by baryonic feedback. We calculate the suppresion in $P(k)$ in four steps:

1. We first fit a linear function to the suppression of the matter power spectrum as a function of $\rm ICM_M$ (the orange line in Fig. 4.4 illustrates the mean fit at $k = 2\,h$ Mpc^{-1}) at a given k. We account for the uncertainties in $\rm ICM_M$ during the fitting process. This procedure is repeated for each available k value within the $0.1 < k[h\ \text{Mpc}^{-1}] < 10$ range. This analysis allows us to calculate the suppression of the matter power spectrum for a given $\rm ICM_M$ value across the k range of $0.1 < k[h\ \text{Mpc}^{-1}] < 10$.

2. We next fit a second-degree polynomial to the marginal log-likelihoods, $\ln\mathcal{L}_{\rm marg}$ (as derived in Section 4.3.2), as a function of $\rm ICM_M$, as shown in Fig. B.1. We account

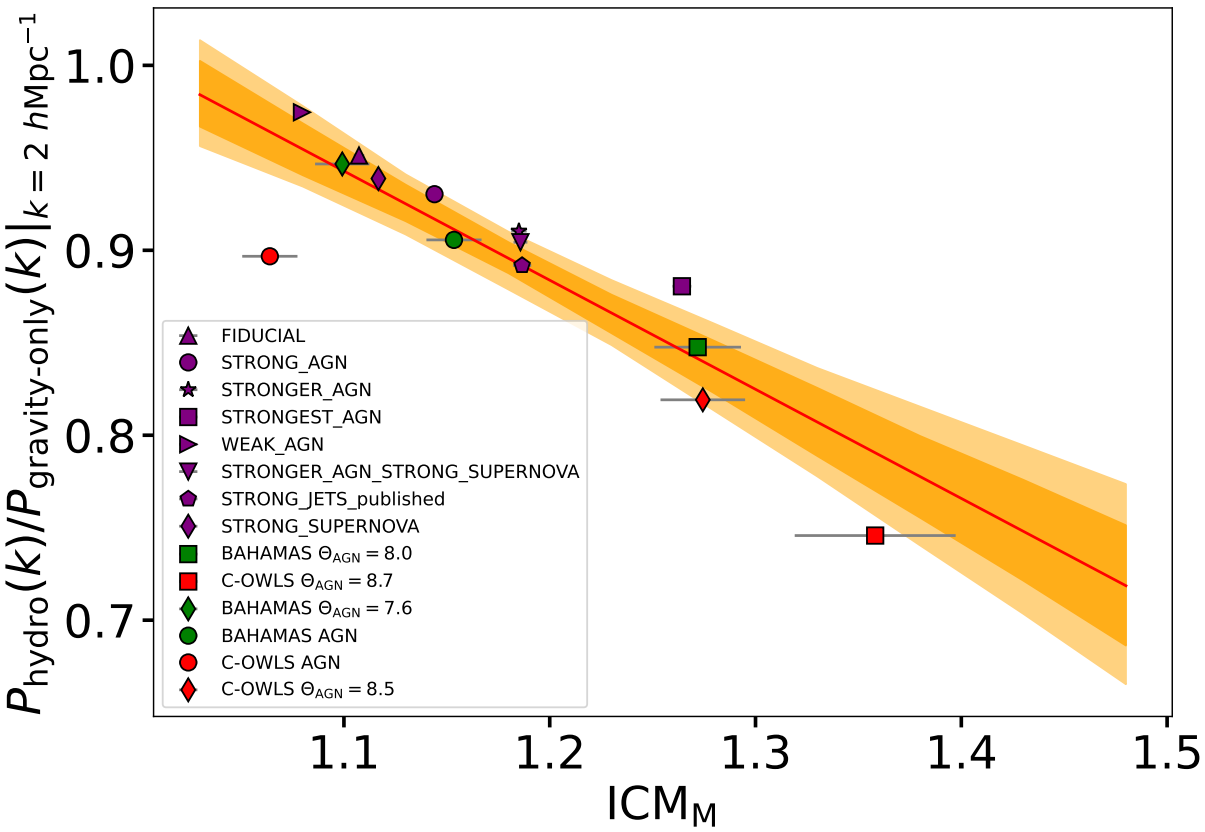

Figure 4.4: Suppression of the matter power spectrum ($z = 0$) at $k = 2\,h$ Mpc^{-1} as a function of the mass trend of the $M_{\rm ICM}$-$M_{\rm 500c}$-z relation for 14 different simulations, as listed in the legend. The orange line shows the mean fit to the relation, and the dark and light orange shaded regions represent the 68% and 95% credible intervals, respectively.

for the uncertainties in both $\ln\mathcal{L}_{\rm marg}$ and ICM$_{\rm M}$ values during the fitting process. The red line and shaded region in Fig. B.1 represent the mean-fit and the 68% credible interval, respectively. These $\ln\mathcal{L}_{\rm marg}$ values serve as weights in our analysis.

3. Given that we can now calculate the amount of suppression and its corresponding weight as a function of ICM$_{\rm M}$, we marginalize over the allowed range of ICM$_{\rm M}$ (inferred from real data; see Table 4.1) to calculate the allowed suppression region. For this, we sample 1,000 values of ICM$_{\rm M}$ from the allowed region and compute $\mathcal{L}_{\rm marg}$ at these ICM$_{\rm M}$ values using the fitted function from step 2. For each of these ICM$_{\rm M}$ values, we also compute the suppression of the matter power spectrum using the fitted function obtained in step 1. This process is repeated for each k value.

4. Using the $\mathcal{L}_{\rm marg}$ values as weights, we determine the weighted suppression of the matter power spectrum at a given k, along with its associated error. Finally, we repeat this analysis across various k values ranging from 0.1 to 10 h Mpc^{-1}. We note that our weights are a function of the mass slope, so the suppression at each k is

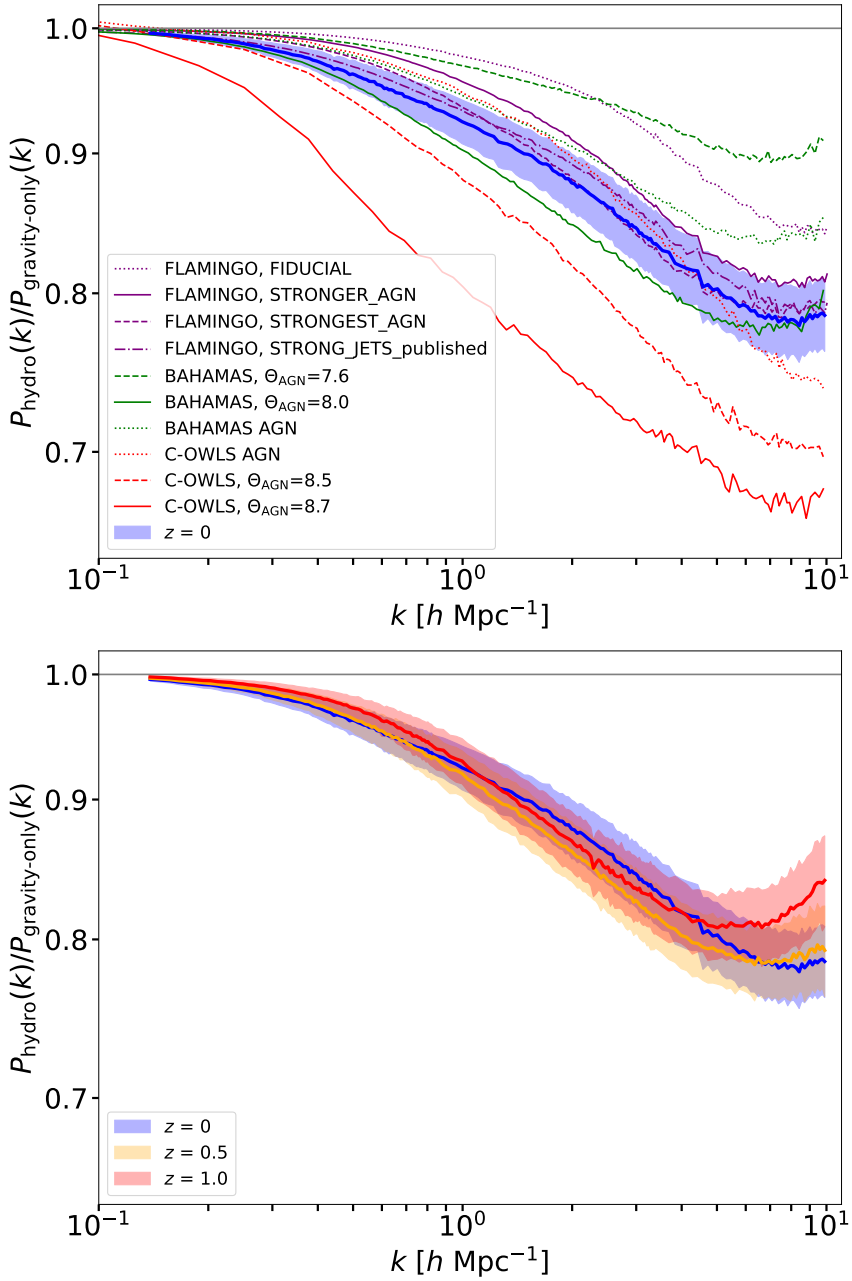

Figure 4.5: Power spectrum suppression from baryonic effects. The top figure shows the power spectrum suppression at $z = 0$, inferred from the cluster $M_{\rm ICM}$-$M_{\rm 500c}$-z relation using numerical simulations, is shown (blue line), with the 68% credible interval represented by the blue band. The red, green, and purple lines show the suppression in specific C-OWLS, BAHAMAS, and FLAMINGO simulations. In the bottom figure, we also compare the power spectrum suppression constrained at redshifts of 0.5 (orange) and 1 (red). The shaded regions represent 68% credible intervals.

weighted using the same set of weights.

We note that we account for the error in the fit of $\mathrm{ICM_M}$ with the power spectrum suppression and the marginal log-likelihood as shown in orange and red shaded regions in Fig. 4.4 and Fig. B.1, respectively. Additionally, we note that the set of simulations used in our analysis spans the 2σ observational constraint on $\mathrm{ICM_M}$ (see Fig. B.1), making it possible to marginalize over this constraint.

The solid blue line in Fig. 4.5 (top panel) shows the constraints on the suppression of the matter power spectrum at $z = 0$. The blue region represents the 68% credible interval. We compare our constraints with C-OWLS, BAHAMAS, and FLAMINGO simulations, represented by the red, green, and purple lines, respectively, in the top panel of Fig. 4.5. Different line styles show different feedback strength/physics within a simulation. FLAMINGO-strongest, FLAMINGO-strong-jets, C-OWLS AGN, and BAHAMAS ($\Theta_{\mathrm{AGN}} = 8.0$) models all agree with our findings within the 1σ region. C-OWLS ($\Theta_{\mathrm{AGN}} = 8.7$), FLAMINGO-fiducial, and BAHAMAS ($\Theta_{\mathrm{AGN}} = 7.6$) are disfavored. In the bottom panel of Fig. 4.5, we compare our constraints on the matter power spectrum suppression at redshifts of $z = 0$, $z = 0.5$, and $z = 1$. We do not find any significant evolution of suppression with redshifts, although at high redshifts, the suppression at $k < 1\,h\,\mathrm{Mpc}^{-1}$ appears smaller than at low redshifts.

4.5 Comparison to previous works

We compare our results with the SP(k) emulator, an empirical model trained on the ANTILLES suite of 400 cosmological hydrodynamical simulations that span a wide range of baryon feedback scenarios (Salcido et al., 2023). The emulator provides predictions of matter power spectrum suppression with an accuracy of approximately 2% for scales up to $k \lesssim 10h\mathrm{Mpc}^{-1}$ and redshifts up to $z = 3$. SP(k) predicts the suppression based on a given baryonic fraction to halo mass relation, which is expressed as:

$$f_b/(\Omega_\mathrm{b}/\Omega_\mathrm{m}) = \left(\frac{e^\alpha}{100}\right)\left(\frac{M_{500\mathrm{c}}}{10^{14}M_\odot}\right)^{\beta-1}\left(\frac{E(z)}{E(0.3)}\right)^\gamma, \tag{4.8}$$

where α sets the power-law normalization, β sets the power-law trend, γ provides the redshift dependence and $E(z)$ is the dimensionless Hubble parameter. f_b is the baryonic fraction measured within $R_{500\mathrm{c}}$.

We assume a Planck cosmology and set $f_b \approx f_{\mathrm{ICM}}/0.94$, where the factor 0.94 accounts for the stellar mass fraction (Chiu et al., 2018), which is assumed to remain constant in our analysis. We fit Eq. 4.8 to the real data (Section 4.2) and infer posterior distributions for the free parameters α, β, and γ. Using the SP(k) emulator and the posterior distributions for the free parameters, we calculate the mean power spectrum suppression and the corresponding 68% credible interval as shown in Fig. 4.6. The SP(k) emulator results are consistent with our constraints at $< 1\sigma$ level but tend to show slightly greater suppression at low k values and slightly smaller suppression at high k values.

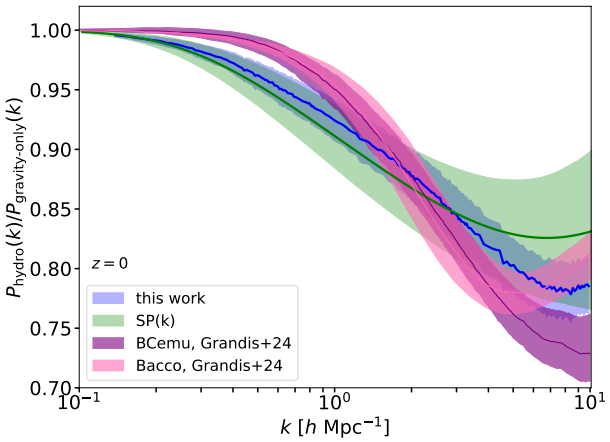

Figure 4.6: Comparison of the baryonic suppression of the power spectrum from our analysis (blue region) to other recent results. The green region shows the suppression of the matter power spectrum inferred using the SP(k) emulator, adopting the same cluster ICM and halo mass measurements used in our analysis. The pink and purple regions show constraints from the Bacco and BCemu models, respectively, as reported in Grandis et al. (2024a). The shaded region in all cases represents the 68% credible interval.

Although SP(k) is trained on a range of model parameters, the underlying simulation and sub-grid models themselves are not varied. Therefore, we expect the constraints from SP(k) to complement those from our main analysis. However, it is important to note that the SP(k) constraints are conditional on a single hydrodynamical model, while our main analysis marginalizes over a wide range of fully independent simulations and hydrodynamical models, appropriately weighted using the real $M_{\rm ICM}$-$M_{\rm 500c}$-z relation.

We also compare our findings with the constraints on the BCemu and bacco models as presented by Grandis et al. (2024a), which are based on semi-analytical baryonification models (Schneider & Teyssier, 2015). Grandis et al. (2024a) used gas density profiles from galaxy clusters and groups to constrain these models. The 68% credible intervals from their analysis are shown in Fig. 4.6 as pink (bacco) and purple (BCemu) shaded regions, with the solid lines representing the mean suppression. At low k values, our inferred suppression is approximately 2σ higher than their results. However, at higher k values, our findings generally agree.

4.6 Calibration of semi-analytical P(k) models

Accurately modeling the impact of baryonic physics on the matter power spectrum is crucial for interpreting large-scale structure observations. Semi-analytical models provide computationally efficient alternatives to full hydrodynamical simulations by parameterizing the effects of baryonic feedback. In this section, we calibrate two models- the HMcode2020 (HM20) and BCemu- against our inferred power spectrum suppression. HM20 models baryonic feedback as a function of AGN heating temperature, while BCemu modifies N-

Table 4.4: Priors and posteriors for the HM20 and BCemu models. For the posterior, we report the mean and 68% credible interval for the well-constrained parameters.

Parameters	Prior	Posterior
HM20		
$\Theta_{\rm AGN}$	$\mathcal{U}(7.3, 9)$	7.95 ± 0.07
BCemu		
$\log_{10}(M_c h/M_\odot)$	$\mathcal{U}(11, 15)$	12.70 ± 0.66
μ	$\mathcal{U}(0, 2)$	$0.66^{+0.18}_{-0.50}$
$\theta_{\rm ej}$	$\mathcal{U}(2, 8)$	$5.30^{+2.0}_{-1.3}$
γ	$\mathcal{U}(1, 4)$	–
δ	$\mathcal{U}(3, 11)$	$7.30^{+1.70}_{-2.10}$
η	$\mathcal{U}(0.05, 0.4)$	–
$\delta\eta$	$\mathcal{U}(0.05, 0.4)$	–

body simulations using physically motivated baryonification techniques. By fitting these models to our constraints, we refine key feedback parameters and assess their consistency with recent studies.

4.6.1 Halo-model: HM20

The HMcode2020 (HM20) models the non-linear power spectrum as a function of a free parameter, $\Theta_{\rm AGN} = \log_{10}(T_{\rm AGN}/{\rm K})$, which modulates the amount of baryonic feedback from AGN (Mead et al., 2021). This parameter scales the halo concentration and the stellar and gas content, resulting in modifications to the overall amplitude and shape of the 'one-halo' term in the halo model. The HM20 model is calibrated to match the power spectrum' response' from the BAHAMAS hydrodynamical simulations (McCarthy et al., 2016; van Daalen et al., 2020) within a $\Theta_{\rm AGN}$ range of 7.6–8.0.

We use the power spectrum suppression inferred in Section 4.4 and fit it using the HM20 emulator, employing a wider prior range on $\Theta_{\rm AGN} = [7.3, 9]$, which allows for more extreme feedback scenarios. We obtain a best-fit value of $\Theta_{\rm AGN} = 7.95$ (Table 4.4), suggesting that our inference prefers slightly less feedback than the BAHAMAS $\Theta_{\rm AGN} = 8.0$ model. This is consistent, as the $\Theta_{\rm AGN} = 8.0$ model causes slightly greater suppression than our constraints (see Fig. 4.5).

4.6.2 Analytical N-body simulation model: BCemu

BCemu is based on the baryonification method proposed by Schneider & Teyssier (2015), which provides a framework for modifying N-body gravity-only simulations to account for baryons and their feedback. This method uses physically motivated profiles around halo centers, introducing small perturbations to simulation particles to mimic the feedback effects. The final baryonified profiles consist of three components: the central galaxy, gas, and

collisionless matter. Collisionless matter primarily includes dark matter but also contains satellite galaxies and stars. Giri & Schneider (2021) provides the density parametrization for gas and stars. The distribution of gas in the halo is parameterized by a cored double-power law of the form

$$\rho_{\rm gas}(r) \propto \frac{\Omega_{\rm b}/\Omega_{\rm m} - f_{\rm star}(M)}{\left(1+10\left(\frac{r}{r_{\rm vir}}\right)\right)^{\beta(M)}\left(1+\left(\frac{r}{\theta_{\rm ej}r_{\rm vir}}\right)^{\gamma}\right)^{\frac{\delta-\beta(M)}{\gamma}}}, \tag{4.9}$$

where $r_{\rm vir}$ is the viral radius, M is the halo mass, $\Omega_{\rm m}$ and $\Omega_{\rm b}$ are the matter and baryon densities of the universe. The β parameter depends on the halo mass and is given by

$$\beta(M) = \frac{3\,(M/M_c)^{\mu}}{1+(M/M_c)^{\mu}}. \tag{4.10}$$

The stellar fraction in satellite galaxies and the fraction of stars in the central galaxy are each modeled by a power-law equation

$$f_i(M) = 0.055\left(\frac{M}{M_s}\right)^{-\eta_i}, \tag{4.11}$$

where $i = \{\rm sga, cga\}$, $M_s = 2.5\times10^{11}M_\odot/h$, with trends $\eta_{\rm sga} = \eta$ and $\eta_{\rm cga} = \eta + \delta\eta$. The BCemu model includes 7 free parameters $(\log_{10}(M_c h/M_\odot), \mu, \theta_{\rm ej}, \gamma, \delta, \eta, \delta\eta)$ that control the gas and star profiles. Given this set of parameters, which determines the amount of feedback, BCemu provides a power spectrum suppression. We use the inferred power spectrum suppression from Section 4.4 to fit the BCemu emulator and constrain the free parameters. These constraints are summarized in Table 4.4, and a contour plot showing the posterior distribution is provided in Fig. B.3. We constrain $\log_{10}(M_c h/M_\odot)$, μ, $\theta_{\rm ej}$, and δ. Our constraint on $\log_{10}(M_c h/M_\odot)$ is $\approx 2\sigma$ lower than that of Grandis et al. (2024a), but the remaining three parameters are in 1σ agreement with their recent analysis.

4.7 Implications for Dark Matter

We compare our constraints on the suppression of the matter power spectrum at small scales, derived from the galaxy cluster $M_{\rm ICM}$-$M_{\rm 500c}$-z relation, with the analyses conducted by Amon & Efstathiou (2022) and Preston et al. (2023) at redshift $z = 0$. Their studies indicate that significant suppression of the matter power spectrum is necessary at scales of $0.2 < k[h\ {\rm Mpc}^{-1}] < 1$ to reconcile the differences between cosmological parameters inferred from cosmic shear analyses (from DES Y3 and KiDS) and the Planck primary CMB results, as shown in the red and orange regions of Fig 4.7 (left panel). Our constraints on the suppression of the matter power spectrum due to baryons (blue region in the left panel of Fig. 4.7) lie above the inferred suppression from the KiDS and DES analyses at scales of $0.2 < k[h\ {\rm Mpc}^{-1}] < 0.8$. This suggests that baryonic suppression alone may not

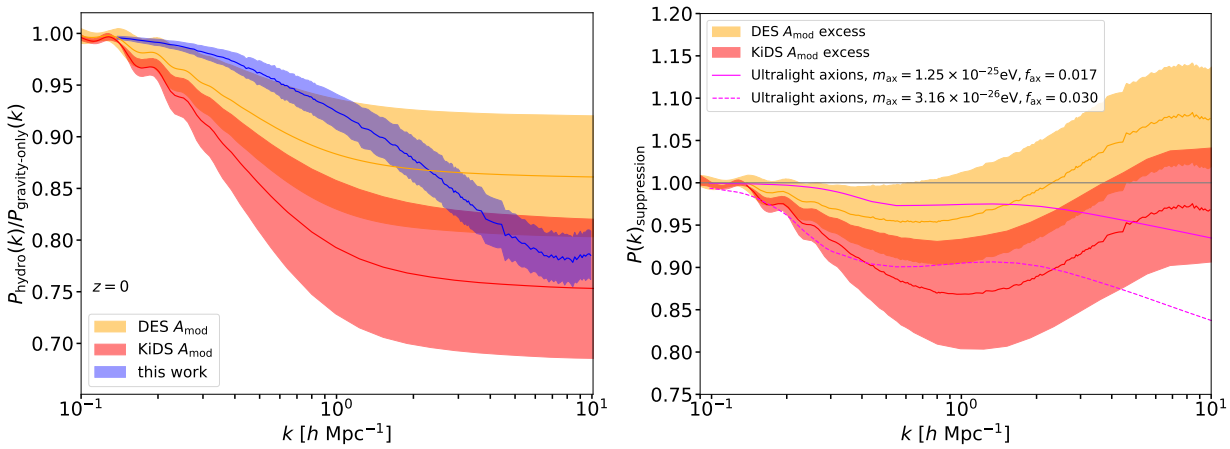

Figure 4.7: The left figure compares the suppression of the matter power spectrum at $z = 0$ due to baryonic effects, as constrained using the cluster $M_{\rm ICM}$-$M_{\rm 500c}$-z relation (blue), with the suppression needed to explain the S_8 tension between Planck and KiDS (red; Amon & Efstathiou, 2022) and that needed to explain the smaller S_8 tension between Planck and DES Y3 (yellow; Preston et al., 2023). The shaded regions represent 68% credible intervals. The right figure shows the estimate of the non-baryonic suppression of the power spectrum required to explain the S_8 tension in DES (orange) and KiDS (red). The KiDS analysis provides evidence of non-baryonic suppression on scales $k \sim 0.2$-$4\,h\,{\rm Mpc}^{-1}$. The pink lines show the suppression expected if a fraction of dark matter consists of ultra-light axions (Vogt et al., 2023). The solid (dashed) line corresponds to a model with $m_{\rm ax} = 1.25 \times 10^{-25}$ eV (3.16×10^{-26} eV) and axion fraction $f_{\rm ax} = \Omega_{\rm ax}/\Omega_{\rm DM} = 0.017$ (0.030). The weaker S_8 tension in the DES analysis requires no additional non-baryonic suppression, but it suggests an excess of power on scales $k > 4\,h\,{\rm Mpc}^{-1}$.

reconcile the S_8 tension. This is especially true for the KiDS cosmic shear analysis, where a significantly greater suppression is required.

Given our constraints on the baryonic suppression of the matter power spectrum, we examine the additional suppression required by lensing analyses. In the right panel of Fig. 4.7, we show the additional suppression required by the DES and KiDS analyses after accounting for the baryonic suppression inferred from our study. For the KiDS analysis, an excess suppression (up to 20%) out to $k \approx 4\,h\,{\rm Mpc}^{-1}$ is needed. In case of DES Y3, the excess suppression required is more or less consistent with zero ($\approx 1\sigma$) but suggests an enhancement around $k \approx 10\,h\,{\rm Mpc}^{-1}$. This could suggest the possibility of unknown physical phenomena, such as interacting dark matter (Mazoun et al., 2024), ultra-light axions (Vogt et al., 2023; Rogers et al., 2023), or early dark energy (Sobotka et al., 2024), that could be responsible for the suppression of the matter power spectrum at these small scales. The figure also presents an example of the suppression caused by ultra-light axions at these scales, with the solid and dashed pink lines representing non-linear suppression for axion masses of $m_{\rm ax} = 1.25 \times 10^{-25}$ eV and 3.16×10^{-26} eV, respectively, and axion fractions $f_{\rm ax} = \Omega_{\rm ax}/\Omega_{\rm DM}$ of 0.017 and 0.030. These scenarios roughly align with the

additional suppression required by the DES and KiDS analyses. Precise measurements of baryonic feedback and cosmic shear could provide further insights into the necessity for non-standard dark matter models and help constrain such models.

4.8 Conclusions

In this work, we calibrate the ICM mass to halo mass relation of galaxy clusters using 122 SPT clusters and X-ray measurements from the Chandra X-ray Observatory and *XMM-Newton*. Halo masses are calibrated using DES-Y3 WL data, where we simultaneously constrain optical, tSZE, and X-ray observable-mass relations. This multi-observable approach yields a robust mass calibration and tighter constraints on individual mass measurements. Our constraint on the ICM to halo mass relation results in a mass trend that is $\approx 3\sigma$ away from the self-similar expectation of 1, and is in good agreement with previous results (Chiu et al., 2018; Bulbul et al., 2019). The amplitude of this relation differs from earlier studies due to updated halo masses, which are $\approx 18\%$ larger than those used by Chiu et al. (2018) and Bulbul et al. (2019), who relied on the galaxy cluster abundance with limited WL data for mass calibration (de Haan et al., 2016).

We then compare our results to several state-of-the-art hydrodynamical simulations, each with different physics and strengths of baryonic feedback. To quantitatively assess the agreement, we calculate the marginal likelihood of the data given the simulations, which we use to weight each simulation. Since feedback affects both the ICM to halo mass relation and the suppression of the matter power spectrum at small scales, we use the observed ICM to halo mass relation to inform the power spectrum suppression. To do this, we fit the suppression as a function of the mass trend ($\mathrm{ICM_M}$) at a given wavenumber (k) value. We repeat this process for wavenumbers up to $10\,h\,\mathrm{Mpc}^{-1}$. Next, we fit the marginal log-likelihood as a function of $\mathrm{ICM_M}$ and then calculate a weighted power spectrum suppression using those marginal likelihoods as weights. Our constraints on the power spectrum suppression rule out a few very strong and very weak feedback scenarios, favoring the FLAMINGO-strongest, FLAMINGO-strong-jets, C-OWLS AGN, and BAHAMAS ($\Theta_{\mathrm{AGN}} = 8.0$) models.

We compare our constraints to estimates from the SP(k) emulator calibrated on the ANTILLES simulation suite. The SP(k) emulator predicts suppression based on the baryonic fraction to halo mass relation. We convert our ICM masses to baryon fraction by assuming a fixed stellar mass fraction from Chiu et al. (2018). Our results agree with SP(k) within 1σ. Additionally, we compare our findings with Grandis et al. (2024a) and find that they exhibit higher suppression (approximately at the 2σ level) in the $k < 0.8h$ Mpc^{-1} region. Finally, we use the inferred power spectrum suppression and provide constraints on the parameters of HM20 and BCemu power spectrum emulators.

In the final section of our analysis, we compare the derived constraints on $P(k)$ suppression with those required to reconcile the cosmological results between the Planck and DES (KiDS) analyses, as discussed by Amon & Efstathiou (2022) and Preston et al. (2023). Our findings suggest that baryonic suppression alone may not account for the required sup-

pression at scales of $k = 0.2 - 0.8h$ Mpc^{-1}. Additional theories, such as interacting dark matter, ultra-light axions, or early dark energy, could be interesting scenarios to resolve this discrepancy, as they induce suppression of the matter power spectrum at those small scales.

In summary, we demonstrate that the ICM to halo mass constraints from observations, coupled with hydrodynamical simulations, can be a powerful tool to precisely measure the baryonic suppression of the matter power spectrum of the Universe at small scales. This precise measurement of the power spectrum will be a crucial ingredient for accurate cosmological constraints from cosmic shear analyses with upcoming surveys like Euclid, LSST, and Roman. As shown in Fig. 4.7, the limits on baryonic suppression of the power spectrum can help constrain non-standard models that could produce the additional suppression at small scales required to address the S_8 tension.

Chapter 5

Conclusions and Outlook

In this thesis, we have developed and applied new techniques to study galaxy cluster matter profiles and their implications for cosmology. By leveraging multi-wavelength data from the South Pole Telescope (SPT), the Dark Energy Survey (DES), ROSAT, and X-ray observations from Chandra and XMM-Newton, along with state-of-the-art hydrodynamical simulations, we have introduced new mass calibration methods and examined the impact of baryonic physics on the matter power spectrum. Our results provide constraints on observable-mass relations, enhance our understanding of galaxy cluster matter profiles, and offer key insights into the suppression of the matter power spectrum due to baryonic feedback.

In the first part of our study, we examined the self-similar properties of galaxy cluster matter profiles in both simulations and observations. We demonstrated that rescaling individual profiles by their characteristic radius and critical density significantly reduces mass and redshift dependence, enabling the combination of clusters across a wide range of parameters. This self-similarity provides a robust framework for studying average cluster matter profiles in a high signal-to-noise regime, which also enables robust mass calibration.

Using this rescaled matter profile method, we calibrated the observable-mass relations for SPT and MARD-Y3 clusters. By incorporating multi-wavelength data from tSZE, X-ray, optical, and weak lensing measurements, we constrained key scaling parameters. Combining these two catalogs helped break degeneracies in the tSZE and optical observable-mass relations, leading to improved mass calibration and tighter cosmological constraints. Additionally, we validated the power-law form of the observable-mass relations by analyzing scatter in cluster observables and found potential evidence for redshift-dependent intrinsic scatter in optical richness.

Furthermore, we extended our analysis to study the matter profiles in the outskirts of galaxy clusters by combining all cluster measurements in self-similar space. While the cluster matter profile aligns well with simulations at redshifts above 0.25, we observe notable deviations at lower redshifts, with hydrodynamical simulations significantly underpredicting the observed lensing signal in the cluster outskirts. This suggests possible evolution in the mass distribution and may indicate new physics beyond the standard ΛCDM model, such as modified gravity or interactions in the dark sector, making it a crucial direction

for future investigation.

Finally, we used our mass calibration results to constrain the intracluster medium (ICM) to halo mass relation by combining X-ray data from Chandra and *XMM-Newton* with DES weak lensing masses. Our results revealed a deviation from self-similar expectations, consistent with previous work, and provided new insights into baryonic feedback processes. By comparing our constraints with state-of-the-art hydrodynamical simulations, we constrained the impact of baryonic physics on the suppression of the matter power spectrum. Our findings suggest that while baryonic effects contribute significantly to power suppression at small scales, they may not fully resolve the discrepancies observed in cosmological constraints from weak lensing and the cosmic microwave background, hinting at the need for additional physics such as interacting dark matter or early dark energy.

The methods and findings presented in this thesis offer a powerful framework for future galaxy cluster studies. The self-similar mass calibration approach will be particularly valuable for upcoming weak lensing surveys such as Euclid, Rubin (LSST), and Roman, which will provide unprecedented data quality and volume. Furthermore, the constraints on the baryonic suppression of the matter power spectrum at small scales will enable the use of upcoming data in this regime during cosmic shear analysis, improving the cosmological constraining power of future surveys.

This work highlights the critical role of multi-wavelength analyses in improving cluster mass calibration and understanding the impact of baryonic physics. By leveraging weak lensing, X-ray, and tSZE data, we have placed some of the strongest constraints to date on cluster observable-mass relations, matter profiles, and the suppression of the matter power spectrum due to baryons. Our results advance current cosmological studies and provide key insights for future research in the era of next-generation surveys.

Appendix A

Appendix

A.1 Cluster matter profile interpolation

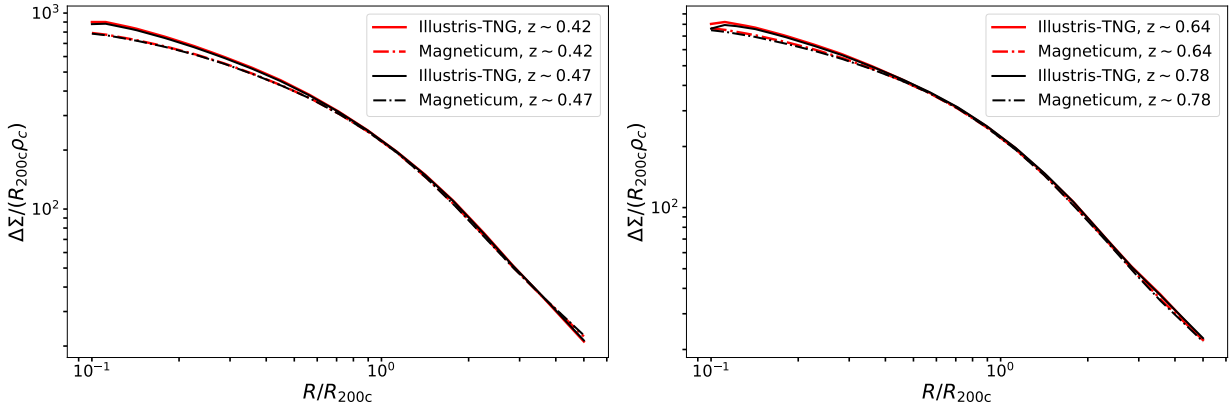

Figure A.1: Comparison of average matter profiles from IllustrisTNG and *Magneticum* at the redshift of 0.42 and 0.47 (top figure) and at the redshift of 0.64 and 0.78 (bottom figure). The profiles exhibit very small differences with a small redshift change for a given simulation throughout the radial range $R/R_{200c} > 0.5$

In Fig. A.1 top figure, we show the differences in the IllustrisTNG average cluster matter profiles at 0.42 vs. 0.47 in solid red and solid black lines respectively. In dashed red and black lines we show a average cluster matter profile in *Magneticum* at the redshift of 0.42 and 0.47 respectively. The profiles show very small differences with slight changes in redshift. Similarly in the bottom figure, we compare the profiles at the redshift of 0.64 vs. 0.78 and find that both simulation profiles exhibit minor differences. The purpose of this plot is not to compare the different simulations themselves, but, the differences in the simulations in the inner radial region at the same redshift are due to different baryonic effects. That region is avoided in the mass calibration method presented in Section 2.4.

A.2 Observable-mass relations

To confirm that the features observed in Fig. 2.13 (top) is a real effect caused by $\hat{\zeta}$ tSZE selection, we analyze a mock SPT catalog along with mock DES Y3 lensing data. We perform a mass calibration analysis on this mock data and plot the debiased $\hat{\zeta}$ as a function of the calibrated M_{200c}, just as we have done with the real data in Section 2.5.2.2. Fig. A.2 illustrates this relation for the mock sample, where the mock data is represented by black dots, the mean relation is shown as a black line, and the shaded regions denote the 68% and 95% credible intervals on that model. We observe the same features at low mass and low debiased $\hat{\zeta}$ as seen in Fig. 2.13 (top). This analysis confirms that the feature is introduced by the tSZE selection, where only clusters exceeding the selection threshold make it into our sample. At low masses, only those clusters that are scattered up in $\hat{\zeta}$ due to the combination of intrinsic scatter and measurement noise are selected. Additionally, we observe the same qualitative features in the mock analysis as those seen in Fig.2.12 and the bottom plot of Fig.2.13.

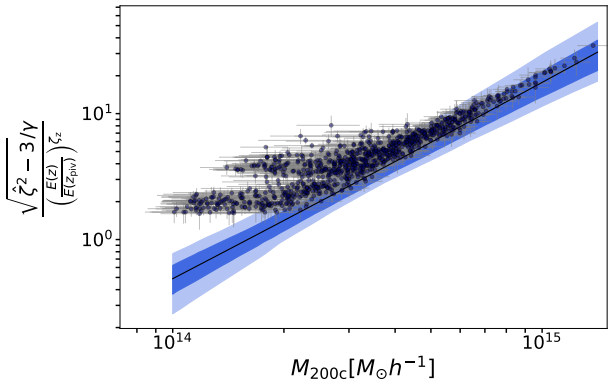

Figure A.2: The observed debiased detection significance, $\hat{\zeta}$, as a function of cluster halo mass for a mock SPT catalog (black dots). The solid black line indicates the intrinsic mean relation, and the shaded regions denote the 68% and 95% credible intervals. The similarities between the deviations of the mock clusters and of the real clusters (Fig. 2.13) about the mean relation are striking.

A.3 Robustness of the mass calibration

In this section, we assess the robustness of our analysis method by changing the inner fitting region of the cluster matter profile and also by changing the binning of the sample in $\hat{\zeta} - \hat{\lambda} - z$. In the top figure of Fig. A.3 we compare the posterior of the observable-mass relation parameter for inner fitting radii of $0.5h^{-1}$Mpc and $0.7h^{-1}$Mpc (Note that for this analysis we have binned our observables in $3 \times 3 \times 3$ bins). The blue posterior ($R > 0.7h^{-1}$Mpc) results in a larger error compared to the red posterior, which is expected given that we have fewer source galaxies as we restrict our fitting range.

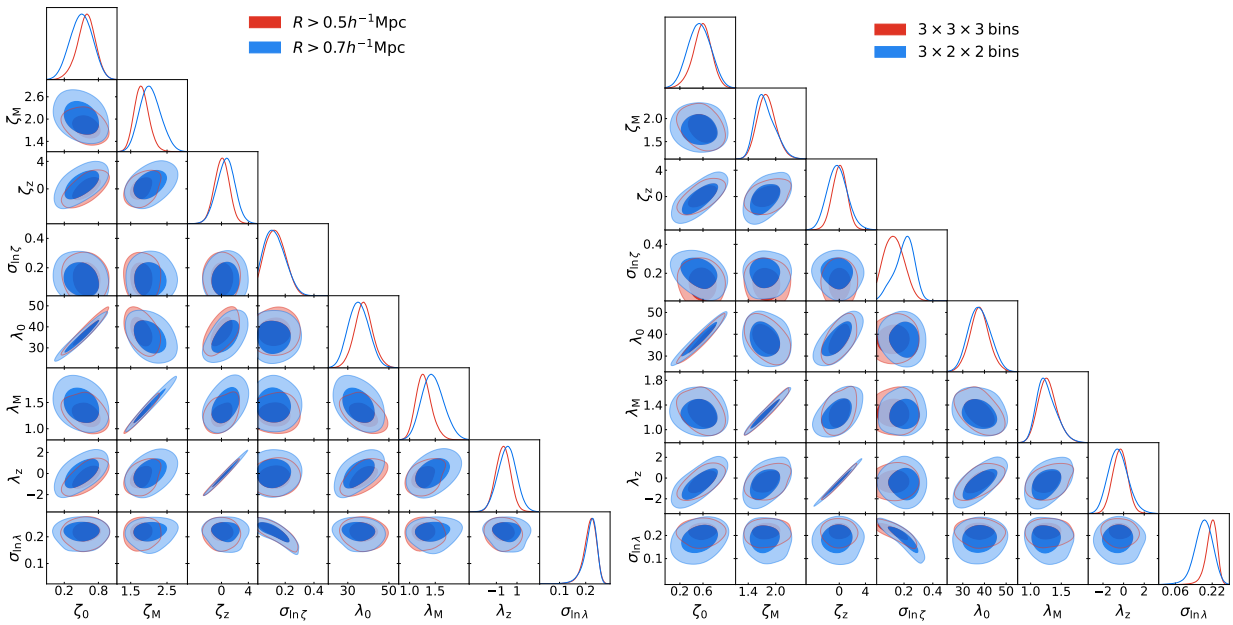

Figure A.3: Comparison of the posterior for the SPT sample with the same binning but different inner radius fit (left figure) of $0.5h^{-1}$Mpc (red) and $0.7h^{-1}$Mpc (blue). The blue posterior is in good agreement with the red posterior with a slightly larger error region. In the right figure, we compare the results from two different observable binning schemes while keeping the inner-fitting radii fixed at $0.5h^{-1}$Mpc. We see good agreement between the two results suggesting our results are not heavily affected by the choice of observable binning.

In the bottom figure of Fig. A.3, we compare the observable-mass relation parameters posterior resulting from different binning of observables for the SPT sample compared to our fiducial $3 \times 3 \times 3$ binning. For the new binning, we divide our observables in $3 \times 2 \times 2$ bins as follows

$$
\begin{aligned}
&0.25 \leq z < 0.33 \\
&\qquad 0 \leq \hat{\lambda} < 80, \quad 80 \leq \hat{\lambda} < 243 \\
&\qquad 4.25 \leq \hat{\zeta} < 6, \quad 6 \leq \hat{\zeta} < 50 \\
&0.33 \leq z < 0.43 \\
&\qquad 0 \leq \hat{\lambda} < 95, \quad 95 \leq \hat{\lambda} < 243 \\
&\qquad 4.25 \leq \hat{\zeta} < 7.5, \quad 7.5 \leq \hat{\zeta} < 50 \\
&0.43 \leq z < 0.94 \\
&\qquad 0 \leq \hat{\lambda} < 85, \quad 85 \leq \hat{\lambda} < 243 \\
&\qquad 4.25 \leq \hat{\zeta} < 6, \quad 6 \leq \hat{\zeta} < 50.
\end{aligned}
$$

The above binning is such that each redshift bin is further divided into observable bins with roughly similar SNR. The blue and red posteriors show good agreement, indicating that the choice of $\hat{\zeta} - \hat{\lambda} - z$ binning does not strongly impact parameter values.

Table A.1: Parameters of the cluster member contamination model as described in Section 2.4.4.2. For each parameter the mean and 68% credible region of the posterior are given.

Parameter	DNF photo-z and MCMF center		
	tomographic bin 2	tomographic bin 3	tomographic bin 4
z_{off_0}	-0.009 ± 0.002	0.050 ± 0.002	0.164 ± 0.007
z_{off_z}	-0.22 ± 0.02	-0.23 ± 0.02	-0.45 ± 0.02
σ_{z_0}	0.047 ± 0.002	0.076 ± 0.002	0.130 ± 0.006
σ_{z_z}	-0.018 ± 0.021	-0.086 ± 0.017	-0.16 ± 0.02
$\log(c_\lambda)$	0.44 ± 0.03	0.51 ± 0.04	0.26 ± 0.06
B_λ	0.78 ± 0.04	0.60 ± 0.04	0.53 ± 0.07
$\rho_{\mathrm{corr}-z}$	0.27 ± 0.01	0.18 ± 0.01	0.494 ± 0.006
A_0	0.12 ± 0.06	-0.32 ± 0.17	0.16 ± 0.03
A_1	0.19 ± 0.04	-0.22 ± 0.13	0.16 ± 0.03
A_2	0.29 ± 0.04	-0.01 ± 0.12	0.17 ± 0.03
A_3	0.42 ± 0.05	0.30 ± 0.12	0.18 ± 0.02
A_4	0.53 ± 0.06	0.64 ± 0.11	0.19 ± 0.03
A_5	0.62 ± 0.06	0.86 ± 0.11	0.19 ± 0.02
A_6	0.68 ± 0.06	0.87 ± 0.12	0.20 ± 0.02
A_7	0.72 ± 0.06	0.69 ± 0.12	0.21 ± 0.02
A_8	0.74 ± 0.07	0.44 ± 0.13	0.22 ± 0.03
A_9	0.75 ± 0.08	0.24 ± 0.17	0.22 ± 0.03
A_{10}	0.75 ± 0.09	0.13 ± 0.21	0.23 ± 0.03
A_∞	-4.94 ± 0.06	-4.61 ± 0.38	-4.76 ± 0.21

Appendix B

Appendix

B.1 Interpolation of likelihood as a function $\mathrm{ICM_M}$

Fig B.1 shows the variation of marginal log-likelihood (as calculated in Section 4.3.2) with the mass trend $\mathrm{ICM_M}$ for simulations. To assign weights to the suppression of the power spectrum (for a given $\mathrm{ICM_M}$), we fit the above relation. We assume a second-degree polynomial and fit the relation with a free scatter parameter and also account for errors in both the likelihood and $\mathrm{ICM_M}$ measurements. The red line shows the mean fit relation and the red region represents the 68% credible interval. The fit results in a $\chi^2_{\mathrm{reduced}}$ of 1.03, suggesting that our assumption of a second-degree polynomial descibes the data well. We account for the error in likelihood interpolation with $\mathrm{ICM_M}$ while calculating the weighted power spectrum.

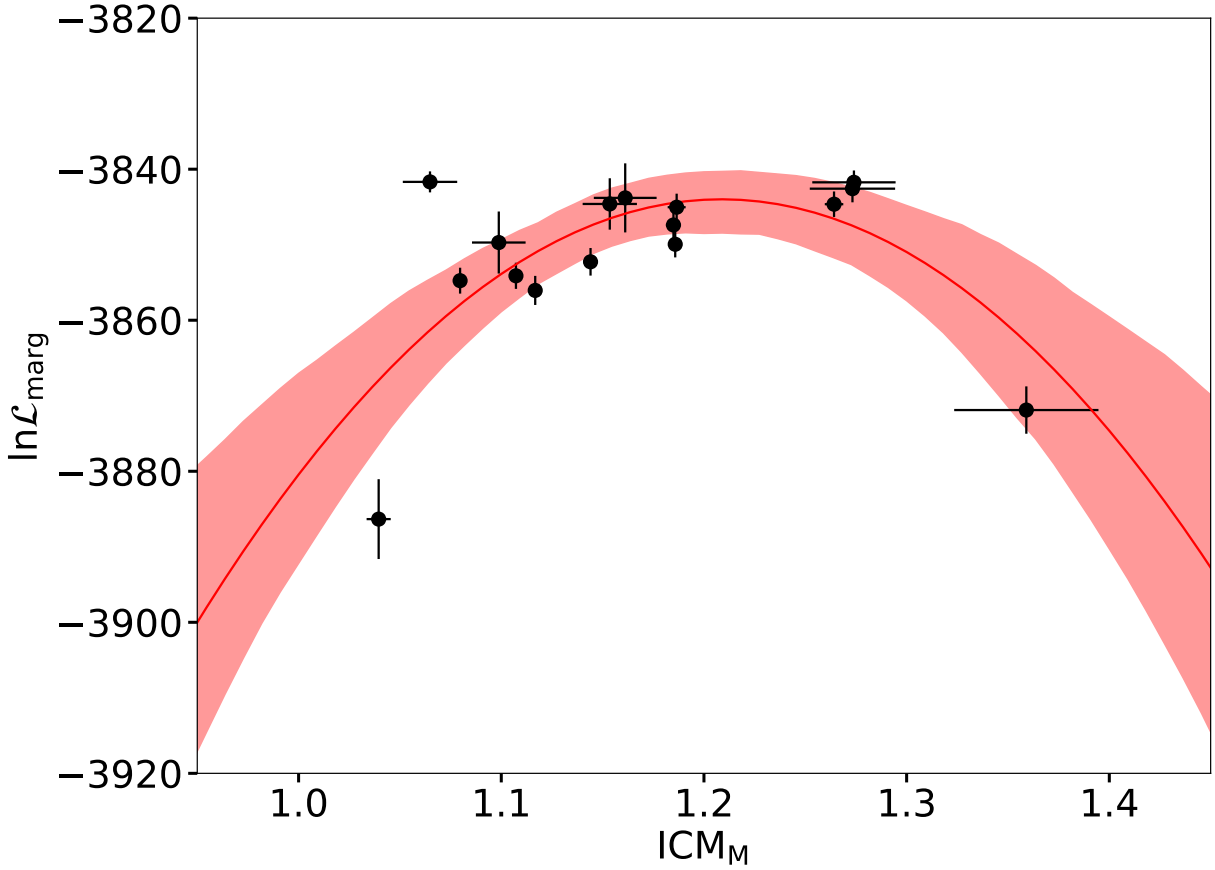

Figure B.1: Marginal log-likelihood as a function of the mass trend of the ICM to halo mass relation for simulations. The black points show measurements for the simulations. The red line represents the mean fit polynomial curve (second-degree), and the red region indicates the 95% credible interval.

B.2 Interpolation of P(k) suppression as a function $\mathrm{ICM_M}$

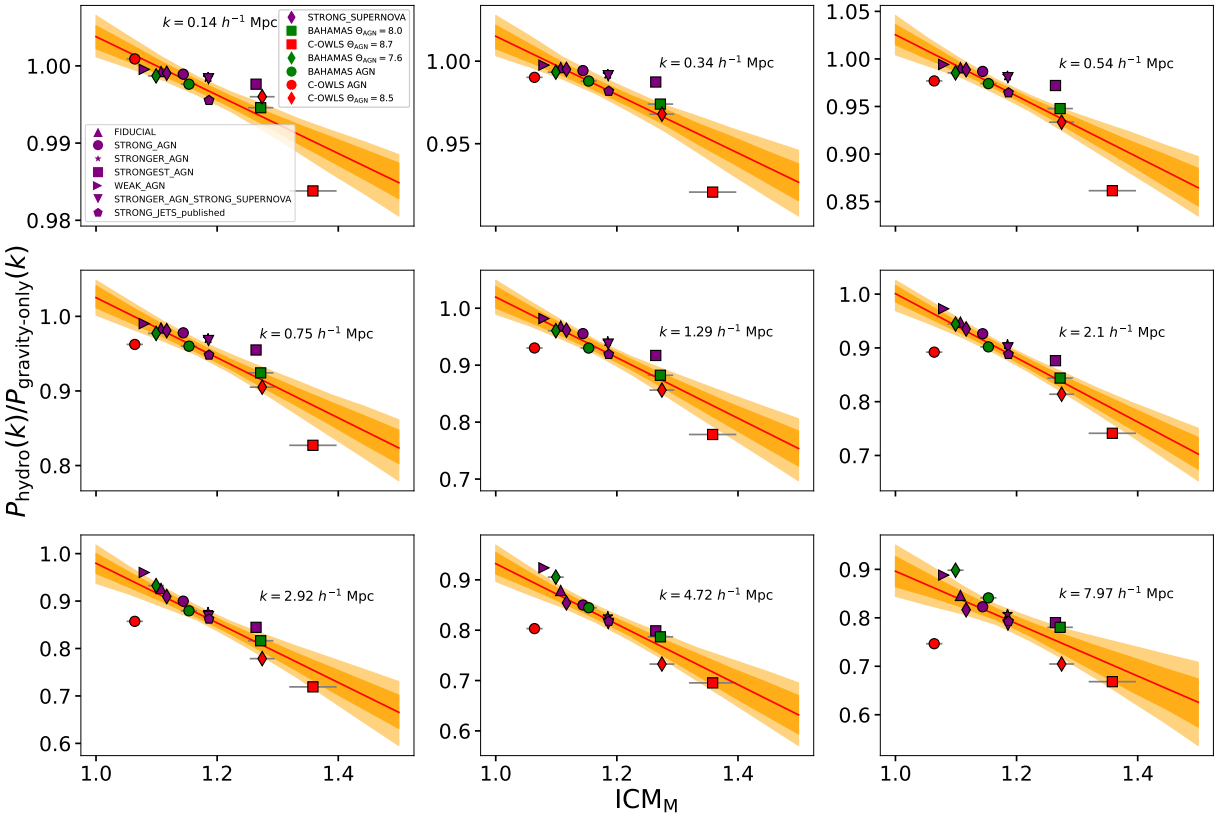

Figure B.2: Suppression of the matter power spectrum (at $z = 0$) as a function of the mass trend of the M_{ICM}-M_{500c}-z relation for 14 different simulations at different wavenumber (k) values. The orange line shows the mean fit to the relation, while the dark and light orange shaded regions represent the 68% and 95% credible intervals, respectively.

B.3 BCemu parameter constraints

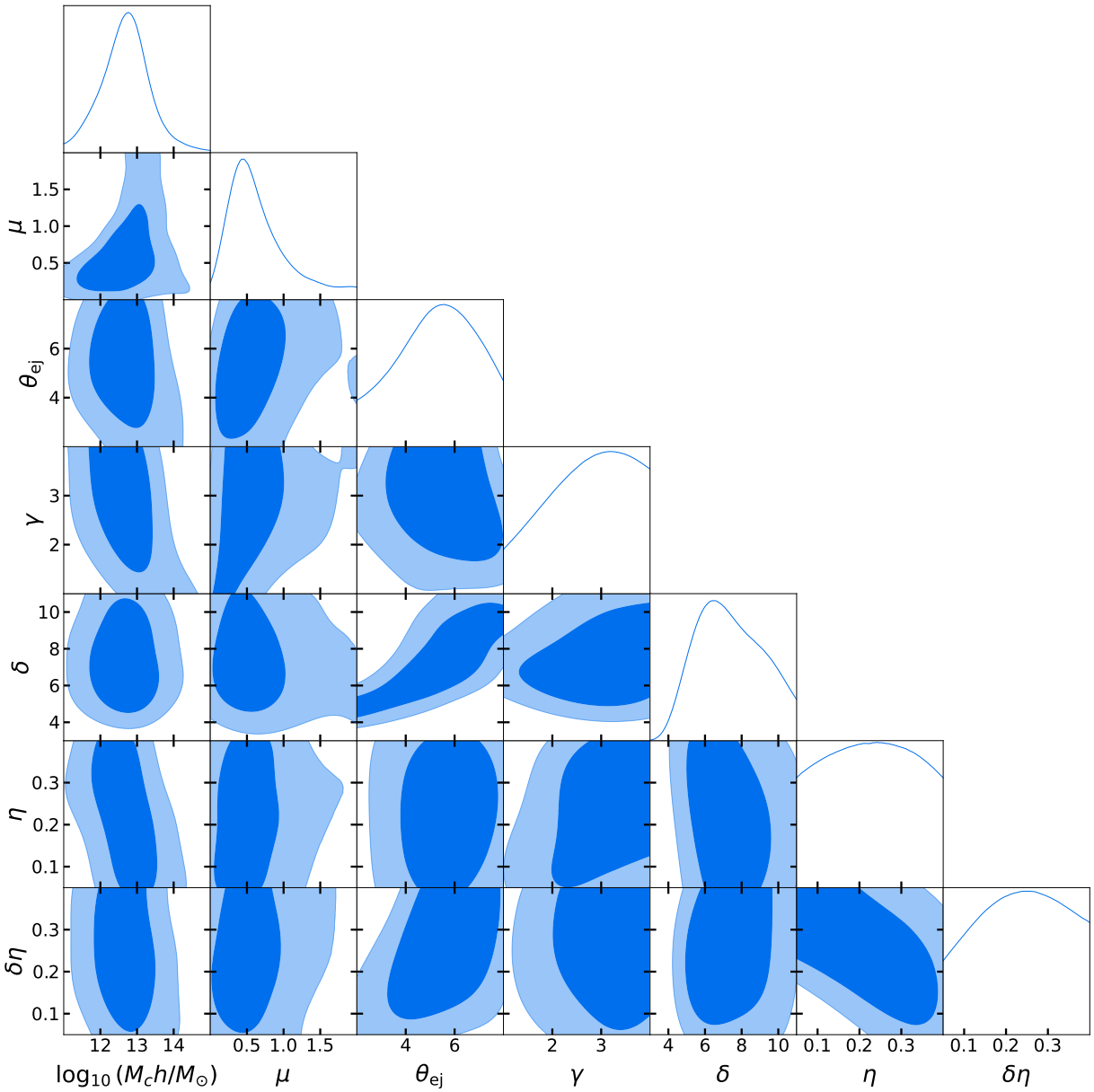

Figure B.3: Contour plot showing the posterior constraints on the BCemu parameters (Section 4.6.2). We constrain the parameters $\log_{10}(M_c h/M_\odot)$, μ, $\theta_{\rm ej}$, and δ.

Bibliography

Abbott, T., Aguena, M., Alarcon, A., et al. 2023, The Open Journal of Astrophysics, 6

Abbott, T. M. C., Abdalla, F. B., Allam, S., et al. 2018, The Astrophysical Journal Supplement Series, 239, 18

Abbott, T. M. C., Aguena, M., Alarcon, A., et al. 2020, Phys. Rev. D, 102, 023509

Abbott, T. M. C., Aguena, M., Alarcon, A., et al. 2020, Phys. Rev. D, 102, 023509

Abbott, T. M. C., Aguena, M., Alarcon, A., et al. 2022a, Phys. Rev. D, 105, 023520

Abbott, T. M. C., Aguena, M., Alarcon, A., et al. 2022b, Phys. Rev. D, 105, 023520

Adhikari, S., Dalal, N., & Chamberlain, R. 2014, Journal of Cosmology and Astroparticle Physics, 2014, 062

Aihara, H., Armstrong, R., Bickerton, S., et al. 2018, Publ. Astron. Soc. Japan, 70, S8

Allen, S. W., Evrard, A. E., & Mantz, A. B. 2011, Annual Review of Astronomy and Astrophysics, 49, 409

Allen, S. W., Rapetti, D. A., Schmidt, R. W., et al. 2008, Monthly Notices of the Royal Astronomical Society, 383, 879

Amon, A. & Efstathiou, G. 2022, Monthly Notices of the Royal Astronomical Society, 516, 5355

Amon, A., Gruen, D., Troxel, M., et al. 2022a, Phys. Rev. D, 105

Amon, A., Gruen, D., Troxel, M. A., et al. 2022b, Phys. Rev. D, 105, 023514

Andreon, S. 2010, Monthly Notices of the Royal Astronomical Society, 407, 263–272

Aricò, G., Angulo, R. E., Zennaro, M., et al. 2023a, Astron. Astrophys., 678, A109

Aricò, G., Angulo, R. E., Zennaro, M., et al. 2023b, Astron. Astrophys., 678, A109

Arnaud, M. & Evrard, A. E. 1999, Monthly Notices of the Royal Astronomical Society, 305, 631

Arnaud, M., Pointecouteau, E., & Pratt, G. W. 2007, Astron. Astrophys., 474, L37

Arnaud, M., Pratt, G. W., Piffaretti, R., et al. 2010, Astron. Astrophys., 517, A92

Bahar, Y. Emre, Bulbul, Esra, Clerc, Nicolas, et al. 2022, A&A, 661, A7

Baldi, A., Ettori, S., Molendi, S., & Gastaldello, F. 2012, Astron. Astrophys., 545, A41

Barbosa, D., Bartlett, J. G., Blanchard, A., & Oukbir, J. 1996, Astron. Astrophys., 314, 13

Bardeen, J. M., Bond, J. R., Kaiser, N., & Szalay, A. S. 1986, Astrophys. J., 304, 15

Bartelmann, M. 1996, Astron. Astrophys., 313, 697

Bartelmann, M. & Schneider, P. 2001, Physics Reports, 340, 291

Beck, A. M., Murante, G., Arth, A., et al. 2016, Mon. Not. R. Astron. Soc., 455, 2110

Becker, M. R. & Kravtsov, A. V. 2011, Astrophys. J., 740, 25

Bellagamba, F., Sereno, M., Roncarelli, M., et al. 2019, Mon. Not. R. Astron. Soc., 484, 1598

Bhattacharya, S., Habib, S., Heitmann, K., & Vikhlinin, A. 2013, Astrophys. J., 766, 32

Bigwood, L., Amon, A., Schneider, A., et al. 2024, Mon. Not. R. Astron. Soc., 534, 655

Bleem, L., Klein, M., Abbott, T. M. C., et al. 2024, OJAp, 7

Bleem, L. E., Bocquet, S., Stalder, B., et al. 2020, Astrophys. J. Suppl. Ser., 247, 25

Bleem, L. E., Stalder, B., de Haan, T., et al. 2015, Astrophys. J. Suppl. Ser., 216, 27

Bocquet, S., Dietrich, J. P., Schrabback, T., et al. 2019, Astrophys. J., 878, 55

Bocquet, S., Dietrich, J. P., Schrabback, T., et al. 2019, Astrophys. J., 878, 55

Bocquet, S., Grandis, S., Bleem, L. E., et al. 2023, arXiv e-prints, arXiv:2310.12213

Bocquet, S., Grandis, S., Bleem, L. E., et al. 2024a, Phys. Rev. D, 110, 083509

Bocquet, S., Grandis, S., Bleem, L. E., et al. 2024b, Phys. Rev. D, 110, 083510

Bocquet, S., Grandis, S., Krause, E., et al. 2024c, submitted to Phys. Rev. D, arXiv:2412.07765

Bocquet, S., Saro, A., Dolag, K., & Mohr, J. J. 2016, Mon. Not. R. Astron. Soc., 456, 2361

Bocquet, S., Saro, A., Mohr, J. J., et al. 2015, The Astrophysical Journal, 799, 214

Boller, T., Freyberg, M. J., Trümper, J., et al. 2016, Astronomy & Astrophysics, 588, A103

Bulbul, E., Chiu, I. N., Mohr, J. J., et al. 2019, Astrophys. J., 871, 50

Bulbul, E., Chiu, I.-N., Mohr, J. J., et al. 2019, The Astrophysical Journal, 871, 50

Bulbul, E., Liu, A., Kluge, M., et al. 2024, The SRG/eROSITA All-Sky Survey: The first catalog of galaxy clusters and groups in the Western Galactic Hemisphere

Bulbul, G. E., Smith, R. K., Foster, A., et al. 2012, The Astrophysical Journal, 747, 32

Carlstrom, J. E., Ade, P. A. R., Aird, K. A., et al. 2011, Publ. Astron. Soc. Pac., 123, 568

Cataneo, M., Rapetti, D., Schmidt, F., et al. 2015, Phys. Rev. D, 92, 044009

Chen, A., Aricò, G., Huterer, D., et al. 2023, Mon. Not. R. Astron. Soc., 518, 5340

Chisari, N. E., Le Brun, A. M. C., Schneider, A., et al. 2018, Monthly Notices of the Royal Astronomical Society, 480, 3962

Chisari, N. E., Mead, A. J., Joudaki, S., et al. 2019, The Open Journal of Astrophysics, 2

Chiu, I., Dietrich, J. P., Mohr, J., et al. 2016a, Mon. Not. R. Astron. Soc., 457, 3050

Chiu, I., Mohr, J., McDonald, M., et al. 2016b, Mon. Not. R. Astron. Soc., 455, 258

Chiu, I., Mohr, J., McDonald, M., et al. 2016c, Mon. Not. R. Astron. Soc., 455, 258

Chiu, I., Mohr, J. J., McDonald, M., et al. 2018, Mon. Not. R. Astron. Soc., 478, 3072

Chiu, I., Mohr, J. J., McDonald, M., et al. 2018, Monthly Notices of the Royal Astronomical Society, 478, 3072

Chiu, I. N., Klein, M., Mohr, J., & Bocquet, S. 2023, Mon. Not. R. Astron. Soc., 522, 1601

Chiu, I.-N., Klein, M., Mohr, J., & Bocquet, S. 2023a, Monthly Notices of the Royal Astronomical Society, 522, 1601

Chiu, I.-N., Klein, M., Mohr, J., & Bocquet, S. 2023b, Monthly Notices of the Royal Astronomical Society, 522, 1601

Chiu, I-Non, Ghirardini, Vittorio, Liu, Ang, et al. 2022, A&A, 661, A11

Collaboration, T. D. E. S. 2005, The Dark Energy Survey

Cooray, A. & Sheth, R. 2002, Phys. Rep., 372, 1

Costanzi, M., Rozo, E., Simet, M., et al. 2019, Mon. Not. R. Astron. Soc., 488, 4779

Costanzi, M., Saro, A., Bocquet, S., et al. 2021, Phys. Rev. D, 103, 043522

Covone, G., Sereno, M., Kilbinger, M., & Cardone, V. F. 2014, Astrophys. J. Lett., 784, L25

Dalal, R., Li, X., Nicola, A., et al. 2023, Phys. Rev. D, 108, 123519

de Haan, T., Benson, B. A., Bleem, L. E., et al. 2016, The Astrophysical Journal, 832, 95

de Jong, J. T. A., Verdoes Kleijn, G. A., Kuijken, K. H., & Valentijn, E. A. 2012, Experimental Astronomy, 35, 25–44

De Vicente, J., Sánchez, E., & Sevilla-Noarbe, I. 2016, Mon. Not. R. Astron. Soc., 459, 3078

Diemer, B. & Kravtsov, A. V. 2014, The Astrophysical Journal, 789, 1

Dietrich, J. P., Bocquet, S., Schrabback, T., et al. 2019, Mon. Not. R. Astron. Soc., 483, 2871

Dodelson, S. 2003, Modern Cosmology

Dolag, K., Mevius, E., & Remus, R.-S. 2017, Galaxies, 5, 35

Dressler, A. 1980, Astrophys. J., 236, 351

Dvali, G., Gabadadze, G., & Porrati, M. 2000, Physics Letters B, 485, 208

Ebeling, H., Edge, A. C., Burgett, W. S., et al. 2013, Monthly Notices of the Royal Astronomical Society, 432, 62

Eifler, T., Krause, E., Dodelson, S., et al. 2015, Monthly Notices of the Royal Astronomical Society, 454, 2451

Einasto, J. 1965, Trudy Astrofizicheskogo Instituta Alma-Ata, 5, 87

Einstein, A. 1916, Annalen der Physik, 354, 769

Eisenstein, D. J., Zehavi, I., Hogg, D. W., et al. 2005, The Astrophysical Journal, 633, 560

Ettori, S., Morandi, A., Tozzi, P., et al. 2009, Astron. Astrophys., 501, 61

Euclid Collaboration, Blanchard, A., Camera, S., et al. 2020, Astron. Astrophys., 642, A191

Fabian, A. C. 2012, Annual Review of Astronomy and Astrophysics, 50, 455

Feroz, F., Hobson, M. P., & Bridges, M. 2009, MNRAS, 398, 1601

Feroz, F., Hobson, M. P., Cameron, E., & Pettitt, A. N. 2019, OJAp, 2

Finoguenov, A., Reiprich, T. H., & Böhringer, H. 2001, Astron. Astrophys., 368, 749

Flaugher, B., Diehl, H. T., Honscheid, K., et al. 2015, Astron. J., 150, 150

Forman, W., Nulsen, P., Heinz, S., et al. 2005, The Astrophysical Journal, 635, 894

Fowler, J. W., Niemack, M. D., Dicker, S. R., et al. 2007, Appl. Opt., 46, 3444

Gatti, M., Giannini, G., Bernstein, G. M., et al. 2022, Mon. Not. R. Astron. Soc., 510, 1223

Gatti, M., Sheldon, E., Amon, A., et al. 2021, Mon. Not. R. Astron. Soc., 504, 4312

Ghirardini, V., Bulbul, E., Artis, E., et al. 2024, Astron. Astrophys., 689, A298

Ghirardini, V., Ettori, S., Eckert, D., Pointecouteau, E., et al. 2019, A&A, 621, A41

Giocoli, C., Marulli, F., Moscardini, L., et al. 2021, Astron. Astrophys., 653, A19

Giri, S. K. & Schneider, A. 2021, Journal of Cosmology and Astroparticle Physics, 2021, 046

Gonzalez, A. H., Sivanandam, S., Zabludoff, A. I., & Zaritsky, D. 2013, The Astrophysical Journal, 778, 14

Grandis, S., Aricò, G., Schneider, A., & Linke, L. 2024a, Monthly Notices of the Royal Astronomical Society, 528, 4379

Grandis, S., Bocquet, S., Mohr, J. J., Klein, M., & Dolag, K. 2021, Mon. Not. R. Astron. Soc., 507, 5671

Grandis, S., Ghirardini, V., Bocquet, S., et al. 2024b, The SRG/eROSITA All-Sky Survey: Dark Energy Survey Year 3 Weak Gravitational Lensing by eRASS1 selected Galaxy Clusters

Grandis, S., Mohr, J. J., Dietrich, J. P., et al. 2019, Mon. Not. R. Astron. Soc., 488, 2041

Guth, A. H. 1981, Phys. Rev. D, 23, 347

Haiman, Z., Mohr, J. J., & Holder, G. P. 2001, Astrophys. J., 553, 545

Hennig, C., Mohr, J. J., Zenteno, A., et al. 2017, Mon. Not. R. Astron. Soc., 467, 4015

Henry, J. P., Mullis, C. R., Voges, W., et al. 2006, The Astrophysical Journal Supplement Series, 162, 304

Hilton, M., Sifón, C., Naess, S., et al. 2021, Astrophys. J. Suppl. Ser., 253, 3

Hirschmann, M., Dolag, K., Saro, A., et al. 2014, Mon. Not. R. Astron. Soc., 442, 2304

Hopkins, P. F., Hernquist, L., Cox, T. J., et al. 2006, Astrophys. J. Suppl. Ser., 163, 1

Huff, E. & Mandelbaum, R. 2017, arXiv e-prints, arXiv:1702.02600

Ivezić, Z., Kahn, S. M., Tyson, J. A., et al. 2019, The Astrophysical Journal, 873, 111

Jarvis, M., Bernstein, G. M., Amon, A., et al. 2021, Mon. Not. R. Astron. Soc., 501, 1282

Kaiser, N. 1986, Monthly Notices of the Royal Astronomical Society, 222, 323

Kaiser, N. 1986, Mon. Not. R. Astron. Soc., 222, 323

Kilbinger, M. 2015, Reports on Progress in Physics, 78, 086901

Klein, M., Grandis, S., Mohr, J. J., et al. 2019a, Mon. Not. R. Astron. Soc., 488, 739

Klein, M., Grandis, S., Mohr, J. J., et al. 2019b, Mon. Not. R. Astron. Soc., 488, 739

Klein, M., Grandis, S., Mohr, J. J., et al. 2019, Monthly Notices of the Royal Astronomical Society, 488, 739

Klein, M., Hernández-Lang, D., Mohr, J. J., Bocquet, S., & Singh, A. 2023a, Mon. Not. R. Astron. Soc., 526, 3757

Klein, M., Mohr, J. J., Bocquet, S., et al. 2023b, arXiv e-prints, arXiv:2309.09908

Klein, M., Mohr, J. J., Bocquet, S., et al. 2024, Mon. Not. R. Astron. Soc., 531, 3973

Klein, M., Mohr, J. J., Desai, S., et al. 2018, Mon. Not. R. Astron. Soc., 474, 3324

Klein, M., Mohr, J. J., & Davies, C. T. 2024, A&A, 690, A322

Komatsu, E., Smith, K. M., Dunkley, J., et al. 2011, Astrophys. J. Suppl. Ser., 192, 18

Kravtsov, A. V. & Borgani, S. 2012, Annual Review of Astronomy and Astrophysics, 50, 353

Lau, E. T., Nagai, D., Avestruz, C., Nelson, K., & Vikhlinin, A. 2015, Astrophys. J., 806, 68

Le Brun, A. M. C., McCarthy, I. G., Schaye, J., & Ponman, T. J. 2014, Monthly Notices of the Royal Astronomical Society, 441, 1270–1290

Lesci, G. F., Marulli, F., Moscardini, L., et al. 2022, Astron. Astrophys., 659, A88

Lesci, G. F., Marulli, F., Moscardini, L., et al. 2022, A&A, 659, A88

Li, S.-S., Hoekstra, H., Kuijken, K., et al. 2023, Astron. Astrophys., 679, A133

Liddle, A. R. & Lyth, D. H. 2000, Cosmological Inflation and Large-Scale Structure

Linde, A. D. 1982, Phys. Lett. B, 108, 389

MacCrann, N., Aleksić, J., Amara, A., et al. 2016, Monthly Notices of the Royal Astronomical Society, 465, 2567

MacCrann, N., Becker, M. R., McCullough, J., et al. 2022, Mon. Not. R. Astron. Soc., 509, 3371

Mandelbaum, R. 2018, Annual Review of Astronomy and Astrophysics, 56, 393

Mantz, A., Allen, S. W., Rapetti, D., & Ebeling, H. 2010, Mon. Not. R. Astron. Soc., 406, 1759

Mantz, A. B., Allen, S. W., Morris, R. G., et al. 2014, Mon. Not. R. Astron. Soc., 440, 2077

Mantz, A. B., Allen, S. W., Morris, R. G., et al. 2016, Mon. Not. R. Astron. Soc., 463, 3582

Mantz, A. B., Allen, S. W., Morris, R. G., et al. 2016, Monthly Notices of the Royal Astronomical Society, 456, 4020

Marinacci, F., Vogelsberger, M., Pakmor, R., et al. 2018, Mon. Not. R. Astron. Soc., 480, 5113

Markevitch, M. & Vikhlinin, A. 2007, Phys. Rep., 443, 1

Mazoun, A., Bocquet, S., Mohr, J. J., et al. 2024, submitted to Phys. Rev. D, arXiv:2411.19911

Mazoun, A., Bocquet, S., Mohr, J. J., et al. 2024, Interacting Dark Sector (ETHOS $n = 0$): Cosmological Constraints from SPT Cluster Abundance with DES and HST Weak Lensing Data

McCarthy, I. G., Schaye, J., Bird, S., & Le Brun, A. M. C. 2016, Monthly Notices of the Royal Astronomical Society, 465, 2936

McCarthy, I. G., Schaye, J., Bower, R. G., et al. 2011, Monthly Notices of the Royal Astronomical Society, 412, 1965

McClintock, T. & et al. 2019, Monthly Notices of the Royal Astronomical Society, 482, 1352

McClintock, T., Varga, T., Gruen, D., et al. 2018, MNRAS, 482, 1352–1378

McDonald, M., Benson, B. A., Vikhlinin, A., et al. 2014a, Astrophys. J., 794, 67

McDonald, M., Benson, B. A., Vikhlinin, A., et al. 2014b, Astrophys. J., 794, 67

McDonald, M., Benson, B. A., Vikhlinin, A., et al. 2013, Astrophys. J., 774, 23

McNamara, B. R. & Nulsen, P. E. J. 2007, Annual Review of Astronomy and Astrophysics, 45, 117

Mead, A. J., Brieden, S., Tröster, T., & Heymans, C. 2021, Monthly Notices of the Royal Astronomical Society, 502, 1401

Mead, A. J., Peacock, J. A., Heymans, C., Joudaki, S., & Heavens, A. F. 2015, Monthly Notices of the Royal Astronomical Society, 454, 1958

Medezinski, E., Umetsu, K., Okabe, N., & et al. 2018, The Astrophysical Journal, 861, 122

Melin, J. B., Bartlett, J. G., & Delabrouille, J. 2006, Astron. Astrophys., 459, 341

Miyazaki, S., Komiyama, Y., Nakaya, H., et al. 2012, in Ground-based and Airborne Instrumentation for Astronomy IV, ed. I. S. McLean, S. K. Ramsay, & H. Takami, Vol. 8446, International Society for Optics and Photonics (SPIE), 84460Z

Mo, H., van den Bosch, F. C., & White, S. D. M. 2010, Galaxy Formation and Evolution (Cambridge, UK: Cambridge University Press)

Mohr, J. J. & Evrard, A. E. 1997, Astrophys. J., 491, 38

Mohr, J. J. & Evrard, A. E. 1997, The Astrophysical Journal, 491, 38

Mohr, J. J., Mathiesen, B., & Evrard, A. E. 1999, Astrophys. J., 517, 627

Mohr, J. J., Mathiesen, B., & Evrard, A. E. 1999, The Astrophysical Journal, 517, 627

More, S., Diemer, B., & Kravtsov, A. V. 2015, The Astrophysical Journal, 810, 36

Murata, R., Nishimichi, T., Takada, M., et al. 2018, The Astrophysical Journal, 854, 120

Murata, R., Oguri, M., Nishimichi, T., et al. 2019, Publ. Astron. Soc. Japan, 71, 107

Myles, J., Alarcon, A., Amon, A., et al. 2021, Mon. Not. R. Astron. Soc., 505, 4249

Naiman, J. P., Pillepich, A., Springel, V., et al. 2018, Mon. Not. R. Astron. Soc., 477, 1206

Navarro, J. F., Frenk, C. S., & White, S. D. M. 1996, Astrophys. J., 462, 563

Navarro, J. F., Frenk, C. S., & White, S. D. M. 1997a, Astrophys. J., 490, 493

Navarro, J. F., Frenk, C. S., & White, S. D. M. 1997b, The Astrophysical Journal, 490, 493

Navarro, J. F., Hayashi, E., Power, C., et al. 2004, Mon. Not. Roy. Astron. Soc., 349, 1039

Nelson, D., Pillepich, A., Springel, V., et al. 2018, Mon. Not. R. Astron. Soc., 475, 624

Nelson, D., Springel, V., Pillepich, A., et al. 2019, Comput. Astrophys. Cosmol., 6, 2

Nelson, K., Lau, E. T., & Nagai, D. 2014, Astrophys. J., 792, 25

Newman, A. B., Treu, T., Ellis, R. S., et al. 2013, The Astrophysical Journal, 765, 25

Niikura, H., Takada, M., Okabe, N., Martino, R., & Takahashi, R. 2015, Publ. Astron. Soc. Japan, 67, 103

Oguri, M. & Takada, M. 2011, Phys. Rev. D, 83, 023008

Okabe, N., Smith, G. P., Umetsu, K., Takada, M., & Futamase, T. 2013, Astrophys. J. Lett., 769, L35

Okabe, N., Smith, G. P., Umetsu, K., Takada, M., & Futamase, T. 2016, The Astrophysical Journal, 822, 131

Okabe, N., Zhang, Y.-Y., Finoguenov, A., et al. 2010, Astrophys. J., 721, 875

Pakmor, R., Springel, V., Coles, J. P., et al. 2023, Monthly Notices of the Royal Astronomical Society, 524, 2539

Paulus, M. 2021, PhD thesis, Ludwig-Maximilians-Universität in Munich, Germany, https://doi.org/10.5282/edoc.28090

Peebles, P. J. E. 1981, The Large-Scale Structure of the Universe

Pillepich, A., Nelson, D., Hernquist, L., et al. 2018, Mon. Not. R. Astron. Soc., 475, 648

Planck Collaboration, Ade, P. A. R., Aghanim, N., et al. 2016, Astron. Astrophys., 594, A24

Planck Collaboration, Aghanim, N., Akrami, Y., et al. 2020, Astron. Astrophys., 641, A6

Planck Collaboration & et al. 2016, Astron. Astrophys., 594, A13

Planelles, S., Borgani, S., Fabjan, D., et al. 2013a, Monthly Notices of the Royal Astronomical Society, 431, 1487

Planelles, S., Borgani, S., Fabjan, D., et al. 2013b, Monthly Notices of the Royal Astronomical Society, 438, 195–216

Pratt, G. W., Arnaud, M., Biviano, A., et al. 2019, Space Sci. Rev., 215, 25

Pratt, G. W., Croston, J. H., Arnaud, M., & Böhringer, H. 2009, Astron. Astrophys., 498, 361

Predehl, P., Andritschke, R., Arefiev, V., et al. 2021, Astron. Astrophys., 647, A1

Press, W. H. & Schechter, P. 1974, Astrophys. J., 187, 425

Preston, C., Amon, A., & Efstathiou, G. 2023, Monthly Notices of the Royal Astronomical Society, 525, 5554

Ragagnin, A., Dolag, K., Biffi, V., et al. 2017, Astronomy and Computing, 20, 52

Ragagnin, A., Saro, A., Singh, P., & Dolag, K. 2020, MNRAS, 500, 5056

Ricker, P. M. & Sarazin, C. L. 2001, The Astrophysical Journal, 561, 621

Rogers, K. K., Hložek, R., Laguë, A., et al. 2023, Journal of Cosmology and Astroparticle Physics, 2023, 023

Rykoff, E. S., Rozo, E., Busha, M. T., et al. 2014, Astrophys. J., 785, 104

Salcido, J., McCarthy, I. G., Kwan, J., Upadhye, A., & Font, A. S. 2023, Monthly Notices of the Royal Astronomical Society, 523, 2247

Sarazin, C. L. 1986, Reviews of Modern Physics, 58, 1

Schaye, J., Crain, R. A., Bower, R. G., et al. 2015, Mon. Not. R. Astron. Soc., 446, 521

Schaye, J., Kugel, R., Schaller, M., et al. 2023, Monthly Notices of the Royal Astronomical Society, 526, 4978

Schneider, A., Giri, S. K., Amodeo, S., & Refregier, A. 2022, Monthly Notices of the Royal Astronomical Society, 514, 3802

Schneider, A., Kovač, M., Bucko, J., et al. 2025, Baryonification: An alternative to hydrodynamical simulations for cosmological studies

Schneider, A. & Teyssier, R. 2015, Journal of Cosmology and Astroparticle Physics, 2015, 049

Schneider, A. & Teyssier, R. 2020, Journal of Cosmology and Astroparticle Physics, 2020, 019

Schneider, P. 2006, Weak Gravitational Lensing (Springer Berlin Heidelberg), 269–451

Secco, L. F., Amon, A., MacCrann, N., et al. 2022, Physical Review D, 105, 023515

Semboloni, E., Hoekstra, H., Schaye, J., van Daalen, M. P., & McCarthy, I. G. 2011, Monthly Notices of the Royal Astronomical Society, 417, 2020

Severini, T. A. 2004, Bernoulli, 10, 421

Sevilla-Noarbe, I., Bechtol, K., Carrasco Kind, M., et al. 2021, Astrophys. J. Suppl. Ser., 254, 24

Sheldon, E. S. & Huff, E. M. 2017, Astrophys. J., 841, 24

Sheth, R. K. & Tormen, G. 1999, Monthly Notices of the Royal Astronomical Society, 308, 119

Sifón, C., Menanteau, F., Hasselfield, M., et al. 2013, The Astrophysical Journal, 772, 25

Sijacki, D., Springel, V., Di Matteo, T., & Hernquist, L. 2007, Mon. Not. R. Astron. Soc., 380, 877

Simet, M., McClintock, T., Mandelbaum, R., et al. 2017, Monthly Notices of the Royal Astronomical Society, 466, 3103

Singh, A., Mohr, J. J., Davies, C. T., et al. 2025, Astron. Astrophys., 695, A49

Singh, A., Mohr, J. J., Davies, C. T., Bocquet, S., et al. 2025a, Constraining the baryonic suppression of P(k) using the galaxy cluster ICM mass to halo mass relation, in preparation

Singh, A., Mohr, J. J., Davies, C. T., Bocquet, S., et al. 2025b, Insights into galaxy cluster matter profiles, in preparation

Singh, P., Saro, A., Costanzi, M., & Dolag, K. 2020, Monthly Notices of the Royal Astronomical Society, 494, 3728

Sobotka, A. C., Erickcek, A. L., & Smith, T. L. 2024, Signatures of Very Early Dark Energy in the Matter Power Spectrum

Springel, V., Pakmor, R., Pillepich, A., et al. 2017, Monthly Notices of the Royal Astronomical Society, 475, 676

Springel, V., Pakmor, R., Pillepich, A., et al. 2018, Mon. Not. R. Astron. Soc., 475, 676

Sunyaev, R. A. & Zeldovich, Y. B. 1972, Comments on Astrophysics and Space Physics, 4, 173

Sunyaev, R., Arefiev, V., Babyshkin, V., et al. 2021, A&A, 656, A132

Teklu, A. F., Remus, R.-S., Dolag, K., et al. 2015, Astrophys. J., 812, 29

Tinker, J., Kravtsov, A. V., Klypin, A., et al. 2008, Astrophys. J., 688, 709

To, C., Krause, E., Rozo, E., et al. 2021, Phys. Rev. Lett., 126, 141301

Tonnesen, S. & Bryan, G. L. 2008, Astrophys. J. Lett., 684, L9

Truemper, J. 1982, Advances in Space Research, 2, 241

Umetsu, K. 2020, The Astronomy and Astrophysics Review, 28

Umetsu, K., Medezinski, E., Nonino, M., & et al. 2014a, The Astrophysical Journal, 795, 163

Umetsu, K., Medezinski, E., Nonino, M., et al. 2014b, Astrophys. J., 795, 163

Umetsu, K., Zitrin, A., Gruen, D., et al. 2016, Astrophys. J., 821, 116

Vainshtein, A. I. 1972, Physics Letters B, 39, 393

van Daalen, M. P., McCarthy, I. G., & Schaye, J. 2020, Mon. Not. R. Astron. Soc., 491, 2424

van Daalen, M. P., Schaye, J., Booth, C. M., & Dalla Vecchia, C. 2011a, Monthly Notices of the Royal Astronomical Society, 415, 3649

van Daalen, M. P., Schaye, J., Booth, C. M., & Dalla Vecchia, C. 2011b, Monthly Notices of the Royal Astronomical Society, 415, 3649

Vanderlinde, K., Crawford, T. M., de Haan, T., et al. 2010, Astrophys. J., 722, 1180

Varga, T. N., DeRose, J., Gruen, D., et al. 2019, Mon. Not. R. Astron. Soc., 489, 2511

Vikhlinin, A. & et al. 2009, The Astrophysical Journal, 692, 1060

Vikhlinin, A., Kravtsov, A., Forman, W., et al. 2006, Astrophys. J., 640, 691

Vikhlinin, A., Kravtsov, A., Forman, W., et al. 2006, Astrophys. J., 640, 691–709

Vikhlinin, A., Kravtsov, A. V., Burenin, R. A., et al. 2009a, Astrophys. J., 692, 1060

Vikhlinin, A., Kravtsov, A. V., Burenin, R. A., et al. 2009b, Astrophys. J., 692, 1060

Vikhlinin, A. et al. 2009, The Astrophysical Journal, 692, 1060

Voges, W., Aschenbach, B., Boller, T., et al. 1999, Astron. Astrophys., 349, 389

Voges, W., Aschenbach, B., Boller, T., et al. 2000, VizieR Online Data Catalog, IX/29

Vogt, S. M. L., Bocquet, S., Davies, C. T., Mohr, J. J., & Schmidt, F. 2024a, Phys. Rev. D, 109, 123503

Vogt, S. M. L., Bocquet, S., Davies, C. T., et al. 2024b, submitted to Phys. Rev. D, arXiv:2409.13556

Vogt, S. M. L., Marsh, D. J. E., & Laguë, A. 2023, Phys. Rev. D, 107, 063526

Voit, G. M. 2005, Reviews of Modern Physics, 77, 207

von der Linden, A., Allen, M. T., Applegate, D. E., et al. 2014, Mon. Not. R. Astron. Soc.,

439, 2

White, S. D. M., Efstathiou, G., & Frenk, C. S. 1993, Mon. Not. R. Astron. Soc., 262, 1023

Willis, J. P., Oguri, M., Ramos-Ceja, M. E., et al. 2021, Monthly Notices of the Royal Astronomical Society, 503, 5624

Zhou, C., Wu, H.-Y., Salcedo, A. N., et al. 2023, Forecasting the constraints on optical selection bias and projection effects of galaxy cluster lensing with multiwavelength data

Zubeldia, Í. & Challinor, A. 2019, Mon. Not. R. Astron. Soc., 489, 401

Acknowledgments

I acknowledge financial support from the MPG Faculty Fellowship program and the Ludwig-Maximilians-Universität (LMU-Munich).

The South Pole Telescope program is supported by the National Science Foundation (NSF) through the Grant No. OPP-1852617. Partial support is also provided by the Kavli Institute of Cosmological Physics at the University of Chicago. PISCO observations were supported by US NSF grant AST-0126090. Work at Argonne National Laboratory was supported by the U.S. Department of Energy, Office of High Energy Physics, under Contract No. DE-AC02-06CH11357.

Funding for the DES Projects has been provided by the U.S. Department of Energy, the U.S. National Science Foundation, the Ministry of Science and Education of Spain, the Science and Technology Facilities Council of the United Kingdom, the Higher Education Funding Council for England, the National Center for Supercomputing Applications at the University of Illinois at Urbana-Champaign, the Kavli Institute of Cosmological Physics at the University of Chicago, the Center for Cosmology and Astro-Particle Physics at the Ohio State University, the Mitchell Institute for Fundamental Physics and Astronomy at Texas A&M University, Financiadora de Estudos e Projetos, Fundação Carlos Chagas Filho de Amparo à Pesquisa do Estado do Rio de Janeiro, Conselho Nacional de Desenvolvimento Científico e Tecnológico and the Ministério da Ciência, Tecnologia e Inovação, the Deutsche Forschungsgemeinschaft and the Collaborating Institutions in the Dark Energy Survey.

The Collaborating Institutions are Argonne National Laboratory, the University of California at Santa Cruz, the University of Cambridge, Centro de Investigaciones Energéticas, Medioambientales y Tecnológicas-Madrid, the University of Chicago, University College London, the DES-Brazil Consortium, the University of Edinburgh, the Eidgenössische Technische Hochschule (ETH) Zürich, Fermi National Accelerator Laboratory, the University of Illinois at Urbana-Champaign, the Institut de Ciències de l'Espai (IEEC/CSIC), the Institut de Física d'Altes Energies, Lawrence Berkeley National Laboratory, the Ludwig-Maximilians Universität München and the associated Excellence Cluster Universe, the University of Michigan, NSF's NOIRLab, the University of Nottingham, The Ohio State University, the University of Pennsylvania, the University of Portsmouth, SLAC National Accelerator Laboratory, Stanford University, the University of Sussex, Texas A&M University, and the OzDES Membership Consortium.

Based in part on observations at Cerro Tololo Inter-American Observatory at NSF's NOIRLab (NOIRLab Prop. ID 2012B-0001; PI: J. Frieman), which is managed by the

Association of Universities for Research in Astronomy (AURA) under a cooperative agreement with the National Science Foundation.

The DES data management system is supported by the National Science Foundation under Grant Numbers AST-1138766 and AST-1536171. The DES participants from Spanish institutions are partially supported by MICINN under grants ESP2017-89838, PGC2018-094773, PGC2018-102021, SEV-2016-0588, SEV-2016-0597, and MDM-2015-0509, some of which include ERDF funds from the European Union. IFAE is partially funded by the CERCA program of the Generalitat de Catalunya. Research leading to these results has received funding from the European Research Council under the European Union's Seventh Framework Program (FP7/2007-2013) including ERC grant agreements 240672, 291329, and 306478. We acknowledge support from the Brazilian Instituto Nacional de Ciência e Tecnologia (INCT) do e-Universo (CNPq grant 465376/2014-2).

This manuscript has been authored by Fermi Research Alliance, LLC under Contract No. DE-AC02-07CH11359 with the U.S. Department of Energy, Office of Science, Office of High Energy Physics.

I am also grateful to the many individuals who have supported and inspired me personally throughout this journey.

First and foremost, I would like to express my deepest gratitude to my supervisor, Joe Mohr, for his invaluable guidance, encouragement, and support throughout my PhD journey. His insights and expertise have been instrumental in shaping my research, and I am incredibly grateful for the opportunity to learn from him.

I would also like to thank Chris Davies, Sebastian Bocquet, Matthias Klein, and Sebastian Grandis for their support and collaboration during my research. Their advice, discussions, and encouragement have made this journey productive and enjoyable.

I am deeply grateful to my friends—Christiane, Daniel, Sophie, Elena, Thomas, Stefan, Tirso, Peter, Matteo, Antonia, Robert, Soumya, Amelie, Rita, Lucía, Adrián, Momo, Jordan, and Iggy—for making life outside of research so much fun. The countless moments of laughter, adventure, and distraction have been invaluable in keeping me balanced and motivated.

Finally, I thank my family for their constant love and support, which means everything to me.